UNIVERSITY OF CAPE TOWN
IYUNIVESITHI YASEKAPA • UNIVERSITEIT VAN KAAPSTAD

A Methodology for Coupled CFD-DEM Modelling of Particulate Suspension Rheology

A Thesis Submitted for the Degree of
DOCTOR OF PHILOSOPHY

by:

Evan Matthew Smuts

Department of Chemical Engineering
Faculty of Engineering and the Built Environment
UNIVERSITY OF CAPE TOWN

July 2015

DECLARATION

I hereby certify that the work embodied in this thesis is the result of original research and has not been submitted for another degree at any other university or institution.

Signature: ……

Name: Evan Matthew Smuts

ACKNOWLEDGEMENTS

I would like to extend my gratitude to the following people for their valuable help and support during the course of this project:

Prof. Dave Deglon and Prof. Chris Meyer: for offering invaluable guidance, support and endless patience during the course of the project.

The Minerals to Metals (MtM) initiative, the Centre for Minerals Research (CMR), as well as the Centre for Research in Computational and Applied Mechanics (CERECAM) at UCT for their support and funding.

Prof. J-P Franzidis: his help and encouragement was always appreciated.

Dr. Chris Goniva and Dr. Christoph Kloss of DCS Computing GmbH: for developing the CFDEM and LIGGGHTS software codes. I really appreciate the many emails and discussions regarding CFD-DEM coupling, and your help with de-bugging software problems.

Bulelwa Ndlovu: for her help in understanding the nature of her experimental work.

Jean-Paul Pelteret and Harish Appa: for their help and guidance with the Fluent® and Gambit® software packages, and many CFD-related discussions.

Jonathan Bergh: for the many thought-provoking discussions about numerical modelling.

Graham Inggs: for software and technical support, especially regarding the Chimera computing cluster.

Andrew Lewis, Timothy Carr, and the UCT ICTS HPC team: for their technical support with the ICTS HPC and HEX computing clusters.

PUBLICATIONS

Peer-Reviewed Publications

The work in this thesis has led to the following peer-reviewed publications:

Smuts, EM, Deglon, DA and Meyer, CJ, 2012. Methodology for coupled CFD-DEM modelling of particulate suspension rheology. *In Proceedings of Ninth International Conference on Computational Fluid Dynamics in the Minerals and Process Industries*, Melbourne, 10-12 December. ISBN 978-1-922173-01-0.

Smuts, EM, Deglon, DA and Meyer, CJ, 2012. Methodology for coupled CFD-DEM modelling of particulate suspension rheology. *In Proceedings of XXVI International Mineral Processing Congress*, New Delhi, 24-28 September. ISBN 81-901714-3-7.

Smuts, EM, Deglon, DA and Meyer, CJ, 2015. A Coupled CFD-DEM Model for Particulate Suspension Modelling. *Progress in Computational Fluid Dynamics*. (submitted for publication).

Conference Presentations

Parts of this work were also presented at the following conferences:

Smuts, EM, Deglon, DA, and Meyer, CJ, 2012. Methodology for coupled CFD-DEM modelling of particulate suspension rheology. *Presented at the 4th Southern African Conference on Rheology*. South African Society of Rheology (SASOR), Cape Town, 10-12 September.

Smuts, EM, Deglon, DA, and Meyer, CJ, 2012. Methodology for coupled CFD-DEM modelling of particulate suspension rheology. *Presented at the Mineral Processing 2012*. SAIMM Conference, Cape Town, 2-3 August.

Smuts, EM, Deglon, DA and Meyer, CJ, 2011. Numerical modelling of particulate suspension rheology. *Presented at Mineral Processing 2011.* SAIMM Conference, Cape Town, 4-5 August.

ABSTRACT

The flow properties, or rheology, of particulate suspensions are highly dependent on the properties of the particles suspended within the base fluid (e.g. size, shape and surface properties). An understanding of the suspension rheology can help in the prediction of its behaviour under various flow conditions. Many studies focus on the experimental measurement of suspension properties, commonly employing devices such as rheometers to measure fluid properties under different conditions. A numerical model that is able to simulate the real-world interactions that determine particulate suspension rheology would complement those experimental studies. Accordingly, this work outlines a methodology for the development of such a model.

Due to the differences between the two phases in a suspension, two different numerical methods were used, namely Computational Fluid Dynamics (CFD) and the Discrete Element Method (DEM). CFD uses a continuum approach to model the fluid component, while DEM resolves the behaviour of each individual particle. Two separate software programmes were used. For CFD, OpenFOAM® was chosen, and for DEM, a programme called LIGGGHTS was used. These two different codes were coupled together with another programme called CFDEM. All three packages are open source software.

To measure the rheology of the mixture, it was decided to simulate a rheometer. In particular, a rate-controlled, concentric-cylinder arrangement was chosen. Flow would be driven by a moving inner wall. Particle surface charge was accounted for by including both the van der Waals and electrostatic long-range forces between particles. This combination is known as the DLVO force. Plain particles, with no DLVO forces, were also considered.

To the author's knowledge, using a coupled CFD-DEM approach to model suspension rheology had never been attempted before. Therefore, it was decided the development of the model would be done in stages, adding more complexity as each stage proved successful.

The first step was to model a reduced rheometer geometry using CFD. Both a Newtonian and a non-Newtonian single-phase fluid were tested. Water and a Herschel-Bulkley mineral slurry were used respectively. Different rheometer geometries were tested. Results from these models correlated well with experimental values. The single-gap rheometer geometry with a 500μm gap between the inner and outer walls was found to perform the best. Final CFD model parameters used in these simulations were used as the basis for the coupled model.

To reduce computational complexity, the model size and shape had to be reduced from a full-sized rheometer to that of a small rectangular box, with opposing flat walls acting as inner and outer cylinders of a rheometer. This improved computational efficiency. CFD tests conducted on the new box geometry showed that a box with sides of length 50μm produced results equivalent to larger, full-sized, single-gap rheometer geometries with curved walls. DEM particles were then added to create a coupled CFD-DEM model. Spherical particles 1.5μm in diameter were used, with water as the suspending fluid.

Tests were conducted with the coupled model using 20% solids volume fraction to determine an appropriate range of settings for the model. Parameters such as time step size and coupling interval were explored to determine the best combination. The rate at which the shear rate changed (ramp rate) and size of the box model dimensions were also investigated.

A baseline DEM time step size of 2.5e-9s and coupling interval of 100 were determined using the Rayleigh time criteria and the particle response time. These baseline values were found to be acceptable for all simulations, though these values could be varied in some cases to improve computational speed. In particular, larger time steps could be used with slower ramp rates and larger domain sizes (i.e. gap widths). A fast ramp rate was initially used due to various model constraints, but was shown to be suitable for all cases. Slower ramp rates generated larger shear stresses at low shear rates, but the simulations became unstable after a certain point. Testing showed the model geometry was size-independent in the flow and vertical directions, but the magnitude of the apparent viscosity was found to be dependent on the gap width size. Gap width was varied from 50 to 500μm, and the viscosity scaled accordingly. This was attributed to wall-slip effects

between the moving wall and the particle-fluid mixture in the wall region. This phenomenon has been noted by other researchers in the literature.

Using suitable model parameters, the coupled model was tested against the influence of particle surface charge and particle volume fraction. Fluid velocity profiles across the gap between the inner and outer walls were examined. The model was also compared against experimental data found in the literature for a suspension of spherical zirconia particles.

When examining the fluid velocity profiles in the gap, plain particles (no DLVO forces) produced flow profiles similar to that of water, though with some lag. This was most likely due to the larger inertia of the dense particles in the fluid. Particles with DLVO forces produced profiles with high shear gradients at the walls, and plug-like flow in the bulk flow in the centre of the gap. This profile indicated that wall slip occurred within the system.

Particle volume fractions ranging from 4.58 to 40% were tested. As expected, the model showed that an increasing volume fraction did increase the resultant viscosity. Different particle surface charges were tested. The resulting DLVO potentials ranged from the fully attractive (where the van der Waals attraction dominated) zeta potential (0mV), to less attractive potentials (up to 50mV zeta potential). As expected, greater attraction forces between particles resulted in higher suspension viscosity. Less attractive DLVO potentials tended to produce viscosities closer to that of plain particles (i.e. no inter-particle forces).

When compared to experimental data, the model produced correct shear-thinning trends. However, the values for the 50μm box were too low. It was found that the 500μm gap width model produced values of similar order of magnitude to the experimental values. This gap width was the same as that used for the experimental tests. This illustrated the gap-width dependence of the model results.

In all cases, no evidence of a yield stress was found. This may be due to the initialisation of the particles in DEM, where the particles were initially evenly spread out and did not have time to form aggregates (a process which can lead to yield stresses in particulate

suspensions). Wall slip in the system would have also influenced the behaviour at low shear rates. However, it should also be noted that some researchers believe the yield stress is not a real phenomenon, and is merely an artefact of an extrapolated yield stress at low shear rates.

In summary, a coupled CFD-DEM model has been developed using the methodology outlined in this thesis. Various numerical parameters were investigated, and an appropriate range for these parameters was found. This model was tested against varying rheological parameters such as particle surface charge and particle volume fraction, and was found to produce reasonable trends. When compared to experimental data, the model produced results within an order of magnitude of the experimental values. This is encouraging for a preliminary model of this type. Future work should look at wall slip in the model and investigate ways to reduce its influence on the results. One example of this is to model the rheometer walls as roughened surfaces.

TABLE OF CONTENTS

LIST OF APPENDICES

LIST OF FIGURES

LIST OF TABLES

LIST OF SYMBOLS

Roman Symbols

$a_{P,N}$	matrix co-efficient of dependent variable ϕ for cell node P or N
A	area (m^2)
A_H	Hamakar constant (J)
C_D	drag coefficient
C_L	lift coefficient
C_O	Courant-Friedrich-Levy (CFL) number
d	vector distance between two computational cell centres (m)
d_i	diameter of particle i (m)
D	separation distance between two particle surfaces (m)
	gap width of concentric cylinder rheometer (m)
E	energy (J)
e	electrostatic charge (C)
	charge on an electron, or elementary charge ($1.60217657 \times 10^{-19}$ C)
f	force experienced by a particle (N)
F	interaction force between fluid and particle (N)
	rheometer conversion factor
g	gravitational acceleration ($m.s^{-2}$)
G	shear modulus of particle (Pa)
h	Planck's constant ($6.62606957 \times 10^{-34}$ $m^2.kg.s^{-1}$)
H	height dimension of rheometer (m)
I	rotational inertia of a particle ($kg.m^2$)
	ionic strength (M, mol/L) (L = litre)
k	spring stiffness of particle ($N.m^{-1}$ or $kg.s^{-2}$)
	consistency parameter for Herschel-Bulkley viscosity model (Pa.s)
k_B	Boltzman constant ($1.3806488 \times 10^{-23}$ $m^2.kg.s^{-2}.K^{-1}$)
K_{pf}	momentum exchange co-efficient (for a CFD cell) ($kg.m^{-3}.s^{-1}$)
m	mass of particle (kg)
n	flow index (exponent) for the Herschel-Bulkley viscosity model
n_i	number concentration of ions per unit volume (for particle i) (m^{-3})

$n_{1,2,3}$	refractive index of media 1, 2, or 3
N_A	Avogadro's constant (6.02214129 x 10^{23} mol^{-1})
p	fluid pressure (Pa)
Pe	Péclet number (for either a particle or a CFD cell)
r	radius of spherical particle (m)
$r_{cut-off}$	cut-off distance for long-range inter-particle forces (m)
R	centre-to-centre distance between two particles (m)
	matrix of source terms
$R_{1,2,3}$	different radii for concentric-cylinder rheometer geometry
Re	Reynolds number
S_M	momentum source term in fluid momentum equation
Sp	linear (implicit) component of the fluid momentum equation source term
Su	explicit component of the fluid momentum equation source term
t	time (s)
T	torque (N.m)
	temperature (K)
Ta	Taylor number
u	fluid velocity vector (m/s)
v	particle velocity (m/s)
V	volume, for a particle or cell (m^3)
Y	Young's modulus (Pa)
z	valence of an ion

Greek Symbols

α	Alpha, under-relaxation factor
	Di Felice drag force exponent
β	Beta, inter-phase momentum transfer coefficient (for particle) ()
γ	Gamma, shear strain
	particle collision damping co-efficient
	blending co-efficient for blended differencing scheme
$\dot{\gamma}$	Gamma dot, rate of shear strain, i.e. shear rate (s^{-1})

Γ	Gamma (capitalised), generic label for diffusion co-efficient (kg/m.s)
δ	Delta, particle overlap (m)
ε_0	Epsilon, permittivity of free space (C^2/J.m)
$\varepsilon_{1,2,3}$	Epsilon, relative permittivity, or dielectric constant, of media 1, 2, or 3 in suspension
$\varepsilon_{f,p}$	Epsilon, fluid (f) or particle (p) volume fraction in a cell
ζ	Zeta, electric or zeta potential (V)
κ	Kappa, inverse Debye constant (m^{-1})
λ	Lambda, second, or bulk, viscosity (kg/m.s) (Pa.s)
λ_e	interpolation co-efficient at cell face *e*
μ	Mu, apparent (dynamic) viscosity (kg/m.s) (Pa.s)
μ_f	friction co-efficient between a particle and another particle or a wall.
ν	Nu, kinematic viscosity (m^2/s)
	Poisson's ratio
ρ	Rho, density (kg/m^3)
σ	Sigma, normal stress (Pa)
τ	Tau, shear stress (Pa)
τ_y	Yield stress (Pa)
υ_e	Upsilon, main absorption frequency in ultra-violet region (Hz)
ϕ	Phi, generic label for dependent variable in CFD
ψ	Psi, (particle) surface potential (V)
ω	Omega, rotational velocity of particle or rheometer (rad/s)
	vorticity of fluid (1/s)

Sub/Superscripts

1, 2, 3	different solid/fluid media
c	contact or collision (e.g. a force)
CnS	Cundall and Strack
i, j, k	particle number, or tensor component direction
ij	force/torque/etc. acting on particle *i* by particle *j* (or other sources)
edl	electric double-layer (electrostatic force)

f	fluid
	cell face
g	gravitational (e.g. a force)
∞	infinity, i.e. medium surrounding body/particle of interest
n	normal direction (usually perpendicular to a plane)
nc	non-contact
N	neighbouring computational cell
p	particle
P	current computational cell
pf	particle-fluid interaction (e.g. a force)
t	tangential direction
vdw	van der Waals
x, y, z	axis directions

** bold symbols denote vector quantities

1. INTRODUCTION

Particulate suspensions are found in a variety of industries, e.g. chemical, mining, food processing, and cosmetics. The flow properties, or rheology, of particulate suspensions are highly dependent on the properties of the particles suspended within the base fluid (e.g. size, shape and surface properties). An understanding of the suspension rheology can help in the prediction of its behaviour under various flow conditions. As a result, the study of particulate suspension rheology has become increasingly important. Many studies focus on the experimental measurement of fluid properties, commonly employing devices such as rheometers to measure fluid properties under different conditions. A numerical model that is able to simulate the real-world interactions that determine particulate suspension rheology would complement those experimental studies. Accordingly, this work outlines a methodology for the development of such a model.

1.1. RHEOLOGY OF SUSPENSIONS

Fluids can be categorised based on their reaction to changes in shear rate (cf. Figure 1.1). Suspensions typically exhibit shear-thinning behaviour (pseudoplastic fluid in Figure 1.1). Macroscopic rheological behaviour of particulate suspensions is controlled on the microscopic level by interactions between individual particles as well as their interaction with the surrounding fluid (Zhou et al., 2001; Zhu et al., 2007). This depends on the nature and density of any inter-particle forces as well as the corresponding microstructure formed by the particles. An increased particle concentration will increase the intensity of interactions, thereby changing the rheology of the fluid. Inter-particle forces can cause particles to stick together, causing agglomerates that restrict fluid flow. Alternatively the particles can repel each other, allowing the fluid to flow more freely. At rest, strong cohesive forces between particles can create physical structures that resist flow, giving rise to a phenomenon called the yield stress. This is considered to be the minimum stress that must be applied to the mixture to initiate flow (Barnes, 1999).

As a result, a base fluid that originally had Newtonian characteristics, can acquire non-Newtonian characteristics through the addition of solid particles. Understanding the relationship of inter-particle forces and the microstructure within the fluid is vital to

understanding the behaviour of particulate suspensions, and producing meaningful results (Zhu et al., 2007). To simplify analyses, most fundamental studies consider suspensions of mono-disperse spheres. However, real systems nearly always differ from this ideal case, being poly-disperse or containing ellipsoids, platelets and more irregular shapes (Mewis and Wagner, 2009).

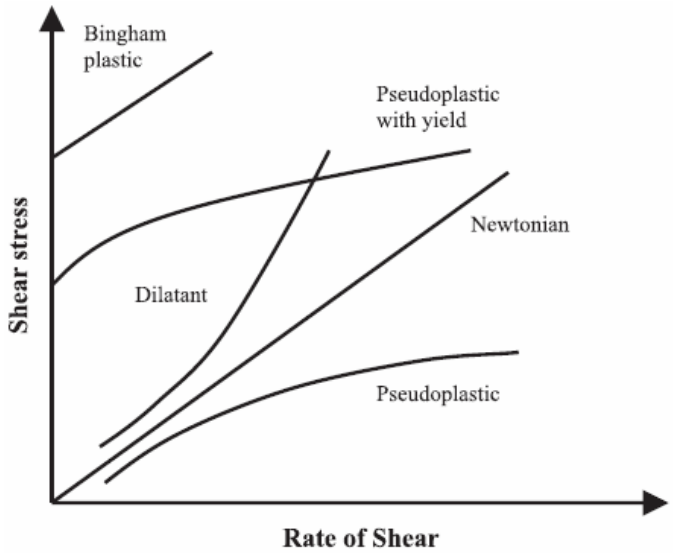

Figure 1.1: Graph showing different types of fluid behaviours (He et al., 2004)

When trying to predict the macroscopic behaviour, few theories account for the behaviour of individual particles on the microscopic level. They only measure the combined macroscopic result of all the interactions. While this may work for simple, homogeneous, systems, they are not strictly valid for more complex systems of say irregularly-shaped particles. Therefore a different approach is needed, one that can take account of the particles themselves. This is where numerical modelling could be of use. Individual particles of any kind can be created in a virtual environment, tailored to suit the dynamics of interest. Inter-particle and particle-fluid interactions can be controlled and the resulting reactions can be studied.

1.2. REASONS FOR CHOOSING A NUMERICAL MODEL

Understanding the interplay of these interactions and their resulting macroscopic behaviour can be aided by visualising and quantifying the processes that occur inside the fluid. This is not always practical, or even possible, with current experimental methods.

In addition, solution algorithms and physical models are becoming more reliable, and computing power is increasing ever faster, which makes simulating real-world processes more practical. Hence numerical models are gaining popularity as a peer methodology to conventional experimental research. Below are some benefits of using a numerical model:

- Numerical models can produce results beyond the range achievable with experimental methods. This is because computer models are not limited by experimental methods or available materials.
- A computer-based numerical model is not constrained by the geometry of a specific apparatus, therefore different test geometries can also be explored, e.g. cylindrical or rotating vane rheometers.
- Physical factors such as particle size, shape and electrical charge can be tightly controlled within a model to determine their exact effect.

As such, a numerical model would complement experimental research, and enhance the understanding of the fundamental factors that affect fluid rheology. Using various mathematical techniques, a virtual fluid with particles can be simulated and studied.

The device commonly used to measure the rheology of a fluid is the rheometer. Therefore, an equivalent rheological study of a virtual fluid would require the simulation of a rheometer, or at least the dominant features of a rheometer (such as the geometry and internal fluid flow).

1.3. AVAILABLE MODELLING TECHNIQUES

There are a number of available methods that can be used to model particles and particle-fluid systems. The merits of these different methods will be discussed here.

1.3.1. Types of Numerical Models

Many numerical methods have been used to model particles in fluid flow. These include Two-Fluid Multiphase (TFM) Models (Anderson and Jackson, 1967), Direct Numerical Simulation (DNS) (Sharma and Patankar, 2005; Apte et al., 2009; Wachs, 2009), and a

coupling of Computational Fluid Dynamics (CFD) and the Discrete Element Method (DEM) (Tsuji et al., 1993; Xu and Yu, 1997; Feng and Yu, 2003). This coupling has also been recently referred to as the Combined Continuum and Discrete Method (CCDM) (Feng and Yu, 2003; Zhu et al., 2007; Yang et al., 2008; Chu et al., 2009).

However, the challenge is to find a model that is sufficiently accurate, without being too computationally expensive. Two-Fluid models are comparatively inexpensive as they are based on basic CFD solvers that model both phases as a fluid continuum. They approximately model the solid phase as a second "fluid" that interacts with the original fluid, and as such do not model the individual particle interactions. DNS models on the other hand are computationally expensive as they directly model the fluid flow on a scale that is much smaller than the particle size. Here the particle-fluid interactions can be modelled directly because particles can be used as solid boundaries within the flow domain. CFD-DEM methods offer a middle ground. They model the fluid phase as a continuum, but directly model the individual particles and their motion. The concept of coupling these two different styles is illustrated in Figure 1.2.

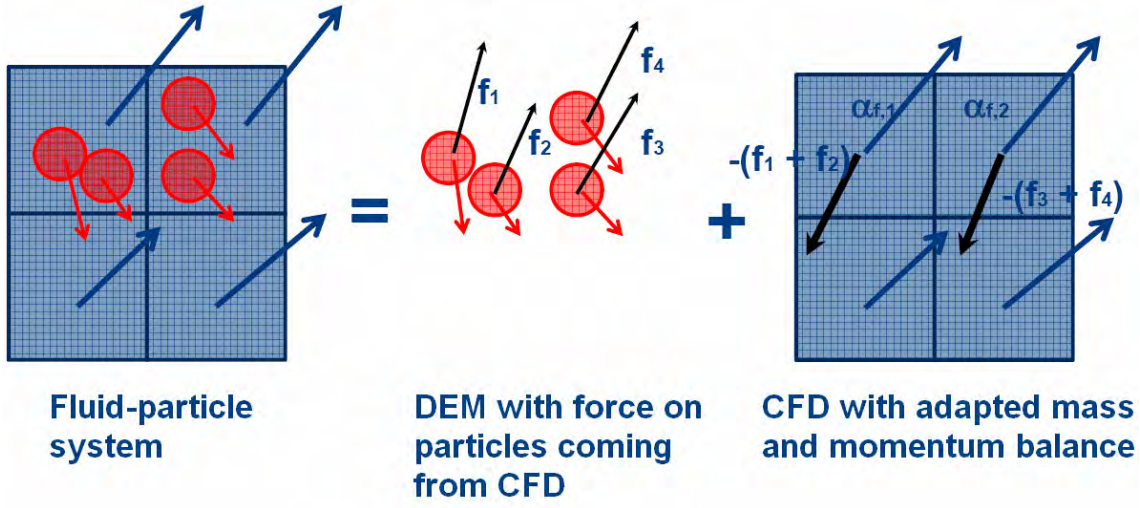

Figure 1.2: Schematic of the CFD-DEM approach showing how the final product results from a combination of the separate fluid and particle components (Goniva et al., 2009)

DEM, originally developed by Cundall and Strack (1979), has several advantages over the Two-Fluid continuum model. For example, particle size and density distribution can be calculated directly in the simulation, because characteristic properties of the individual

particles such as size and density can be specified. Another advantage is that parameters affecting inter-particle collisions can be determined from material properties such as the Young's modulus, Poisson ratio and coefficient of restitution. In addition, long-range forces, which are of interest in this study, can be directly applied to specific particles. This means that discrete-particle approaches require fewer assumptions than a Two-Fluid model.

One disadvantage of the DEM approach is that the computation time becomes extremely long when the number of particles is of the same order as found in real flows of fine materials (Tsuji et al., 1993). Therefore the size of the system would have to be limited when looking at finer particle sizes.

Coupling of DEM with a finite-volume, continuum description of the fluid-phase based on the Navier–Stokes equations was first reported in literature by Tsuji et al. (1993). They used the "soft-sphere" approach of Cundall and Strack (1979) to handle particle collisions. Hoomans et al. (1996) are credited with first using the "hard-sphere" approach for CFD-DEM modelling (Deen et al., 2007). Tsuji et al. (1993) proposed using CFD cells that were much larger than the particle size, thereby modelling the particles as a continuous porous medium to calculate the pressure gradient. This was essentially the same approach as used in the so-called Model A that is often discussed in more recent literature (cf. Section 3.4). Depending on the complexity of the system's physics, certain interactions are often ignored for simplicity and computational efficiency. Models that only consider the influence of one medium on another (e.g. for a few light particles transported by air, the influence of the particles on the fluid can be ignored). This is known as one-way coupling. If the exchange between the phases becomes important (e.g. turbulence or large particle concentrations), then two-way coupling is required. Four-way coupling accounts for all interactions (particle-fluid, fluid-particle, and particle-particle).

Numerical modelling of particulate suspension flow properties (rheology) is not common. Of the few papers that covered this topic, most (Patankar and Hu, 2002; Cho et al., 2005; Mammoli, 2002) used DNS to model the fluid flow and particle motion. However, when considering general simulations of particle-fluid interactions, most of the literature concerned fluidised bed models, where a fluid is injected into a bed of granules causing

fluidic motion of that bed. Fluidised beds were also the main focus of research using CFD-DEM methods to model particle-fluid systems (Hoomans et al., 1996; Mikami et al., 1997; Xu and Yu, 1997; Feng and Yu, 2003; Deen et al., 2007; Zhu et al., 2007). In addition, much of the earlier work using CFD-DEM made many assumptions to simply the problem, such as assuming inviscid fluid flow (e.g. Tsuji et al., 1993).

1.3.2. Particle Shape

Particles in mineral slurries, for example, can vary in shape quite dramatically depending on the material type. Shapes range from cylindrical tubes, to flat plate-like particles, to more regular cubic forms. Their shape affects their motion in the suspending fluid, and determines the location of the surface charge on the particle. However, most literature was concerned with the simulation of spherical particles (e.g. Hoomans et al., 1996; Mikami et al., 1997; Xu and Yu 1997; Feng and Yu, 2003; Li and Kuipers, 2003; Beetstra et al., 2007; Deen et al., 2007; Zhu et al., 2007). This was because spherical particles were easy and computationally inexpensive to model due their simple shape (based solely on a radius).

There have been a limited number of studies where the drag force on other particle shapes had been considered (Yamamoto and Matsuoka, 1999; Yin et al, 2003; Markauskas, 2006; Holzer and Sommerfeld, 2009). Some studies approximated ellipsoids and cubes by using “super-quadrics” (Cleary, 2007; Hilton et al., 2010). Here the exponents of an equation, which describes the particle shape, can be made to approximate different shapes from spherical, to ellipsoid, to cubic. Super-quadrics are convenient in describing complex particle shapes, though assigning collision and electrostatic forces to these shapes would not be simple.

One solution is to model particles as a collection of spheres, similar to that of Yamamoto and Matsuoka (1999). Particles are formed by locking the position of the spheres in relation to each other to create the desired shape. The interaction of these connected particles can also be controlled to simulate the behaviour of the particle. This maintains simplicity in that only distinct points need to be handled, while also describing a more complex overall shape. The resulting drag and collision force calculations can also be simplified by this arrangement. It is assumed that the particles are small enough (much

smaller than the computational cell size) to neglect the error introduced by simplifying the particle structure into a number of closely positioned spheres.

1.4. CHOICE OF SOFTWARE

Open source software has numerous advantages over its commercial software counterparts. A major benefit is that the user has direct access to the source code, or inner workings, of the software. As a result, additional features can be added by the user as necessary for their specific requirements. Furthermore, because a philosophy of open source is to focus on bare-basic functionality, and the fact that there are often a number of contributors working on the same features, open source software is generally optimised to run efficiently. This means it often outperforms commercial software when it comes to speed comparisons.

It was decided to use OpenFOAM® (Weller et al., 1998 - www.openfoam.com) to model the CFD portion of the model. For DEM, a package called LIGGGHTS was chosen (Kloss et al., 2012 - www.cfdem.com). LIGGGHTS is based on a molecular dynamics package called LAMMPS (Plimpton, 1995), but has improved features for DEM-specific modelling. LIGGGHTS uses the soft-sphere approach for modelling particle collisions, and includes long-range inter-particle forces. Both which are necessary for this work. By default, LIGGGHTS uses spherical particles, but also has the necessary framework to extend the model to multi-sphere particles. LIGGGHTS' developers had also created a programme to couple together OpenFOAM® and LIGGGHTS for CFD-DEM simulation. This coupling software is called CFDEM (Goniva et al., 2010 - www.cfdem.com). It operates as a native OpenFOAM® solver, using LIGGGHTS as a C++ library of functions that are called when the relevant functionality is needed. CFDEM supports full four-way coupling where particle-fluid interactions, fluid-particle interactions, and particle-particle interactions are all considered.

1.5. SCOPE AND OBJECTIVES OF STUDY

The aim of this study is to develop a methodology for the creation of a numerical model to simulate particle suspensions within a rheometer. In order to do this, the method of coupled CFD-DEM is used. Combining CFD and DEM is expected to result in a

relatively inexpensive numerical model, but still provide enough detail to simulate individual particles with long-range particle-particle interactions. Spherical particles are used due to their numerical simplicity.

The particle-fluid mixture is simulated under the same conditions found inside a rheometer to see if it could provide similar readings to those obtained by experimental means. Specifically, the model will be used to test the influences of particle volume fraction, and surface charge on the suspension rheology. The effect of surface charge, and the resulting inter-particle force, is accounted for through the use of the van der Waals and electrostatic forces. The combination is commonly known as the DLVO force (Derjaguin and Landau, 1941; Verwey and Overbeek, 1948).

Small particle diameters are used because they tend to provide a more intense rheological response than larger particles. As such, the size of the model is limited due to computational expense as a balance has to be found between the model size and accuracy. In other words, full-sized rheometer geometries are only considered for the single-phase CFD simulations, while the coupled CFD-DEM models use much smaller model geometries due to the computational expense of these simulations.

Combining all these aspects into a consistent model is a complex task. To the author's knowledge, a coupled CFD-DEM model has not been used before to study suspension rheology. So in order to achieve this, a systematic approach is adopted in order to develop the model, where complexity is added over a number of stages. Each of these steps is tested against known experimental values.

1.6. METHODOLOGY FOR MODEL CREATION

Development of the model is done in stages, adding more complexity as each stage proves successful. The steps in this methodology are illustrated graphically in Figure 1.3. Step 1 considers a single-phase Newtonian fluid in a basic geometry that is representative of a full rheometer. This only requires the use of CFD to model the fluid. A non-Newtonian fluid is tested as well to determine the response of the CFD model to a fluid

whose viscosity changes with shear rate. Once the parameters of these models are understood, then particles can be added to the model.

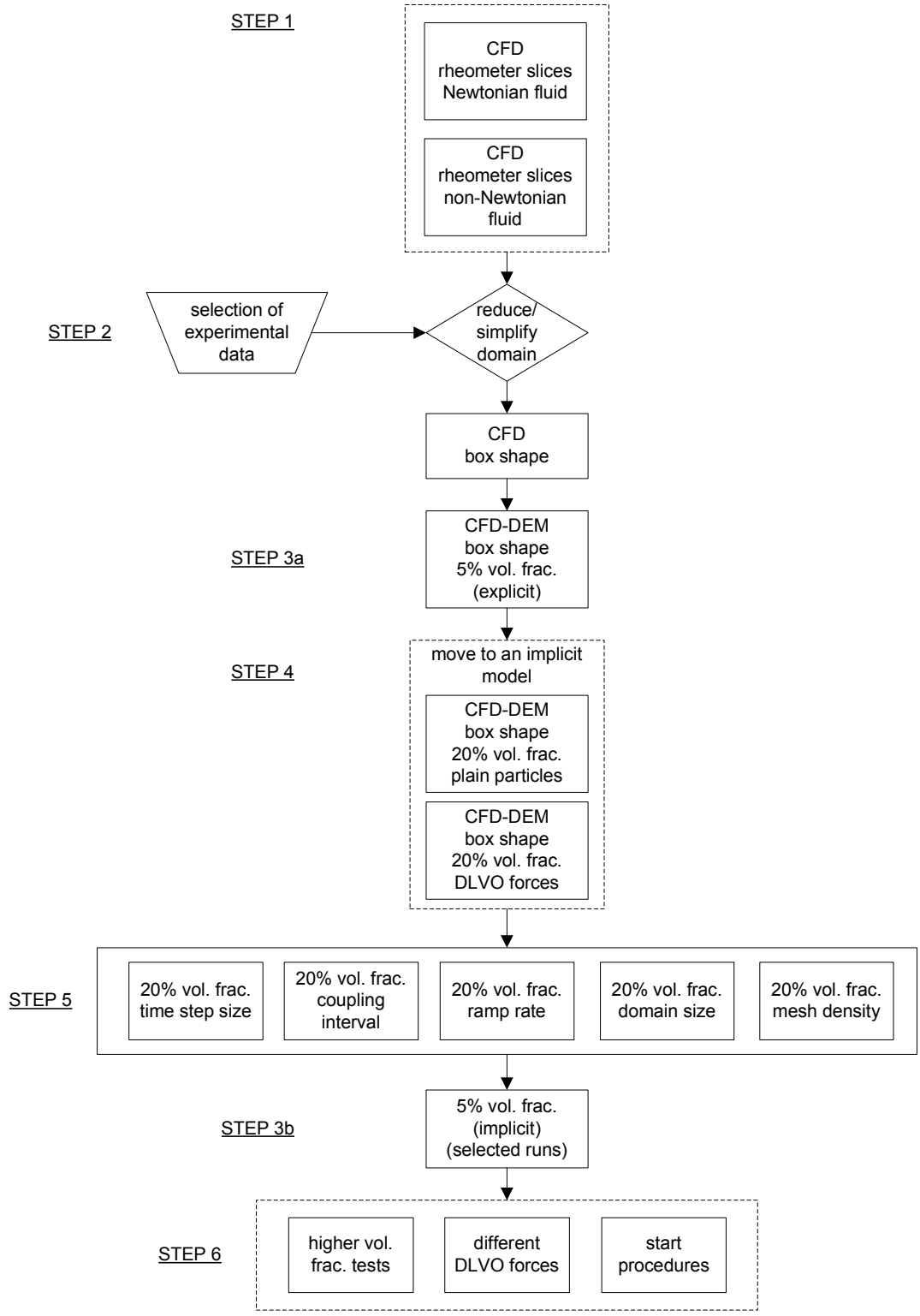

Figure 1.3: Flow chart illustrating the progression of model development

Step 2 discusses the selection of experimental data for the particle suspension. As a result of the selection, the model geometry had to be altered slightly.

Particles are added to the model in Step 3. Particle volume fraction is initially kept low (<5%) to reduce complexity. With the introduction of the implicit model formulation (cf. Section 3.5), larger volume fractions became practical. Step 4, with a larger particle volume fraction (20%), is implemented to set the benchmark case for the model. This is because larger particle volume fractions result in a more intense rheological behaviour and thus would give a better idea of the model's performance. For these steps, plain particles are tested first to reduce the complexity. After the successful completion of the tests, the inter-particle forces are added (i.e. the van der Waals and electrostatic forces).

The next step (Step 5) is to characterise the model and find out which model parameters are required for reliable performance, but which still give accurate results. These parameters include numerical settings, like the time step, and physical considerations like model geometry and size. After this further development of the model, the low volume fraction set up of Step 3 is revisited using the implicit model formulation (Step 3b).

The final step (Step 6) looks at important rheological parameters like particle volume fraction and particle surface charge. The model is judged on how well it responds to these changes.

During the development of the model, the geometry was gradually evolved away from that of a full-sized rheometer, to a small rectangular box of only a few microns in size. The reasons for this are discussed in Chapters 4 and 5. It was felt that this evolution of the geometry was acceptable as, at each stage, the reduced model was found to be equivalent to the larger models because they still reproduced the important flow features. The final, reduced model was used to produce the results in Chapters 6 and 7.

1.7. OUTLINE OF THESIS

This thesis begins with two chapters that review background theory relevant to this work. Chapter 2 presents a more detailed look into the complexities associated with particulate

suspensions. Chapter 3 discusses some theory behind CFD and DEM. Emphasis is placed on components specifically related to coupled CFD-DEM models.

Chapter 4 covers the first stage of the modelling process (Step 1), namely the generation of a plain CFD model of a rheometer. Results for this step are also presented in this chapter. Building on this work, Chapter 5 discusses the complexity of adding particles to the CFD to create a coupled model (Steps 2, 3a and 4).

The next two chapters present and discuss the results of the coupled model. Chapter 6 focuses on the testing of important model parameters to determine the correct working set-up of the model (Step 5). Chapter 7 (Steps 6 and 3b) presents results for two rheological characteristics, namely particle volume fraction and particle surface charge. The model's responses to these changes are discussed. Finally, Chapter 8 draws conclusions on the model's performance and its suitability for future work.

2. PARTICLE SUSPENSION RHEOLOGY

This chapter discusses some of the important factors that affect the rheology of particulate suspensions. Initially, an overview of the measurement of suspension viscosity is given in Section 2.1. Following from there, Section 2.2 outlines the use of rheometers to measure suspension viscosity. Section 2.3 discusses important properties that affect suspension rheology. Lastly, in Section 2.4, theories describing the inter-particle electric forces, which are important in this work, are discussed in more detail.

2.1. RHEOLOGY OF SUSPENSIONS

Rheology is the study of flow and deformation of matter. It considers the relationship between the applied force (shear stress, τ) and the resultant rate of deformation (shear rate, $\dot{\gamma}$) of a fluid element. The response of a fluid can be highly variable, ranging from elastic solids to viscous fluids. If the deformation of a substance in response to an applied stress is reversible, it is an elastic solid. However, if the deformation is irreversible, then it is called a viscous fluid. Many systems lie between these two extremes, exhibiting varying degrees of viscoelastic behaviour. The relationship between the two, described by Equation 2.1, is typically represented in the form of a flow curve in a rheogram.

$$\tau = \mu \frac{\partial u_x}{\partial y} = \mu \dot{\gamma} \tag{2.1}$$

Viscosity (μ) is a measure of the internal friction of a fluid and how much the fluid resists deformation under a certain amount of shear force. It is dependent on the rate at which it is deformed (sheared). Newtonian fluids are characterised by a linear relationship between shear stress and shear rate, implying a constant μ. In suspensions, such behaviour is generally displayed by dilute suspensions of spherical particles in a Newtonian medium. However, most concentrated suspensions will deviate from such behaviour and exhibit non-Newtonian behaviour. This means their viscosity changes as a function of shear rate. The resulting viscosity is called the “apparent viscosity” as it is the observed viscosity for that shear rate/shear stress combination. Non-Newtonian fluids can

be classified according to how they deviate from Newtonian fluids. Different relationships between shear stress and strain rate are illustrated in Figure 1.1.

Pseudoplastic fluids exhibit shear-thinning behaviour, where the apparent viscosity reduces as the shear rate is increased. In mineral suspensions, shear-thinning may be attributed to the gradual breakdown of particle aggregates, allowing the bulk fluid to flow more easily and leading to a decrease in the effective solids concentration (Chhabra and Richardson, 2008). This results in a decrease in apparent viscosity. Shear-thinning is also typical of non-spherical particles, where originally randomly aligned particles are progressively aligned in the direction of the flow with increasing shear. Shear-thinning can also be described in terms of the balance between Brownian motion and hydrodynamic forces. The Péclet number is the ratio of hydrodynamic force to the thermal force, which causes particle diffusion (Barnes, 2000). It can be used to gauge the dominance of either component. This number includes factors such as particle size, temperature and bulk fluid viscosity. In general, the importance of Brownian motion decreases during shear-thinning as the particles become more aligned with the flow. This is characterised by high Péclet numbers (>>1).

Conversely, the apparent viscosity of a dilatant fluid increases as the shear rate is increased, becoming more resistant to flow. This shear-thickening behaviour occurs when hydrodynamic interactions are of less importance, which is characterised by low Péclet numbers (<<1). Such behaviour is observed in concentrated mineral suspensions. Shear-thickening properties have been attributed to a transition from two-dimensional, ordered, layered structures, to a disordered, three-dimensional state at very high shear rates. The bulk fluid is believed to act as a lubricant at low shear rates, but is unable to fill the gaps between the particles at higher shear rates (Chhabra and Richardson, 2008). This results in the increased friction between particles, and the increase in viscosity.

2.1.1. Suspension Yield Stress

In moderately concentrated suspensions, where the net force between particles is attractive, particle-particle interactions dominate the suspension by forming continuous inter-particle networks. This causes the material to behave as an elastic solid. When subjected to stress, the system resists flow until the applied stress exceeds the inherent

elastic strength of the particulate network. At this critical stress, the network of interconnected particles fails and the material behaviour becomes more liquid-like, with less resistance to flow (Barnes, 1999; Chhabra and Richardson, 2008). This critical stress is termed the yield stress. Suspensions where the inter-particle network structure breaks down to a fully dispersed state are known as Bingham plastic fluids. These suspensions flow as a fully viscous fluid upon yielding, unlike pseudoplastic or dilatant fluids which demonstrate viscoelastic behaviour in this flow region.

The concept of the yield stress was first proposed by Bingham and Green (1920). Since then, it has generated much debate in rheological literature. The definition of a yield stress is not simple, and is not a well specified quantity which can be defined precisely (Barnes, 1999). In his paper, Barnes (1999) debated the existence of the yield stress entirely. While referring to an earlier paper of Barnes and Walters (1984), he argued that that the "yield stress" was in fact an idealization, and that given accurate measurements, no yield stress actually exists. Further comments on the Barnes and Walters (1984) paper were made by Harnett and Hu (1989), who felt that the yield stress was an engineering reality. In other words, for all practical purposes, one could assume that a liquid has a yield stress when considering it on a reasonable length and time scale. According to Chhabra and Richardson (2008), the yield stress can be viewed as the transition from a solid-like (high viscosity) to a liquid-like (low viscosity) state which occurs abruptly over an extremely narrow range of shear rates or shear stress. These two values of viscosity can differ from each other by several orders of magnitude. Nonetheless, Barnes (1999) did concede that there may well be a "yield stress" for suspensions, mostly because the particles could form structures within the fluid that prevent flow of the suspension.

With such a definition, the concept of a yield stress has proved useful in many applications. In the case of particulate mineral slurries, the yield stress and viscosity are useful indicators of the degree of aggregation and dispersion of particles within that suspension (Subbanna et al., 1998; Johnson et al., 2000), and are very important for the analysis of structure forming systems (Ndlovu, 2011).

A number of researchers have found the yield stress to be dependent on particle size, though there is no clear consensus on the exact relationship (Johnson et al., 2000). In

general, smaller particles result in higher yield stresses. This infers that the inter-particle forces are important in determining the yield stress.

2.1.2. Viscosity Models

A number of correlations have been proposed to describe the change in shear stress with shear rate of different fluids. Some examples are the Bingham, Casson, and Cross models. Most models can describe a variety of behaviours, depending on the choice of relevant empirical parameters. One example of this, described by Equation 2.2, is the Herschel-Bulkley model. It considers a fluid with a yield stress (τ_y). The model can be used to describe either shear-thinning or shear-thickening fluids depending on the choice of the *k* (consistency) or *n* (flow index) parameters.

$$\tau = \tau_y + k\dot{\gamma}^n \tag{2.2}$$

2.2. MEASUREMENT OF RHEOLOGY

A rheometer is a device used to measure the way in which a liquid substance flows and deforms in response to applied forces, i.e. it measures the rheology. There are two distinct types of rheometers that differ in the way they apply load to the sample. Shear rheometers apply a shear stress or shear strain to the fluid such that the fluid elements flow past one another. They typically involve components that rotate. Extensional rheometers apply a purely extensional stress or strain to the sample so that the fluid elements move towards or away from each other. Extensional rheometers are not as easy to implement as shear rheometers. Two major types of shear rheometers are capillary and rotational rheometers. In capillary rheometers, the fluid flows through a narrow tube. These rheometers can be very precise, but are mostly limited to Newtonian and some non-Newtonian fluids. Rotational rheometers differ in that the fluid is continuously sheared between two surfaces, of which one or both surfaces are rotating. In general, rotational systems are better suited for concentrated suspensions and low shear rates.

In particular, concentric-cylinder rotational rheometers are of interest due to their uncomplicated design geometry (cf. Figure 2.1). Here a cylindrical rotor rotates inside the cup (outer stationary wall). A vane rotor can also be used for suspensions that contain

larger particles, or where particle settling is a problem. But this arrangement has a more complex geometry and flow pattern.

There are two types of rotational measurements: Shear stress controlled or shear rate controlled. In shear stress controlled (controlled-stress) measurements, a constant torque is applied to the rotating cylinder in order to generate rotation, and the resulting rotational speed is then determined. The rotational speed can be converted into the shear rate, if the geometry is known. In shear rate controlled (controlled-rate) measurements, a constant rotational speed is maintained and the resulting torque generated by the sample is determined using a suitable stress-sensing device, such as a torsion spring or strain gauge.

2.2.1. Concentric-Cylinder Rheometer Geometries

Three common concentric-cylinder rheometer arrangements are the single-gap, double-gap, and DIN bob. They appear similar, but vary slightly in their geometries and their uses. Figure 2.1a shows the double-gap arrangement on the left, where the blue region represents the volume occupied by the fluid. The single-gap geometry is similar the double-gap, but with only one gap, not two. Double-gap rheometers are typically more sensitive than single-gap versions due to the extra surface area in contact with the fluid. The DIN bob (Figure 2.1b) can be thought of as a type of single-gap geometry, but with a different geometry at the tip of the rotor that is intended to reduce end-effects (e.g. air entrainment under the rotor). DIN stands for "Deutsches Institut für Normung", meaning "German institute for standardisation".

2.2.2. Fluid Flow inside a Concentric-Cylinder Rheometer

The flow inside a concentric-cylinder rotational rheometer is assumed to be simple Couette flow. It is characterised by laminar flow of a viscous fluid between two surfaces, one moving and one stationary. The flow is driven by the viscous drag force acting on the fluid by the moving surface. For a Newtonian fluid, the shear gradient is constant throughout the domain. This is not necessarily the case for a non-Newtonian fluid. The flow will be steady for a constant shear rate (wall velocity). It is also assumed that the fluid is incompressible, which is appropriate for most liquids.

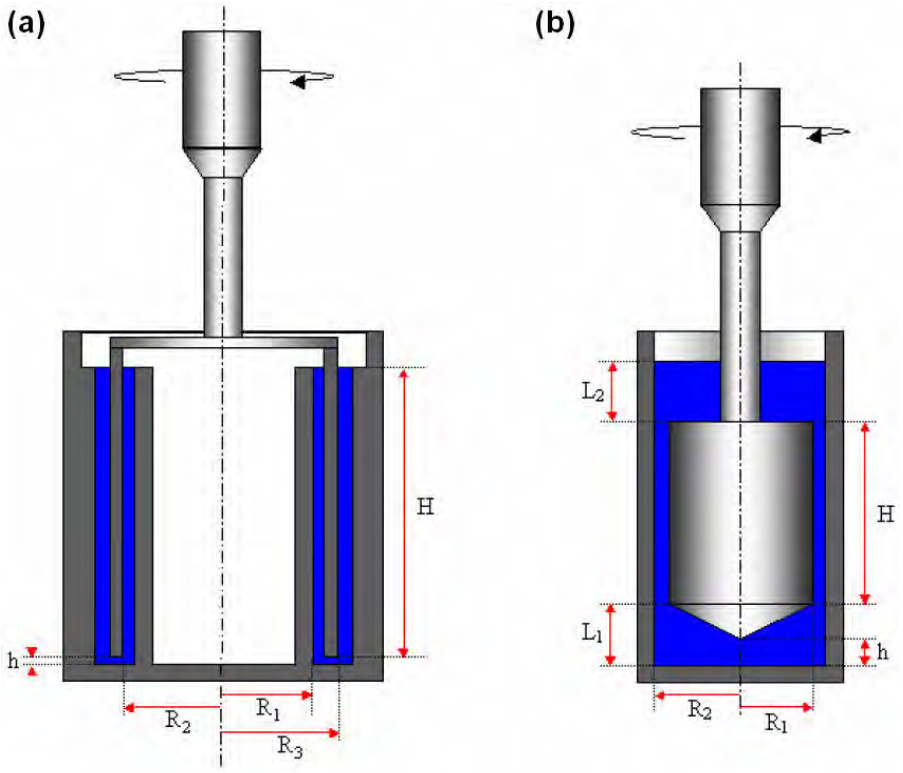

Figure 2.1: Schematic of the double-gap (a) and DIN bob (b) arrangements, with dimension labels (TA Instruments)

High-speed testing of low-viscosity fluids can result in inertia-driven secondary flow occurring within the annular region. This flow takes the form of three-dimensional, laminar, toroidal vortices, known as Taylor vortices. The extra dissipation caused by these vortices can be mistaken for an increase in the effective fluid viscosity at higher shear rates. Little can be done about this phenomenon, though changing the rheometer geometry may help (Barnes, 2000). The onset of this flow is measured by the critical Taylor number, which predicts it will occur at about 1700. The Taylor number is defined as (White, 1998):

$$Ta = \frac{\omega_1^2 R_1 (R_2 - R_1)^3}{\nu^2} \tag{2.3}$$

where ω_1 is the rotational speed of the inner wall, ν is the kinematic viscosity, and R_1 and R_2 are the radii of the inner and outer cylinders respectively. Figure 2.2 illustrates

the flow pattern of the Taylor vortices. The image on the left is a cross-section of the flow, showing flow lines which indicate the vortices.

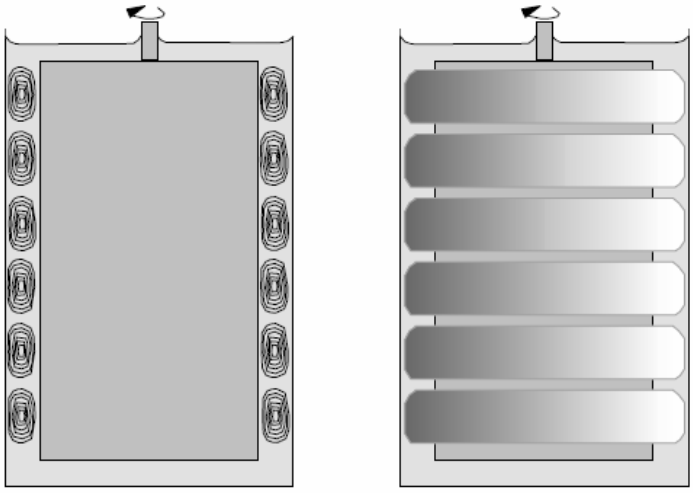

Figure 2.2: Taylor vortex secondary flow pattern between rotating concentric cylinders (Barnes, 2000)

At higher Taylor numbers, the vortices also develop a circumferential periodicity, but are still laminar. Conversely, if the outer cylinder is rotated while the inner is kept stationary, there is a sharp and catastrophic transition to turbulent flow (without any Taylor-like secondary flows). These kinds of inertial-driven behaviour (both secondary flow and turbulence) limit the range over which concentric-cylinder viscometers can be used for low-viscosity liquids (Barnes, 2000).

2.2.3. Analytical Solution for Couette flow between Concentric Cylinders

For Couette flow between two concentric cylinders, there is an analytical solution for the fluid velocity across the gap region. This solution can be used to compare against the results of the numerical model. Equation 2.4 gives this solution for the case when the inner cylinder is rotating (White, 1998). Constant density and viscosity are assumed.

$$u(R) = w_1 R_1 \left(\frac{R_2/R - R/R_2}{R_2/R_1 - R_1/R_2} \right) \tag{2.4}$$

where R_1 denotes the radius of the inner (rotating) wall, R_2 the radius of the outer (stationary) wall, ω_1 is the rotational velocity at the inner wall, and R is the position at

which the fluid (tangential) velocity is being evaluated. For example, the fluid velocity profile of a single-gap rheometer (for a 500μm gap width, and $R_1/R_2 = 0.977$) is expected to be linear.

2.2.4. Shear Stress and Shear Rate Measurements

Shear stress and rate are related to mechanical properties of the experiment and the geometry of the apparatus. The shear stress and shear rate can be calculated from the torque and rotational speed respectively, through the use of conversion factors which take into account the geometry of the device. These equations, given below, are taken from Whorlow (1992). Relevant dimensions used in these factors are labelled in Figure 2.1.

Shear rate: $$\dot{\gamma} = F_{\dot{\gamma}} \cdot \omega \tag{2.5}$$

Shear stress: $$\sigma = F_{\sigma} T \tag{2.6}$$

where ω is the rotational speed of the rotor, and T is the torque experienced by the rotor. The different conversion factors are:

Shear rate factor: $$F_{\dot{\gamma}} = \frac{R_1^2 + R_2^2}{R_2^2 - R_1^2} \tag{2.7}$$

Shear stress factor (DIN bob): $$F_{\sigma} = \frac{1}{4\pi H}\left(\frac{R_1^2 + R_2^2}{R_1^2 R_2^2}\right) \tag{2.8}$$

Shear stress factor (double-gap): $$F_{\sigma} = \frac{1}{4\pi H}\left(\frac{R_1^2 + R_2^2}{R_2^2\left(R_1^2 + R_3^2\right)}\right) \tag{2.9}$$

2.3. FACTORS AFFECTING SUSPENSION RHEOLOGY

The macroscopic behaviour of particulate suspensions is controlled by the interaction between individual particles as well as their interaction with the surrounding fluid (Zhou et al., 2001; Zhu et al., 2007). This depends on the nature and density of the inter-particle forces as well as the corresponding microstructure formed by the particles. An increased particle loading will increase the intensity of interactions, thereby changing the rheology of the fluid. In addition, the shape and size of the particle can influence its hydrodynamic

behaviour as it moves within the suspending liquid. Understanding the interplay of inter-particle forces and the microstructure within the fluid is vital to understanding the behaviour of particle-laden fluids, and producing meaningful results (Zhu et al., 2007). Some factors influencing suspension rheology will now be discussed.

2.3.1. Solids Volume Concentration

For the same particle size, increasing the solids volume concentration increases the number of particles in the system. The number of particles in the system scales linearly with the increase in volume concentration. As the solids volume fraction in the system increases, the particles become more closely packed together and it becomes more difficult for them to move freely. In addition, the number of inter-particle interactions increases, which consequently increases the resistance to flow.

Suspensions with relatively low volume fraction tend to behave as Newtonian fluids. Increasing the volume fraction can lead to a more viscous mixture with shear-thinning behaviour. This is because an increased volume fraction results in more particle-particle interactions, but the forces between particles can be broken down at high shear rates. However, as the volume fraction nears the maximum for the sample, the viscosity rises very steeply. At these solids loadings, free movement of particles is significantly hindered as collisions between particles increase. Viscosity therefore increases with increasing shear rate; and the system becomes shear-thickening at very high shear rates.

More particles also mean more solid mass in the fluid, thereby increasing the transfer of momentum between the particles and the fluid. This would also increase the viscosity of the system.

2.3.2. Particle Size

Reducing the particle size also increases the number of particles in the domain (for the same solids volume fraction). As a particle's volume scales with a cubic relation to particle size, the number of particles increases much quicker by reducing the size. Thus, there are many more particle-particle interactions. Furthermore, for smaller particle sizes, the particle inertia will also be reduced, allowing the particles to be more vulnerable to inter-particle forces. Smaller particles are able to get closer together, where inter-particle

and fluid-particle forces are typically stronger. For attractive inter-particle forces, the resulting suspension will have a much higher viscosity than for larger particle sizes. This effect becomes less noticeable at high shear rates, where hydrodynamic forces are able to break the inter-particle bonds.

In addition, as the particle size decreases, the surface area to volume ratio becomes larger. This increases the significance of particle-fluid interactions as there is more fluid in contact with the particle.

2.3.3. Particle Shape

Particle shape also makes a difference to the apparent viscosity, as is illustrated in Figure 2.3 (Barnes et al., 1989). In particular, particle shape affects various physical parameters such as the drag force, effective particle volume fraction, and the agglomeration of particles.

The drag force on a particle is dependent on the shape of the particle in relation to the direction of fluid flow. For example, thin, flat particles can have very little drag when lying parallel to the flow direction, but a significantly larger drag when oriented perpendicular to the flow (Gunes et al., 2008). In addition, particles which are longer in one of their dimensions are considered to fill a larger effective volume when moving within a fluid. This will increase the effective particle volume fraction in the suspension, thereby increasing the viscosity (Barnes, 2000).

Shape also influences how particles agglomerate. More regular shapes, such as spheres, can easily move past each other, with only glancing blows during collisions. Conversely, long, fibrous particles can easily intertwine and form bigger aggregates. This connection between irregular particles can be shear rate dependent. At higher shear rates, particles separate and start aligning themselves to the flow, the viscosity tends to reduce (Barnes, 2000; Chhabra and Richardson, 2008). This results in a shear-thinning liquid. Alternatively, particles that are more regular in each dimension can only rely on inter-particle forces to bind them together, but these can be easily broken as particles move past one another (Chhabra and Richardson, 2008).

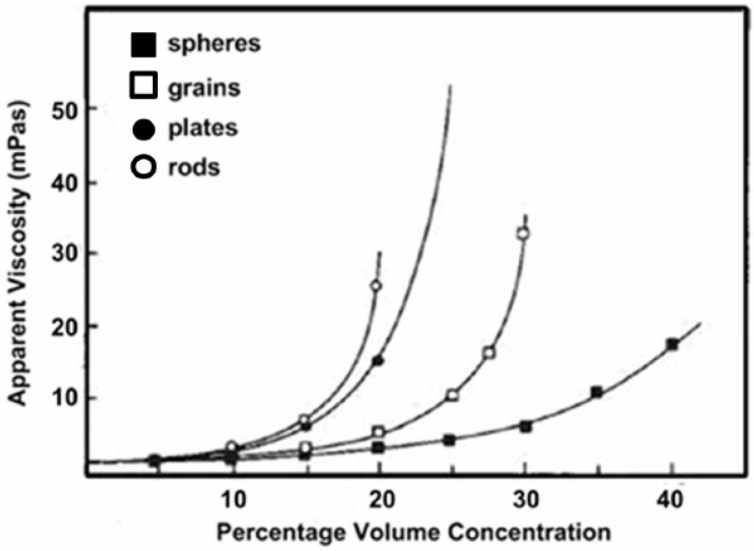

Figure 2.3: Effect of solids concentration on apparent viscosity of suspensions for different particle shapes (Barnes et al., 1989)

2.3.4. Inter-Particle Forces

There are a number of forces that act between particles in a suspending liquid, including the hydration, hydrophobic, steric, and liquid bridging forces. Hydrophobic and liquid bridging forces are attractive forces, due to the fluid surrounding the particle. Conversely, hydration forces tend to repel particles in an aqueous medium (Johnson et al., 2000). Steric stabilisation involves the addition of polymeric molecules to the suspension in order to disperse particles. The repulsive force comes from the adsorbed molecules on the particle surface which prevents particles from coming close together which negates the attraction forces (He, et al., 2004).

Two long-range inter-particle forces that arise from a particle's surface charge are the van der Waals and electrostatic forces. When the surface potential is zero, the attractive forces dominate over the repulsive electrical double-layer forces. The particles move closer together and coagulate, resulting in a high yield stress and viscosity. Alternatively, when the surface potential is high, the repulsive forces are stronger and the particles disperse, resulting in a low yield stress and viscosity. This is illustrated in Figure 2.4. Together, these forces form the basis of the DLVO interaction force, which will be discussed in more detail in the following section.

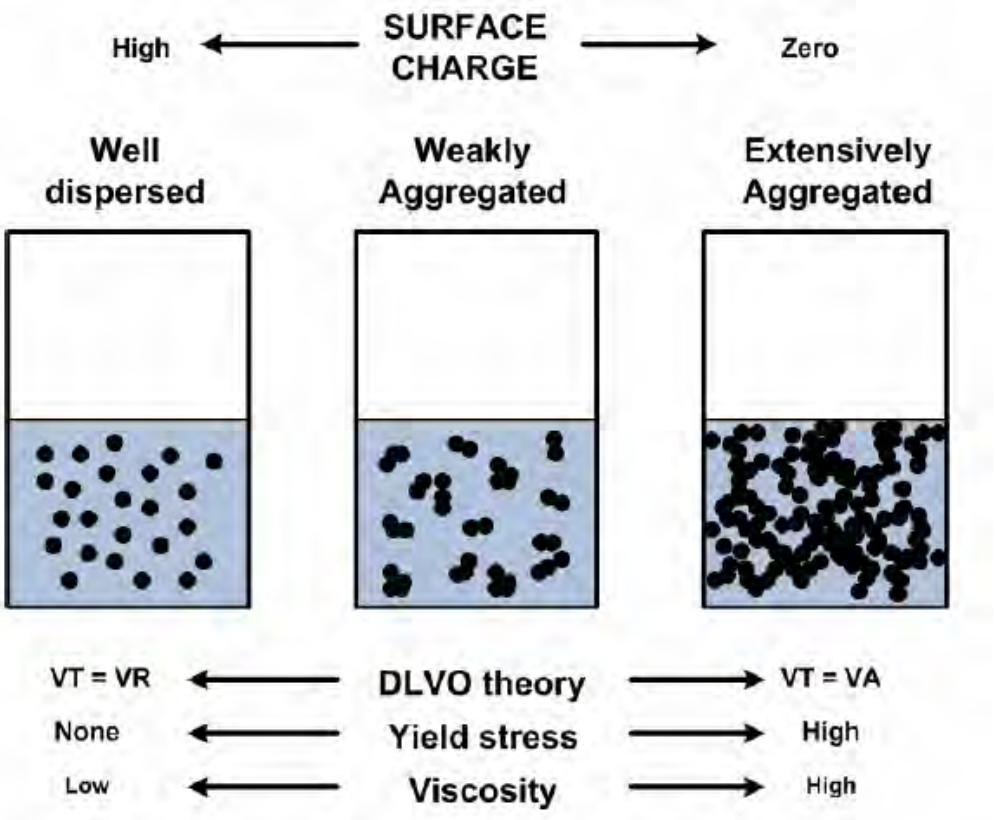

Figure 2.4: Schematic illustrating the relationship between surface charge and rheological properties (adapted from Ndlovu, 2011 and Laskowski and Pugh, 1992)

These electric forces depend on the distribution of the charge on the particle surface. Mineral suspensions tend to have anisotropic distributions due to their shape and mineralogy (Ndlovu, 2011). However, spherical particles typically have an isotropic distribution, which means the surface charge is the same at every point on the surface.

2.4. DLVO THEORY

The overall electrostatic interaction considered in this study is the DLVO force, named after the theories proposed by Derjaguin and Landau (1941) and Verwey and Overbeek (1948). It is a combination of the attractive van der Waals forces, and the repulsive electric double-layer that surrounds the particles. Figure 2.5, taken from Israelachvilli (1992), shows different energy vs. distance profiles for the DLVO potentials that illustrate how DLVO interactions can vary. The shapes of these profiles depend on both the fluid and particle properties.

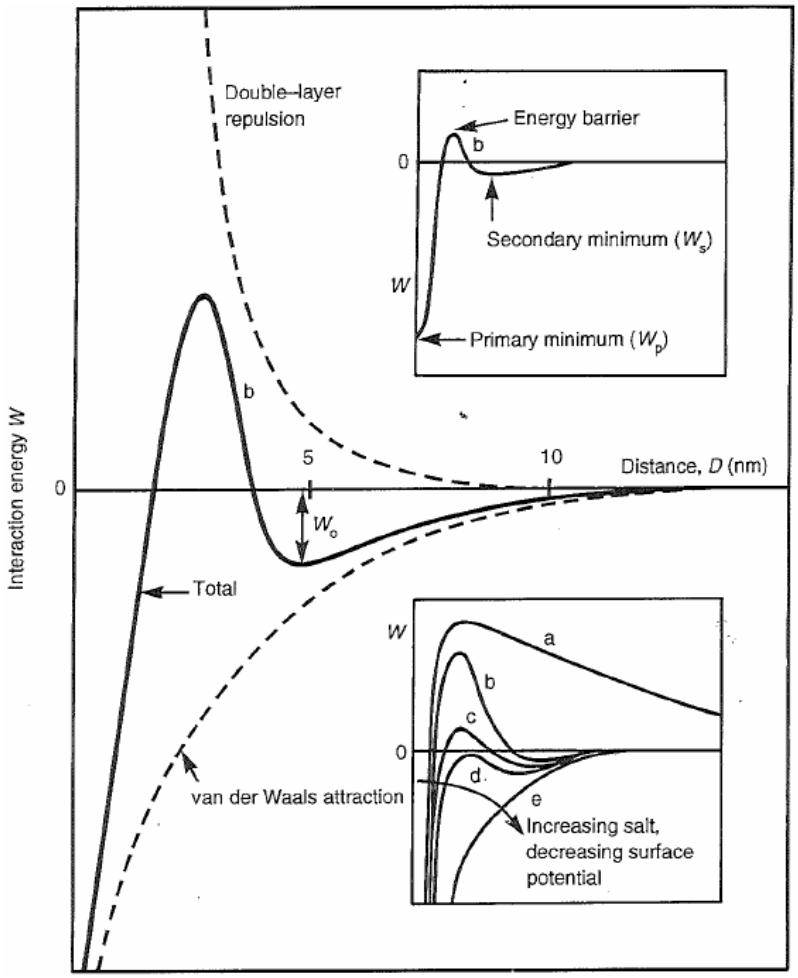

Figure 2.5: Different DLVO interaction potentials, showing how they change with distance (Israelachvilli, 1992)

Descriptions of the labels in Figure 2.5 (Israelachvilli, 1992): (a) surfaces repel strongly; small colloidal particles remain stable. (b) Surfaces come into stable equilibrium at secondary minimum if it is deep enough; colloids remain "kinetically" stable. (c) Surfaces come into secondary minimum; colloids coagulate slowly. (d) The "critical coagulation concentration". Surfaces may remain in secondary minimum or adhere; colloids coagulate rapidly. (e) Surfaces and colloids coalesce rapidly.

2.4.1. van der Waals Forces

These forces have their roots in the van der Waals equation of state for non-ideal gases. The total van der Waals force is comprised of three components (Nguyen and Schulze, 2004):

- Keesom (orientation) interaction between randomly oriented dipoles
- Debye (induction) interaction between randomly oriented dipole and induced dipole
- London (dispersion) interaction between fluctuating dipole and induced dipole

The dispersion force dominates the net van der Waals forces between bodies in a solution. The net force is always positive (attractive) for similar bodies (Johnson et al., 2000) and decays with the sixth power of the separation distance between the molecules (Nguyen and Schulze, 2004; Zhu et al., 2007). The van der Waals forces are largely independent of system pH and the presence of surfactants and other polymeric species (Johnson et al., 2000).

In multiphase fluids it is more convenient to describe the van der Waals forces in a continuum, rather than on a molecular basis. Equation 2.10 describes the van der Waals interaction energy between two spherical molecules in an aqueous solution (Nguyen and Schulze, 2004). Here r_i is the radius of (spherical) particle i, D is the separation distance, and A_H in Equation 2.10 represents the Hamaker constant given by Equation 2.14 (for $D << r$).

$$E_{vdw} = -\frac{A_H}{6D}\frac{r_i r_j}{r_i + r_j} \tag{2.10}$$

The van der Waals force (Equation 2.12) is derived via the relationship between energy and force (Equation 2.11) (Nguyen and Schulze, 2004). This relationship shows that as two particles move closer together during contact, and the separation distance between them reduces to zero, the force will become infinite.

$$f(D) = -\frac{dE}{dD} \tag{2.11}$$

$$f_{vdw} = -\frac{A_H}{6D^2}\frac{r_i r_j}{r_i + r_j} \tag{2.12}$$

For completeness, a more general formula is given in Equation 2.13 for the interaction between two differently sized particles, i.e. one large and one small (Nguyen and Schulze 2004). Here R is the centre to centre distance between the particles.

$$E_{vdw} = -\frac{A_H}{6}\left[\frac{2r_i r_j}{R^2-(r_i+r_j)^2}+\frac{2r_i r_j}{R^2-(r_i-r_j)^2}+\ln\left(\frac{R^2-(r_i+r_j)^2}{R^2-(r_i-r_j)^2}\right)\right] \qquad (2.13)$$

The Hamaker constant described by Equation 2.14 is calculated according to the Lifshitz, or continuum, approach for two bodies interacting across a medium (Johnson et al., 2000; Nguyen and Schulze 2004). Here k_B is the Boltzmann constant, T is the absolute temperature, h is Planck's constant, υ_e is the main absorption frequency in the ultraviolet region, n_1, n_2, n_3 are the refractive indices and ε_1, ε_2, ε_3 are the dielectric constants (relative permittivity) of the three media. The subscripts 1, 2, and 3 denote the three different media, namely the continuum (3) and the two interacting bodies (1 and 2), hence the new subscript for the Hamakar constant.

$$A_{132} = \frac{3k_BT}{4}\left(\frac{\varepsilon_1-\varepsilon_3}{\varepsilon_1+\varepsilon_3}\right)\left(\frac{\varepsilon_2-\varepsilon_3}{\varepsilon_2+\varepsilon_3}\right)+\frac{3h\upsilon_e}{8\sqrt{2}}\frac{(n_1^2-n_3^2)(n_2^2-n_3^2)}{(n_1^2+n_3^2)\sqrt{n_2^2+n_3^2}+(n_2^2+n_3^2)\sqrt{n_1^2+n_3^2}} \qquad (2.14)$$

2.4.2. Electric Double Layer Force

When a mineral particle is placed in an aqueous environment, it often acquires a substantial surface charge (Johnson et al, 2000). The presence of a charged surface causes ions in solution to re-arrange themselves. The combination of the charged surface and the region of re-arranged ions in the surrounding solution (diffuse layer) is referred to as the electric double-layer (Nguyen and Schulze, 2004; Johnson et al., 2000). The double-layer is illustrated in Figure 2.6. Nguyen and Schulze (2004) comment that when double-layers overlap, the resultant force is stronger than other surface forces, and acts over a longer range. However, Zhu et al. (2007) claim that when compared to the van der Waals forces, the double-layer force is one order of magnitude less for micro-sized particles.

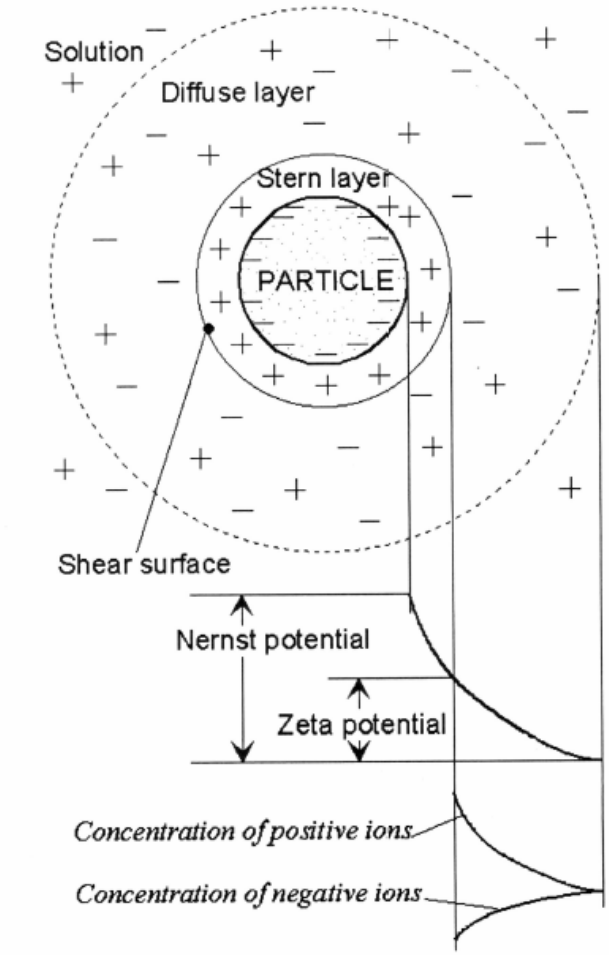

Figure 2.6: Electric double layer surrounding a particle with a surface charge (Nguyen and Schulze 2004)

The hydrodynamic diameter of a particle includes not only the particle diameter itself, but also the Stern layer and a portion of the diffuse layer (Peker and Helvacı, 2008). For some ions, the attractive electrostatic forces are greater than the hydrodynamic shear forces acting on the particle during its motion.

The ratio of the Coulombic potential to the thermal energy gives a measure of the thickness of the double-layer. This ratio is the called the Debye constant, κ, and is described by the generalised equation (Nguyen and Schulze, 2004):

$$\kappa = \left(\frac{e^2 \sum n_i(\infty) z_i^2}{\varepsilon \varepsilon_0 k_B T} \right)^{1/2} \tag{2.15}$$

or, in an alternate form,

$$\kappa = \left(\frac{2N_A I e^2}{\varepsilon \varepsilon_0 k_B T} \right)^{1/2}$$

where e is the charge on an electron, $n_i(\infty)$ is the number per unit volume of electrolyte ions of type i with valence z_i in the bulk solution far from the surface, ε_0 is the permittivity of free space, ε is the dielectric constant (relative permittivity) of the solution medium. The summation is over all the electrolyte ions in solution. In the second form, N_A is Avogadro's constant, and I is the ionic strength. The quantity of $1/\kappa$ is known as the Debye length, and has units of length.

The force of the electric double-layer interaction depends on the charging mechanism that occurs between the particle surfaces during the interaction. Three different cases occur as a result (Nguyen and Schulze, 2004):

- Surface potential remains constant
- Surface charge remains constant
- Surface charge and surface potential change by charge regulation

In the first two cases, either the surface potential or charge is known. The zeta potential (ζ) is often used instead of the surface potential (ψ) (Nguyen and Schulze, 2004; Leong and Ong, 2003). As the third case is very complex, the first two cases are often used instead. The case of constant potential is a perfect regulation of the surface charge as observed by Verwey and Overbeek (1948) in their DLVO theory (Nguyen and Schulze, 2004). This method was also used by Apostolou and Hrymack (2008). For two particles of the same radius and equal surface potential, these three methods will result in the same magnitudes for both force and energy.

For constant surface potentials (ψ), the interaction energy and force are given by Equation 2.16 and Equation 2.17 respectively. As can be seen in these equations, the double-layer is very susceptible to changes in the fluid properties which can be

manipulated easily during experiments. It is much more susceptible than the van der Waals forces.

$$E^{\psi} = \frac{\varepsilon\varepsilon_0 \pi r_i r_j}{r_i + r_j}\left[4\psi_i\psi_j a\tanh\left(e^{-\kappa D}\right) + \left(\psi_i^2 + \psi_j^2\right)\ln\left(1 - e^{-2\kappa D}\right)\right] \tag{2.16}$$

$$f^{\psi} = \varepsilon\varepsilon_0\kappa\frac{2\pi r_i r_j}{r_i + r_j}\frac{2\psi_i\psi_j e^{\kappa D} - \psi_i^2 - \psi_j^2}{e^{2\kappa D} - 1} \tag{2.17}$$

2.4.3. Superposition Approximation

If the double layers of two interaction particles are weakly overlapped, i.e. κD >>1, $\coth(\kappa D) \rightarrow 1$, and $\mathrm{cosech}(\kappa D) \rightarrow 0$, then the surface charge (ψ_i) does not significantly differ from the undisturbed surface charge (ψ_∞). Therefore all three charging regimes described above approximate the same surface interaction asymptotically. The result is a linear superposition of the potentials generated by each surface independently ($\psi_{i\infty}$) (Nguyen and Schulze, 2004). Application of the Derjaguin approximation results in Equation 2.18 for the electric double layer interaction energy and Equation 2.19 for the interaction force.

$$E_{edl} = \varepsilon\varepsilon_0\psi_{i\infty}\psi_{j\infty}\frac{4\pi r_i r_j}{r_i + r_j}e^{-\kappa D} \tag{2.18}$$

$$f_{edl} = \varepsilon\varepsilon_0\kappa\psi_{i\infty}\psi_{j\infty}\frac{4\pi r_i r_j}{r_i + r_j}e^{-\kappa D} \tag{2.19}$$

2.4.4. Limitations of the DLVO Theory

DLVO forces are generally calculated as forces between two spheres, each with a uniform surface charge. For this reason the DLVO theory cannot truly account for the effect of edge charges that are commonly found on non-spherical particles in mineral slurries (Missana and Adell, 2000). One way around this, would be to use multiple points (spheres) to describe the non-spherical particles. With this system, the individual contributions from different charges (each assigned to one sphere) can be calculated.

3. BACKGROUND THEORY TO NUMERICAL MODELLING

This section introduces the reader to fundamental concepts of numerical modelling in relation to the CFD and DEM methods. Important aspects to consider during the practical application of these methods are also discussed. Section 3.1 introduces the basic principles of DEM. Next, the inter-particle forces, which are modelled by the DEM, are discussed. Section 3.3 provides a brief numerical background to CFD. Section 3.4 presents numerical formulations that are more specific to particle-fluid flows. Section 3.5 discusses different techniques used to solve numerical models, in particular coupled CFD-DEM systems. Finally, Section 3.6 examines different particle-fluid forces that can occur. A detailed explanation of the solver algorithm used in the coupling software is given in Appendix D.

3.1. DISCRETE ELEMENT MODELLING

The Discrete Element Method (DEM) is used to simulate the forces acting on, and motion of, each individual particle. It was originally proposed by Cundall and Strack (1979). In granular flow, a particle can have two types of motion: translational and rotational. Typically in DEM, momentum and energy are exchanged during collisions as particles contact their neighbouring particles or a boundary wall. In this work however, long-range non-contact forces acting between particles, as well as a particle-fluid interaction force between a particle and the suspending medium, are also important. The resultant force on a particle can be determined from combining all these force contributions on that particle. Newton's Second Law of Motion can be used to calculate the resultant trajectories of each individual particle from these different forces acting on them (e.g. fluid drag force).

3.1.1. Particle Equations of Motion

The equations which govern particle motion are given by Equations 3.1 and 3.2. They describe the translational and rotational motion respectively for a particle i with mass m_i and rotational inertia I_i. Here, $\boldsymbol{v}_i$ and $\boldsymbol{\omega}_i$ are the translational and rotational velocities of

particle *i*. For this work, long-range non-contact inter-particle forces and particle-fluid interaction forces also need to be considered. Thus the relevant forces acting on a particle are: the contact force ($\boldsymbol{f}_{ij}^{c}$) and torque ($\boldsymbol{T}_{ij}$) acting on particle *i* exerted by particle *j* or wall boundaries, the long-range non-contact force ($\boldsymbol{f}_{ik}^{nc}$) acting on particle *i* by particle *k* or other sources, the particle-fluid interaction force ($\boldsymbol{f}_{i}^{pf}$), and the gravitational force ($\boldsymbol{f}_{i}^{g}$). Contact and non-contact forces include contributions from all relevant particles within the relevant range (superscripts *a* and *b* respectively). Figure 3.1 illustrates these forces.

$$m_i \frac{d\boldsymbol{v}_i}{dt} = \sum_{j=1}^{a} \boldsymbol{f}_{ij}^{c} + \sum_{k=1}^{b} \boldsymbol{f}_{ik}^{nc} + \boldsymbol{f}_{i}^{pf} + \boldsymbol{f}_{i}^{g} \qquad for: i \neq j, i \neq k \qquad (3.1)$$

$$I_i \frac{d\boldsymbol{\omega}_i}{dt} = \sum_{j=1}^{a} \boldsymbol{T}_{ij} \qquad for: i \neq j \qquad (3.2)$$

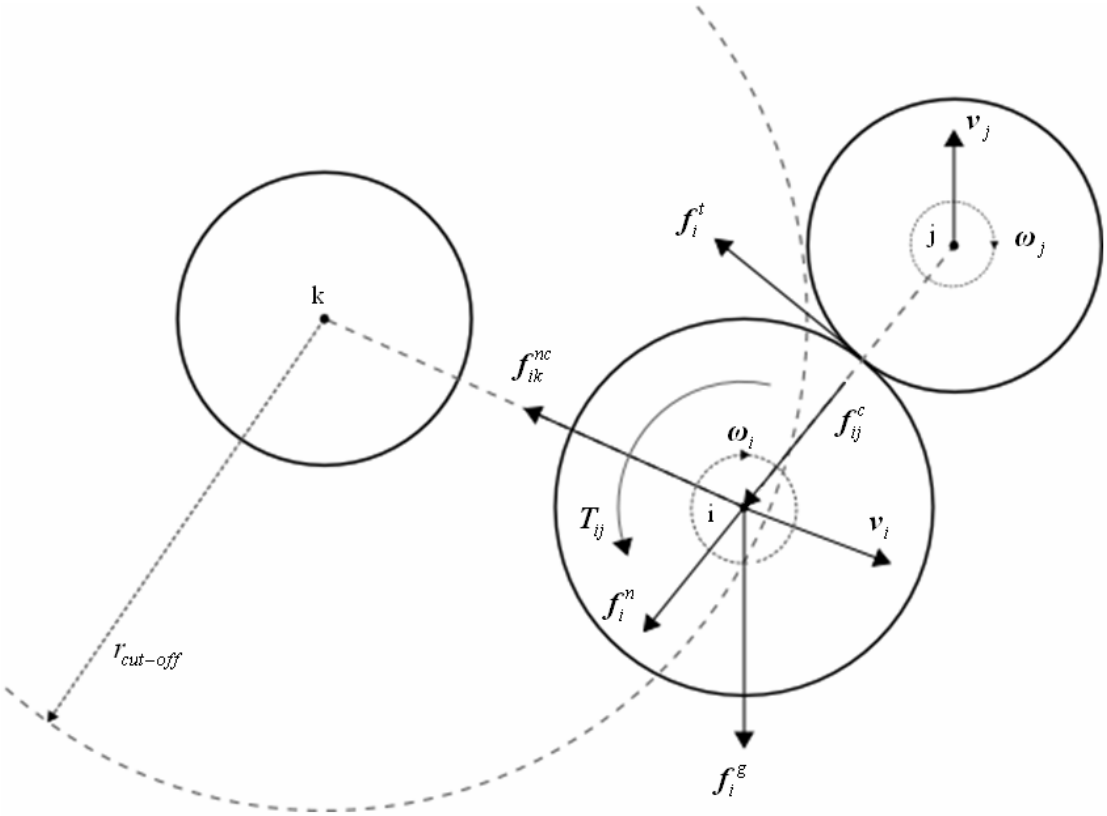

Figure 3.1: Illustration of forces and torques acting on a particle *i*, from contacting particle *j*, and non-contacting particle *k*

3.1.2. Soft and Hard-Particle Collisions

There are two different approaches to model particle collisions: “soft-particle” and “hard-particle” (also soft/hard sphere). In their seminal paper, Cundall and Strack (1979) described what was to become the soft-particle method. In this approach, a particle pair is allowed to “deform”, or rather overlap, during a collision which lasts multiple time steps. This deformation is used to calculate the elastic, plastic and frictional forces between particles. The main advantage of a soft-particle model is that it greatly simplifies collision modelling by allowing particles to overlap, relative to a scheme which has to enforce that particles do not overlap. In addition, lengthy collisions between several particles are allowed, where chains or clusters of particles can form. Furthermore, all inter-particle forces are accounted for during the collision. These are the main two elements necessary for capturing the behaviour of suspensions (Hoomans et al., 1996; Apostolou and Hrymack, 2007). Small time steps are required so that the collision event can be integrated over multiple time steps. This can increase the computational time of the simulation. According to Gantt et al. (2006), soft-particle models have been proven for use in dense flows of granular particles.

Alternatively, hard-particle models assume collisions are instantaneous and binary, i.e. only one collision per time step is considered. Here the forces between particles are often not explicitly considered due to the instantaneous nature of the collision. Therefore the hard-particle method is most applicable to rapid flows of dilute systems (Zhou et al., 2007). According to Mikami et al. (1997), the hard-sphere model is not suitable for dense (fluidised) beds, where cohesive particles are simulated.

In an attempt to reduce computational effort, many DEM formulations use simplified models to determine the forces and torques resulting from the contact between particles. This is because complex models do not necessarily give more accurate results relative to the increase in computational expense (Di Renzo and Di Maio, 2004; Zhu et al., 2007). Generally, linear models are the most intuitive and simplest. The most common linear model is the linear spring–dashpot model proposed by Cundall and Strack (1979), where the spring component models elastic deformation, and the dashpot accounts for the viscous dissipation.

3.1.3. Time Step Size for Soft-Particle Collisions

In dense particle-fluid systems, a particle's movement is not only affected by particles and fluid in direct contact with it, but also by far away particles and fluids through the propagation of disturbance waves (Xu and Yu, 1997). However, the complexity of this problem has prevented this behaviour from being solved analytically (Zhu et al., 2007). In DEM, it is typically assumed this problem is solved by choosing a numerical time step less than a critical value so that during a single time step the disturbance cannot propagate from a particle farther than its immediate neighbouring particles (Cundall and Strack, 1979). For linear contact models, the critical time step is related to the ratio of the contact spring stiffness to the particle density. However, the critical time-step for non-linear spring models (e.g. Hertz) cannot be calculated a priori (Li et al., 2005).

Cundall and Strack (1979) used a simple relationship to estimate the critical time step for their simulation. Due to the explicit nature of the model, a time step less than this critical time was used to keep the model stable. Their time step was based on a single degree-of-freedom system of mass m, and particle spring stiffness k. It was given as:

$$t_{CnS} = 2\sqrt{\frac{m}{k}} \tag{3.3}$$

While other approaches for determining the critical time step have been used in the literature (e.g. Apostolou and Hrymak, 2007; Deen et al., 2007), no consensus on the best method has been found. LIGGGHTS uses two criteria for determining the critical time step size, namely the Rayleigh and Hertz criteria. According to Li et al. (2005), in simulations it can be assumed that all the energy is transferred by Rayleigh waves on the particle's surface. Kremmer and Favier (2001) noted that calculating the critical time step size based on the frequency of the Rayleigh waves was a common approach. Generally, the Rayleigh criterion is more important, especially for dense systems, while the Hertz criterion can be used for dilute systems (Kloss personal communication, 2012). The Rayleigh criterion is usually smaller in magnitude, thus requiring a smaller time step size. Kremmer and Favier (2001) and Li et al. (2005) give the Rayleigh time step criterion (for particle i) as:

$$t_{Rayleigh} = \frac{\pi r_i}{(0.1631\nu_i + 0.8766)}\sqrt{\frac{\rho_i}{G_i}} \tag{3.4}$$

where G is the particle's shear modulus given by:

$$G_i = \frac{Y_i}{2(\nu_i + 1)} \tag{3.5}$$

Here ν is the Poisson's ratio and Y is the Young's modulus of the particle. From this relationship it is clear that the Rayleigh criterion is solely dependent on the particle properties, and thus will not change during the simulation unless the particle properties change. For the second criteria, the Hertz time step is given as:

$$t_{Hertz} = 2.87\left[\frac{m_{eff}{}^2}{r_{eff} * Y_{eff}{}^2 * v_{max}}\right]^{0.2} \tag{3.6}$$

where the effective mass is: $m_{eff} = \left(\frac{1}{m_i} + \frac{1}{m_j}\right)^{-1}$

effective radius is: $r_{eff} = \left(\frac{1}{r_i} + \frac{1}{r_j}\right)^{-1}$

effective Young's modulus is: $Y_{eff} = \left(\frac{1-\nu_i^2}{Y_i} + \frac{1-\nu_j^2}{Y_j}\right)^{-1}$

Subscripts i and j denote the two particles involved in the collision and v_{max} is the magnitude of the maximum relative velocity between the particles. Thus this relationship will change during the simulation as the velocity of the particles change.

Cundall and Strack (1979) warn that the system will only be stable with a small enough time step, due to the explicit nature of the DEM model. Hence the time step is often chosen to be a fraction of the critical time step. In the modern context of non-spherical particle shapes, the time step is often calculated based on an average particle diameter, which is also an incentive for running at a fraction of the full time step (Li et al., 2005).

When accuracy is required, a fraction of 1-5% is recommended, while for more industrial applications it can sometimes go as high as 30% in order to increase the time step size and thus reduce the computational time (Kloss, personal communication, 2012). Keeping the time step sufficiently low is important in controlling the kinetic energy in the system. If the energy in collisions increases too much, particle velocities can become very high and particles can escape out of the simulation domain. For example, smaller time steps are generally more suitable for larger particle volume fractions due the increased number of interactions generating higher energies (Kloss, personal communication 2013).

A frequently used technique to artificially increase the time step size (and reduce computational time) is to lower the particle stiffness (i.e. Young's modulus). Decreasing this value by two orders of magnitude can reduce the Rayleigh time step size by one order of magnitude. Physically, relaxing the particle stiffness would increase the duration of the particle contact. This allows larger time steps to be used, while still having sufficient steps to resolve the collision event (Hoomans et al, 1996; Wassgren and Sarkar, 2008). Experience has shown that reducing the particle stiffness by two to three orders of magnitude does not significantly affect the overall simulation behaviour (Tsuji et al., 1993; Hoomans et al., 1996).

3.2. INTER-PARTICLE FORCES

Forces discussed in this section relate to inter-particle interactions only, and are not influenced by the fluid. As such, these forces only affect the DEM portion of the model.

3.2.1. Contact Forces

Cundall and Strack (1979) assumed that the contact forces between the particles could be approximated by a linear spring and dashpot system. They assumed that the deformations of the individual particles are small in comparison to the overall dimensions of the system. Therefore exact modelling of the particle deformations is not necessary to obtain a good approximation of the overall mechanical behaviour of the system (Cundall and Strack, 1979). A well-known linear spring and dashpot contact model is the Hooke model. For the Hooke model, the normal component of the contact force is described as (Zhu et al., 2007):

$$\boldsymbol{f}_{ij}^{\,n} = -k_n \delta_n \boldsymbol{n}_c - \gamma_n \left(\boldsymbol{v}_{ij} \cdot \boldsymbol{n}_c\right)\boldsymbol{n}_c \tag{3.7}$$

where k_n is the normal spring stiffness, γ_n is the normal damping coefficient, $\boldsymbol{n}_c$ is the unit normal vector at contact, and $\boldsymbol{v}_{ij}$ is the relative velocity between particles i and j, such that $\left(\boldsymbol{v}_{ij} \cdot \boldsymbol{n}_c\right)\boldsymbol{n}_c$ gives the normal component of the relative velocity between the two particles. The particle overlap δ_n (in the normal direction) is defined as:

$$\delta_n = r_i + r_j - R \tag{3.8}$$

where R is the separation distance between the centres of the colliding particle. Tangential shear forces can also occur in collisions, giving rise to a torque. Most models use a Coulomb-type friction law, sometimes with damping, to determine the tangential contact force. The tangential overlap is limited to satisfy this relationship, which results in the (simplified) form of the tangential force:

$$\boldsymbol{f}_{ij}^{\,t} = \min\left(\boldsymbol{f}_t\,; -\mu_f \left|\boldsymbol{f}_{ij}^{\,n}\right| \boldsymbol{n}_t\right) \tag{3.9}$$

where: $\boldsymbol{f}_t = -k_t \delta_t + \gamma_t \left(\boldsymbol{v}_{ij} \times \boldsymbol{n}_c\right) \times \boldsymbol{n}_c$

Here k_t is the tangential spring stiffness, γ_t is the tangential damping coefficient, μ_f is the friction coefficient, $\boldsymbol{n}_t$ is the tangential unit vector, and δ_t is the tangential displacement between particle centres (Zhu et al., 2007).

The total contact force is just the summation of these two components:

$$\boldsymbol{f}_{ij}^{\,c} = \boldsymbol{f}_{ij}^{\,n} + \boldsymbol{f}_{ij}^{\,t} \tag{3.10}$$

A non-linear contact relationship, such as Hertzian contact, could also be employed if greater collision accuracy is required. It uses the same form as Equation 3.7, but has different stiffness and damping coefficients that introduce the non-linearity because they are dependent on the particle-particle overlap (LIGGGHTS manual, 2013).

3.2.2. Particle-Wall Impacts

Particle-wall impacts are calculated using the same contact model as particle-particle collisions. As such, the same equations are used, but in the limit of one of the particles going to infinite radius and mass (i.e. a flat wall). This is taken into account via the spring stiffness and damping coefficients.

3.2.3. Numerical Implementation of DLVO Forces

Here the numerical implementation of the DLVO forces will be discussed. The theory for the forces was covered in Section 2.4. Separate long-range potentials are used to model the van der Waals and electrostatic forces as they are easier to manipulate for different simulations. The combination results in an equivalent DLVO force.

van der Waals Force

Equation 3.11 describes the van der Waals interaction energy between two spherical particles of different size in an aqueous solution (LIGGGHTS manual, 2013). Here r_i is the radius of (spherical) particles i and j, R is the separation distance between the particle centres, and A_H represents the Hamaker constant given by Equation 2.14. Equation 3.11 computes the van der Waals force between two spherical "colloid" particles.

$$E_{vdw} = -\frac{A_H}{6}\left[\frac{2r_i r_j}{R^2-(r_i+r_j)^2}+\frac{2r_i r_j}{R^2-(r_i-r_j)^2}+\ln\left(\frac{R^2-(r_i+r_j)^2}{R^2-(r_i-r_j)^2}\right)\right] \tag{3.11}$$

The resulting van der Waals force is given as:

$$f_{vdw} = -\frac{A_H}{6D^2}\frac{r_i r_j}{r_i+r_j} \tag{3.12}$$

This relationship shows that as two particles move closer together during contact, and the separation distance reduces to zero, the force will become infinite. In reality a minimum separation distance is introduced to limit the magnitude of this force as particles collide. In other words, for separation distances smaller than this pre-defined value, the distance becomes fixed to this value.

Alternatively, as the separation distance increases, the force slowly reduces, but never reaches zero. However, it does reach a point where it can be assumed to be zero. But this distance is not recognised by the numerical model. So if the force takes a long time to reduce to zero, there will be many interactions that have to be calculated, especially for smaller particle sizes. Thus in order to reduce computational expense, a maximum "cut-off" distance ($r_{cut-off}$) is set such that the long-range potential is not calculated for particles outside this distance (i.e. $R < r_{cut-off}$). This distance is a trade-off between accuracy and computational efficiency.

Both the minimum separation distance and the maximum cut-off distance can be altered before the simulation starts to suit the particular physics required. Appropriate values can be determined by plotting the strength of the DLVO potential as a function of separation distance to determine the extent of the useful range.

Electric Double-Layer

For the electrostatic force, the interaction energy is given below as (LIGGGHTS manual, 2013):

$$E_{edl} = \frac{A_H}{\kappa} e^{-\kappa\left(R-\left(r_i+r_j\right)\right)} \tag{3.13}$$

This is equivalent to the expressions discussed in Section 2.4.2, after the application of the Derjaguin approximation (Equation 3.14). A cut-off distance is also imposed for this potential ($R < r_{cut-off}$). The force is given by:

$$f_{edl} = \varepsilon\varepsilon_0\kappa\psi_{i\infty}\psi_{j\infty}\frac{4\pi r_i r_j}{r_i + r_j}e^{-\kappa D} \tag{3.14}$$

3.3. CFD EQUATIONS FOR FLUID FLOW

Computational Fluid Dynamics (CFD) provides a numerical solution which can be used to study the flow detail. In CFD, the fluid volume is broken down in a number of small control volumes, or cells, in which the Navier-Stokes equations that govern the fluid flow

are solved. This is sometimes known as the "continuum", or Eulerian, approach where the fluid is assumed to act as a continuum throughout the domain.

3.3.1. Governing Equations of Fluid Flow

Most CFD codes use the Finite Volume Method (FVM) to model the fluid flow in the domain. Here, the fluid domain is split into small control volumes, or cells, in which the fluid properties are calculated and stored. The equations that govern the fluid flow are integrated over these cells to calculate the fluid properties.

To define the fluid flow through the domain within these cells, the mass and momentum conservation equations have to be solved. For incompressible flow, where fluid density is constant, the mass conservation (continuity) equation reduces to Equation 3.15. This is in fact a statement of the conservation of volume. The set of momentum equations used to define the fluid flow are the Navier-Stokes equations, which, for incompressible laminar flow, are summarised by Equation 3.16. Both equations are for time-dependent, three-dimensional flows and are written in Cartesian tensor form.

$$\frac{\partial}{\partial x_i}(u_i) = 0 \tag{3.15}$$

or simply: $div(\boldsymbol{u}) = 0$

$$\frac{\partial}{\partial t}(\rho u_i) + \frac{\partial}{\partial x_i}(\rho u_j u_i) = -\frac{\partial p}{\partial x_i} + \frac{\partial}{\partial x_j}\left[\mu\left(\frac{\partial u_i}{\partial x_j} + \frac{\partial u_j}{\partial x_i}\right)\right] + S_M \tag{3.16}$$

or simply: $\frac{\partial}{\partial t}(\rho u_i) + div(\rho u_i \boldsymbol{u}) = -\frac{\partial p}{\partial x_i} + div(\mu\, grad(u_i)) + S_M$

where ρ is the fluid density, and μ is the (first) dynamic viscosity of the fluid. The momentum source term S_M is comprised of body forces acting on the fluid in the cell, such as gravity or momentum exchange from a dispersed phase (i.e. particles in the flow). Subscripts i and j denote different components (x, y, and z) of the velocity vector $\boldsymbol{u}$ and the direction vector $\boldsymbol{x}$.

According to Newton's Third Law of Motion, the forces acting on the particles themselves will react on the fluid, exchanging momentum and altering its flow. Numerically, this momentum exchange is conveniently accounted for by the momentum source term (S_M). Here the momentum generated by each particle within a cell is added together in order to determine the total momentum reaction from all the particles in that cell. Different formulations for handling this are discussed in Section 3.4.

3.3.2. Fluid Force Measurement

For Couette flow, it is assumed that the flow is constant and two-dimensional (no vertical flow in this case). Also, there is no flow perpendicular to the wall, which is true for an impermeable wall surface. Thus the viscous force on a flat wall can be calculated from

$$F = \mu A \frac{du_x}{dy} \tag{3.17}$$

where u_x is the flow parallel to the surface, y is the direction of maximum shear (usually perpendicular to the wall) and A is the area over which the force is acting.

3.4. PARTICLE-FLUID FLOW – MODEL A VS. MODEL B

This section discusses the theory of the coupled model formulation, which requires a slightly different treatment from that of a single-phase fluid. A detailed walk-through of the implementation of the numerical solver that was used in this work is given in Appendix D.

When including contributions from particles in the fluid flow, both Equations 3.15 and 3.16 need to be re-formulated slightly. Two well known formulations are commonly used in various particle-fluid flow applications (e.g. Feng and Yu, 2003; Zhu et al., 2007). These are the "Model A" and "Model B" formulations (Xu and Yu, 1997; Zhou et al., 2010). The main difference between the two approaches is how the pressure term in the formulation is treated. Model A assumes that the pressure is shared between the fluid and solid phases, while Model B assumes it is handled by the fluid phase only. These formulations are generally the same as those used in the Two-Fluid Multiphase (TFM) methods where both phases are considered to be fluid continuums.

In an effort to determine which model was the most applicable, Zhou et al. (2010) investigated the origins of these models. They claim that there are in fact three particle-fluid formulations that can be derived from continuum TFM models (Sets I, II, III). Both Set II and Set III are derived from the base formulation, Set I. Zhou et al. (2010) claim that Set I and Set II are essentially the same, apart from some small differences arising from the treatment of the fluid stress tensor. Set III on the other hand, is a simplified version of the original formulation (Set I) due to some assumptions made about the flow. As such, Set III is only strictly valid when the flow through the particle phase is steady and uniform. Model A corresponds to Set II, while Model B corresponds to Set III. Set I has since been forgotten in literature.

In their paper, Zhou et al. (2010) compared the applicability of all three models to different particle-fluid flow systems that were typically found in literature, namely fluidised beds, pneumatic conveying, and hydrocyclones. They found that all three models were acceptable for fluidised systems and, for the most part, pneumatic conveying as well (i.e. flows that are largely 1D). However, for more complicated flows like hydrocyclones (truly 3D for both phases), Set I or Set II were the only acceptable models. This difference was based on how the particle-fluid interaction force was treated. In Set III (Model B), the pressure gradient force, which excluded the buoyancy force, was lumped together with the drag force. This treatment is fine when the forces act in the same direction, but this is not always the case for all flow systems. Combining this finding, with the fact that Set III's application was conditional due to the constraints placed on it during its formulation, Set III (Model B) was not considered suitable for general flows. This was despite the fact that Model B was often used in many fluidised bed applications (e.g. Feng and Yu, 2003). In summary, they found that Set I was the most appropriate and accurate in all cases, but because of their similarities, Set II (Model A) performed equally well. Therefore they recommend Model A for future use in general-purpose CFD-DEM modelling.

The generic continuity equation for compressible flow of coupled fluid-particle systems is shown in Equation 3.18. Equations specific to Models A and B are given in Equations 3.19 and 3.20 respectively (Zhou et al., 2010). Equation numbers with a, b, and c denote the momentum equation, the volumetric particle-fluid interaction force, and the DEM

particle-fluid interaction force on particle i. The particle-fluid interaction force (part c) is handled by the particle model (DEM in this case). For brevity, $\boldsymbol{\tau}_{ij}$ represents the viscous shear stress tensor (the second term on the right hand side of Equation 3.16).

$$\frac{\partial(\rho_f \varepsilon_f)}{\partial t} + \frac{\partial}{\partial x_i}(\rho_f \varepsilon_f u_i) = 0 \tag{3.18}$$

For Model A:

$$\frac{\partial}{\partial t}(\rho_f \varepsilon_f u_i) + \frac{\partial}{\partial x_i}(\rho_f \varepsilon_f u_j u_i) = -\varepsilon_f \frac{\partial p}{\partial x_i} - \boldsymbol{F}_{pf}^{A} + \varepsilon_f \frac{\partial \boldsymbol{\tau}_{ij}}{\partial x_j} + \rho_f \varepsilon_f \boldsymbol{g} \tag{3.19a}$$

where $$\boldsymbol{F}_{pf}^{A} = \frac{1}{V_{cell}} \sum_{i=1}^{n} \left(\boldsymbol{f}_{drag,i} + \boldsymbol{f}_i^{''} \right) \tag{3.19b}$$

$$\boldsymbol{f}_{pf,i} = \boldsymbol{f}_{drag,i} + \boldsymbol{f}_{\nabla p,i} + \boldsymbol{f}_{\nabla \cdot \tau,i} + \boldsymbol{f}_i^{''} \tag{3.19c}$$

and for Model B:

$$\frac{\partial}{\partial t}(\rho_f \varepsilon_f u_i) + \frac{\partial}{\partial x_i}(\rho_f \varepsilon_f u_j u_i) = -\frac{\partial p}{\partial x_i} - \boldsymbol{F}_{pf}^{B} + \frac{\partial \boldsymbol{\tau}_{ij}}{\partial x_j} + \rho_f \varepsilon_f \boldsymbol{g} \tag{3.20a}$$

where $$\boldsymbol{F}_{pf}^{B} = \frac{1}{\varepsilon_f V_{cell}} \sum_{i=1}^{n} \left(\boldsymbol{f}_{drag,i} + \boldsymbol{f}_i^{''} \right) - \frac{1}{V_{cell}} \sum_{i=1}^{n} \left(\rho_f V_i \boldsymbol{g} \right) \tag{3.20b}$$

$$\boldsymbol{f}_{pf,i} = \frac{\left(\boldsymbol{f}_{drag,i} + \boldsymbol{f}_i^{''} \right)}{\varepsilon_f} - \rho_f V_i \boldsymbol{g} \tag{3.20c}$$

Here, ε_f is the fluid volume fraction, V_{cell} is the computational (CFD) cell volume, $f_{pf,i}$ the total fluid-particle interaction force on an individual particle i, and $\boldsymbol{f}_i^{''}$ is the sum of other, not-so-dominant, particle-fluid interaction forces, such as: buoyancy, virtual mass, Saffman lift, Magnus force, etc. Generally, the drag, pressure gradient, and viscous forces are regarded as the dominant particle-fluid interaction forces (Zhou et al., 2010).

CFD coupling is achieved at the computational cell level with the volumetric particle-fluid interaction force ($\boldsymbol{F}_{pf}$), which is constructed from the particle-based drag forces in each respective cell. For the solid phase in DEM, this is achieved via the particle-fluid interaction forces, $\boldsymbol{f}_{pf,i}$.

3.5. SOLUTION TECHNIQUES FOR CFD-DEM SYSTEMS

In order to solve the governing equations, they are first discretised into a system of algebraic equations. This system is then solved for the relevant variable ϕ using appropriate numerical techniques. This can be done in several ways, but in general, either a direct or iterative method is used (Rusche, 2002). An iterative method starts with an initial guess and then improves the current approximation until some tolerance is met. Direct methods are not efficient for large systems, and so iterative methods are preferred. However, they impose some requirements on the solution matrix. This section discusses some factors that influence solution stability and accuracy in relation to particle-fluid flow. Stability is an important consideration for coupled particle-fluid problems.

3.5.1. Spatial Discretisation of Flow Equations

An important step of the finite volume method is to transform one or more continuous governing equations into a corresponding system of algebraic equations that can be solved at discrete points of a control volume. This involves the integration of the governing equations over the control volume, and time, to yield a discretised equation for that cell. The solution to this new system approximates the solution of the original equations.

The typical momentum equation for fluid flow is a second-order equation, because the diffusion term includes the second derivative of $\boldsymbol{u}$ in space. For good accuracy, it is necessary for the order of the discretisation to be equal to or higher than the order of the equation that is being discretised (Jasak, 1996). This is not always achievable in practice though. Any deviation from the order of accuracy creates a discretisation error, which only disappears in the limit of an excessively fine mesh. This is because the leading truncation error term is proportional to the grid spacing. The order only determines the rate at which the error goes to zero as the time step goes to zero, and this only after the step size has become small enough (Ferziger and Perić, 2002).

Discretisation produces a linear algebraic equation for each control volume. The exact form of these equations depends on the governing equation and the discretisation practises used, but they can be re-written into the generic form:

$$a_P \phi_P^{new} + \sum_N a_N \phi_N^{new} = R_P \tag{3.21}$$

This equation requires that the sum of the value at the current node (P) plus the values at the neighbouring nodes (N) is equal to any additional terms (R) occurring in current cell P (usually source terms). The superscript "new" implies the ϕ values are implicit, and depend on values from neighbouring cells during the same iteration. Whereas R_P can also depend on values from a previous time step. Equation 3.21 can be further re-arranged into:

$$[A][\phi] = [R] \tag{3.22}$$

where $[A]$ is a sparse matrix with coefficients a_P on the diagonal and a_N on the off-diagonals, $[\phi]$ is a column vector of the dependent variable and $[R]$ is the vector of source terms. Terms which are treated implicitly always contribute to the $[A]$ matrix coefficients, but can also contribute to the source vector $[R]$. Explicit terms, however, only contribute to the source vector. It is this system of linear algebraic equations that need to be solved to obtain the CFD results.

All terms in the governing equations that cannot be written as convection, diffusion or temporal terms are treated as source terms. Source terms can take many forms, but in general, they are first “linearised” before discretisation and take the form of Equation 3.23. This is due to its interaction with other terms in the system of equations that need to be solved. Implications of linearisation are discussed further in Section 3.5.2 and 3.5.3.

$$S_M = Su + Sp\phi_P \tag{3.23}$$

where Su is considered the “explicit” component and Sp the “implicit” or “linear” component. Both Su and Sp can be a function of the dependent variable ϕ.

3.5.2. Explicit vs. Implicit Formulations

In CFD, the governing equations are non-linear, and the number of unknowns is often very large. These conditions typically encourage iterative solution techniques. If a system of equations is calculated from known values (e.g. values from previous iterations or time steps), the calculation is said to be explicit. If the system contains only values from the current iteration (usually requiring matrix or iterative techniques), then it is called an implicit calculation.

Explicit formulations (including the linearised source term based on ϕ_P^{old}) have the form of Equation 3.24. While this form is convenient to compute, it has a limitation that the coefficient of ϕ_P^{old} can become negative, and therefore reduce diagonal dominance of $[A]$. For the coefficient to be positive, the time step would need to be small enough such that $a_P^{old} > a_E + a_W$, otherwise physically unrealistic results could occur.

$$a_P\phi_P = a_W\phi_W^{old} + a_E\phi_E^{old} + \left(a_P^{old} - \left(a_W + a_E - Sp\right)\right)\phi_P^{old} + Su \tag{3.24}$$

where $a_P = a_P^{old}$

The implicit scheme (including the linearised source term based on ϕ_P) results in a slightly different format of

$$a_P\phi_P = a_W\phi_W^{old} + a_E\phi_E^{old} + a_P^{old}\phi_P^{old} + Su \tag{3.25}$$

where $a_P = a_P^{old} + a_W + a_E - Sp$

It is clear from the implicit formulation that all the coefficients are positive, which makes the implicit scheme unconditionally stable for all time step sizes. Small time step sizes are still required for accuracy as the scheme is only first-order accurate in time (Versteeg and Malalasekera, 2007). OpenFOAM® has a mixed-source discretisation procedure that is implicit when the coefficients are greater than zero and explicit for coefficients less than zero (OpenFOAM® programmer's guide, 2012).

3.5.3. Source Terms and Stability Considerations

Coupled CFD-DEM solvers include the interaction of the particulate phase via a source term in the fluid governing equation. The treatment of the source has some implications on the solution method. In this work, an iterative solution method is used.

Iterative solvers require diagonal dominance in order to guarantee convergence (Rusche, 2002). A matrix is said to be diagonally dominant if the magnitude of at least one diagonal coefficient is larger than the sum of the magnitudes of the off-diagonal coefficients in its row, i.e. $|a_P| > \sum_N |a_N|$. In order to improve solver convergence, it is desirable to increase diagonal dominance of the system whenever possible. One way of doing this is to "linearise" the source term before discretisation (see Equation 3.23).

Discretisation of the linear part of the source term (Sp) only affects the diagonal coefficients of the matrix as it is connected to the ϕ_P terms (Rusche, 2002). If $Sp < 0$, the diagonal dominance of the coefficient matrix $[A]$ is increased (Equation 3.22), and thus Sp is included into the diagonal coefficients. But if $Sp > 0$, the diagonal dominance is decreased, and it would be better to include this term into the source $[R]$, which is updated when the new solution is available. However, this measure is not sufficient to guarantee diagonal dominance of the matrix.

According to Jasak (1996), it is advisable to treat the source term as implicitly as possible. This will increase its contribution to the coefficient on the diagonal (increasing diagonal dominance), and reduce the contribution to the source term. Patankar (1980) discusses the extent to which this should be done.

Diagonal dominance can also be influenced by the choice of discretisation schemes for the other terms. For example, the convection term only creates a diagonally equal matrix when upwind-differencing is used. Any other differencing scheme will create negative coefficients, and potentially create an unbounded solution. Alternatively, the diffusion term only creates a diagonally equal matrix if the mesh is orthogonal. Diffusion terms on non-orthogonal meshes tend to introduce extra terms with negative coefficients into the

solution matrix, thus violating diagonal equality. Therefore boundedness of the solution cannot be guaranteed as a consequence of mesh non-orthogonality (Jasak, 1996). Discretisation of the temporal derivative creates both a diagonal coefficient and a source term contribution, thus increasing diagonal dominance.

3.5.4. Momentum Source Term for Particle-Fluid Coupling

In their flow equation, Goniva et al. (2012) represent their momentum exchange term in the form of Equation 3.26. For numerical stability reasons, the momentum exchange term was split-up into an implicit part ($\boldsymbol{u}$) and an explicit part that uses the cell-based ensemble-averaged particle velocity, $\langle \boldsymbol{v} \rangle$. Here, the term explicit is used because the component involves known particle velocity values from the previous set of DEM iterations.

$$\boldsymbol{F}_{pf}^{A} = K_{pf}\boldsymbol{u} - K_{pf}\langle \boldsymbol{v} \rangle \tag{3.26}$$

where $$K_{pf} = -\frac{\left|\sum_i \boldsymbol{f}_{pf}\right|}{V_{cell}\left|\boldsymbol{u} - \langle \boldsymbol{v} \rangle\right|}$$

and $\sum \boldsymbol{f}_{pf}$ represents the sum of all the particle-fluid forces acting on particles in a cell, of which the primary force of interest is the drag on the particle. K_{pf} is the momentum exchange coefficient for the cell.

3.5.5. Explicit vs. Implicit DEM Drag Force

Explicit methods require less computational effort per time step than implicit methods. As such, DEM typically uses an explicit formulation because these are more efficient for DEM/molecular dynamics type applications (Kloss, personal communication, 2012). However, as has been mentioned already, explicit schemes can introduce instability into the calculation, especially if the time step is too high.

Equation 3.27 illustrates this new implicit formulation (for Model A). This allows the drag force to vary with the new particle velocity ($\boldsymbol{v}_i$) calculated on each DEM time step,

while the fluid velocity ($\boldsymbol{u}$) is held constant until it is updated during the coupling event. This is contrasted by the explicit formulation of the drag force, which is set at a constant value until the CFD solver is run again (Equation 3.28). Both the fluid and individual particle velocities ($\boldsymbol{v}_i^{old}$) are only updated at the coupling event, and kept constant over the following DEM time steps.

$$\boldsymbol{f}_{pf,i} = \beta V_i \left(\boldsymbol{u} - \boldsymbol{v}_i\right) \tag{3.27}$$

$$\boldsymbol{f}_{pf,i} = \beta V_i \left(\boldsymbol{u} - \boldsymbol{v}_i^{old}\right) \tag{3.28}$$

The coefficient β is the inter-phase momentum transfer coefficient (not the same as K_{pf} in Section 3.5.4). This implicit formulation for the drag introduces stability improvements when particle velocities are changing significantly between coupling events which is where the flow variables are updated. This could even allow for bigger coupling intervals and/or CFD time steps, which is the caveat of implicit methods.

3.5.6. Time Step Size and the Courant Number

A transient solver calculates the flow solution at a certain point in time, and then steps forward in time to the next calculation point. The solver continuously steps forward in time until the simulation reaches its predefined limit. A time step is the amount in virtual time that the solution moves forward between calculations. To maintain stability in a calculation, the time step size should be small enough to allow the flow to develop properly. The Courant-Friedrich-Levy (CFL) number, or simply Courant number, is used as a guide to set the upper limit of the time step size. The Courant number in a single cell is defined by the equation

$$C_O = \frac{dt|\boldsymbol{u}|}{dx} \tag{3.29}$$

where dt is the time step size, $|\boldsymbol{u}|$ is the magnitude of the flow velocity through the cell, and dx is the size of the cell in the direction of the flow. To achieve temporal accuracy and numerical stability a Courant number of less than 1 is required throughout the flow

domain (OpenFoam user guide, 2012). In particular, explicit schemes can become unstable for C_O > 1. So when setting the maximum time step size, Equation 3.29 is calculated for the worst case scenario. However, when using Euler implicit time discretisation, the system can be stable for C_O values greater than one (Jasak, 1996).

3.5.7. Coupling Interval

Because the two methods (CFD and DEM) run separately, an interval needs to be set which governs when information is exchanged between the solvers. For best accuracy, there should be one DEM time step for every CFD time step. However, it is usually the DEM time step that sets the lower limit of the time step size to keep the simulation stable. Most CFD simulations could run quite happily at higher time steps. Therefore if the CFD portion of the simulation could run at a higher time step, this would reduce computational expense and speed up the solution speed.

Therefore it is typical to set a coupling interval, which governs how many DEM time steps are run before the information is passed to the CFD solver. Typically, this interval is set in the range of 50 - 100 (Goniva, personal communication, 2012), which means that the DEM code runs for 50 - 100 time steps before coupling with the CFD code. This is acceptable if the DEM time step is very small (or the particle motion is very small) as the particle would not have moved far before the flow/particle information is updated. However, it is important to make sure that the CFD time step is not too large.

A good guideline is to keep the CFD time step smaller than the momentum response time (also called the particle relaxation time), as is illustrated in Figure 3.2. This allows both the flow and particle to adjust to each others movement, without any large changes in velocity and consequently, the forces involved. The momentum response time describes the time required for a particle to respond to a change in fluid velocity. Crowe et al., (1998) derive this time value by considering the equation of motion of a spherical particle in the limit of low Reynolds number (Stokes) flow:

$$m\frac{dv}{dt} = \frac{1}{2}C_D\frac{\pi d^2}{4}\rho_f(u-v)|u-v|$$

which results in: $$\frac{dv}{dt} = \frac{1}{t_V}(u - v) \tag{3.30}$$

where $$t_V = \frac{\rho_p d^2}{18\mu_f} \tag{3.31}$$

is the momentum response time, with units of reciprocal time. For a constant fluid velocity (u) and an initial particle velocity (v) of zero, the solution of Equation 3.30 gives:

$$v = u\left(1 - e^{-t/t_V}\right) \tag{3.32}$$

Thus the momentum response time is the time (t) taken for a particle to accelerate from rest and reach 63% of the free stream fluid velocity (Equation 3.32). As can be seen, the momentum response time is particularly dependent on the particle size. Further re-arranging Equation 3.32 gives t as:

$$t = -\frac{\rho_f d^2}{18\mu_f}\ln\left(1 - \frac{v}{u}\right) \tag{3.33}$$

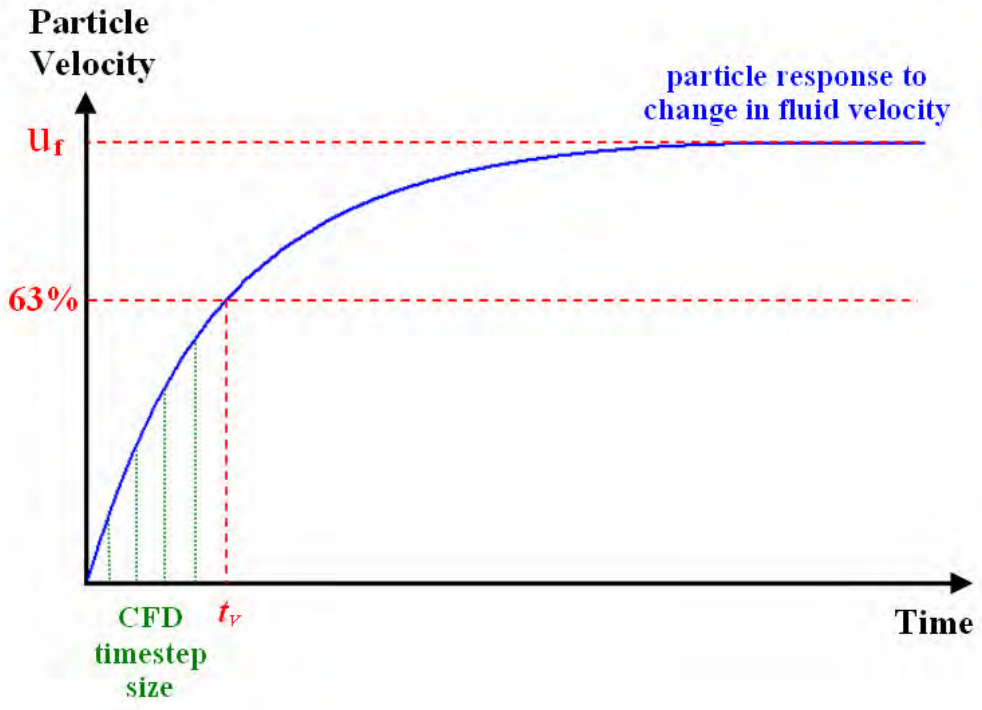

Figure 3.2: Coupling interval diagram, showing CFD time step size

3.5.8. Continuity Error Calculation

Because the solver runs through an iterative process to achieve the final result, there needs to be some measure of how accurate the solution is becoming with successive iterations. Typically, the solution is evaluated to see how well mass is conserved. Ideally the change in mass should be zero (conservation of mass), unless mass is allowed to exit or leave the system through a boundary. For iterative solutions, the value should at least tend towards zero to indicate a converging solution.

To calculate this, the divergence of the cell-face mass flux is taken for every cell, and then added together. Because the flux out of one cell flows into the adjacent cell, all the internal field values cancel, and so only the flux at the boundaries is considered. This technique is quick and easy to calculate. The cumulative error is the sum of these errors over all the past simulation time steps (or iterations for steady-state solvers). Sometimes the magnitude of the error is also of importance, as this should also tend to zero for a converging solution. For a multiphase system, mass conservation also needs to be checked for the secondary phase (e.g. particles) as well.

3.5.9. Mesh Considerations

While the assumption that DEM particles are "much" smaller than the CFD cells drives most CFD-DEM methods, no criteria have been brought forward to define how much smaller they should be. Relative size seems to be case specific, with the cell size being tailored to the problem. However, experience has shown that cell dimensions can be made as small as 3-4 particle diameters and still result in stable simulations (Goniva, personal communication, 2012). This is generally the lower limit; otherwise the cell becomes “too full" of particle matter, with too little fluid inside of it. This could mean that any assumptions made about locally-averaged values of in a cell (i.e. cell-centred values varying smoothly across the cell) could become invalid at that size.

3.6. FLUID-PARTICLE FORCES

Changes in fluid viscosity occur due to the interaction of the particles with the fluid. The fluid imparts momentum onto the particles, while the particles resistance to motion is fed back into the fluid, altering its flow. The resulting momentum exchange adheres to

Newton's third law of motion (Xu and Yu, 1997; Feng and Yu, 2003). This change in the flow around the particles alters the macroscopic flow of the fluid which we see as a change in viscosity. This is a result of increased energy dissipation in the fluid due to the disturbance of the flow field by the particles (Zhu et al., 2001). Consequently, it is important to correctly determine the interaction of the fluid and the particles to determine the extent to which the particles affect the flow. Apart from the Reynolds Number, the drag acting on a particle depends strongly on the particle shape, angle of incidence, and angle of rotation (Holzer and Sommerfeld, 2009). However, much of the literature focuses on spherical particles due to their simplicity and computational efficiency.

3.6.1. Particle Drag Force

There are two different methods to determine the particle-fluid drag force. The first, more common, method is the use of empirical correlations relating the drag force to the pressure drop in the fluid. The second requires detailed modelling of the particles at the micro-scale, using DNS for example (Zhu et al., 2007). This study shall be concerned with the use of empirical relations to account for the drag due to its simplicity.

The drag force on an isolated (spherical) particle in a fluid is given as (Zhu et al., 2007):

$$\boldsymbol{f}_{drag\,(sphere)} = \frac{C_D \pi \rho_f d_i^2 |\boldsymbol{u} - \boldsymbol{v}_i| (\boldsymbol{u} - \boldsymbol{v}_i)}{8} \tag{3.34}$$

where C_D is the particle drag coefficient, ρ_f is the fluid density, d_i is the particle diameter, $\boldsymbol{u}$ is the velocity vector of the fluid around particle i, and $\boldsymbol{v}_i$ represents the particle velocity vector. However, the presence of many particles in a fluid reduces the space for a fluid which generates a sharp fluid velocity gradient. As a result, there is an increased shear stress on the particle surface (Zhu et al., 2007). A voidage function of some description is included into this formulation to account for the effect of surrounding particles. This voidage function is usually a simple exponential function based on the fluid volume fraction, ε_f.

Ergun's (1952) expression of this relation re-defines the friction coefficient as a function of Reynolds number to give the form shown in Equation 3.35 (Gidaspow, 1994; Zhu et

al., 2007). His relation describes the rate of momentum dissipation due to the relative motion between the fluid and a particle (Gidaspow, 1994).

$$\boldsymbol{f}_{drag\,(Ergun)} = \beta V_i(\boldsymbol{u} - \boldsymbol{v}_i) \tag{3.35}$$

where V_i is the particle volume. The coefficient β is the inter-phase momentum transfer coefficient, and relates the friction coefficient to the (particle) Reynolds number. There is no real consensus on the best way to calculate β, and is subject to ongoing scrutiny (Goniva et al., 2012). However, a number of theories have been proposed and have been commonly employed in the modelling of particle drag in fluidised beds. Some of these relations will be considered in this study as they are applicable to flows with high particle densities (like the conditions found in fluidised beds). The particle Reynolds number, i.e. the number describing the flow surrounding a particle i, is given by:

$$Re_{p,i} = \frac{\rho_f \varepsilon_f d_i |\boldsymbol{u}_i - \boldsymbol{v}_i|}{\mu_f} \tag{3.36}$$

In the literature covering fluidised beds, two drag force models are favoured. These are the models by Ergun (1952), and Di Felice (1994). Both models were intended for spherical particles, and depended on the Reynolds number and a porosity factor (ε_f). The porosity factor accounts for the fact that the flow around a single particle is much different to the flow around multiple particles in close proximity to each other. Wen and Yu's (1956) formulation adjusts Ergun's equation for porosity values above 0.8 (80% particle loading by volume). However this introduces a step jump in the C_D values around porosity values of 0.8. Di Felice's formulation, described by Equation 3.37, eliminates this discontinuity (Feng and Yu, 2003). Here, a voidage function is multiplied by Equation 3.34 to give the drag force:

$$\boldsymbol{f}_{drag\,(DiFelice)} = \boldsymbol{f}_{drag\,(sphere)}\left(\varepsilon_f^{-\alpha}\right) \tag{3.37}$$

where $$\alpha = 3.7 - 0.65\exp\left[-\frac{\left(1.5 - \log_{10}\left(Re_{p,i}\right)\right)^2}{2}\right]$$

Re_p is the particle Reynolds number for particle *i*. In the literature, there are actually a number of variations for the exponent in Equation 3.37 (e.g. Xu et al., 2000). In CFDEM, an exponent of $2-\alpha$ is used because this value fits best with other correlations in literature (like the Koch and Hill model discussed below).

Another, more recent, model was proposed by Koch and Hill (2001) and based on lattice-Boltzmann simulations for gas-solid suspensions. The formulation was developed for $Re_p << 1$ and $St \geq O(1)$. The implementation of this model gives (Goniva et al., 2012; van der Hoef et al., 2005):

$$\boldsymbol{f}_{pf,i} = \frac{V_i \beta}{\varepsilon_p}(\boldsymbol{u} - \boldsymbol{v}_i) \tag{3.38}$$

where $$\beta = \frac{18\mu_f (1-\varepsilon_f)\varepsilon_f^2}{d_p^2}\left(F_0(\varepsilon_p) + \frac{1}{2} F_3(\varepsilon_p) Re_p \right)$$

$F_0(\varepsilon_p)$ is the non-dimensional Stokes-flow drag force of Koch and Sangani (1999). $F_0(\varepsilon_p)$ and $F_3(\varepsilon_p)$ are defined below as:

$$F_0(\varepsilon_p) = \frac{1 + 3\left(\frac{\varepsilon_p}{2}\right)^{1/2} + \left(\frac{135}{64}\right)\varepsilon_p \ln(\varepsilon_p) + 16.14\varepsilon_p}{1 + 0.681\varepsilon_p - 8.48\varepsilon_p^2 + 8.16\varepsilon_p^3} \quad \text{for } \varepsilon_p = 1-\varepsilon_f < 0.4 \tag{3.39a}$$

$$F_0(\varepsilon_p) = \frac{10\varepsilon_p}{(1-\varepsilon_p)^3} \quad \text{for } \varepsilon_p \geq 0.4 \tag{3.39b}$$

$$F_3(\varepsilon_p) = 0.0673 + 0.212\varepsilon_p + \frac{0.0232}{(1-\varepsilon_p)^5} \tag{3.40}$$

This version of the Koch and Hill model is used in CFDEM. A variation of that model, proposed by Hill et al. (2001) for $Re_p > 40$, is presented in Deen et al. (2007). However, Deen et al. (2007) suggested that a version of Hill's model, modified by Beetstra et al. (2006), is better as it is applicable over a wider range of Reynolds numbers. This

formulation for β is shown below in Equation 3.41. This expression for β is applicable up to a Reynolds number of 1000.

$$\frac{\beta d_p^2}{\mu} = A\frac{\varepsilon_p^2}{\varepsilon_f} + B\varepsilon_p Re_p \tag{3.41}$$

where $$A = 180 + \frac{18\varepsilon_f^4}{\varepsilon_p}\left(1 + 1.5\sqrt{\varepsilon_p}\right)$$

and $$B = \frac{0.31\left(\varepsilon_f^{-1} + 3\varepsilon_f\varepsilon_p + 8.4Re^{-0.343}\right)}{1 + 10^{3\varepsilon_p}Re^{2\varepsilon_f - 2.5}}$$

Alternatively, particle shape can be included in the formulation to make it more accurate for non-spherical particles. Holzer and Sommerfeld (2009) gives drag coefficient values of non-spherical shapes that were calculated in numerical simulations. The same authors also published a drag coefficient formulation for non-spherical particles that is based on the sphericity of the particle (Holzer and Sommerfeld, 2008). Hilton et al. (2010) used Holzer and Sommerfeld's (2008) relation and showed reasonably accurate results. This shows that using a formulation based on projected areas of the particle face is more accurate than one based on relative sphericity. This will most likely be an area of intense future research as many real-life particulate suspensions do not have spherical particles, and while particle shape is an important factor in suspension rheology, there is not much systematic data on these systems (Mewis and Wagner, 2009).

3.6.2. Gravitational Force and Buoyancy

Particle weight due to gravity will be countered by the buoyancy force imparted on the particle by the surrounding medium. This is of particular importance when the suspending medium is a dense liquid, resulting in a more significant buoyancy force. The combination of these two effects can be described by Equation 3.42 (Apostolou and Hrymack, 2008) for a particle, i, of density ρ_s.

$$\boldsymbol{f}_{bouy} = -V_i\left(\rho_s - \rho_f\right)\boldsymbol{g} \tag{3.42}$$

3.6.3. Pressure Gradient Force

The pressure gradient force is caused by an uneven pressure distribution around a particle, which pushes particles away from high-pressure regions (Zhou et al., 2010). The buoyancy force only takes partial account of the pressure force on the particle. In reality, the particle cannot distinguish between the contribution arising from gravity, and any other contribution to the fluid pressure gradient, such as acceleration pressure gradients in the fluid. Therefore all contributions from the fluid pressure gradient should also be considered, along with buoyancy (Anderson and Jackson, 1967). This pressure gradient force can be regarded as an important force in particle-fluid flow (Anderson and Jackson, 1967; Zhu et al., 2007), though it is only significant if a large pressure gradient exists, or if the particle density is smaller than the fluid density. For the general case of flow with diverging streamlines, Anderson and Jackson (1967) give the combined force due to gravitational and pressure effects as:

$$\boldsymbol{f}_i = -V_p\left(\rho_s - \rho_f\right)g_i + \rho_f V_p u_i \frac{du_i}{dx_i} \tag{3.43}$$

which results in the generalised pressure gradient force being defined as:

$$\boldsymbol{f}_{pgrad,i} = -V_p\left(-\rho_f g_i - \rho_f u_i \frac{du_i}{dx_i}\right) = -V_p \frac{dp}{dx_i} \tag{3.44}$$

where V_p is the particle volume, and g_i is the gravitational acceleration in direction i.

3.6.4. Viscous Force

The viscous force is another important force in particle-fluid flow. It occurs due to the fluid shear stress set up by the fluid's velocity gradient. By means of its definition, this force tends to move particles towards regions of lower shear. This force is defined as:

$$\boldsymbol{f}_{visc} = -V_i\left(div(\boldsymbol{\tau})\right) = -V_i\left(\nabla \cdot \boldsymbol{\tau}\right) \tag{3.45}$$

where

$$div(\boldsymbol{\tau}) = -\nabla\cdot(\mu\nabla\boldsymbol{u}) - \nabla\cdot\left[\mu\left(dev\left((\nabla\boldsymbol{u})^T\right)\right)\right] = -\nabla\cdot(\mu\nabla\boldsymbol{u}) - \nabla\cdot\left[\mu\left((\nabla\boldsymbol{u})^T - \frac{1}{3}tr\left((\nabla\boldsymbol{u})^T\right)\right)\right]$$

Because the fluid is assumed to be incompressible, this reduces to:

$$-\nabla\cdot\left[\mu\left(\nabla\boldsymbol{u} + (\nabla\boldsymbol{u})^T\right)\right] = -\nabla\cdot\left[\mu\left(\frac{d\boldsymbol{u}_i}{dx_j} + \frac{d\boldsymbol{u}_j}{dx_i}\right)\right]$$

therefore $$\boldsymbol{f}_{visc} = V_i\left[\nabla\cdot\left(\mu\left(\frac{d\boldsymbol{u}_i}{dx_j} + \frac{d\boldsymbol{u}_j}{dx_i}\right)\right)\right] \tag{3.46}$$

3.6.5. Lubrication Force

The lubrication force arises from hydrodynamic pressure in the interstitial fluid that is squeezed out from the space between two solid surfaces as they approach each other (Zhang et al., 2005). As the particles move apart, a negative pressure (relative to the bulk fluid) results as fluid is drawn in to fill the gap between the receding surfaces. This creates a tensile stress that opposes the motion of the particles and limits their rebound velocity (assuming that the tensile stress does not become large enough to cause cavitation in the fluid) (Davis et al., 1986). The result of this lubrication force is to produce a damping effect on the particles, causing kinetic energy to be dissipated during both the approaching and separating stages (Zhang et al., 2005).

This force only becomes significant when the particle separation distance is much smaller than the particle radius ($D \approx 0.01r$). The force is given by (Zhang et al., 2005):

$$\boldsymbol{f}_{lube} = \frac{6\pi\mu r^2\boldsymbol{v}_{rel}}{D} \tag{3.47}$$

where v_{rel} is the relative velocity between the particles. Due to this relative velocity component, the force is repulsive when particles move towards each other, but becomes attractive when particles move away from each other.

From Equation 3.47, it can be seen that the force becomes very large ("infinite") as the separation distance reduces to zero (which would happen when particles contact each other). This implies that the particles can never come into contact (Zhang et al., 2005, Davis et al., 1986). However, when other attractive inter-particle forces are included, such as the van der Waals force, then it is possible for the particles to overcome the lubrication force and come into contact (Serayssol and Davis, 1986). Zhang et al. (2005) propose other realistic scenarios in which particles can also make contact.

The lubrication force can be significant for particles with large inertia, i.e. large particles or particles with large relative velocities. Colliding particles would rebound without physically touching. However, the fluid pressure between particles causes them to slow down, which leads to a decrease in fluid pressure (Davis et al., 1986). The tensile stress would also limit the rebound velocity of the particles. Thus it is possible for low-inertia particles (e.g. approaching at low speeds) to eventually come to a rest next to each other, without necessarily contacting (Serayssol and Davis, 1986).

Thus this force is only significant when particles are large, the surrounding fluid is very viscous, the relative particle velocities are large (i.e. during a potential collision), and when the particle separation distance is much smaller than the particle radius ($D \approx 0.01r$).

3.6.6. Mei (Saffman) Lift force

Lift on a particle is generated by the difference in fluid pressure on opposite sides of a particle due to the different fluid velocities resulting from the velocity shear gradient. Saffman (1965) developed this force for creeping flows (where $Re_p << 1$) and a linear shear velocity profile. According to Loth and Dorgan (2009), the lift force is one of the more difficult forces to model as there are a number of physical factors that can contribute to lift generation. Two of the primary mechanisms are the vorticity in the continuous (fluid) phase, and particle rotation.

The Saffman lift force, described by Zhu et al. (2007), is given as:

$$\boldsymbol{f}_{Saffman} = 1.615\, d_i^2 \left(\rho_f \mu\right)^{1/2} \left|\boldsymbol{\omega}_f\right|^{-1/2} \left[\left(\boldsymbol{u} - \boldsymbol{v}_i\right) \times \boldsymbol{\omega}_f\right] \tag{3.48}$$

where $\boldsymbol{\omega}_f$ is the vorticity of the flow (and equivalent in magnitude to $\dot{\gamma}$ for plain Couette flow). The cross product of the relative velocity and the vorticity gives the direction of the force. However, the work of Saffman was extended by McLaughlin (1991) and Mei (1992) to limit the restriction of $Re_p << Re_\omega^{1/2}$, which applied to the above formulation (Equation 3.48). Loth and Dorgan (2009) discuss further extensions, and while the full discussion is omitted here for the sake of brevity, the final result is given by Equation 3.49 (using their notation). This formulation is valid up to $Re_p = 50$, and includes the influence of particle rotation on the lift force.

$$C_L = J^* \frac{12.92}{\pi} \sqrt{\frac{\omega^*}{Re_p}} + \Omega^*_{p,eq} C^*_{L,\Omega} \tag{3.49}$$

where ω^* and Ω^*_p are related to the vorticity and particle angular velocity respectively. The CFDEM implementation of this force makes use of Equation 3.49 and its notation to calculate the lift force as:

$$\boldsymbol{f}_{Mei\ lift} = 0.125 \pi d_i^2 \rho_f C_L \left|\boldsymbol{u} - \boldsymbol{v}_i\right| \left[(\boldsymbol{u} - \boldsymbol{v}_i) \times \frac{\boldsymbol{\omega}}{|\boldsymbol{\omega}|} \right] \tag{3.50}$$

This lift force is due to the velocity gradient across the particle, which means the force is going to be larger for larger particles. When looking at the ratio of Saffman lift force to Stokes drag for simple shear flows, it is evident that the Saffman force is negligible at very small shear rates, or very low Re_p (Johnson, 1998). However, this force can be significant when the slip velocity is large in the vicinity of high (shear) strain rates, e.g. in the wall boundary layer for turbulent bubbly flows (Fluent user guide, 2005).

3.6.7. Virtual Mass Force

Another effect that is sometimes accounted for is the "virtual mass" effect. This occurs when a secondary phase (i.e. particles) accelerate relative to the primary phase (i.e. the fluid). The inertia of the primary phase's mass is felt by the particles as they accelerate, and they feel what is called a virtual mass force. It can be regarded as the force required

to accelerate the fluid surrounding the particle (Fluent user guide, 2005). The force, per unit mass, is given by (Fluent user guide, 2005):

$$\boldsymbol{f}_{u.vol} = \frac{1}{2}\frac{\rho_f}{\rho_p}\frac{d}{dt}(\boldsymbol{u} - \boldsymbol{v}_i) \tag{3.51}$$

But the full force is given by:

$$\boldsymbol{f}_{vmass} = \frac{1}{2}\rho_f V_i \frac{d}{dt}(\boldsymbol{u} - \boldsymbol{v}_i) \tag{3.52}$$

As Equation 3.51 illustrates, the virtual mass effect is only significant when the secondary phase density (particle) is much smaller than the primary phase density (fluid), e.g. bubbles in a fluid. Zhu et al. (2007) suggests the force becomes insignificant at $\rho_f / \rho_p \approx 10^{-3}$.

3.6.8. Basset Force

The Basset force, or alternatively, the history force, accounts for the unsteady component of the drag force which develops over time by the viscous region in the vicinity of the particle (Loth and Dorgan, 2009). This means the force can decay over time provided the particle reaches a constant velocity (e.g. terminal velocity). Anderson and Jackson (1967) however, feel that a term like the Basset force is unnecessary for dense particle-fluid flows because the presence of many particles near each other would erase any historical effects that a particle has on the fluid motion. In addition, Zhu et al. (2007) suggests the force becomes insignificant at $\rho_f / \rho_p \approx 10^{-3}$. Furthermore, this term can be computationally expensive to calculate (Loth and Dorgan, 2009).

4. CFD MODEL RESULTS

This chapter outlines the first step in the methodology, namely the design of a CFD model of a rheometer. To this end, two types of CFD models were tested: one for a basic Newtonian fluid, and the second for a shear rate dependent non-Newtonian fluid. If the data retrieved from the model can predict the behaviour of both these types of fluid, then this model would form a good base from which more complex systems can be studied. The addition of particles is discussed in subsequent chapters.

Section 4.1 describes the design of the model, including the generation of the CFD mesh and boundary conditions. The mesh shape and boundary conditions are what allow the model to mimic a rheometer. Section 4.2 discusses results for the Newtonian fluid simulations, while Section 4.3 covers results for a non-Newtonian fluid. Finally, Section 4.4 considers the implications of these results for the coupled CFD-DEM model. Terms specific to the software code are highlighted in the text in a different font style.

4.1. MODEL OUTLINE

A few assumptions were made when generating the rheometer model. It is often assumed that there is no flow variation in the vertical direction within a rheometer. This is not strictly true due to end effects at the bottom of the gap (at the end of the rotor) and free-surface effects at the top (where the fluid free surface is usually unconstrained in an open cup). However, for a sufficiently long cylinder, these end effects are not significant. Narrow gap widths also reduce the influence of these effects (Hughes et al., 1998). Consequently, preliminary tests indicated that modelling the full geometry of a rheometer was not necessary. Therefore only a thin horizontal sliver was modelled (cf. Figure 4.1). Modelling a reduced section of the rheometer would keep computational costs low.

Furthermore, the flow around the entire circumference of the cylindrical gap is assumed to be exactly the same (the rheometer is a Couette flow device of constant cross section), so only a section of this ring needed to be modelled. An axi-symmetric model was found to be equivalent to a full 360° model after running comparative tests.

4.1.1. Geometry and Mesh Description

Figure 4.1 shows a cutaway of the reduced geometry and its surface mesh that represents a double-gap rheometer. The two fluid regions that make up the double gap can be seen. Single-gap geometries have just a single fluid region. A further reduction of the geometry resulted in a 5° axi-symmetric section. Dimensions for both the single and double-gap geometries are given in Table 4.1 as per the labels used in Figure 4.1. Because of the uncomplicated geometry, a regular, structured hexahedral mesh was used.

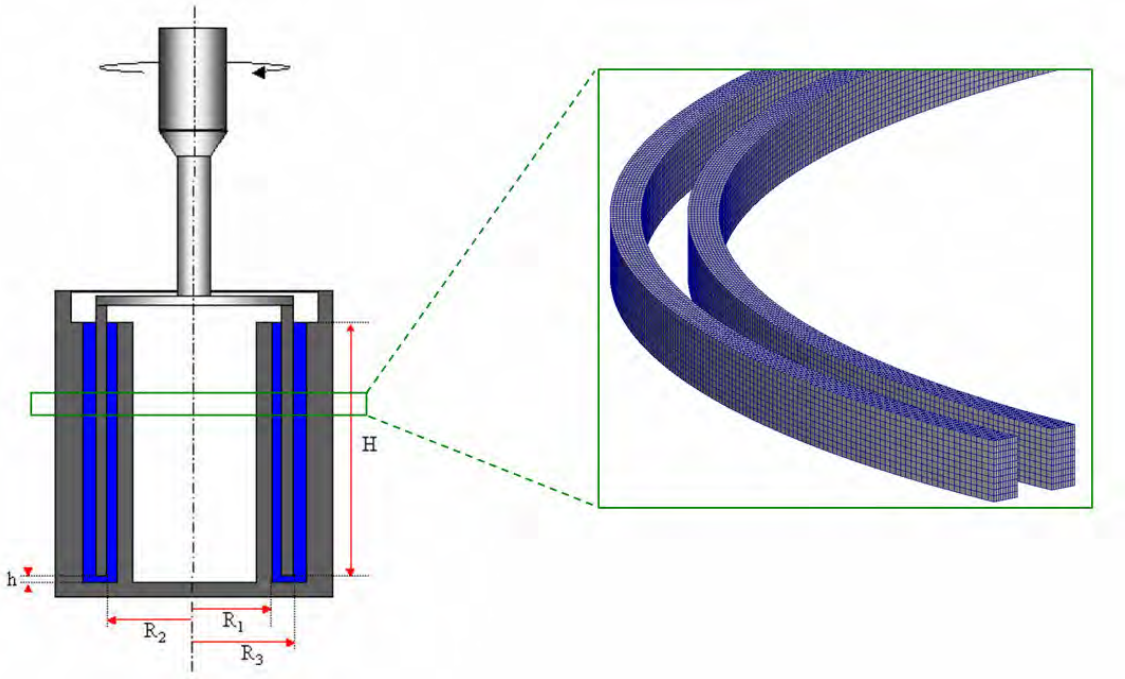

Figure 4.1: Reduced rheometer geometry used for CFD mesh

Table 4.1: Single and double-gap rheometer dimensions for CFD model

Dimensions	Single-gap (mm)	Double-gap (mm)
R1	22	22.25
R2	22.5, 23, 24	22.75
R3	-	23.5
R4	-	24
H	1	1

To replicate the DIN bob's geometry, a slightly different approach was used. The geometry is similar to a single-gap arrangement, but the cylindrical bob has a conical tip to mitigate end effects. To include this tip geometry, the bob was modelled as a 2D, axi-

symmetric, vertical slice (illustrated in Figure 4.2). This limited computational expense, while still representing the important features of its shape. A 90° version of the DIN bob was also tested. It had roughly 1000 000 cells versus 25 000 cells for the axi-symmetric geometry. The bigger model showed comparable results to the axi-symmetric version, but because it was significantly more computationally expensive this geometry was not pursued further. For comparison, the 90° single-gap geometry had 27 000 cells. Dimensions of the DIN bob geometry were based on those of TA Instruments' AR1500ex rheometer. Values for these dimensions are given in Table 4.2.

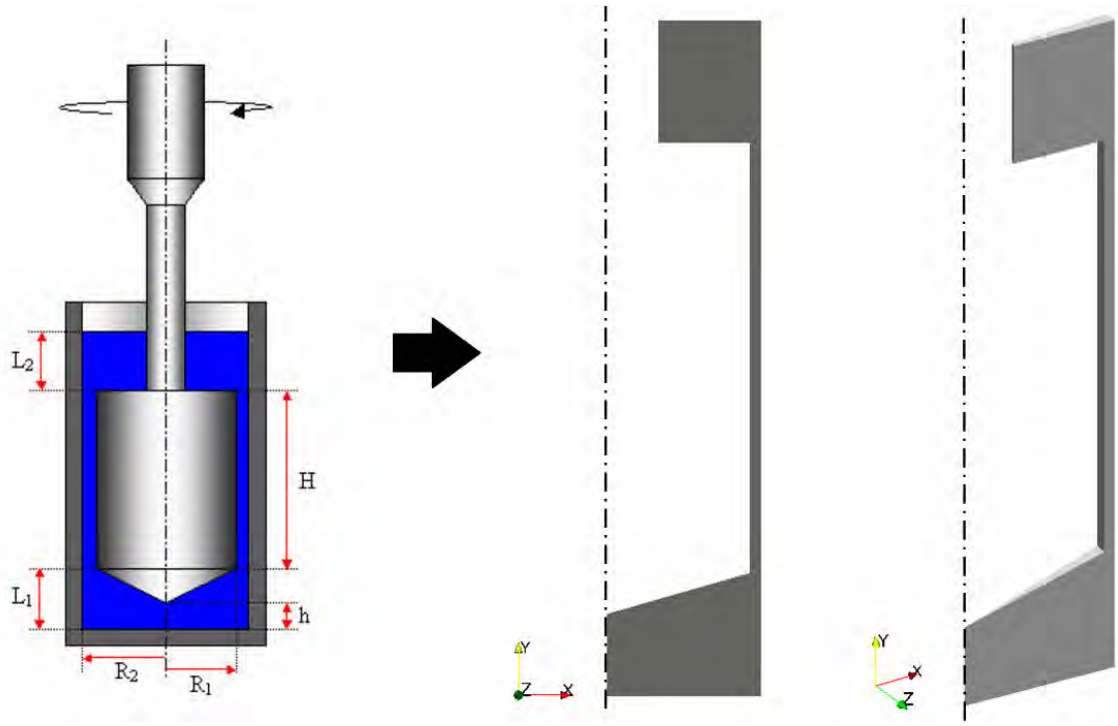

Figure 4.2: Axi-symmetric DIN bob geometry used in CFD model

Table 4.2: DIN bob rheometer dimensions for CFD model

Dimensions	**Values (mm)**
R1	13.98
R2	15
H	42
h	8
L1	12
L2	12

4.1.2. Boundary Conditions

Boundary conditions describe computationally how the fluid interacts with the rheometer components. As such, they should describe the physics of the rheometer as closely as possible. The conditions used are outlined below and illustrated in Figure 4.3 for the single-gap geometry.

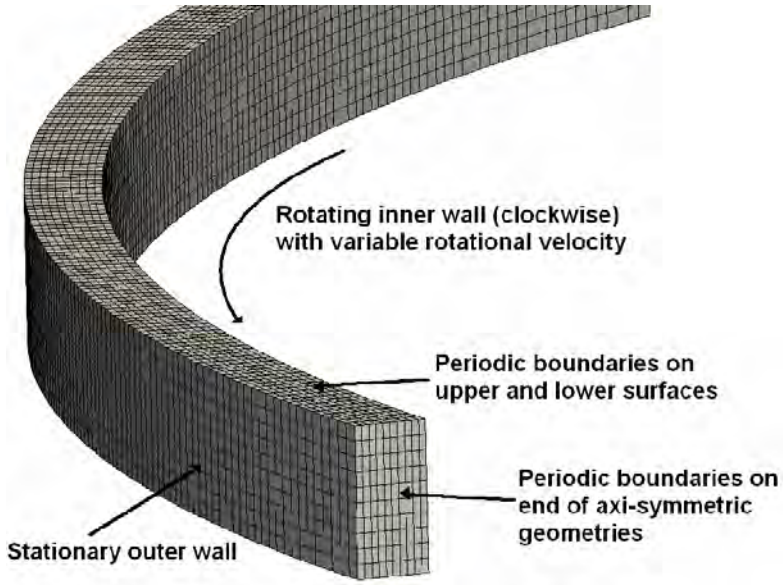

Figure 4.3: Boundary conditions for CFD model

Rotating Inner Wall

The driving force of the rheometer is the rotating surface (usually a cylinder) that creates the shear gradient in the fluid. By specifying the speed at which the surface rotates, and knowing its shape and position, the tangential velocity of the entire boundary can be calculated. This approach replicates a controlled-rate rheometer. The velocity in this approach would need to change with time to simulate the ramp up of shear rate used in many rheological tests. Specifying a wall velocity was more efficient than implementing a controlled-stress rheometer arrangement.

To achieve the controlled-rate arrangement, a new boundary condition was created in OpenFOAM®. This allowed the velocity of the wall to be calculated from the specified rotational speed (ω in rad/s) at each time step. The relevant rotational speed for a particular time step was interpolated from a table of speeds at their respective times. This table was supplied in a text file placed in the model case directory.

A no-slip condition was imposed on the wall boundary. Therefore the fluid in contact with the wall boundary moved at the same speed as the wall. Pressure was defined with a "zero-gradient" condition where the pressure gradient normal to the wall is zero, i.e. the pressure at the boundary was taken to be the same as the value just above the wall.

Stationary Outer Wall

Many rheometers use a combination of one moving and one stationary surface to create the shear gradient. Therefore a stationary wall boundary condition was used for the relevant wall where the fluid velocity was specified as zero in all directions. A no-slip condition at the wall was assumed. Pressure was defined as zero-gradient, the same as for the rotating wall.

Periodic Boundaries

Because of the periodic nature of the model (repeated geometry), many of boundaries were defined as cyclic patch boundaries. These included the top and bottom mesh surfaces (due to the horizontal slicing) and the ends of the 90° section of the ring. The 5° geometry was handled slightly differently as a 2D axi-symmetric case.

4.1.3. Initial Flow Conditions and Solution Procedure

Following the approach of a controlled-rate type of experiment, the shear rate (rotational speed) was increased over time. Typically the fluid sample is started from rest, before the shear rate is increased at a pre-determined rate. Thus the initial fluid velocity was set to zero. Gravity was assumed to be negligible for a single homogeneous fluid in such a small device. Therefore it was not included in the calculation. In a closed, incompressible system, pressure values are relative. So a reference pressure of 0 Pa was specified.

4.1.4. Shear Stress and Shear Rate Measurements

The shear stress and shear rate can be calculated from the torque and rotational speed, respectively, through the use of the conversion factors mentioned in Section 2.2.4. The speed of the rotating geometry was set via the rotating wall boundary condition. So from the known geometry and the user-specified rotational speed, the shear rate at a particular time could easily be determined beforehand.

Shear stress was calculated from the measured torque at the stationary wall. Pressure forces are normal to the wall surface and were ignored as they did not contribute to the tangential force on the wall (which resulted in the torque). Only the viscous force component was captured.

It should be noted that the correct shear stress and viscosity values were only obtained when the geometry's wall area encompassed a full 360°. This was due to the shear stress conversion factors used in the calculations (cf. Section 2.2.4). Because smaller periodic and axi-symmetric models were used, the measured torque values had to be scaled, such that the final wall area used in the measurement would be equivalent to a 360° model.

4.1.5. Solver and Solution Scheme Settings

The pressure-velocity coupling option of PISO was used. PISO is OpenFOAM's default scheme for time-dependent solvers, and so was hard-coded into the `icoFoam` and `nonNewtonianIcoFoam` solvers that were used for the CFD models. Some of the algorithm settings are given in Table 4.3. It should be noted that Newtonian models only required two pressure-corrector loops in the PISO scheme to resolve the expected fluid behaviour, while non-Newtonian versions required four. This was most likely required due to the higher viscosities of the fluids used. The extra corrector loops would add stability to the calculation.

Table 4.3: CFD solver specifications

Solver Names	icoFoam (unsteady, laminar flow) nonNewtonianIcoFoam
Solver Type	Pressure-based, segregated solver
Time Dependence	Unsteady
Pressure-Velocity Coupling	PISO
nCorrectors (pressure corrector loops)	2 4 (for non-Newtonian model)
nNonOrthogonalCorrectors	0
Formulation	Implicit
Solver Accuracy	Double Precision (default)

Specific linear solvers for different equation variables could be individually chosen based on the required performance. For this type of problem (laminar, incompressible), only the values of pressure (`p`) and velocity (`U`) were required. Details of both equation solvers

used in `icoFoam` are given in Table 4.4. For these simulations, p is calculated using the Pre-conditioned Conjugate Gradient (PCG) linear solver for symmetric matrices, with the corresponding Diagonal Incomplete-Cholesky (DIC) pre-conditioning (also for symmetric matrices). The velocity field on the other hand, was calculated with a Pre-conditioned Bi-Conjugate Gradient (PBiCG) linear solver (for asymmetric matrices), and a corresponding Diagonal Incomplete-LU (DILU) preconditioning. The Conjugate Gradient solver, originally proposed by Hestens and Steifel (1952), guarantees the exact solution will be obtained in the number of iterations smaller than, or equal to, the number of equations in the system (Jasak, 1996). The convergence rate of the solver can be improved through pre-conditioning (Ferziger and Perić, 2002).

Solver tolerances for each variable were also set. As the algorithm solved each variable in an iterative manner, the solver used a tolerance to know when each variable had been solved with sufficient accuracy and would then stop. In this case, this solver would stop when either the residual falls below the tolerance, or when the ratio of current to initial residuals falls below the solver relative tolerance (`relTol`).

Table 4.4: Linear solver and tolerance settings for icoFoam

	p	**U**
Solver	PCG	PBiCG
Preconditioner	DIC	DILU
Tolerance	1e-06	1e-05
relTol	0.01	0.1

OpenFOAM® allows complete control over the numerical schemes used to calculate the different terms that appear in the equation solution system. These schemes can range from derivatives (e.g. gradient operator) to interpolation of values from one set of points to another. An example of this are the derivative terms, where a discretisation practice needs to be selected (standard Gaussian finite volume integration is the common choice), which may then require an interpolation scheme to calculate values at cell faces from cell centres. Both schemes would then need to be specified for that term.

The different schemes used are outlined in Table 4.5. As the flow was convection driven, upwind differencing was acceptable for the convection term. Gradient and Laplacian

terms were discretised with Gaussian integration combined with second-order, central differencing. The unbounded characteristic of central differencing was not expected to be a problem in this flow problem. Surface normal gradients (`snGrad`) were calculated with non-orthogonal correction due to the curvature of the geometry. These gradients are the components, normal to the face, of the gradients of values at the centres of the two cells that share the face. They are evaluated at the cell face. A surface normal gradient was also required to evaluate a Laplacian term because Gaussian integration was used.

Table 4.5: Discretisation schemes for icoFoam

Term Type	Scheme	Attributes
ddtSchemes	Euler	first order, bounded, implicit
Interpolation: interpolate(U)	linear	linear interpolation (central differencing – second-order, unbounded)
snGradSchemes	corrected	explicit, non-orthogonal correction
GradSchemes: grad(p) grad(U)	Gauss linear	second-order Gaussian integration with linear interpolation, unbounded
DivSchemes: div(phi,U)	Gauss upwind	first-order, bounded
Laplacian schemes: laplacian(nu,U) laplacian((1|A(U)),p)	Gauss linear corrected	Gaussian integration, linear interpolation, corrected snGrad scheme – together this gives an unbounded, second-order, conservative scheme
Flux Required	p	field for which flux is generated (only p equation in this case)

4.1.6. Hardware Specifications

All CFD simulations were run on a desktop computer, whose specifications are given in Table 4.6. All simulations were run on a single CPU core as the meshes were not large enough to benefit from running in parallel. For the single-gap geometries, run times typically took around 6.5 hours for 30 seconds of simulation time (for 90° geometries), while the axi-symmetric versions took around 4 minutes for the same simulation time. Axi-symmetric DIN bob models typically took around 4.5 hours for 30s of simulation time. The typical time step size was 0.001 seconds.

Table 4.6: Hardware and software specifications

Hardware	
CPU	Intel® Core 2 Quad (four-core) 2.4 GHz
Memory (RAM)	8 Gb
Video	On-board graphics
Software	
Operating System	Ubuntu 10.04 (Linux-based OS)
OpenFOAM®	v.1.6 (for single and DIN bob runs)

4.2. RESULTS FOR NEWTONIAN FLUID

The model was first validated against data for a basic Newtonian fluid. Water was chosen as its properties are well known, and because it usually forms the base fluid for particle suspensions. Performance of the model was judged on how closely it could match the value for water's dynamic viscosity at 20°C. To simulate water, only its kinematic viscosity had to be specified, but its density was also needed for the force calculation. Values used were 1.004×10^{-6} m^2/s for kinematic viscosity and 998.29 kg/m^3 for density.

4.2.1. Time Step Size

A time step of 0.001 seconds was chosen. This kept the Courant number below or around one for most situations, which could be handled by the PISO algorithm (Issa, 1986). Time step sizes above and below this nominal value were tested, but the results did not vary significantly. A time step size of 0.01s for the single-gap geometry showed instability at higher shear rate ranges ($>400s^{-1}$). This was linked to high Courant numbers in the numerical solution. Because of this instability, the 0.01s time step was not tested for the DIN bob geometry. The smallest time step of 0.0001s was also not tested for the DIN bob as the total solution time was expected to take about seven days.

4.2.2. Mesh Test

Testing showed that changes to the CFD cell size did not significantly change the results for both geometries. As such, the geometries were considered to be mesh-independent. Mesh grading (i.e. smaller cells near boundary walls, but bigger near the gap centre) was evaluated as well, but did not enhance the results. As a result, a uniform mesh was used. For the 90° single-gap model, a cell size of 50µm (direction of gap) by 100µm (vertical) by 128µm (direction of curvature) per cell was generally used. This gave 10 cells for a

500µm gap and 20 cells for 1mm gap, with 270 cells to resolve the curvature. Axi-symmetric models only had one cell in the direction of curvature. DIN bob models had a cell size in the gap of 100µm in the direction of the gap width by 140µm in the vertical direction. All axi-symmetric DIN bob models were only one cell wide.

4.2.3. Pressure and Velocity Plots

Figure 4.4 shows pressure and velocity plots of the flow inside the single-gap model with a 500µm gap. Values shown here are for the cell-centred values. Each cell is coloured according to their respective value, which results in a step-jump in the cell colours across the gap. Velocity is given in m/s and pressure is in Pascals (Pa). The pressure plot is in terms of relative pressure, thus the values show the change in pressure, not the actual absolute pressure value. The velocity plot shows the highest velocity at the inner rotating wall, and an essentially zero velocity at the stationary wall. Pressure showed an opposite trend to velocity, with higher values towards the stationary outer wall. This was due to the fluid being accelerated inwards as it flowed around the curved geometry.

Figure 4.5 interpolates the velocity field across the gap, providing a smoother depiction of the velocity profile. This field is for a single-gap rheometer with a 500µm gap width ($R_1/R_2 = 0.977$) at a shear rate of about 600s^{-1}. The inner (rotating) wall is at the zero position on the gap-width scale. This figure compares the profile from the CFD model against that of the analytical solution for Couette flow described by Equation 2.4. The linear velocity profile follows the expected trend exactly, and thus confirms that the Couette flow assumption holds for this model.

At low shear rates, the DIN bob model showed similar flow patterns in the gap region. However, secondary flow features did manifest at higher shear rates. These are discussed in more detail in Section 4.2.5 and plotted in Figure 4.10.

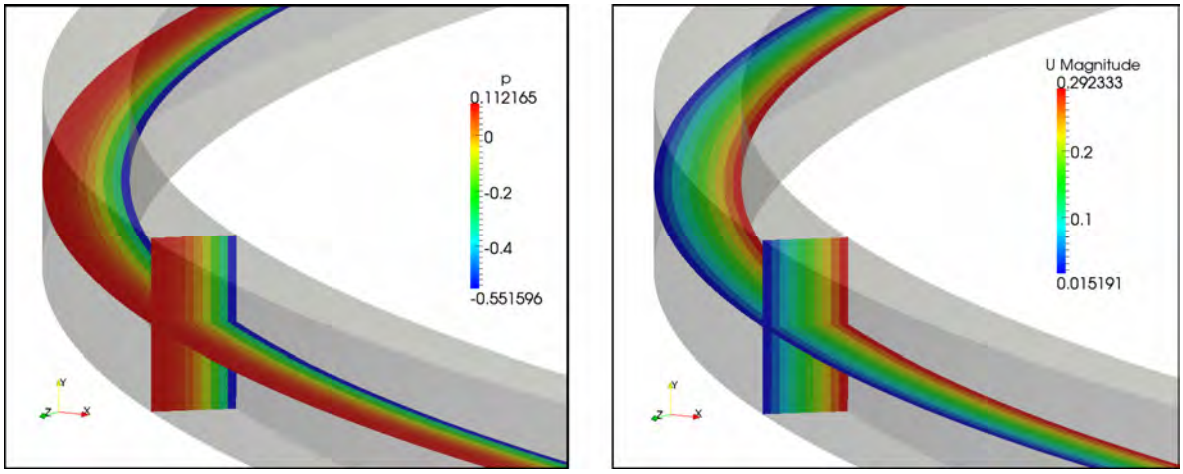

Figure 4.4: Pressure, p (in Pa), and velocity, U (in m/s), distribution in single-gap model

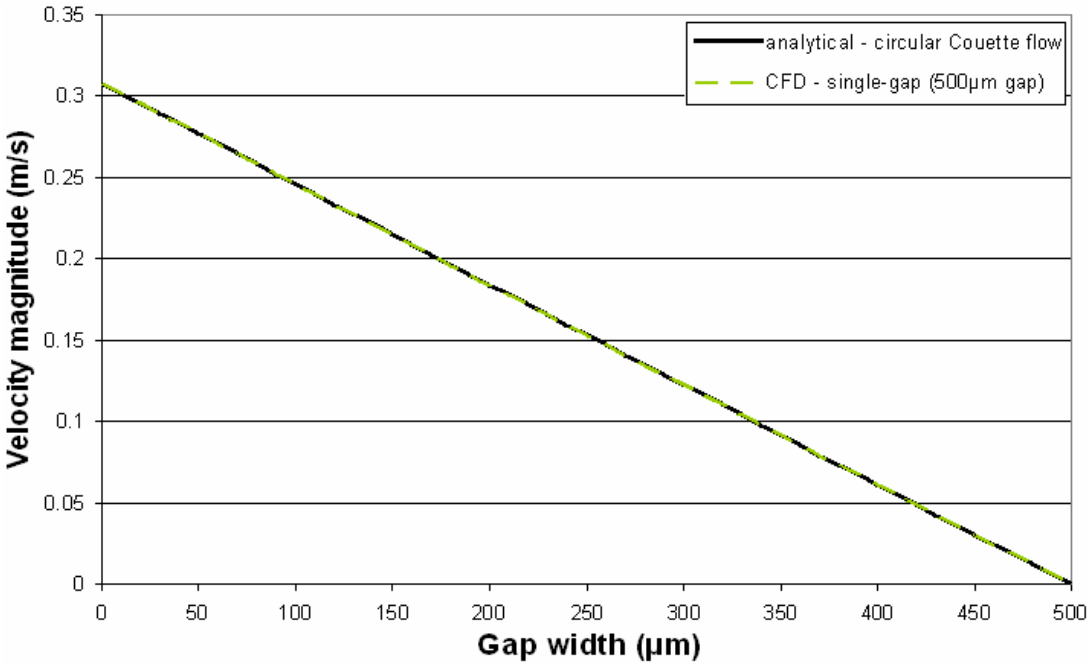

Figure 4.5: Fluid velocity across the gap of the single-gap model comparing the CFD model against the analytical solution (inner wall set as zero on the bottom axis)

4.2.4. Shear Rate Ramp Speed

The rate at which the shear rate changed over time (termed "ramp rate" here) was also investigated. This was done to determine the influence of the change in wall rotational speed over different lengths of time. Figure 4.6 provides a graphical illustration of how the shear rate was changed with time. These shear rate values were based on the wall rotational speed and the gap width. Figure 4.7 shows the rheogram obtained for single-gap geometries for different changes in shear rate. Viscosity values are shown instead of

shear stress because they show the trends more clearly. In all cases, the change was ramped up in a linear fashion from zero to the final value as shown in Figure 4.6.

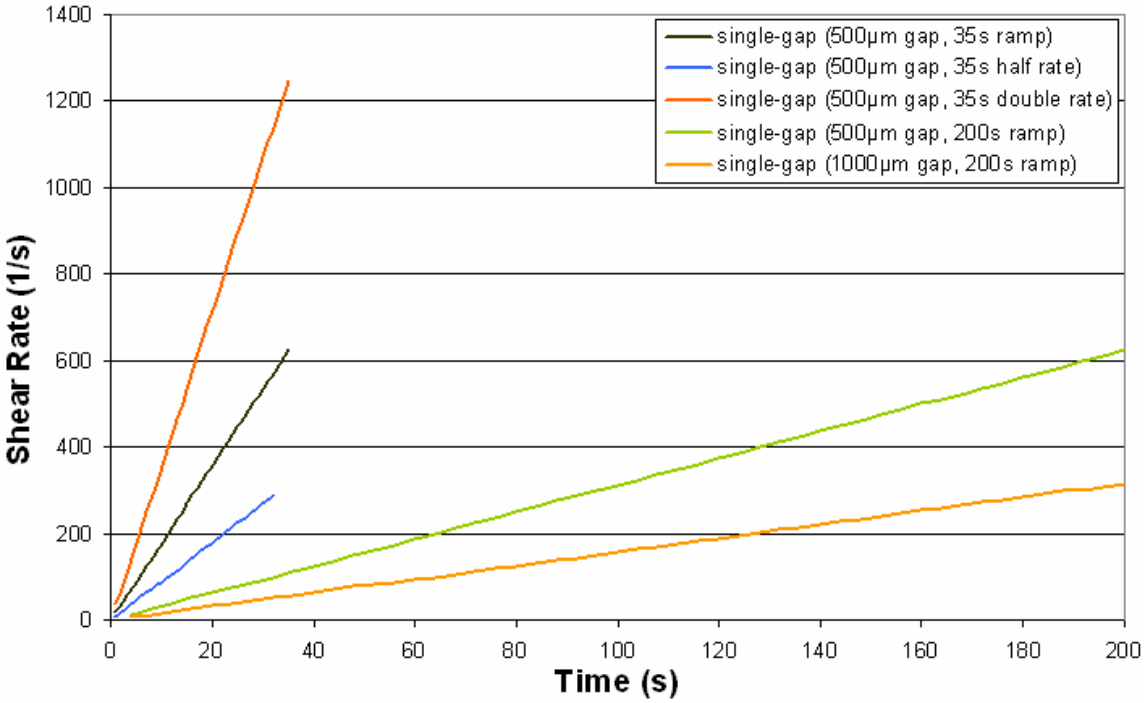

Figure 4.6: Shear rate vs. time for different shear rate ramp variations used in Figure 4.7

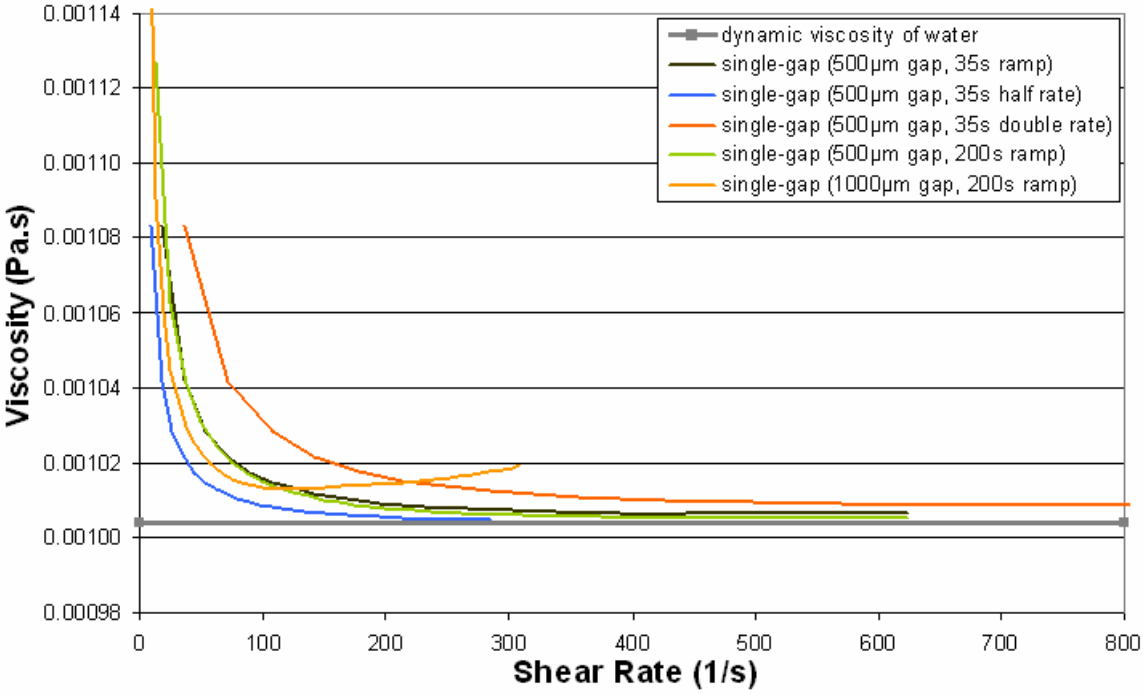

Figure 4.7: Viscosity vs. shear rate for different shear rate ramp variations in the single-gap rheometer model

The ramp rate had the greatest effect at lower shear rates. Discrepancies between CFD values and the experimental viscosity at these lower shear rates were thought to be as a result of the fluid being accelerated from rest relatively quickly. The mass of fluid would take a while to react to the acceleration of the rotating wall. Therefore a slower change in the shear rate was better as the correct viscosity could be measured much sooner.

While there was an improvement when running for longer solution times, the 2% improvement between the 35 and 200s runs was not worth the extra computational time. Therefore using a solution time much longer than 35s was not necessary. Conversely, using a faster ramp rate increased the viscosity values too much to be useful, even when run to 35s (see "double rate" in Figure 4.7 where the speed increase was double that of the standard 35s rate). Real-world experimental tests typically run from 30s to 180s, depending on the suspension materials (Massalova personal communication, 2012).

4.2.5. Gap Width

It is possible to change the gap width in concentric-cylinder rheometers by changing certain components, thus the influence of this parameter was investigated. All simulations were run for a maximum of 35s in real time. Figure 4.8 shows the influence of two typical gap widths for the single-gap geometry at two different ramp rates. For the 500μm gap, the viscosity values tended towards the expected value for water much quicker. The effect was more noticeable at lower shear rates. Narrower gaps imply less fluid in the domain. Less fluid would be able to get up to speed quicker as it has less inertia. Similar trends are shown for the DIN bob geometry in Figure 4.9, except that the values for the narrow gap width with the slower shear rate are still much larger than the expected value for water. Therefore a narrower gap provides better results, but the influence of the gap width is not as significant as for the change in ramp rate. In addition, the narrower gap prevents the rise in viscosity at higher shear rates.

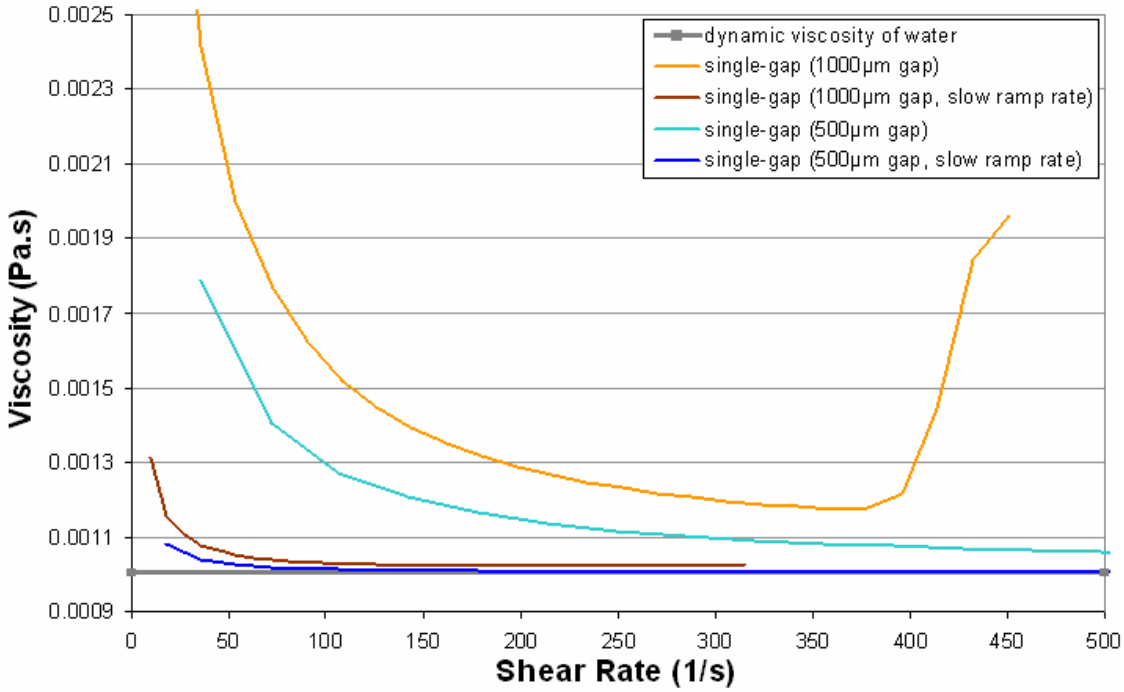

Figure 4.8: Comparison of shear rate ramp rate for single-gap geometry

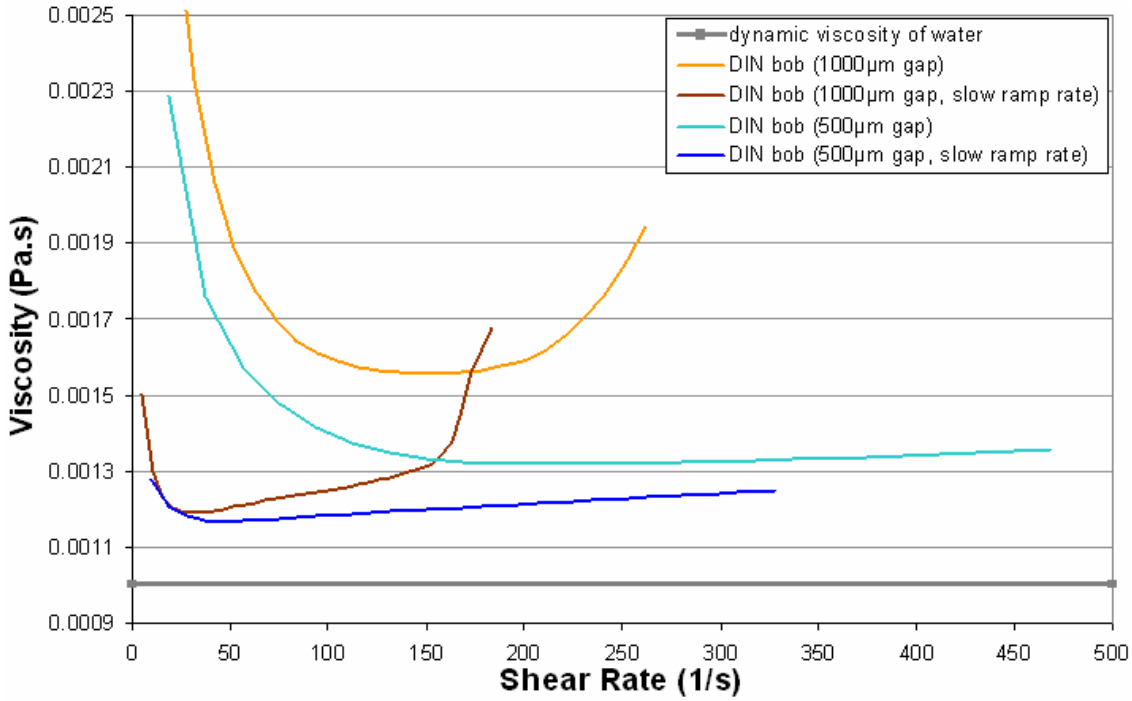

Figure 4.9: Comparison of shear rate ramp rate for DIN bob geometry

For wider gap thicknesses (1000µm and above), Taylor vortices formed within the gap at high shear rates. These vortices were the most likely cause of the sharp increases in viscosity shown in both Figure 4.8 and Figure 4.9 at the high shear rates (Barnes, 2000;

Mezger, 2002). This follows experimental observations. Furthermore, these vortices were more likely to form in the DIN bob geometry. Velocity plots for the 1000µm thick DIN bob geometry at a shear rate of $184s^{-1}$ are shown in Figure 4.10 to illustrate the behaviour of the vortices. It appears that vortex formation in the gap is encouraged by the outward flow from both the horizontal rotor section above the gap, and the angled tip at the bottom of the rotor. Vortices even form in the DIN bob for the slower shear rate ramp speed. This shows the influence of the geometry on the flow in the gap region.

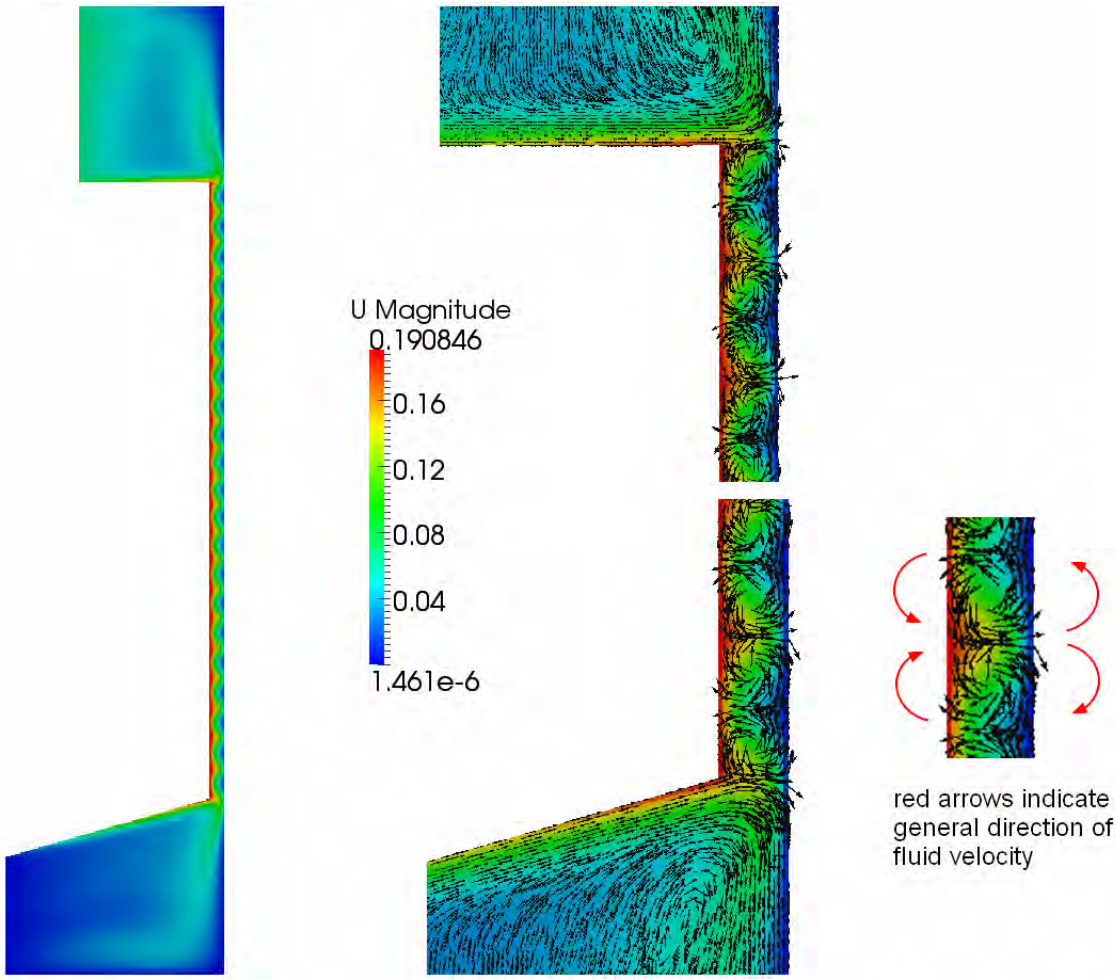

Figure 4.10: Velocity plots showing Taylor vortices in DIN bob gap (in m/s)

Figure 4.11 shows Taylor vortex formation in the single-gap model with a 1000µm wide gap. Due to the periodic nature of this model, this flow pattern would repeat itself above and below the pictured geometry, resulting in a pattern similar to that in the DIN bob gap region.

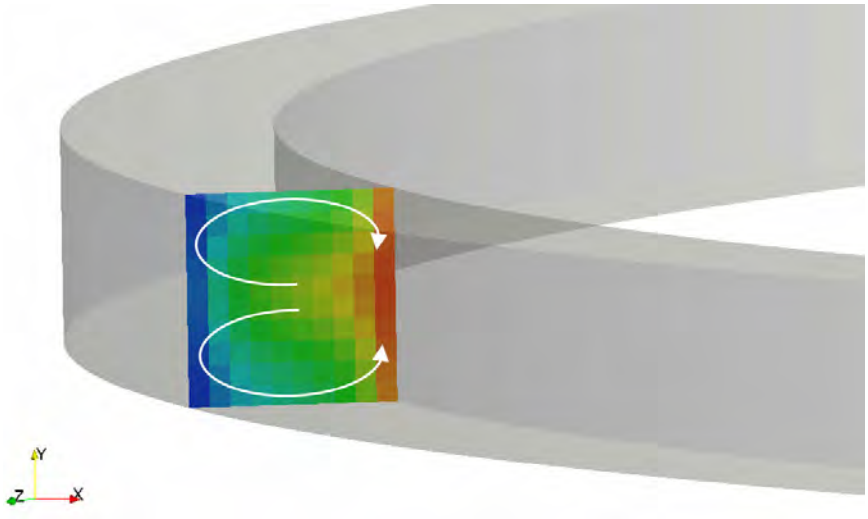

Figure 4.11: Velocity plot in 1mm wide single-gap geometry showing Taylor vortex formation

4.3. RESULTS FOR NON-NEWTONIAN FLUID

Most suspensions are non-Newtonian. Therefore it was decided to also simulate a non-Newtonian fluid in the CFD model. A non-Newtonian fluid was selected based on the properties of a vermiculite-quartz slurry (Ndlovu et al., 2011). Herschel-Bulkley model parameters were fitted to the data and are given in Table 4.7. These model parameters resulted in a very linear portion of the rheogram after the yield point, similar to that of a Bingham fluid.

4.3.1. CFD Description of the Fluid

A mineral slurry with Herschel-Bulkley behaviour was used. This meant the fluid would have a yield stress, i.e. the fluid would not flow until sufficient shear stress was applied. CFD models are designed to describe flowing fluids, and as such are generally unable to handle the discontinuity in the model as the fluid transitions from unyielded fluid to highly sheared flow. As a result, in CFD, the Herschel-Bulkley model includes a finite region of Newtonian behaviour (with high viscosity) to mimic the unyielded fluid (cf. Equation 4.1). At a pre-defined shear rate, the region of high Newtonian viscosity would switch to a yielded fluid. This feature can be seen in Figure 4.12 at a shear rate of $24s^{-1}$.

$$\mu = \min\left\{\begin{array}{l}\mu_0 \\ \dfrac{1}{\dot{\gamma}}\left(\tau_y + k.\dot{\gamma}^n - k\left(\dfrac{\tau_y}{\mu_0}\right)^n\right)\end{array}\right\} \tag{4.1}$$

Table 4.7: Herschel-Bulkley fluid parameters (for standard and modified models)

Standard HB Model		**Modified for CFD**	
τ_y	2.344 Pa	τ_y	2.4 Pa
k	1.272e-3 Pa.s	k	1.272e-3 Pa.s
n	1.2	n	1.2
		μ_0	0.1024 Pa.s

4.3.2. Discussion of Results

Figure 4.12 shows the viscosity and shear stress results of the Herschel-Bulkley model tests for different shear rates. Only the single-gap and DIN bob geometries were tested. Similarly with the Newtonian case, a good correlation was found between the fitted Herschel-Bulkley model and the CFD results. The DIN bob performed much better in this case, but still deviated slightly at higher shear rates. Figure 4.12 shows a model with a relatively low-viscosity Newtonian region (up to shear rate of $24s^{-1}$). This feature is exaggerated in the figure for clarity. However, the model performed similarly when a much higher Newtonian viscosity region (steeper gradient) was specified, as can be seen in Figure 4.13. The single-gap geometry followed the expected curve closely, while the DIN bob showed a greater overshoot before it gradually tended towards its previous behaviour. Curves for the shallower gradient version are also shown in Figure 4.13 for comparison. This shows the model was able to handle fluids that are more complex than basic Newtonian liquids. The simpler single-gap rheometer geometry performed the best under all circumstances.

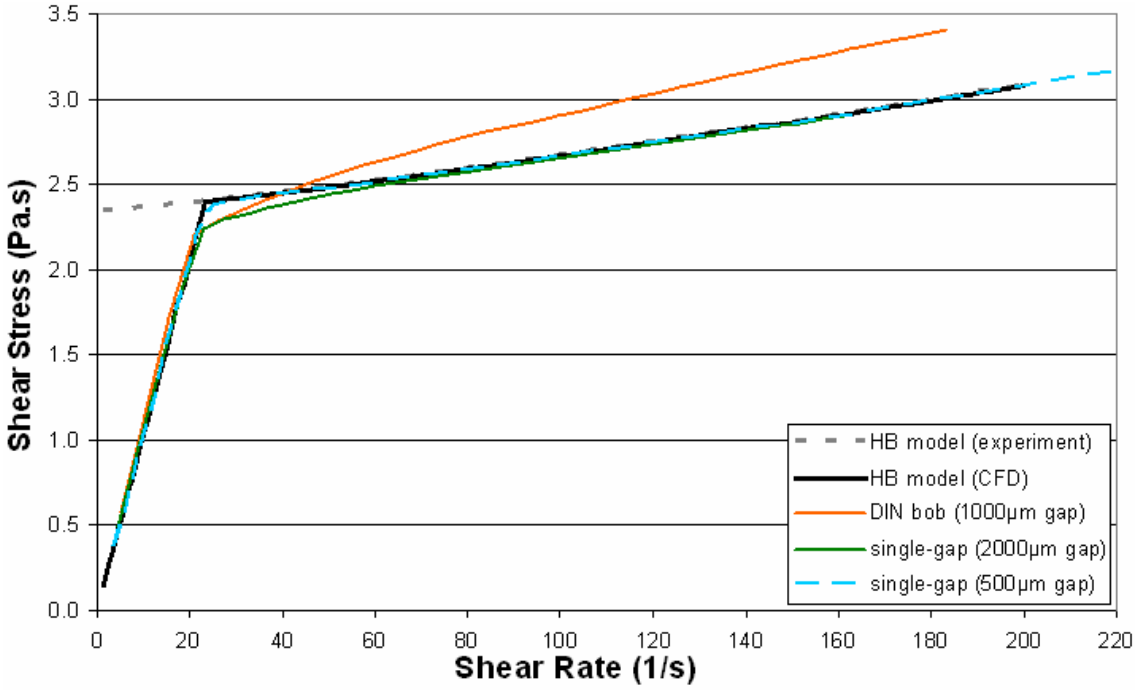

Figure 4.12: Results of non-Newtonian CFD model showing shear stress vs. shear rate

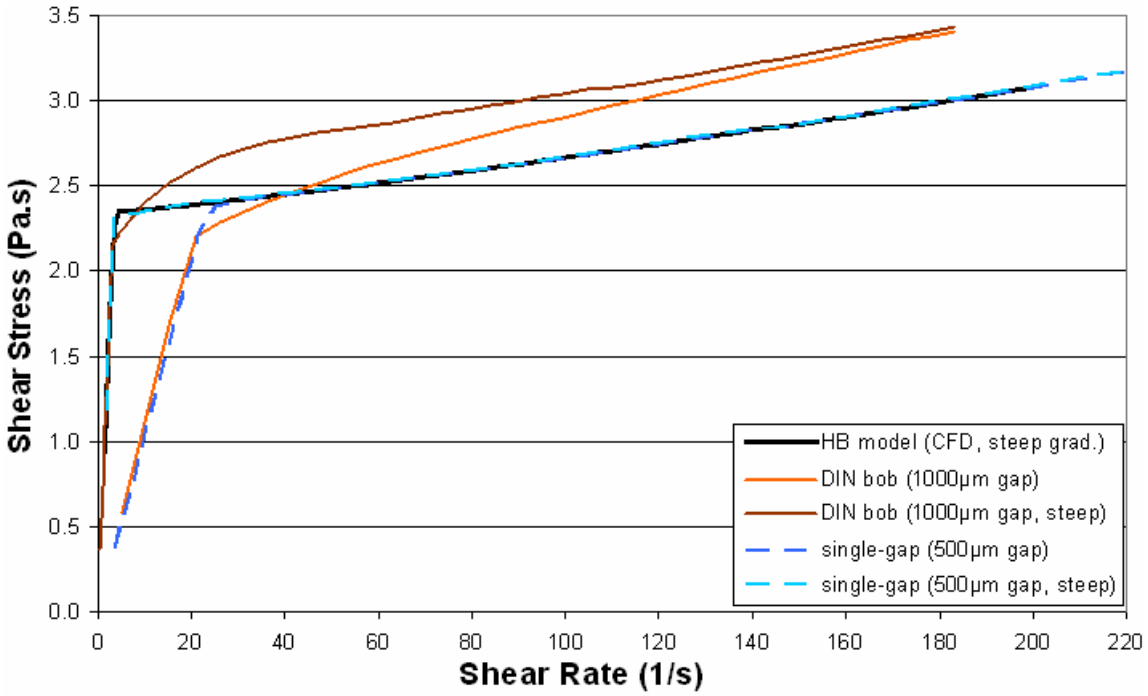

Figure 4.13: Results of non-Newtonian CFD model for steeper transition region

4.3.3. Gap Width

Gap thickness for the single-gap geometries showed no significant variation in the results other than a deviation at the transition point from the steep Newtonian section to the non-

Newtonian section. However, the gap size was quite large (2mm), so this result was not surprising. None of the wider gap geometries showed any sign of Taylor vortex formation. This could be attributed to the higher viscosity values for the non-Newtonian fluid than for the Newtonian case, i.e. any fluctuations in the solution were damped out and so did not affect the overall result. Higher shear rates would also be required to form the vortices.

4.4. SUMMARY OF IMPORTANT FINDINGS FOR CFD MODEL

Properties of the CFD models discussed in this chapter form the basis for the coupled model. Important findings are summarised here.

4.4.1. Rheometer Geometry

The shape of the single-gap model was straightforward to mesh, and the results were very reliable. On the other hand, the DIN bob geometry tested here generally suffered from more instability due to the inclusion of the regions above and below the narrow gap. These regions encouraged Taylor vortex formation. To model all those features also required many more cells, which added to the computational cost of the model.

The DIN bob values never came close to matching the expected results for water, though it did perform better with the non-Newtonian fluid. While the results may have been affected by the early development of vortex flow in the gap, the exact cause was not determined. It was decided that these effects would not be further investigated because the single-gap models were already showing their superiority over the DIN bob models. Therefore no more time was spent on developing the DIN bob models with their extra tip and free surface regions. Double-gap models performed just as well as the single-gap models, but for double the computational time as they required twice the amount of cells.

4.4.2. Time Step Size

From the models tested, it was found that they could sustain a relatively high time step size of 0.001s, while still providing good results. This value would serve as the upper bound for CFD models.

4.4.3. Ramp Rate

The rate of change of shear rate had a sizeable influence on the model accuracy and performance. It is important that the rates change over a realistic time-frame, as would be found in real-world experiments. Nonetheless, changing the shear rate over a period of more than about 35s was found to be unnecessary. Reducing the gap width however, would ease this restriction.

4.4.4. Gap Width

Reducing the gap width was a good way to stabilise the solution and produce an accurate result. This was most likely because the fluid could accelerate quicker in the smaller gap and assume the correct profile without any lag. Narrower gaps also reduce the likelihood of secondary flow features occurring in the domain.

4.4.5. Pressure-Corrector Loops

It should be noted that for the non-Newtonian fluids, the number of pressure-corrector loops in the PISO algorithm had to be increased from two to four. This setting would need to be carried across to the coupled models, as those simulations would most likely exhibit non-Newtonian behaviour.

4.4.6. Implications for Model Geometry Size

It has been shown that smaller model geometries produce results equivalent to full-sized rheometer geometries. For example, axi-symmetric 5° sections produced comparable results, especially for gap widths of 500μm or less. Therefore larger models are not necessary.

5. DEVELOPMENT OF A CFD-DEM COUPLED MODEL

The next step in the methodology was to include particles into the model. This chapter discusses practical issues that had to be considered when adapting the CFD model to create a coupled CFD-DEM model. First, a new geometry for the model is evaluated in Section 5.1. Then in Section 5.2, the experimental data used to validate the particle-fluid model are presented. These data would also define the material properties used in the model. Sections 5.3 and 5.4 explain the limitations and practical decisions made when implementing the model in LIGGGHTS, OpenFOAM®, and CFDEM. Software-specific settings for these programmes are discussed where applicable. Terms specific to these software codes are highlighted in a different font style in the text. Input scripts for both the DEM and CFD portions of the model are also included in the appendices. Lastly, Section 5.5 describes how the coupled model was initially tested for a low particle volume fraction and the explicit drag scheme.

Experimental data for zirconia particles was chosen to test the coupled model. The data were selected because they used small particles (roughly 1μm in diameter), as well as data for DLVO forces were provided. Small particles would produce a more pronounced rheological response, which would provide good test conditions for the model. However, for the geometries considered in Chapter 4, this resulted in a large number of particles (about 10 billion particles at 15% volume fraction for the 360° single-gap model with a 1mm gap). This number of particles would significantly increase computational expense.

In addition, periodic boundaries in LIGGGHTS were limited to being opposing planar faces that had to be aligned with the principal planes (x, y, and z). Therefore axi-symmetric geometries could not easily be modelled without creating new, specialised boundaries. Thus the geometry was evolved into that of a rectangular box. This shape was periodic in the flow direction as well as the vertical direction, while keeping the boundary faces aligned with the principal planes.

Consideration of all these factors led to a re-design of the shape and, in particular, the size of the geometry. These changes would improve computational efficiency, while not affecting the applicability of the model. From the findings in Chapter 4, smaller geometries did not affect the final results. Importantly, the smaller box-shaped geometry would still represent the important features of a rheometer (i.e. Couette flow between a moving and a stationary wall). From the findings in Section 5.1.3, these expectations were proven correct.

5.1. CFD RESULTS FOR BOX-SHAPED GEOMETRY

This section evaluates the performance of the new box-shaped model. The box model will be assessed in the same manner as the rheometer models in the previous chapter. OpenFOAM® v.2.0.1 was used for the CFD calculations.

5.1.1. Description of Geometry and Boundary Conditions

The ideal computational domain is one that is small enough to limit the number of cells required to mesh it, but that is large enough not to impede the development of the important flow features. Thus it was decided to base the dimensions on how many particles would be generated in the domain, and how many would be acceptable for practical considerations (time, computer resources, etc.). A cubic shape was selected, as at this stage it was not clear which dimension had the most effect on the model behaviour. A length of 50μm along each side was chosen for the box geometry. This gave about 14 000 particles for a 20% particle volume fraction.

Boundary conditions for the box shape did not change from the previous single-gap geometries (see Figure 5.1). Periodic boundaries were used in the vertical direction again, and in the direction of the flow (now no longer curved). The rotating wall boundary condition was the same as that used for the curved geometry because the method for calculating the tangential velocity was generic enough to handle walls of different curvature (including the case of a flat wall). In the limit of a flat face, the translational velocity would be the same for the whole face. To suit various conventions in LIGGGHTS, the model was oriented with the flow direction along the x axis, the gap width in the y-direction, and gravity acting in the vertical z-direction.

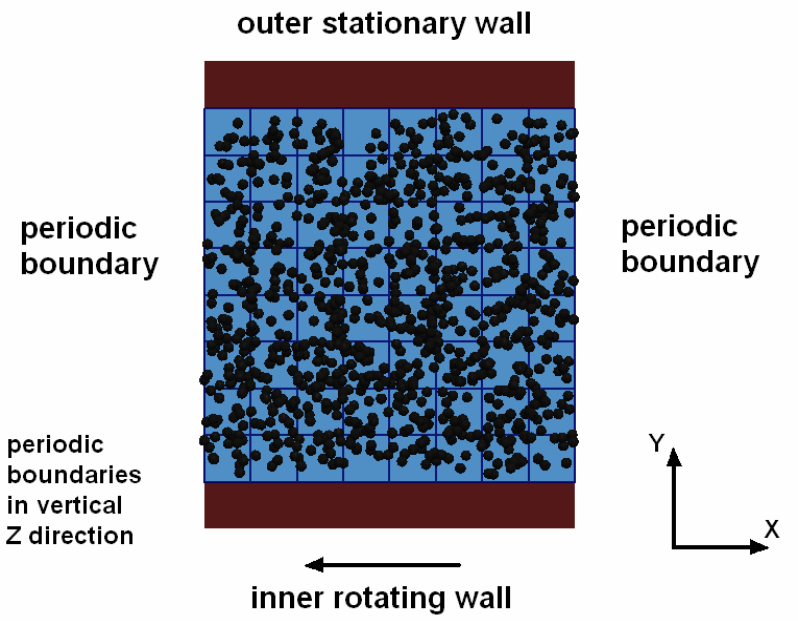

Figure 5.1: Boundary conditions for the box geometry

5.1.2. Shear Rate and Shear Stress Calculation

Because the box shape had no curvature, standard relations were used to calculate the shear rate and shear stress in the domain. This method gave similar results to the method used in Chapter 4 (with the single-gap rheometer factors) for the box domains tested here. For shear rate, the standard relation is

$$\dot{\gamma} = \omega\left(\frac{R}{D}\right) = \omega\left(\frac{R_1}{L_y}\right) \tag{5.1}$$

where R_1 is the radius of the inner wall (distance from rotational axis), and D is the gap width. Here in this model, the gap width is the length of the fluid domain in the y-direction (L_y). Shear stress is given by:

$$\tau = \frac{F}{A} = \frac{F_x}{L_x \times L_z} \tag{5.2}$$

where F_x is the force in the x direction, and L_x and L_z are the box dimensions in the x and z-directions, giving the wall area over which the viscous force acts.

5.1.3. Validation of Box Geometry

Viscosity values for different box geometries were compared against that of the single-gap model from the previous chapter to determine if it was an acceptable geometry. Only results for the Newtonian fluid of water are discussed here. Results for the non-Newtonian fluid with this new geometry were similar and produced equivalent trends when compared to the other geometries. For brevity, these results are not discussed here.

Shear Stress Comparisons for Newtonian Fluid

From the viscosity plots, it was clear that the box models closely approximated the expected value for water's dynamic viscosity. Due to a much narrower gap width, the box geometries performed better than the wider-gapped single-gap rheometer models at lower shear rates, as they tended to the final value much quicker. Because of the narrow gap width, the shear rate increases quickly with time, and the formation of secondary flow effects like the Taylor vortices is inhibited.

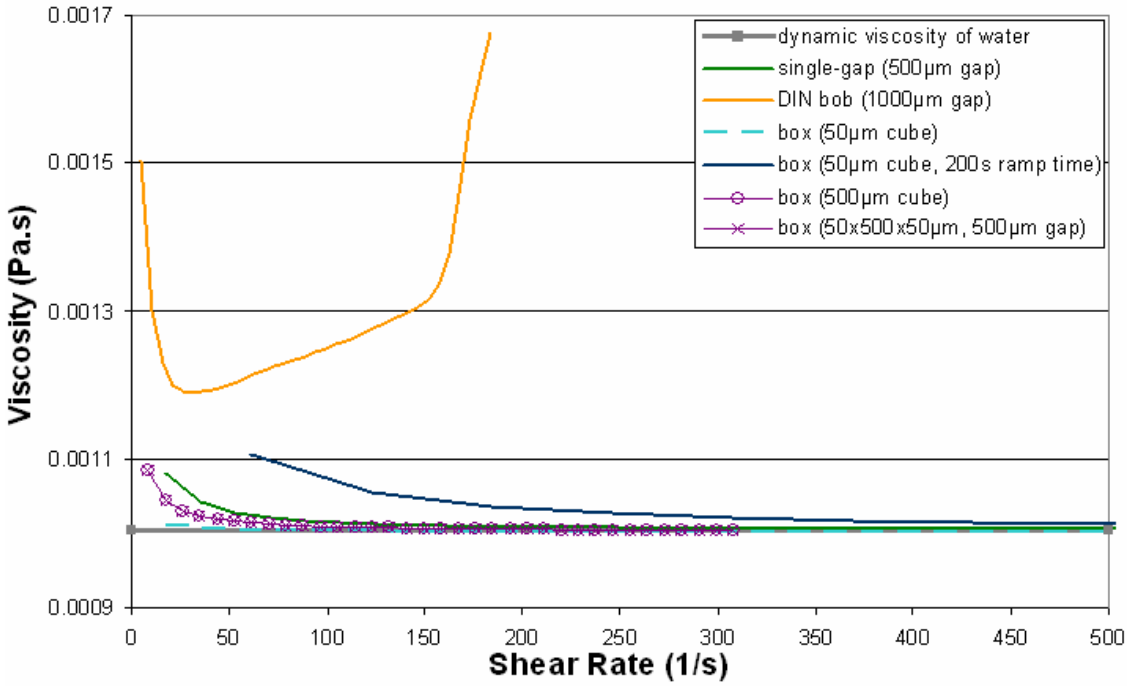

Figure 5.2: Comparison of viscosity vs. shear rate for box and single-gap geometries

Further tests (not shown here) indicate that the force result was not affected by increasing the box dimensions in the x- (flow direction) and z- (height) directions. Changing the gap

width had a slight effect. For the smaller gap widths, the box results tended to reach the expected viscosity at lower shear rates.

Analytical Solution for Linear Couette Flow

The analytical relationship for the fluid velocity (u) at some point in the gap (y), with the bottom wall moving, is given by:

$$u = u_o\left(1 - \frac{y}{D}\right) \tag{5.3}$$

where u_o is the wall velocity and D is the gap width. The solution gives a linear velocity profile across the gap.

Pressure and Velocity Plots

Flow inside a box with parallel walls is closer to true linear Couette flow. As a result, the fluid velocity follows the analytical solution for Couette flow (cf. Equation 5.3). This type of flow profile is visualised in Figure 5.3 using velocity vectors. The interpolated velocity values follow the analytical solution of Equation 5.3 exactly (similar to the performance of the single-gap model in Figure 4.5). While a pressure gradient occurs in rotational rheometers, it does not exist in linear Couette flow. As such, the pressure did not show the significant profile seen before in the curved geometries. This would not affect the force calculation, which only depends on the velocity gradient. However, the lack of a clear pressure gradient may introduce some inaccuracy. Any pressure gradient effects acting on the particles in curved geometries would not be the same as in linear Couette flow. But the particles would no longer be flowing in a curved streamline as they would in a cylindrical geometry, so this should not be a problem. From testing, it was found that the box model required at least three pressure-corrector loops in the PISO formulation for the simulation to complete successfully.

These tests showed the box geometry produced results that were comparable to the single-gap rheometer models. This meant that the correct flow behaviour was being measured by the box geometry. In addition, the reduced size of geometry resulted in a

more efficient computational model. Therefore this model would form a good foundation for the coupled CFD-DEM model. The only compromise could be the lack of a dominant pressure gradient across the gap. The absence of this gradient would not affect the particle flow, which is now essentially linear because the flow no longer follows a curved path. Furthermore, the particles selected in the next section, are small and denser than the fluid medium. Thus they would not be easily affected by pressure gradient forces.

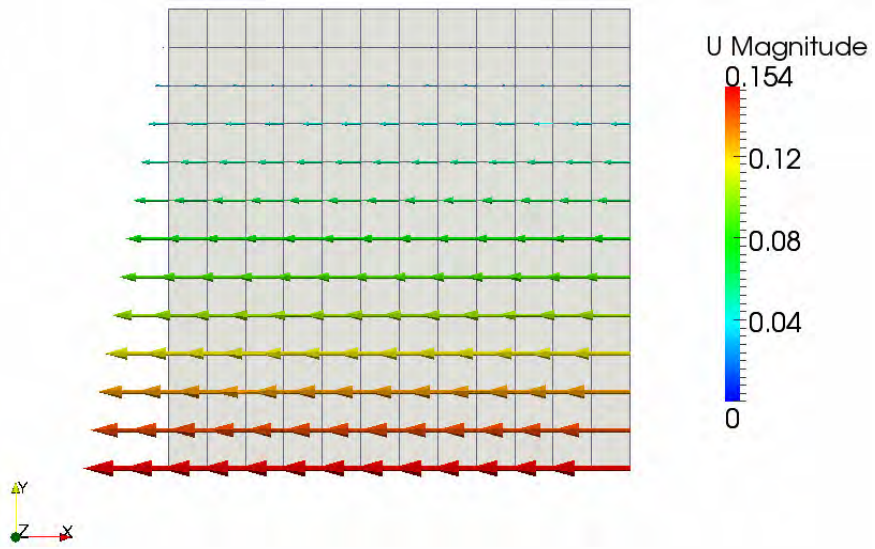

Figure 5.3: Velocity plots for 50μm box geometry (in m/s)

5.2. EXPERIMENTAL DATA

To test the coupled model, experimental data from the paper of Megías-Alguacil et al. (2000) was chosen. They had presented data for small particles size (≈1μm diameter), and provided well-documented data for the DLVO forces. This simplified the calibration and testing of the equations used for the long-range electric forces in LIGGGHTS.

In their paper, Megías-Alguacil et al. (2000) used zirconia particles that had been specially manufactured to be spherical. Particles were suspended in a NaCl solution. Suspension properties are listed in Table 5.1, while Figure 5.4 shows a Transmission Electron Micrograph (TEM) image of the spherical particles. Figure 5.5 illustrates the inter-particle energy potentials and forces (first derivative) against the separation distance between particles. Calculations correspond to the NaCl concentrations indicated (spherical particles are indicated by “sph”). These were used to determine the DLVO

input parameters for LIGGGHTS. While not all physical properties were supplied in the paper, they could be inferred from other widely available values for zirconia material. Results of shear stress vs. shear rate for these particles are given in Figure 5.6. The NaCl concentration was 10^{-3} M. These results were used to test the majority of the simulations in this work.

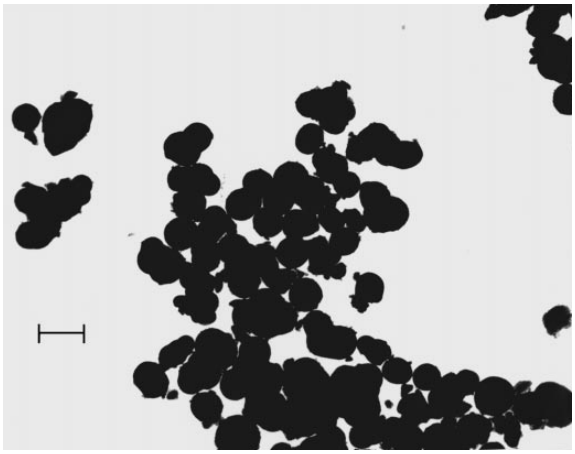

Figure 5.4: TEM image of spherical zirconia particles (bar length = 1μm) (Megías-Alguacil et al., 2000)

Table 5.1: Properties of spherical zirconia particles in suspension

Particle Properties	
Young's Modulus (GPa)	88
Radius (m)	1e-6
Density (kg/m^3)	6000
Poisson's Ratio (ν)	0.3
Coefficient of restitution	0.8
Coefficient of Friction	0.05
Shear Modulus (GPa)	33.8
DLVO Potential Parameters	
Zeta potential (mV)	32.5
Relative permittivity (ε)	78.55
Debye length (1/κ) (m)	9.62e-9
Hamaker constant (J)	9.24e-20
`Sigma_cc` (size of water molecule) (nm)	0.278
Fluid Properties	
Density (kg/m^3)	998.29
Kinematic viscosity (m^2/s)	9.03e-7
Temperature (°C)	25

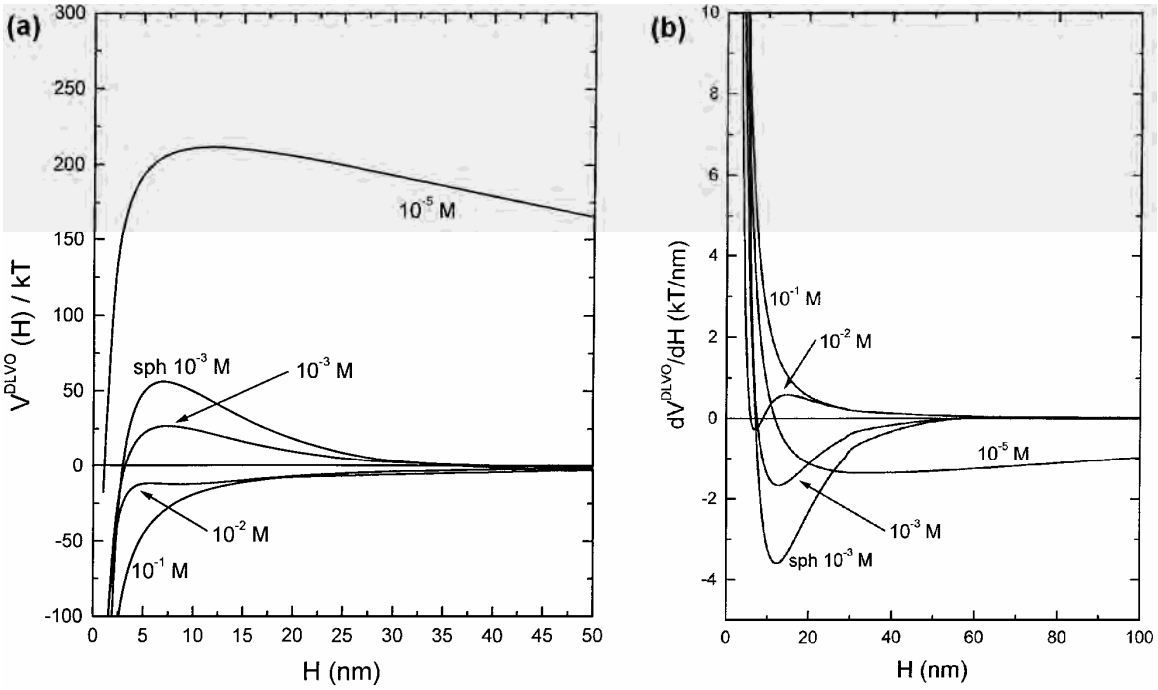

Figure 5.5: Interaction energy (a) and first derivative (with respect to distance) of interaction energy (b) as a function of inter-particle distance (H) (Megías-Alguacil et al., 2000)

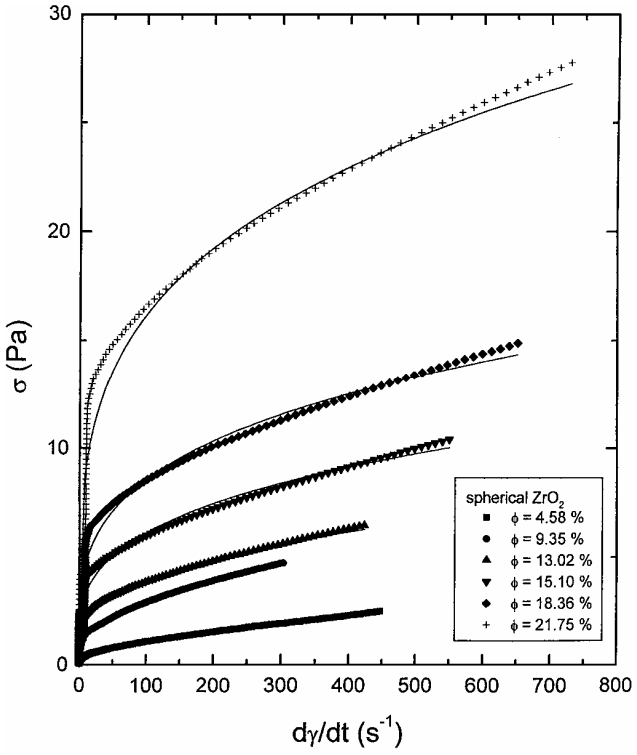

Figure 5.6: Experimental shear stress vs. shear rate data for spherical zirconia particles (Megías-Alguacil et al., 2000)

5.3. SOFTWARE LIMITATIONS

This section highlights some limitations of the software used for the coupled model and how these restrictions affected the choice of certain model parameters.

5.3.1. Limit of Particle Size

To preserve numerical precision, individual particle volumes in LIGGGHTS had to have a value larger than 10^{-12} (only the numerical value is important, the unit depends on the chosen unit system). Therefore particle diameters had to be larger than 1.25×10^{-4}. Due to a lack of machine precision, any round-off errors resulting from small particle sizes would introduce errors in the calculations. Bigger numbers could also be used to raise the values above the machine limits. To do this, LIGGGHTS had to be operated in the CGS (centimetre-gram-second) unit system. OpenFOAM® could be kept in SI units, with all values being converted before being transferred between the programmes. However, it was decided to also run OpenFOAM® in CGS mode (cf. Appendix C) to improve its accuracy when handling small numbers (which can be negatively affected by round-off errors). As a result of the number limit mentioned above, the particle diameter was chosen to be 1.5×10^{-6}m (or 1.5μm). This diameter was sufficiently above the lower limit to ensure the calculations were valid. However, this meant that the particle diameter was slightly bigger than those in the selected experimental data, but it was felt the larger size would make no appreciable difference to the results.

5.3.2. Number of Time Steps

Another restriction of earlier versions of LIGGGHTS was that it was limited to just over two billion time steps. This was because the number of time steps was stored as a signed 32-bit integer variable type, which had a maximum value of 2,147,483,647. This limit had a major affect for the time step size used in many of the simulations. For a time step size of 1×10^{-9}s, this meant the simulation could only reach just over two seconds of "real" time. The variable type was changed to a 64-bit integer from v.2 onwards, which allowed the number of time steps to reach a value of 2^{63} minus 1. This effectively eliminated the limitation.

5.3.3. Interpolation of Particle Forces within a CFD Cell

Typically values of flow field variables are calculated at specific places in the cell, e.g. at a cell or face centre. But particles are not always positioned at those points. Therefore interpolation of the values from these specific points allowed the flow variables to be evaluated at the actual point the particle was located. However, it was found that using CFDEM's interpolation feature on the pressure gradient, viscous, and drag forces made the simulations unstable, and they crashed soon after commencing. A possible explanation for this instability could be due to the small numbers that were being used in the calculations (≈1μm). Any small error could have had a knock-on effect and cause the simulation to crash with a segmentation fault. Thus interpolation had to be turned off for stability reasons.

5.4. COUPLING DEM WITH CFD

The fluid component of the model was laid out in Section 5.1. This section covers some practical concepts that had to be considered when combining DEM with CFD. Some considerations relating specifically to the use of both LIGGGHTS and OpenFOAM® are discussed. Examples of full input scripts are given in Appendix C. Particle properties used in the simulations are provided in Section 5.2. For the initial phase of the work with explicit coupling, LIGGGHTS version 2.0.4 was used. LIGGGHTS was upgraded to version 2.3.6 for the rest of the work. There were no major changes to the quality of the results, so the discussion here will focus primarily on the newer versions. However, influences carried down from older versions will be mentioned where appropriate.

5.4.1. Boundary Conditions for DEM

Boundaries were specified to match the CFD model of the box. Periodic boundaries were specified in x and z directions, with two opposing walls in the y direction. Because the geometry was flat, the "basic" wall type was specified in LIGGGHTS. Interactions with these wall types were efficient for the code to compute. LIGGGHTS was also able to handle complex geometry imported into the model as STL files, but exchanges with these wall types took longer to compute. Documentation from an older version of LIGGGHTS (v.1.5) stated that moving these STL walls was as costly as moving 11 particles.

5.4.2. DEM Time Step Size

Using particle values from Table 5.1 and a calculated shear modulus, *G*, the Rayleigh time step was calculated to be 1.07e-9s. The minimum value for the Hertz time step was calculated to be 9.66e-9s, though this value could change every time step as v_{max} changed. To obtain the initial estimate, the v_{max} term was taken as the maximum wall velocity imposed on the moving wall (experienced at the end of the simulation). Final values used for the calculation of the Hertz time step are given in Table 5.2.

Table 5.2: Parameters for calculation of Hertz time step for zirconia particles

Radius (m)	1.5e-6
ρ (kg/m^3)	6000
m_{eff} (kg)	5.301e-15
r_{eff} (m)	3.75e-7
Y_{eff} (Pa)	6.29e10
v_{max} (m/s)	0.044

In order to improve computational performance, it was decided to enlarge the time step size by reducing the particle stiffness (Young's modulus) by three orders of magnitude. It is standard practice to reduce the stiffness to allow for larger time steps, as it does not significantly affect the simulation results (Tsuji et al, 1993; Hoomans et al, 1996). Preliminary tests with plain particles confirmed that reducing the stiffness by three orders of magnitude made no significant difference to the results. In addition, flow-driven movement of the particles would be less affected by collision energy. Therefore the final Rayleigh time step was found to be 3.39e-8s and the Hertz time step was found to be 1.53e-7s. From these initial calculations, the Rayleigh time proved to be the limiting factor. Rayleigh time was also recommended as the limiting criterion due to the high volume fractions expected in the system (Kloss personal communication, 2012). Remembering that it was more accurate to run at <10% of the time step suggested by the Rayleigh criterion, a DEM time step size of 2.5e-9s was selected for the 1.5μm zirconia particles.

5.4.3. Particle Response Time and Coupling Interval

To gauge the size of the coupling interval, and hence the CFD time step, the particle response time was calculated using Equation 3.31. For zirconia particles, the response time was calculated as 8.27e-7s. Based on the selected DEM time step of 2.5e-9s, the coupling interval would have to be smaller than 330 for the CFD time step to be smaller than the response time. Typical coupling intervals are in the range of 50-100. Therefore a coupling interval of 100 would be acceptable in terms of accuracy, but allow for quicker simulations.

5.4.4. Solution Time and Wall Velocity Ramp Rate

When the same 35s ramp rate from the single-gap rheometer models was used on the much smaller 50μm box, it resulted in a maximum shear rate of about $180s^{-1}$ after two seconds of real time. The reason for the two second time limit was discussed in Section 5.3.2. This restriction on the simulation time imposed a practical limit on the model runtime. For example, a simulation for 20% volume fraction, on a 12-core, 2.9GHz computer took about two weeks to compute (for plain particles). Running for a more realistic 30 seconds, or the usual three minutes, would have been excessive. Only a larger time step would allow for practical simulation times, but this was not strictly allowed due to various criteria already mentioned.

This restriction was thought to be acceptable as the zirconia particles had relaxation time of 8.27e-7s, which was very small when compared to the overall solution time of two seconds. Thus the particles would be able to get up to speed within the given time.

5.4.5. Contact Force Model

The Hooke model was selected as the contact model. The tangential shear force between particles was also incorporated. This force can be thought of as a “history” effect that accounts for tangential displacement between the particles for the entire duration of their contact (LIGGGHTS manual, 2013). Therefore the `hooke/history` interaction was used in LIGGGHTS to model particle contact. The same model was used for particle-wall contact. Because the Hooke model was used, the characteristic impact velocity had to be specified. Based on the wall speed, it was assumed to be 1.4e-4 $m.s^{-1}$.

5.4.6. DLVO forces

DLVO forces were modelled as a combination of `colloid` (van der Waals) and `yukawa/colloid` (electrostatic) potentials. These features were already available in LIGGGHTS, as they came from the LAMMPS software platform (Plimpton, 1995). Equations for these models are discussed in Section 3.2.3.

For practical reasons, some alterations had to be made to the standard potentials available in the software. A minimum separation limit was instituted so the energy potentials between particles, and therefore the force, did not tend to infinity as particles came together and overlapped. This was done to allow for situations when particles collided. In addition, the standard `colloid` potential included an extra repulsive potential that was added to keep particles from overlapping. This extra potential was no longer necessary due to the changes made by the author, therefore it was removed. Energy in the system was monitored by outputting the sum total of all the energy potentials between particles.

5.4.7. Shear Stress Measurements

The DEM component of the wall force was measured to evaluate particle contribution to the overall shear stress. The force of particles colliding with the inner (moving) wall were calculated and stored at the same time that the fluid force was calculated. The `compute reduce sum` and `fix ave/time` functions were used to achieve this. The forces were measured as the force of the wall acting on the particles, and so would be opposite in direction to the force experienced by the wall. The contributions from both the DEM and CFD components of the wall force were added together to get the total force, and thus the total shear stress, on the wall.

5.4.8. Particle Insertion

Before the coupled model was started, LIGGGHTS was run on its own to initialise the particles. Firstly, all particles were inserted into the domain at the beginning of the DEM run using `fix insert/pack`. Particles were checked during the insertion procedure to make sure they did not overlap. Then the simulation was iterated for a number of time steps to allow the system of particles to relax, i.e. the kinetic energy in the system is reduced by allowing particles to move apart and find equilibrium. For this initialisation,

gravity was turned off so the particle motion was only affected by particle overlap (for plain particles), or DLVO forces (when they were included). Particle insertion was typically done on one processor, to ensure consistent spacing between particles.

For plain particles at volume fractions below about 30%, no iteration was needed as particles did not touch each other, and so there was no energy in the system that had to be dissipated. However, for particles with DLVO forces, 1 million DEM iterations were used. This allowed the energy to reduce by three orders of magnitude to the point where it changed very little per iteration, which was a sign the system was settling down.

The insertion method had difficulties inserting particles for particle volume fractions above about 30%. This was the practical limit of the insertion algorithm used in the procedure. Therefore, for larger volume fractions, particles were allowed to overlap during insertion so more particles could be inserted. But because there was a chance the particles would overlap, the DEM simulation had to be run for many iterations (1.5 million for plain particles) to let the particles move apart and allow the system to relax. To prevent the energy in the system from rising quickly with so many overlapping particles, both the stiffness (Young's modulus) and the coefficient of restitution were reduced. These values reduced the energy generated during collisions. The upper limit for the particle volume fraction is usually recommended to be 60%, as particles should not be constantly overlapped in DEM simulations. The largest possible volume fraction for randomly packed spheres is about 63%.

5.4.9. Solution Initialisation

It was decided to not pre-shear the system as is often done in experimental systems. In real systems, the particles often have time to form particle structures due to their inter-particle forces. Samples are then pre-sheared to break apart these structures in an attempt to make the system more homogeneous. It was felt that there was no significant particle structure at the beginning of these simulations. Also, including pre-shearing adds another variable that could affect the readings at the beginning of the simulation. Therefore it was decided to start the fluid and particles from zero velocity.

5.4.10. CFD Mesh Size

The CFD cell size should be bigger than three particle diameters. With a domain size of 50μm in each direction, this resulted in 12 cells of 4.17μm in length (2.8 diameters) being used in each direction. This was done to increase the number of cells in the domain, and so improve the accuracy and smoothness of the fluid solution.

5.4.11. Changes to Solver Settings and Discretisation Schemes

For the coupled model, a solver called `cfdemSolverPiso` was used. This solver was developed by CFDEM (Goniva et al., 2012). The solver was designed for unsteady problems (needed for CFD-DEM modelling); with either laminar or turbulent flow (cf. Table 5.3). Hence the PISO algorithm was used (the convention for OpenFOAM® solvers). Linear solver settings were kept the same as for the single-phase model, except that the tolerances were tightened (reduced) (cf. Table 5.4). From the non-Newtonian fluid tests in Section 4.3, it was decided to use four pressure-corrector loops. Discretisation schemes were left as default (cf. Table 5.5). After evaluating other options, it was found that these schemes performed the best anyway. The `snGrad` schemes were changed to "uncorrected" as the mesh was totally orthogonal and the flow was assumed to be largely aligned with the cells in the x and z directions.

Table 5.3: Coupled solver specifications

Solver Names	cfdemSolverPiso
Solver Type	Pressure-based, segregated solver
Time Dependence	Unsteady
Pressure-Velocity Coupling	PISO
nCorrectors (pressure-corrector loops)	4
nNonOrthogonalCorrectors	0
Formulation	Implicit
Solver Accuracy	Double Precision (default)
OpenFOAM® version	2.1.1.
LIGGGHTS version	2.3.6
CFDEM version	2.5.3

Table 5.4: Linear solver and tolerance settings for cfdemSovlerPiso

	p	**U**
Solver	PCG	PBiCG
Preconditioner	DIC	DILU
Tolerance	5e-08	5e-07
relTol	0	0

Table 5.5: Discretisation schemes for coupled model

Term Type	**Scheme**	**Attributes**
ddtSchemes	Euler	first order, bounded, implicit
Interpolation: interpolate(U)	linear	linear interpolation (central differencing – second-order, unbounded)
snGradSchemes	uncorrected	no non-orthogonal correction
GradSchemes: grad(p) grad(U)	Gauss linear	second-order Gaussian integration with linear interpolation, unbounded
DivSchemes: div(phi,U)	**Terms with flux specified** Gauss limitedLinear(V) 1 **Terms without flux** Gauss linear	First/second-order, bounded (1 = TVD conformance and best convergence, 0 = best accuracy) (V for vector field terms) second-order, unbounded
Laplacian schemes: laplacian(nu,U) laplacian((1|A(U)),p)	Gauss linear uncorrected	Gaussian integration, linear interpolation, uncorrected snGrad scheme – together this gives an bounded, first-order, non-conservative scheme
Flux Required	p	field for which flux is generated (only p equation in this case)

5.4.12. Settings for Lagrangian/Eulerian Data Transfer

Three settings for the coupled solver governed the transformation of information between the Lagrangian (DEM) and Eulerian (CFD) systems. These are discussed below.

The `locateModel` locates the CFD cell ID corresponding to a given spatial position. More specifically, it was used to find the cell in which a particle was located. The sub-model called `engine` used different algorithms to do this. Setting the `treeSearch` parameter to "false" executed a geometric (linear) search using the last known cell ID. Setting `treeSearch` to "true" used a recursive tree structure to find the cell. The latter option was generally recommended as it was much quicker than a geometric search.

The `voidfractionModel` calculated the DEM particle's volume in the CFD domain via a `voidfraction` field. The `divided` sub-model was recommended for use when the particles were in the size range of a CFD cell. It used satellite points to divide a particle's volume between the cells it touches. Thus it was more accurate than the `centre` model which assumed all the mass was in the same cell as the particle centre.

The `averagingModel` mapped data from the Lagrangian to Eulerian system (e.g. particle velocities). It calculated the average particle velocity inside a CFD cell. The `dense` sub-model (used in this work) applied to cases where the granular phase is rather dense. The particle velocity inside a CFD cell was evaluated as an ensemble average of the particle velocities.

5.5. INITIAL MODEL TESTS: EXPLICIT VS. IMPLICIT DRAG FORMULATIONS

Preliminary tests of the coupled model were done with a low particle volume fraction (4.58%) as this was more computationally efficient to compute. The baseline parameters selected in the chapter (e.g. time step size) were used. Initially, only the explicit version of the DEM drag model was available in LIGGGHTS (cf. Section 3.5.5). Therefore this model was used in the initial investigations. However, when moving to higher volume fractions (20%), the model became unstable to the point where it was unusable. This prompted the move to the implicit formulation.

Re-testing the 4.58% model with the implicit scheme produced a different result to the explicit scheme. Figure 5.7 compares the differences due to the implicit and explicit formulations, to a single-phase CFD simulation of water. The curves in Figure 5.7 are for particles that have DLVO forces between them. Plain particles showed virtually no difference to the single-phase water. In Figure 5.7, both curves show that shear stress increases with increasing shear rate. The explicit model curve showed a slight shear-thinning trend. In both cases, the coupled model produced higher shear stresses than plain water, which was expected.

The variable nature of the curves was thought to be due to the transient distribution of particles in the near-wall region. Any movement into, or out of, the near-wall region would change the measured shear stress. Wall forces were measured instantaneously, without being averaged over a number of time steps. Importantly, the relative smoothness of the data improved with the implicit scheme. This can be attributed to the superior stability of the implicit scheme. The higher shear stress values exhibited by the explicit formulation at low shear rates could be due to the instability of the system, i.e. excess particle motion artificially generates higher shear stresses.

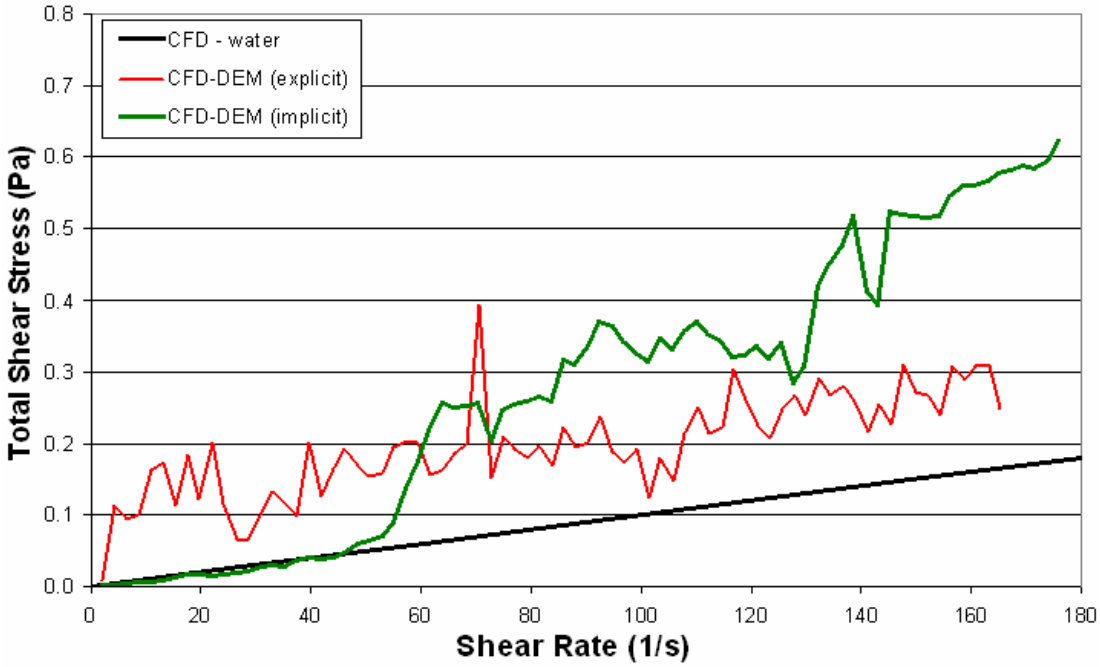

Figure 5.7: Shear stress vs. shear rate graph for 4.58% volume fraction of zirconia (with DLVO forces) showing differences between the explicit and implicit formulations

It should be noted that the implicit scheme uses the Koch-Hill drag force model while the Di Felice drag model was used with the older explicit scheme. For later runs, OpenFOAM® also ran in CGS mode. All models had to be run with the interpolation features turned off to prevent them from becoming unstable and crashing. Some models lost all particles in the system due to high collision energies, while others had problems in the CFD solver (most likely due to round-off errors from small numbers).

For preliminary tests, these simulations performed adequately, showing that the coupled CFD-DEM model did work. Importantly, these tests demonstrated that using the implicit scheme was more stable than the explicit scheme. This information was used to construct the 20% particle volume fraction models. These models were used to investigate appropriate values of important model operational parameters (e.g. time step size). The results of these investigations are discussed next in Chapter 6.

6. CFD-DEM COUPLED MODEL RESULTS (20% VOLUME FRACTION)

Five model parameters were expected to have the most influence on the accuracy and sensitivity of the simulations, namely the CFD mesh, times step size, coupling interval, wall velocity ramp rate, and the domain size. This chapter investigates the influence of these factors in order to determine appropriate ranges of parameters that can be used in the coupled model. These values will be used in the subsequent tests in Chapter 7. It was decided to use a particle volume fraction of 20%. It was thought this volume fraction would produce a notable difference in rheological behaviour when parameters were changed, but still be acceptable in terms of computational expense (with 14147 particles).

Section 6.1 presents results for the baseline model, to which other model parameters are compared. Section 6.2 explores different CFD mesh arrangements to find a mesh-independent solution. Section 6.3 discusses the merits of different scenarios for the start procedure (e.g. particle initialisation). Appropriate ranges of the time step size and coupling interval are investigated in Sections 6.4 and 6.5 respectively. The influence of the velocity ramp rate is determined in Section 6.6. In Section 6.7, the size of the box geometry is investigated to determine the correct bounds of the model geometry. A short discussion on the hardware requirements for these simulations is given in Section 6.8. In conclusion, a summary of important findings is given in Section 6.9.

A DEM time step of 2.5e-9s and a coupling interval of 100 were considered to be the baseline setup, with all parameters varied relative to that. Typically, when referring to a particular set up, only the DEM time step and the coupling interval will be quoted. The CFD time step can be calculated from those values. In terms of the geometry, a length of 50μm was used for each dimension of the box unless otherwise specified. Many cases were tested for both plain particles, and particles with DLVO forces included. Graphs of "total" viscosity (or shear stress) include contributions from both the fluid (CFD) and particle (DEM) portions of the model. In all cases, "viscosity" refers to the apparent viscosity.

6.1. RESULTS FOR BASELINE MODEL

Using the baseline model parameters discussed in Chapter 5, viscosity curves for both plain particles, and those with DLVO forces between them were generated (cf. Figure 6.1). The DLVO force used in this chapter simulates the case where there is a pure attraction between particles (a zeta potential of 0mV, i.e. the van der Waals force dominates). This would provide a more intense rheological response when contrasted to plain particles (i.e. particles with a more neutral charge).

As seen in Figure 6.1, particles with DLVO forces between them do indeed generate a higher viscosity than plain particles, which was expected. In both cases, there was a slight shear-thinning trend from around $35s^{-1}$ (illustrated by the smooth trend lines in Figure 6.1). Shear-thinning was expected for these suspensions. The variable nature of the CFD-DEM model results was thought to be due to a combination of the transient distribution of particles in the near-wall region and the instantaneous measurement of the wall forces. Trend lines were included in Figure 6.1 to show the overall trend of the results.

The viscosity curves show no evidence of a yield stress. Viscosity values below $30s^{-1}$ were initially very low, but gradually increased until a shear rate of around $35s^{-1}$ (after which shear-thinning occurred). This behaviour was different to the expected trend, where viscosity is initially very high, but reducing fairly quickly at low shear rates (due to shear-thinning). It was felt this discrepancy was not a numerical problem, as all subsequent models showed similar behaviour.

A yield stress in particle suspensions is sometimes related to solid structures in the mixture, formed by agglomerated particles. These structures have to be broken up before, or as, the mixture flows. In the coupled model used here, particles are evenly distributed at the start of the simulation, with little particle agglomeration occurring during the DEM initialisation phase. Therefore a yield stress due to this phenomenon was not expected.

Another influence is wall slip. Lower-than-expected viscosity values have been attributed to the occurrence of slip between the moving wall and the particle-fluid mixture. This is discussed in more detail in Section 7.1.1. However, it should also be noted that some

researchers believe the yield stress is not a real phenomenon (e.g. Barnes, 1999), but is merely an artefact of an extrapolated shear stress curve at low shear rates, a region where rheometers have not been accurate enough to measure the correct behaviour (e.g. Herschel-Bulkley model).

It is the author's opinion that the behaviour seen here at low shear rates was mostly due to the even distribution of particles at the start of the simulation. Wall slip in the model would also influence the behaviour at low shear rates. However, once the simulation had started, the system attained realistic conditions.

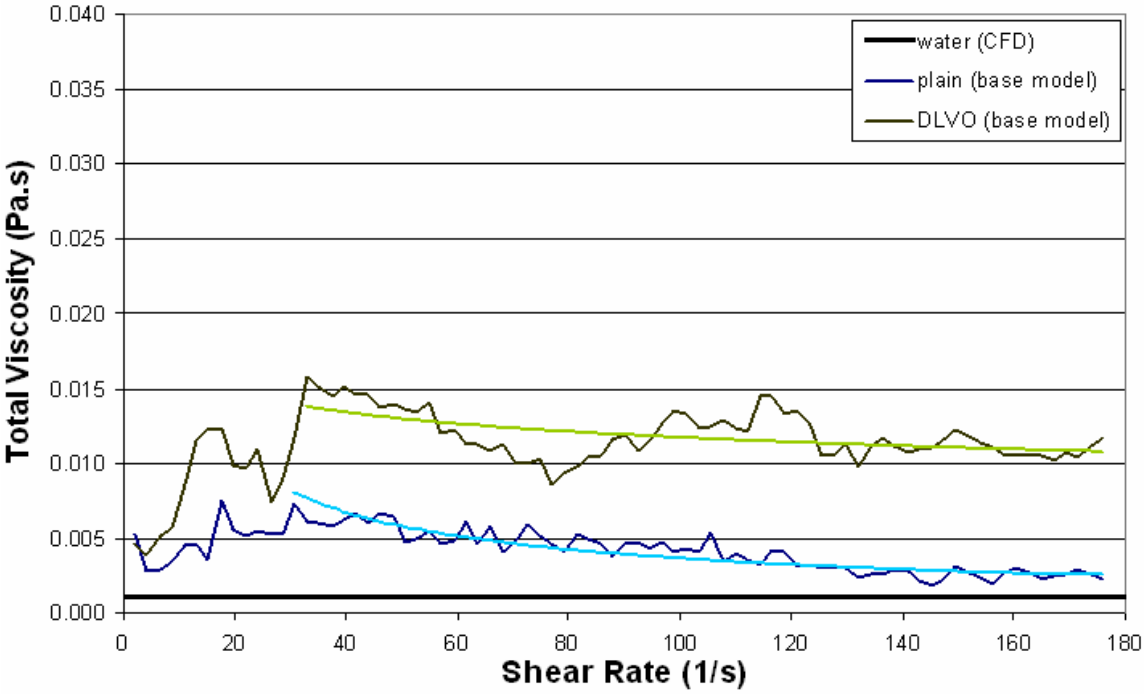

Figure 6.1: Total viscosity vs. shear rate for the baseline model parameters

6.2. CFD MESH GRADING

CFD mesh sizes were limited due to the size of the particles. However, some slight variations from the base mesh were tested to check their influence. The base mesh consisted of 12x12x12 cells (in the x, y, and z directions), with uniform spacing. Mesh grading was also tested. The mesh was made finer at the walls and more coarse in the middle (mesh 1), and vice-versa (mesh 2). Reducing the density was also tested (mesh 3). Mesh 4 combined the coarser mesh with a finer mesh grading at the wall. As can be seen

from Figure 6.2, it is evident there is no significant change in the overall performance of the different meshes (when allowing for the variation of the curves due to particle motion). Thus it is not necessary to change from the base mesh cells with uniform grading. One noticeable trend was that a finer mesh near the wall resulted in slightly higher viscosity values than the base case, while the coarser meshes had lower values.

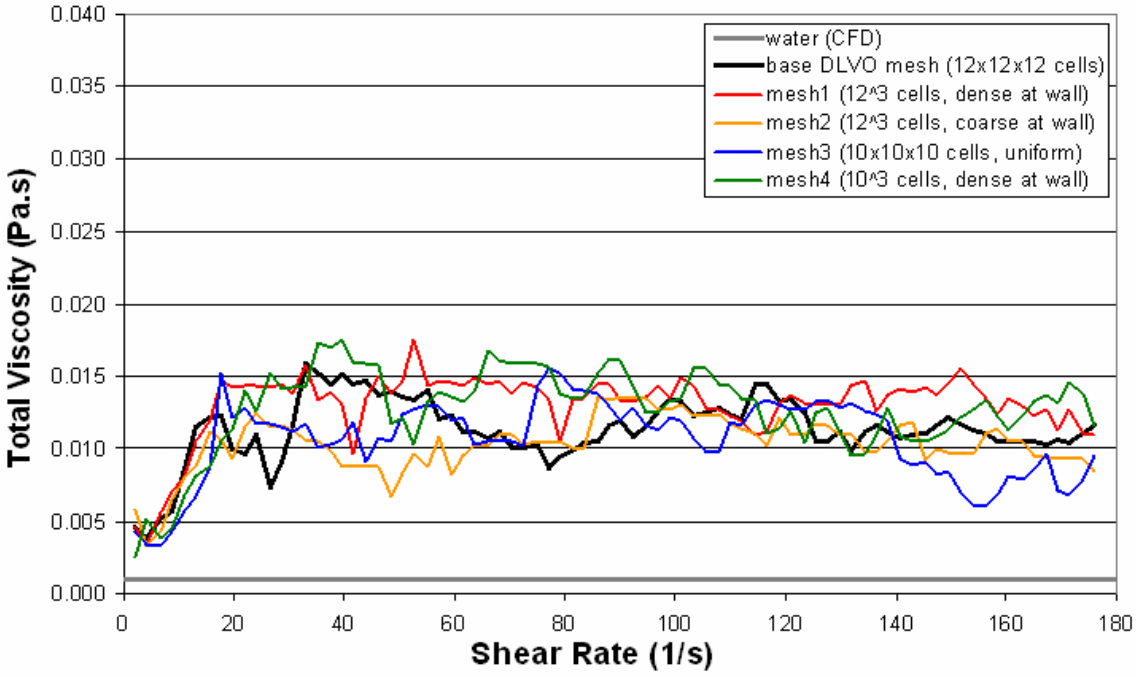

Figure 6.2: Total viscosity vs. shear rate for different CFD mesh arrangements

Taking this to the extreme, the wall mesh was reduced to be one particle diameter wide (in the gap direction) and smaller. The rest of the mesh was left largely the same size as before. For the case when the cell was one particle diameter wide, the curve showed no significant difference over most of the shear rate range, except for between 30 and 80 s^{-1} when it was slightly higher. Making the cell width smaller than this reduced the viscosity values over most of the range. Therefore these extreme cases were not an improvement over the standard mesh.

6.3. START PROCEDURE

Initially, simulations were started from rest (both particle and fluid phases). This worked well and was a simple procedure. Other variations were tried, including inserting particles with an initial downward velocity, and allowing more time for particles to

agglomerate before the coupled simulation was started (while at 0.1s this extra time was still very short, it was significantly longer than normal). However, these changes had no significant impact on the initial results, except for when gravity was turned off.

Turning off gravity for the particles did have an effect. When starting from rest, the viscosity was the same as the pure fluid. It picked up slowly until it reached normal values at a shear rate of $25s^{-1}$, and started following the data of the base case from about $90s^{-1}$. Therefore gravity seems to influence the shear stress at low shear rates.

Simulations were also tested where the particles were given a downward initial velocity. There was no significant alteration to the general trend, except that the first data point was slightly lower than normal. This indicated the coupled model started off with a lower viscosity due to the particle motion. One possible explanation was that the fluid was no longer accelerating from rest anymore as the moving particles helped accelerate the flow.

6.4. TIME STEP SIZE

While the time step was suggested by various criteria (based on material properties), other step sizes were investigated to explore the sensitivity of the system to the time step size. If a larger time step were possible (for the same behaviour), then it would allow for faster computational times. In these tests, only the DEM time step was varied. The coupling interval was kept at 100 because this was thought to be the upper limit of the interval size, and it would result in quicker simulation times. This combination ultimately set the CFD time step. A DEM time step size of 2.5e-9s was considered to be the baseline (c.f. Section 5.4.2).

6.4.1. Plain Particles

Viscosity results for plain particles with different time steps are shown in Figure 6.3. All curves indicated some sort of shear-thinning behaviour as the shear rate is increased. Increasing the time step size made the simulations more unstable, hence the spikes in the viscosity curves. A time step size of 5e-9s gave reasonable values, though it did not show as strong a shear-thinning behaviour as the baseline time step of 2.5e-9s. DEM time steps bigger than 5e-9s (with a coupling interval of 100) were too unstable to be practical. All

but the largest time step (2.5e-8s) showed a noticeable dip right after the start of the simulation before increasing again.

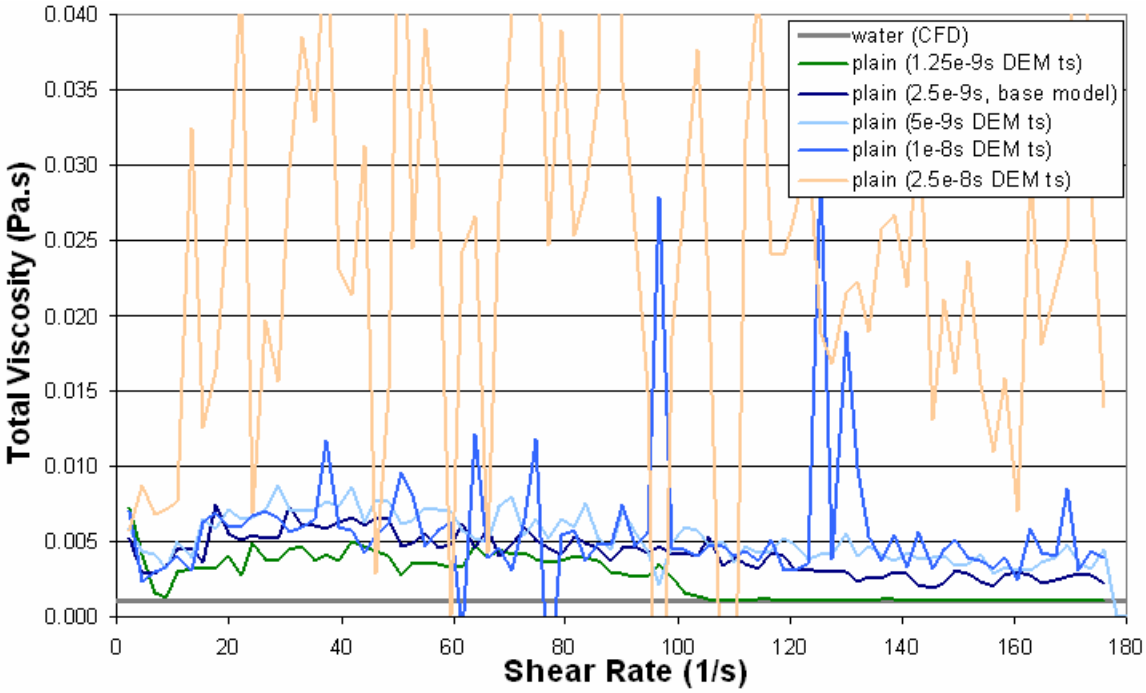

Figure 6.3: Total viscosity vs. shear rate for plain particles with different DEM time steps (coupling interval of 100)

The smallest time step size of 1.25e-9s showed unexpected behaviour. At a shear rate of $100s^{-1}$ the viscosity curved dropped down to that of plain water. Looking at the particle distribution in the domain provided the answer for this (Figure 6.4). At this shear rate, the particles migrated away from the inner boundary (rotating) wall, leaving less than 5% (by volume) of particles in the row of cells next to the wall. So the model essentially only saw water when calculating the force. In experiments, this phenomenon is often called wall depletion, or simply wall "slip", where the particles move away from the wall and there is only fluid in contact with the rotational surface. However, it was unlikely that the phenomenon observed here was true wall slip, as this typically happens at low shear rates (Barnes, 1995). This behaviour was thus attributed to numerical instability that may arise with small time steps (Goniva personal communication, 2014). Small disturbances may get amplified with small time steps, instead of smeared out as with larger time steps.

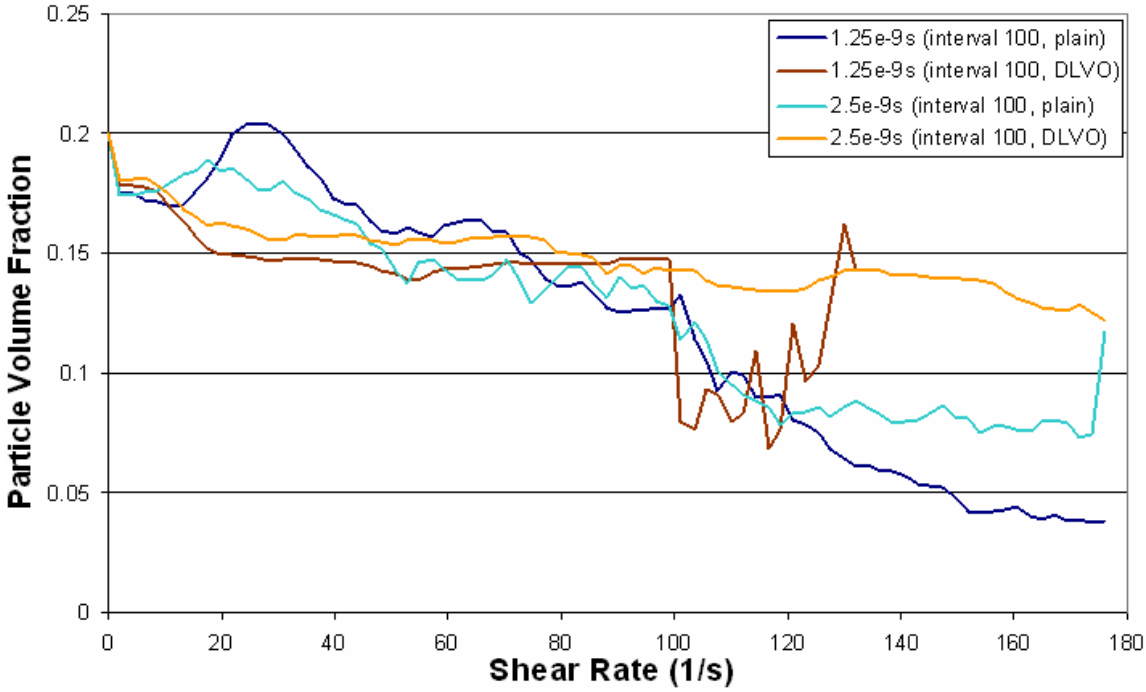

Figure 6.4: Particle volume fraction (in the wall region) vs. shear rate for the base model and 1.25e-9s DEM time step model, for both plain and DLVO cases

6.4.2. Particles with DLVO Forces

The curves all display similar behaviour, even with bigger time steps (cf. Figure 6.5). The dip in the curve at low shear rates was still visible for the smaller time steps (<5e-9s). This was most likely because the bigger time steps did not give the temporal precision to resolve this response. While there was no significant difference between the curves, larger time steps generally exhibited higher viscosities than the rest of the curves. Shear-thinning of these models was less pronounced, though still noticeable. This was expected as the stronger DLVO forces would keep the particles together for longer. Adding DLVO forces to the model appeared to stabilise the particles and produced much smoother viscosity curves when compared to the plain particles.

In a similar manner to the plain particles, the data for the smallest time step (1.25e-9s) indicated that particles had migrated from the wall surface at $100s^{-1}$ (cf. Figure 6.4). The resultant viscosity after the migration was similar to that for plain particles (i.e. higher than plain water). This shows that there were more particles in the near-wall region than for plain particles, roughly 10% versus 5%. However, this was not evident from the total viscosity displayed in Figure 6.5 because the particle force component becomes very

erratic and the values increase by an order of magnitude. Therefore they become significant enough to influence the total viscosity value. Figure 6.6 shows only the fluid force component of the same data, which highlights the particle migration phenomenon more clearly. The simulation for the 1.25e-9s time step was stopped before it completed as it no longer showed any useful trends.

From these trends, a smaller time step such as 2.5e-9s was preferred, even though 5e-9s was relatively stable for a coupling interval of 100. In general, anything with a CFD time step smaller than 5e-7s should produced a stable result.

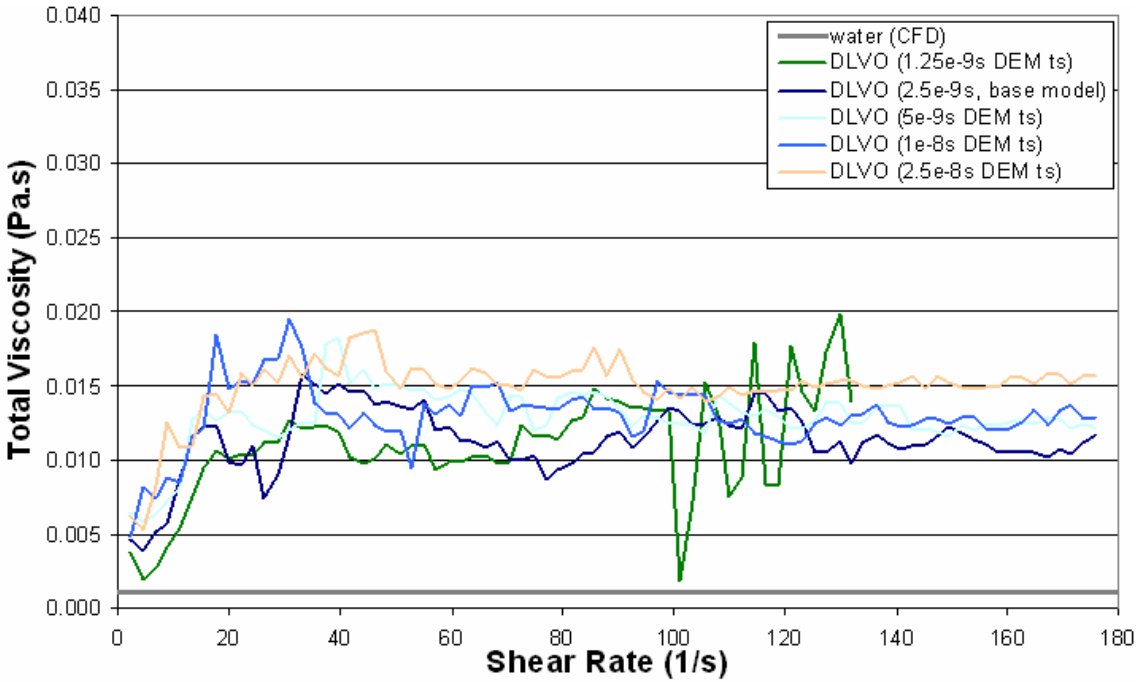

Figure 6.5: Total viscosity vs. shear rate for different DEM time steps (with DLVO forces)

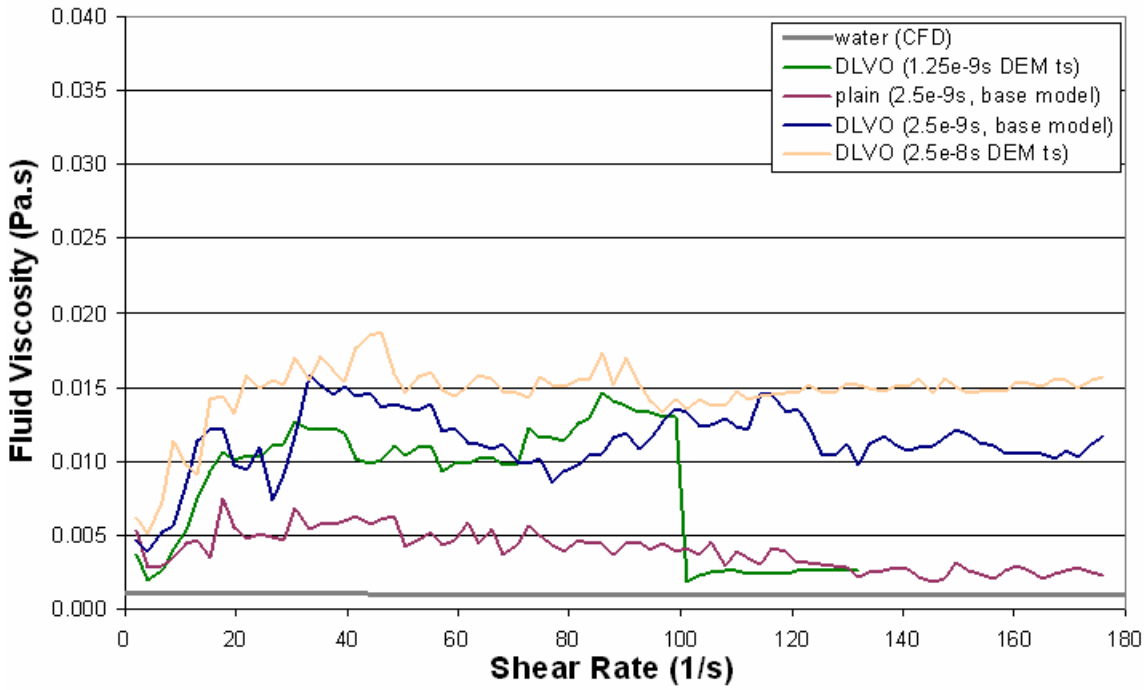

Figure 6.6: Fluid viscosity vs. shear rate for different DEM time steps (with DLVO forces)

6.5. COUPLING INTERVAL SIZE

Another factor affecting the choice of time step size was the coupling interval between the DEM and CFD time steps. For the majority of the results shown here, the DEM time step was kept constant at 2.5e-9s, while the CFD time step varied depending on the coupling interval. Based on the particle properties, the response time of the zirconia particles was calculated to be 8.27e-7s (Section 5.4.3). In theory, as long as the coupling interval was kept below this value, the simulation would allow the particles to adequately respond to the change in flow velocity. Therefore, the baseline coupling interval of 100 was considered acceptable because it was below the upper limit of the interval size. Larger coupling intervals were also tested to investigate the sensitivity of the response time prediction.

6.5.1. Plain Particles

Here in Figure 6.7, the particles showed a similar trend as for the larger time step sizes, where the larger coupling intervals curves did not show as much shear-thinning behaviour. However, the differences were not as large. Also, only the curve for the

coupling interval of 500 showed unstable behaviour. The corresponding CFD time step of 1.25e-6s lay between the unstable CFD time steps of the 1e-8s and 2.5e-8s series discussed in the previous section (coupling interval of 100). An interval of 200 corresponded to the CFD time of the 5e-9s series of the previous section, which was thought to be acceptable. What was also noticeable was that for a coupling interval of 50, the same phenomenon of particles migrating from the wall could be seen. This was not too surprising as the CFD time step was the same as for those series (1.25e-8s).

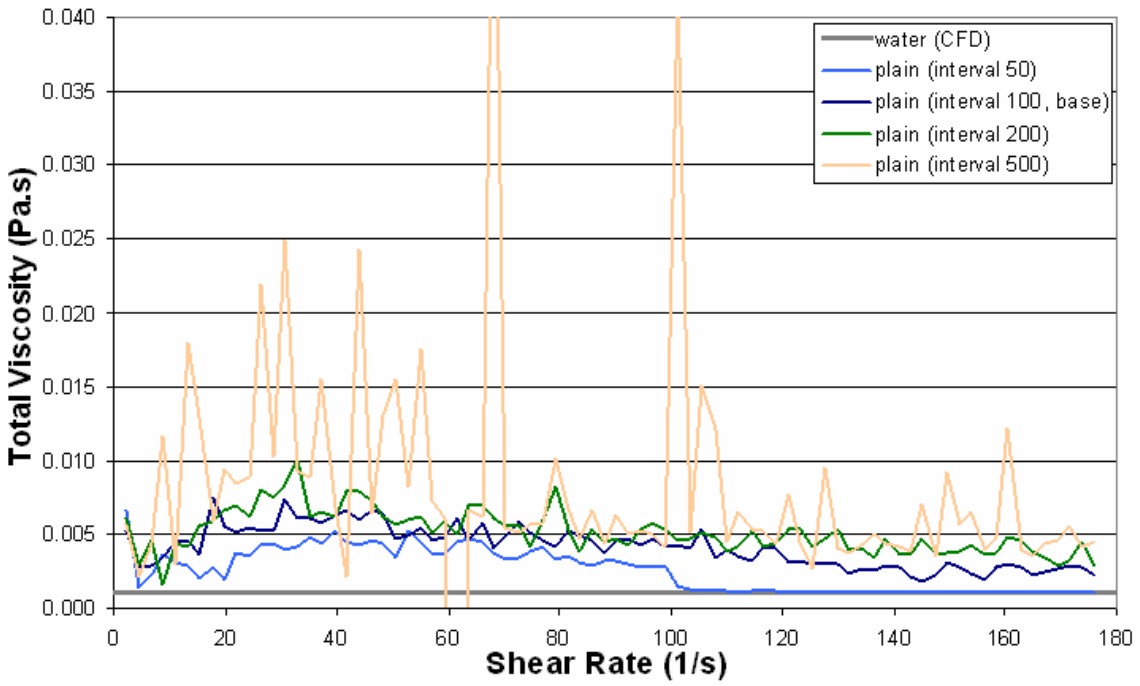

Figure 6.7: Total viscosity vs shear rate showing affect of coupling interval for plain particles with a DEM time step of 2.5e-9s

6.5.2. Particles with DLVO Forces

Again, the curves for particles with DLVO forces indicated a stable model, with a much more flat viscosity value. Even the interval of 500 showed a plausible result, though without a dip at the beginning. The particle migration phenomenon was also seen here for an interval of 50. As such, the results shown in Figure 6.8 are just the fluid component.

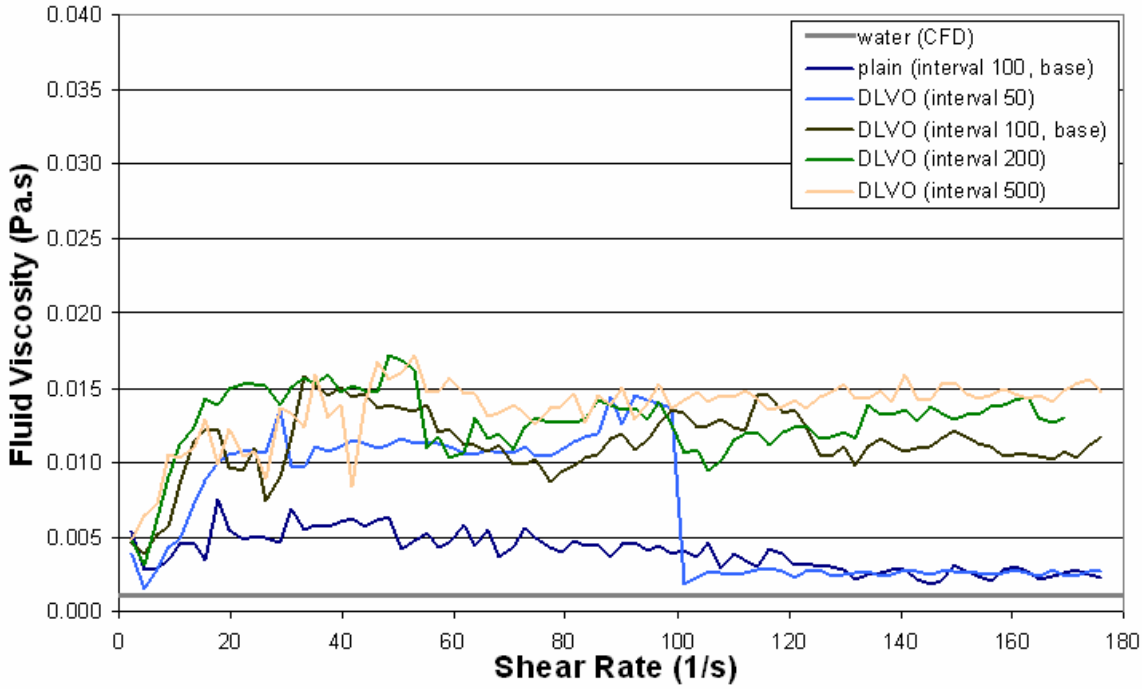

Figure 6.8: Fluid viscosity vs shear rate showing affect of coupling interval for a DEM time step of 2.5e-9s (with DLVO forces)

6.5.3. Small Coupling Intervals

Smaller coupling intervals were better because they are more stable. However, they would require more computational time and from the earlier results, they also showed signs of particle migration. Therefore, smaller coupling intervals were tested in combination with larger DEM time steps because it was apparent that the DEM component was more forgiving (i.e. stable and accurate) than the CFD component for bigger time steps. Overall solution times were also sped up because the extra effort used on more frequent coupling procedures was outweighed by the reduction in the DEM computations.

Figure 6.9 and Figure 6.10 show results for different combinations. All combinations shown in these graphs provide the same general performance. One noticeable trend in the curves is that larger time steps (CFD and to some extent DEM too) do not dip at $5s^{-1}$, a feature which had been noted in previous sections. Another interesting observation was that all combinations with a CFD time step below 1.25e-7s had a problem with particle migration. This is the same CFD time step of all the previous combinations that experienced this phenomenon. CFD time steps larger than 1e-6s tended to be unstable,

except for the combination of DEM time step 5e-8s and coupling interval of 25 (CFD time step = 1.25e-6s). Speed-ups were notable, for example, the combination of 1e-8s (DEM) with an interval of 25 was 2.5 faster than the base case.

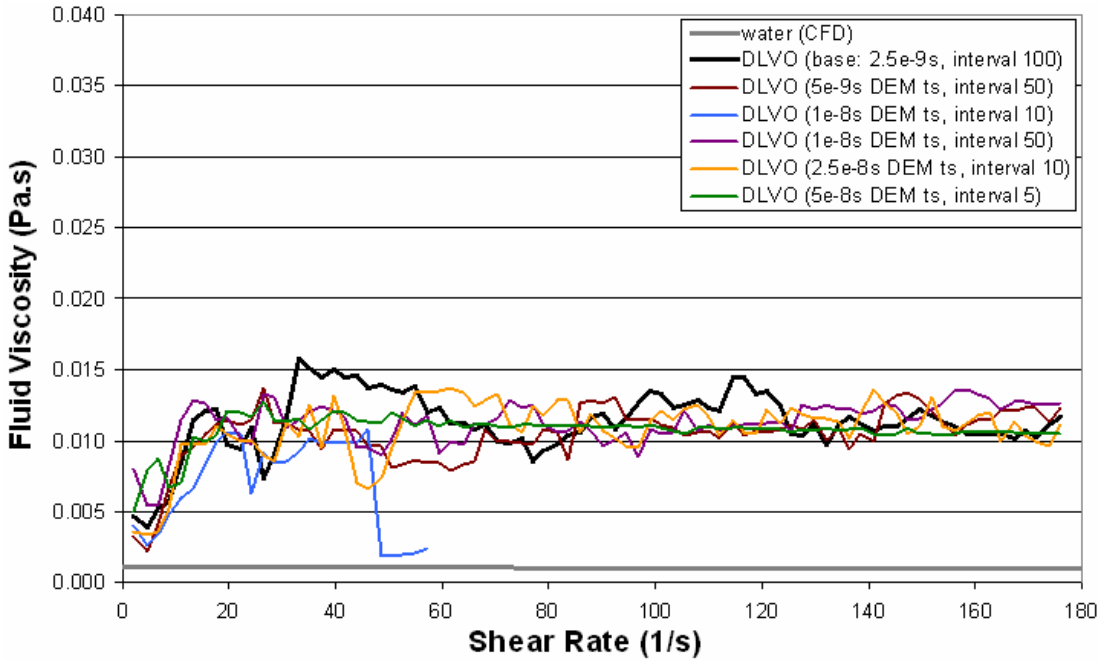

Figure 6.9: Fluid viscosity vs. shear rate for different combinations of DEM time steps and coupling intervals

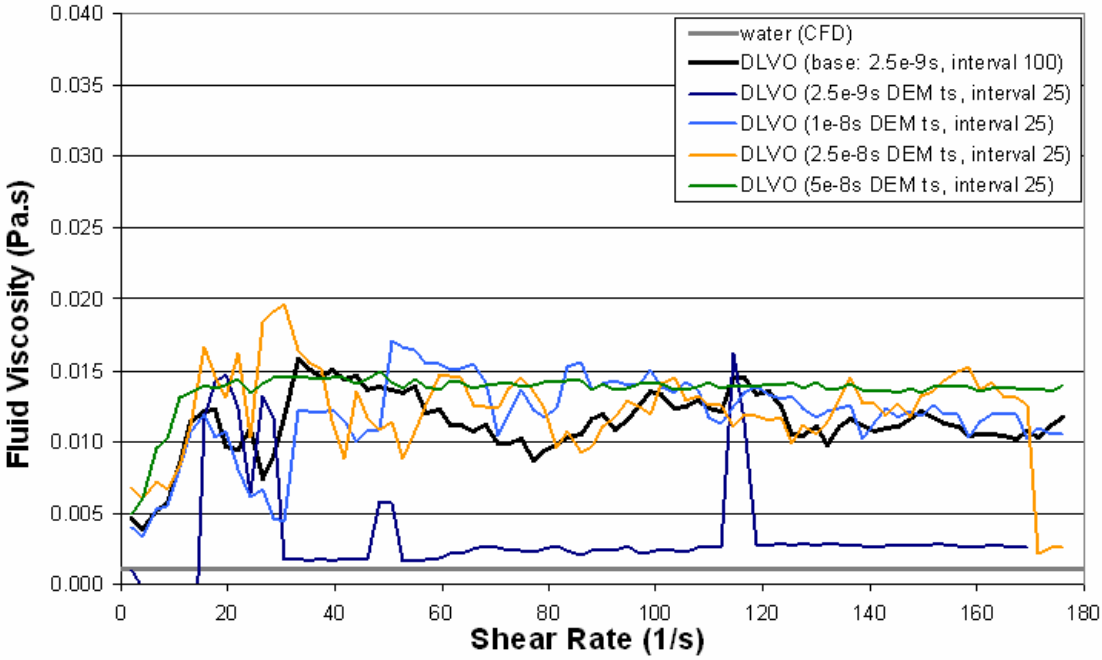

Figure 6.10: Fluid viscosity vs. shear rate for different DEM time steps and a coupling interval of 25

From these tests there was evidence that it was actually the CFD time step size that was of importance for stability, not the size of the DEM time step, which was more forgiving. While the base set up of 2.5e-9s (DEM time step) and an interval of 100 was good, the combination of 1e-8s and an interval of 25 would be suitable as well (and faster). Within reason, larger time steps could be used as long as the coupling interval was kept small.

6.6. WALL-VELOCITY RAMP RATE

Another factor that could have affected the response of the model was the time taken to reach the final shear rate. Initially this time was limited to two seconds of real time, due to various computational restrictions. This time was therefore extended to see if it influenced the physical behaviour of the model. Solution times of two, eight, and 20 seconds were tested. Results for both plain particles and those with DLVO forces shall be discussed together as the trends are the same.

6.6.1. Apparent Viscosity for Different Ramp Rates

Figure 6.11 shows the results for particles with DLVO forces at different ramp rates with the basic model configuration. For low shear rates ($<20s^{-1}$), the viscosity curves of the slower ramp rates tended to be slightly higher than the curve of the base model. However, all curves for the slower ramp rates exhibited the particle migration phenomenon mentioned in earlier sections. This was confirmed by tracking the change in volume fraction with time in the vicinity of the wall.

As a result, larger time step combinations were tested. For the eight second ramp rate, the only combinations that did not exhibit this phenomenon were when the combined DEM time step and coupling interval gave a CFD time step above 2.5e-7s (cf. Figure 6.12). Of those combinations, only the one with a DEM time step of 1e-8s (and coupling interval of 100) was usable, though not faultless. The larger DEM time steps of 2.5e-8s (coupling interval of 25) and 1.25e-8s (interval of 25) showed areas of instability in the viscosity curves and so were thought to be unsuitable. A DEM time step of 1e-8s for the eight second ramp, corresponded to a four times increase in the time step for a four times slow down in the ramp rate. Keeping this ratio the same was enough to keep the simulation

stable and allow it to run to completion. For the 20s ramp rate, the CFD time step had to be kept above 2.5e-6s.

In summary, slowing down the ramp rate increased the viscosity at lower shear rates, but these simulations eventually became unstable. The ramps rates that did complete (with larger time steps) produced viscosity values that were very similar to the base model with a two second ramp rate. Therefore, the faster two second ramp rate was thought to be acceptable (especially at higher shear rates), even though it was less realistic than a slower ramp rate.

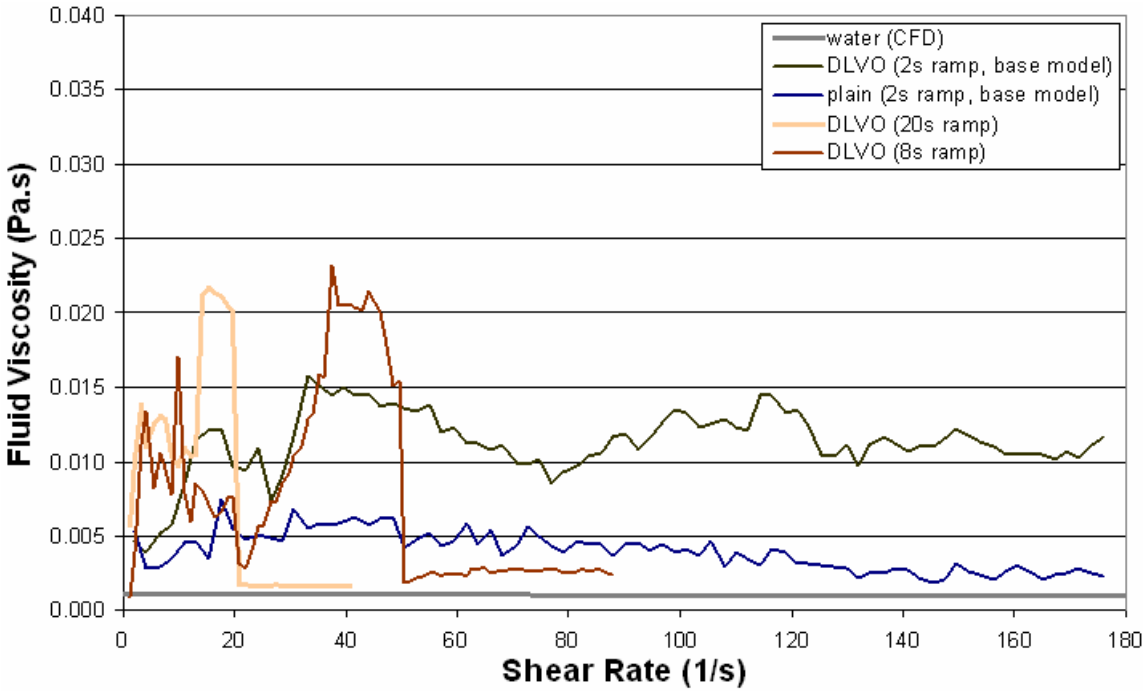

Figure 6.11: Fluid viscosity vs. shear rate comparing different ramp rates for the baseline time step configuration

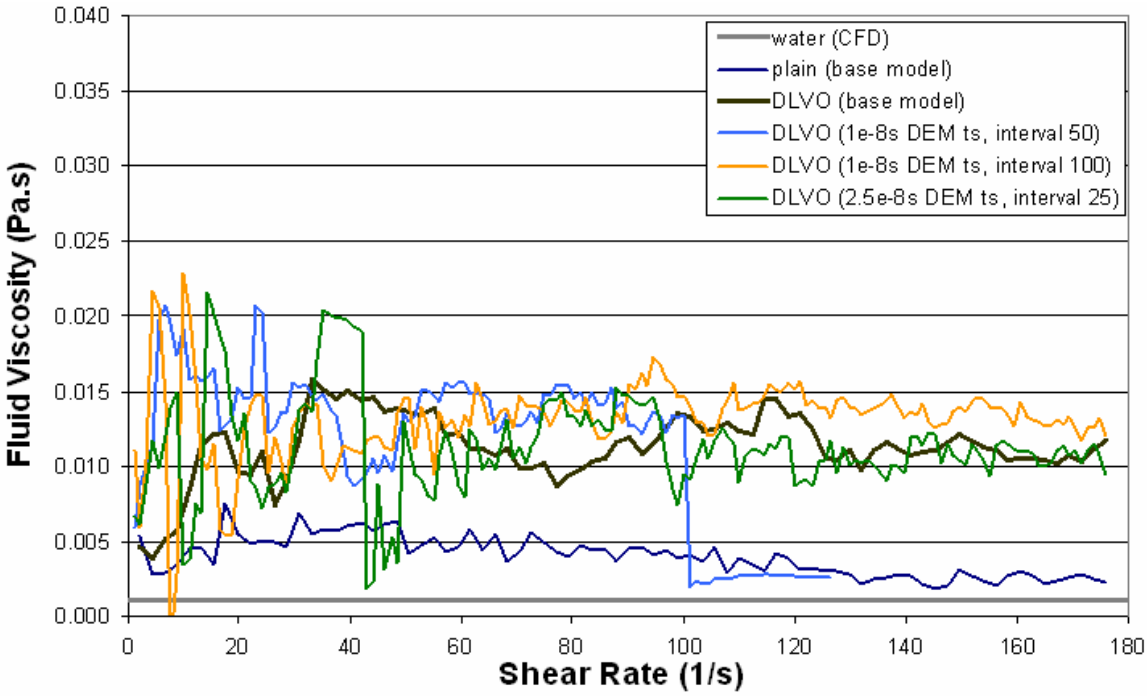

Figure 6.12: Fluid viscosity vs. shear rate for combinations of larger time steps and smaller coupling intervals (for the eight second ramp rate)

6.6.2. Particle Migration

Particle migration happened at a shear rate of $50.6s^{-1}$ for the eight second ramp. For the 20s ramp rate (2.5 times slower), it happened at a shear rate of $20.9s^{-1}$. This was roughly 2.42 times slower, which was essentially the same ratio when one allows for data being saved at set intervals. So here again, slowing down the changes in the fluid flow produced the phenomenon of particles migrating from the wall. From previous sections, when the CFD time step was halved, the particles migrated around $101s^{-1}$. This was double that of the eight second ramp which can be considered to slow down the flow by four times (2x4=8). Therefore slowing down the change in fluid flow by a certain factor (either through the time step or the flow velocity), reduced the shear rate at which particle migration occurs by that same factor.

This behaviour was not expected, and shear-thinning does not occur to such a degree, and with such precision, in experiments. Therefore this was most likely some numerical phenomenon that manifested itself at these combinations of flow speed and time step size. In fact, by lowering the ramp rate (i.e. slower speeds), the numerical problem becomes more and more dominated by the diffusion and source terms. This would make

the flow equations more unstable when solved with explicit schemes (Goniva personal communication, 2014). Thus it was indeed a numerical problem that caused this behaviour, and so cannot be attributed to any physical phenomenon. However, this occurred while making the model more "realistic". Larger time steps can be used to mitigate the problem, but these bring their own instability concerns. Therefore, the only solution would be to maintain a faster ramp rate, which seems to give good results.

6.6.3. True Wall-Depletion Effects

An interesting feature of the viscosity curve for the base ramp rate was that it dipped around a shear rate of $5s^{-1}$ and again at $25s^{-1}$, before increasing again. For lower shear rates (before particle migration occurs), the slower ramp rates showed generally higher viscosity values, though they were a bit erratic. This was also evident for the same ramp rates with larger time steps (data not shown here). Initially, this behaviour was thought to be due to the inertial response of the fluid (Section 6.4.1). But if faster ramps rates lead to lower viscosity values, then this was most likely an indicator of wall depletion in the mixture (Barnes, 1995).

6.7. DOMAIN SIZE

The box geometry was increased in size to determine if the dimensions of the box influenced the results, and if it did, were there any limits to the size. This would indicate if the original choice of a 50μm box was appropriate. As part of this, the flow direction (x) and vertical (z) dimensions were increased to 200μm. Gap width (y-direction), in particular, was considered important as it determined the space between the only two fixed boundaries (inner and outer walls) in the model. Periodic boundaries would not restrict the flow and so wouldn't play a major role in the model behaviour. As such, gap widths of 200μm and 500μm (0.5mm) were tested. A 500μm gap width is typical for many rheometers.

Within this investigation of different domain sizes, two further variations were also considered. Initially, the ramp rate (change in wall velocity with time) would be kept the same. This meant the shear rate would be reduced according to the change in gap width (i.e. shear rate is four times smaller for 200μm width than the 50μm gap). Therefore the

simulation had to run correspondingly longer to reach the same shear rate as the other runs. Secondly, the ramp rate was increased such that the shear rate would be the same as before ($176s^{-1}$) after two seconds (i.e. wall velocity is four times faster for 200µm width than the 50µm gap). It was thought this would show the difference made by the increased geometry alone, without adding the influence of a slower ramp rate as well. As larger domains would increase computational expense, time steps were made bigger in certain cases to see if the extent of the increase could be mitigated.

6.7.1. Dimensions in Flow and Vertical Directions

The lengths of the geometry in the x (flow) and z (vertical) directions were increased to 200µm. This meant a larger wall area. Once the force was corrected for this larger area, it was clear that the resultant shear stresses were the same as for the base case (Figure 6.13). This result was expected and shows that the periodic boundaries did not influence the results. Therefore the domain does not have to be bigger in these directions.

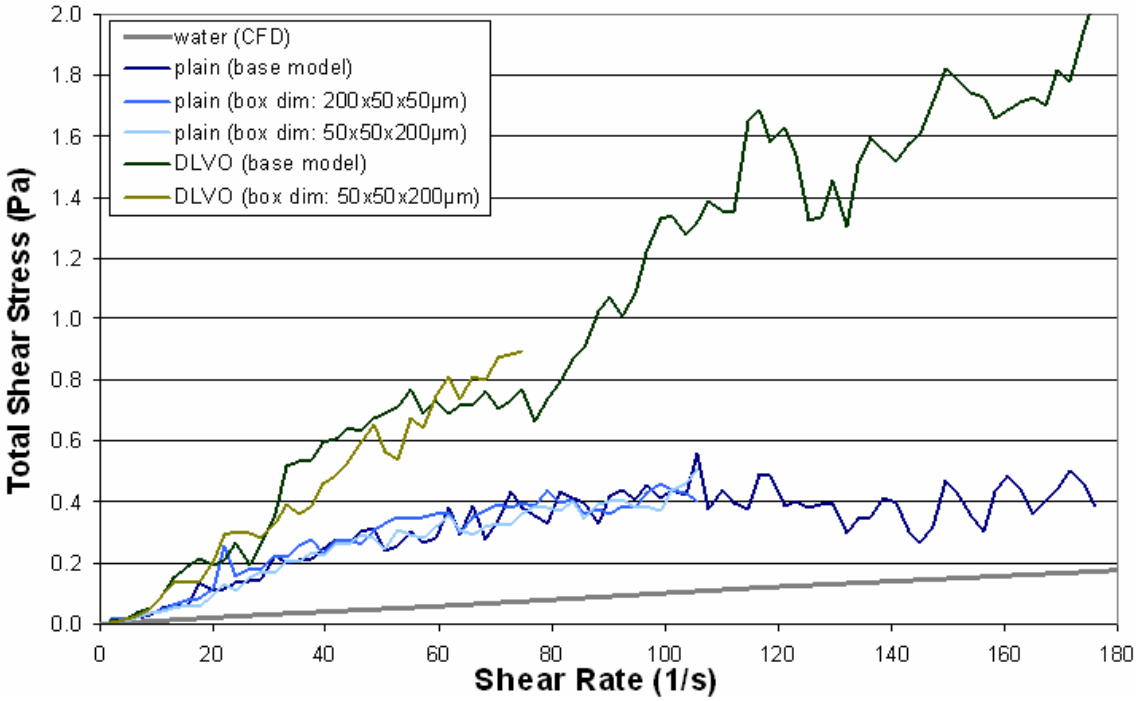

Figure 6.13: Shear stress vs. shear rate comparing increases of the geometry size in the x and z directions (dimensions given as XxYxZ)

6.7.2. Gap Width Dimension for Original Ramp Rate

Discussions here will revolve mainly around particles with DLVO force, but the trends for plain particles were similar. Figure 6.14 compares the total viscosity values for gap widths larger than the base model. The ramp rate was kept the same as before. A larger time step was also used for the 500µm case so that a useful shear rate could be reached within a reasonable time (three weeks). It was clear that the larger gaps produce a large increase in viscosity. The curve for the 200µm gap showed that particles migrated at about a shear rate of $50s^{-1}$. This is related to the issued with the ramp rate as discussed in the previous section. The 500µm gap (with the 2.5e-9s DEM time step) had not reached that point yet due to the long simulation time. The 500µm gap with the larger DEM time step (2.5e-8s) had a larger time step/ramp rate combination, and so did not experience particle migration problem.

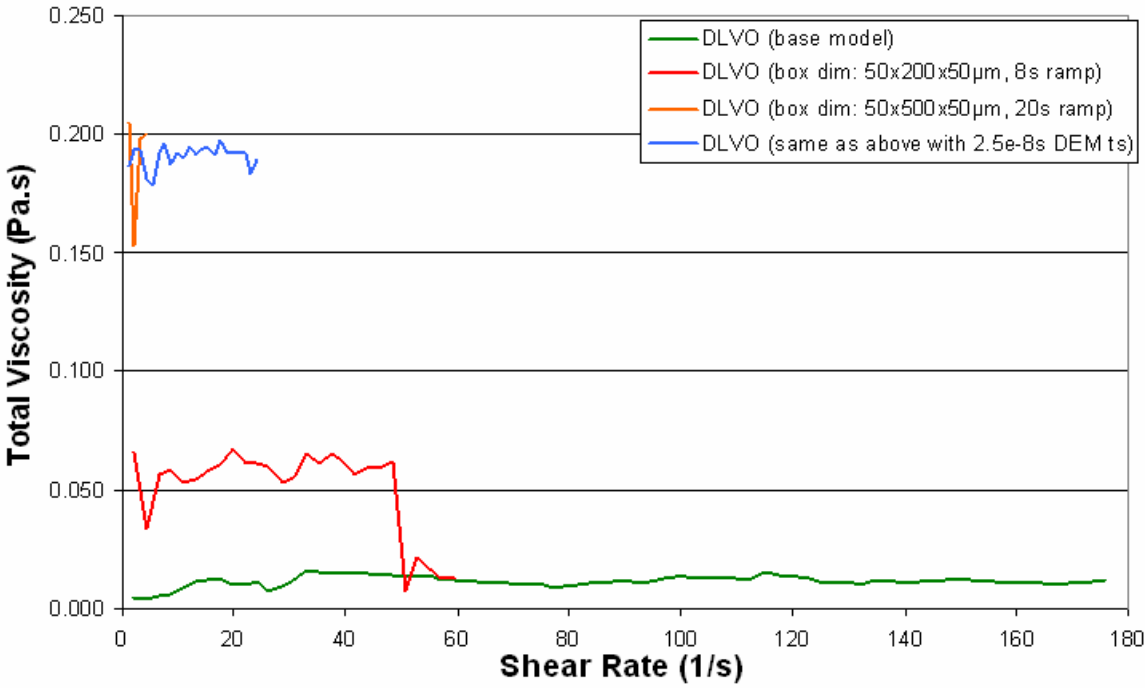

Figure 6.14: Total viscosity vs. shear rate for different gap width sizes (particles with DLVO forces)

In terms of the trends produced here, these larger gap widths produce larger, more realistic viscosity values. However, these values seemed to be very gap dependent. Upon investigating this trend, the reason became clear when the CFD component of the wall force (the major contributor to shear stress) was plotted against wall velocity (Figure

6.15). The CFD force remained essentially the same for all gap widths (only a slight increase with the gap width) as the wall velocity increased. This makes sense as the same mesh and particle parameters were used in the wall region. However, the shear rate, which was calculated from the gap width, reduced dramatically. Viscosity, which is just shear stress divided by the shear rate, thus increased dramatically due to the increased gap width. Hence, the shear rate (via the gap width) becomes a type of scaling factor. Thus, while the viscosity values changed significantly, the wider gap did not affect the actual flow in the near-wall region very much. Possible explanations for this scaling effect are explored in Section 7.1.1 in relation to the flow velocity profile across the gap.

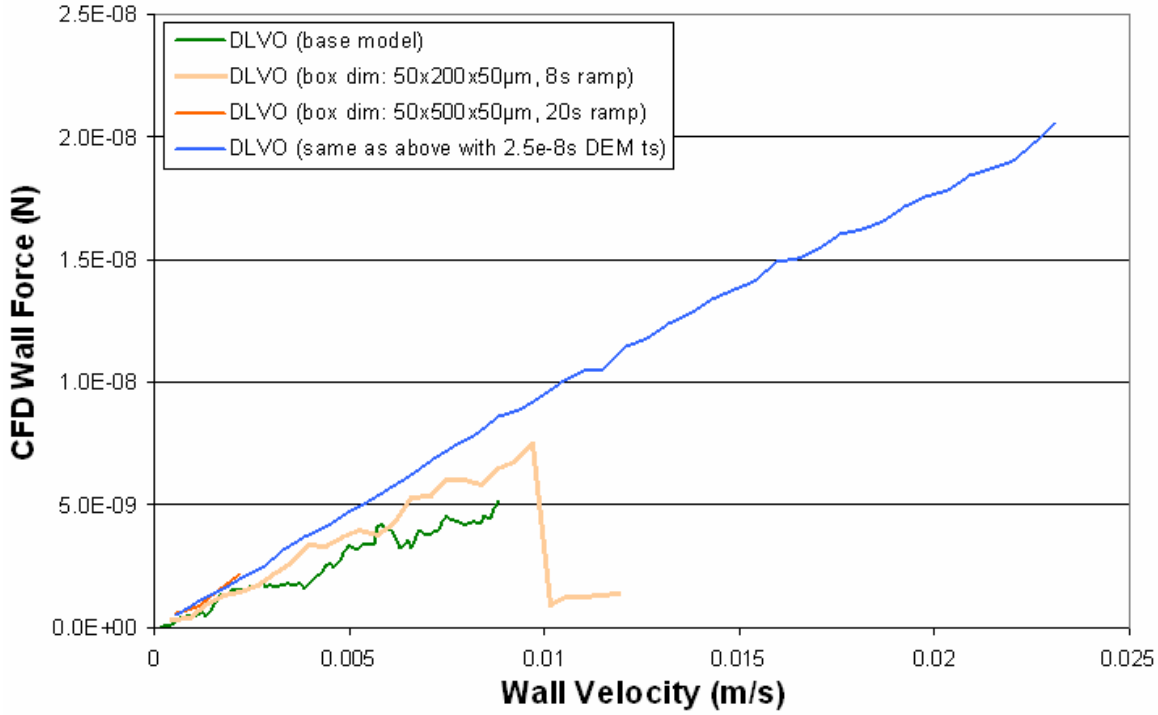

Figure 6.15: Fluid viscous force at the wall vs. wall velocity to illustrate the fluid force that contributes to shear stress calculation (particles with DLVO forces)

6.7.3. Results for Shorter 2s Ramp Rate

A shortened ramp rate was used to determine if the slower ramp rate or the wider gap width had the over-riding effect on the results. The ramp rate was adjusted (sped up) for the different gap widths to make sure the shear rate reached $176s^{-1}$ at two seconds of simulation time. On the surface, this was expected to make the simulation less realistic, as the physics would be sped up as well. However, fairly realistic behaviour was

produced by the 200µm and 500µm gap widths (with DLVO forces). Plain particles performed satisfactorily as well. Figure 6.16 shows how the 200µm gap produced a sizeable initial viscosity followed by a shear-thinning trend as the shear rate increased. The initial viscosity rose quickly from the start. The slope of the curve indicated a zero viscosity at zero shear rates, which implied no yield stress.

The 500µm gap width shows similar behaviour at low shear rates, though the viscosity values are roughly 2.5 times larger. For these models of the 500µm gap width, the DEM time step was ten times larger than for the 200µm case. Different coupling intervals were tried with the 500µm models. An interval of 25, showed relatively stable behaviour, with a clear shear-thinning trend. However, larger coupling intervals did not show a shear thinning trend and followed the trend shown in Figure 6.16 for the interval of 50. A coupling interval of 100 performed similarly, until it became unstable half way through the shear rate range and crashed suddenly. Larger time step and coupling interval combinations were also unstable. This shear-thinning trend was related to the particle volume fraction in the cell layer against the wall. At the point where the shear-thinning became evident, the number of particles in the cell layer had reduced to virtually nothing.

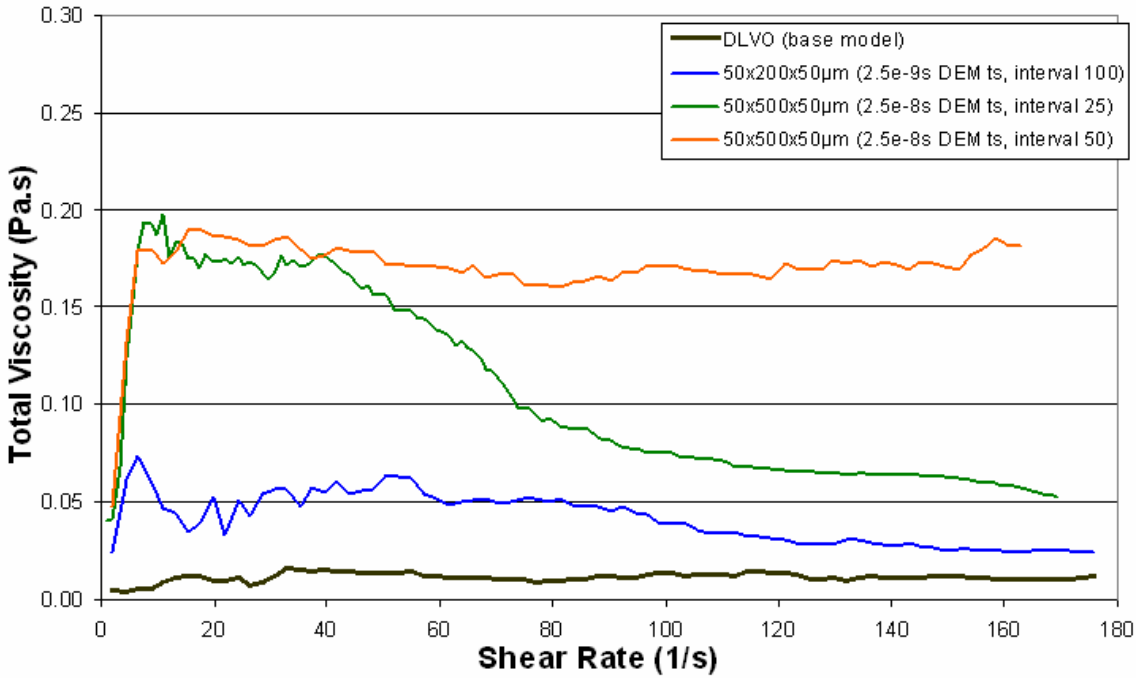

Figure 6.16: Total viscosity vs. shear rate for larger gap widths with the shortened 2s ramp rate (particles with DLVO forces)

When comparing the performance of the different ramp rates (Figure 6.17), the difference at low shear rates becomes noticeable. Typically, simulations using the fast 2s ramp rate show a large, very sudden, increase in viscosity up to about $6s^{-1}$. This implied there was no yield stress. However, simulations with the longer ramp rate produce higher values, with a more level trend. This seemed to indicate some sort of "yield stress". These trends were in line with those observed during the ramp rate tests.

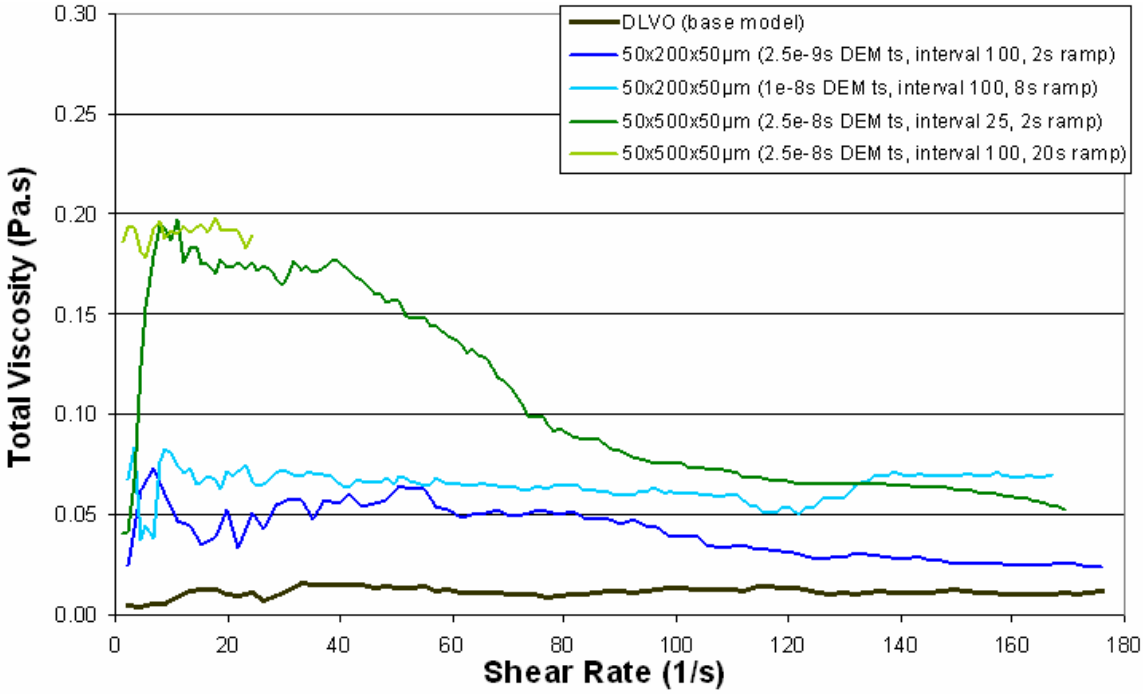

Figure 6.17: Total viscosity vs. shear rate for larger gap widths with different ramp rates (particles with DLVO forces)

6.7.4. Total Simulation Time

From the performance of these curves, it appears that using larger time steps to increase the calculation speed of the larger models can produce reasonable results. Also, the ramp rate can be fast (2s ramp rate), while still producing reasonable results. Though even for the larger gap widths, the time steps must be small enough to keep the simulation stable (e.g. 2.5e-8s with a coupling interval of 25, and the original shear rate). Shortened ramp rates also allowed for shorter computational times, as the simulations did not have to run for as long (e.g. 2s vs. 8s for the 200µm gap). Thus, larger models can be run in a similar timeframe to smaller geometries.

6.7.5. Divergence of Results

It should be noted that for the wider gaps, with larger time steps and 2s ramp rates, divergence of the results occurred when one of the runs was repeated (500µm gap, 2.5e-8s DEM time step). In other words, for the same set up (including particle initialisation), different shear stress curves were produced. They were statistically similar, in that produced similar magnitude values, and similar trends, but the values were not exactly the same. This can be the case for DEM-related models (LIGGGHTS manual, 2013). The cause of the divergence might be linked to the larger time step sizes, where collision or DLVO energy was resolved less accurately.

6.8. HARDWARE REQUIREMENTS AND SOLVER TIME

Most of the simulations presented in this chapter were run on 12-core nodes (CPUs) of various cluster computers. While most nodes available to the author only had 12 cores, it was found that the 20% volume fraction simulations (with 14 147 DEM particles) could benefit from running on more than 12 cores. However, the speed increase was usually cancelled by the loss due to inter-node communication on the cluster network. DEM scales well with the number of cores, whereas the small size of the CFD component meant it would run faster on a single core. Therefore, in the beginning of the simulations, it was better to run on fewer cores. Though as the simulation progressed, and the DEM component became more dominant, more cores were faster. Models for the larger domain sizes were typically run on 24 cores for the 200µm gap width, or 48 cores for the 500µm gap. Larger volume fraction simulations (c.f. Section 7.2) of 30 and 40% solids volume fraction (with 21 221 and 28 294 particles respectively) were run using 24 cores

Compute nodes had a processing speed of 2.2 – 2.9 GHz. Memory (RAM) requirements were not an issue as most simulation only required a couple of GB of memory, and compute nodes typically had much more memory than was required. Though more cache memory did significantly improve compute times. Table 6.1 gives an indication of how long it took to complete the respective simulations with the typical number of CPUs used to complete a simulation of that size. Simulation times are given as if they were completed on the 2.9GHz machine.

Table 6.1: Typical time taken (in days) for 20% volume fraction simulations to complete

Model Description	Typical number of CPU cores used	Plain (d)	DLVO (d)
Base model	12	14	19
DEM time step 2.5e-9s, coupling interval of 500	12	5	17
DEM time step 1e-8s, coupling interval 100	12	2.5	5
DEM time step 1e-8s, coupling interval of 25	12	6	8
200μm gap, DEM time step 2.5e-9s, coupling interval 100, ramp rate 8s	24	150	230
Same as above, but for 2s ramp rate	24	45.5	67
500μm gap, DEM time step 25e-8s, coupling interval of 25, ramp rate 2s	48	14	17

6.9. SUMMARY OF FINDINGS FOR CFD-DEM MODEL PARAMETERS

The parameters investigated in this chapter determine the accuracy and performance of the coupled CFD-DEM model. Important findings are summarised here.

6.9.1. Mesh Density

The results were largely insensitive to changes in the CFD mesh density. Even changing the mesh density at the wall had little effect on the results. CFD cell dimensions of 3-4 particles diameters were found to be acceptable.

6.9.2. Start Procedure

Initially, the system (both fluid and particles) was started from rest. Variations to this starting arrangement were also tested. However, they did not make any significant difference to the initial response of the system. Thus starting the system from rest was found to be acceptable.

6.9.3. Time Step Size

For a set coupling interval of 100, the two DEM time steps of 2.5e-9s and 5e-9s were found to be acceptable. The 1e-8s DEM time step showed a few instabilities for plain particles, but was adequately stable for particles with DLVO forces. The largest time step of 2.5e-8s for plain particles was far too unstable to be used. It performed adequately for particles with DLVO forces, though produced higher viscosity values than the other combinations across the whole shear rate range. Higher time steps sizes tend to show largely constant viscosity values, with no shear-thinning trend.

A DEM time step size of 1.25e-9s (with a corresponding CFD time step of 1.25e-7s) was found to cause particles to migrate away from the moving wall. This occurred for both plain particles and particles with DLVO forces.

6.9.4. Coupling Interval

For the base DEM time step of 2.5e-9s, coupling intervals of 100 and 200 were found to be acceptable. For plain particles, an interval of 500 was far too unstable. However, for particles with DLVO forces, the interval of 500 was stable, but produced viscosity values slightly higher than the other combinations. For an interval of 50 (corresponding to a CFD time step of 1.25e-7s), the particle migration phenomenon appeared again.

An interval of 100 was found to be the most reliable option. However, for time step sizes larger than the base size, smaller coupling intervals of around 25 also provided good results. The bigger the increase in time step, the smaller the interval should be. For the 50μm box with the 2s ramp rate, the resulting CFD time step size must be greater than or equal to 2.5e-7s to prevent particle migration.

6.9.5. Wall Velocity Ramp Rate

Slower ramp rates produced higher viscosities at low shear rates ($<35s^{-1}$), especially for larger DEM time step sizes. However, for low CFD time step sizes, these slower ramp rates exhibited the particle migration phenomenon. Therefore larger CFD time step sizes should be used for these slower ramp rates, but this can potentially introduce other instabilities due to the larger time steps. There was not much improvement over the base

2s ramp rate for shear rates above $40s^{-1}$. Therefore the 2s ramp rate was thought to be acceptable for all cases.

6.9.6. Domain Size

Increasing the domain size in either the vertical or flow directions did not affect the results. However, the results were found to be gap-width dependent, as increasing the gap width greatly increased the resulting viscosity values. Using the 2s ramp rate for the larger gap widths produced results comparable to the slower ramp rates, but was obviously much quicker to compute. Combining slow ramp rates and small time steps led to particles migrating away from the walls. Large time steps (~2.5e-8s) could be used to improve the speed of calculation, but then small coupling intervals (~25) were needed for stability and to produce a shear-thinning trend.

7. RHEOLOGICAL SIMULATIONS USING THE CFD-DEM COUPLED MODEL

Once a suitable range for model parameters had been established, the model was used to test some important influences on particle suspension rheology. These tests were conducted to demonstrate the model was capable of producing similar rheological trends as seen in experimental work. In particular, the effect of solids volume concentration and surface charge (DLVO potential) were investigated. Section 7.1 examines the fluid velocity profile across the gap between the two walls to show model produces realistic flow behaviour. Section 7.2 investigates the behaviour of the model for particle volume fractions up to 40%. Section 7.3 explores the influence of different surface charges (DLVO potentials) on the suspension rheology. Section 7.4 compares the coupled model against the experimental data of Megías-Alguacil et al. (2000). Section 7.5 summarises the important findings from this chapter.

7.1. FLOW PROFILES ACROSS THE GAP WIDTH

The particle force contributions are roughly one order of magnitude smaller than the corresponding fluid force, thus the major contributor to the viscosity behaviour was actually the fluid force component. To further investigate the nature of the flow between the two solid walls, the fluid velocity was calculated at different locations across the gap. The velocity values in the graphs were plotted at their corresponding position in the gap (cell centres). Each value shown was averaged over the respective CFD cell layer at that position (there were 12 cell layers across the 50μm gap, therefore 12 values are plotted).

7.1.1. Fluid Velocity Profiles for the Baseline Model

Figure 7.1 and Figure 7.2 show the fluid velocities across the gap (in the direction of the flow) for plain particles and particles with DLVO forces respectively. In the figures, the x-axis represents the position across the gap (for a 50μm box), and the y-axis represents the velocity in the x-direction. Wall velocity was defined to be in the negative x-direction, thus the flow was typically in the negative direction. Velocity values along the

y-axis are the moving-wall velocities at those times. Flow was zero at the stationary wall (y = 50μm). Overlaid on these graphs are fluid velocities for a plain water simulation.

Plain Particles

Water produced a typical Newtonian profile of a straight line from the velocity of the moving wall on the left, to zero velocity at the right wall (shown by the dashed lines in Figure 7.1). Plain particles follow a similar trend, though there was some lag in the fluid velocities. This was most likely due to the heavier particles in the fluid resisting the flow. The fluid closer to the moving wall sped up much quicker than the fluid farther into the gap, particularly near the stationary wall. However, as time went on, the flow velocities of the mixture eventually increased, tending to that of plain water. Velocity plots give an indication of the shear gradient in the flow, which ultimately determines the shear stress in the fluid. These plots show that plain-particle suspensions have low viscosity/shear stresses because they flow quite easily.

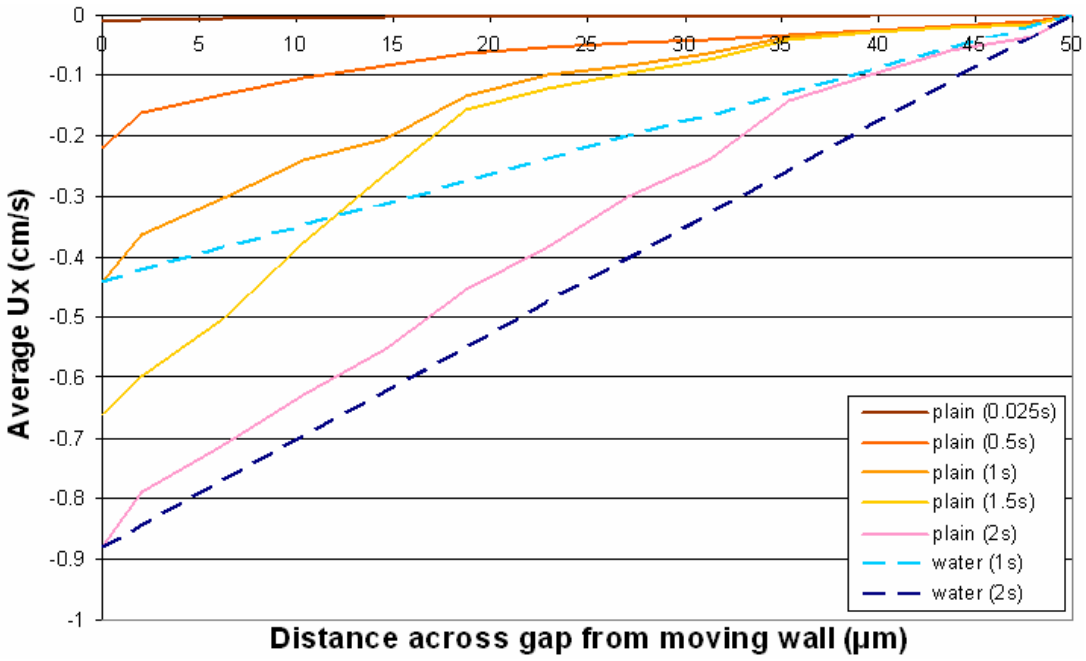

Figure 7.1: Fluid velocity profiles across the gap for the base model of 20% particle volume fraction (plain particles)

Particles with DLVO Forces

Suspensions with DLVO forces between particles produced very different behaviour (cf. Figure 7.2). There were narrow regions of high shear at the walls, while the bulk flow in

the centre had not sheared at all, indicating some sort of plug flow in the centre region. Physically this is plausible, as the overall DLVO force used in the base model was very attractive, so the particles would have most likely aggregated and prevented the adjacent particle (and fluid) layers from moving past one another. This velocity profile is very different from the linear profile expected of Couette flow (e.g. the dashed lines for water in Figure 7.2), which is normally assumed to occur in the rheometer gap. While this assumption works well for homogenous fluids, particle suspensions are not strictly homogenous, as local particle concentration can vary. Thus suspensions may not always experience Couette flow with a linear flow profile.

The plug flow seen here was formed very early on in the simulation (about 0.15s). Only the magnitude varied after that point. Due to the plug flow, the fluid velocity in the bulk near the moving wall was lower than would be expected with plain water (dashed lines in Figure 7.2). In addition, the plug flow caused the fluid near the stationary wall to flow faster than expected. This led to much higher shear at both walls. Higher shear at the moving wall resulted in higher measured viscosities for particles with DLVO forces.

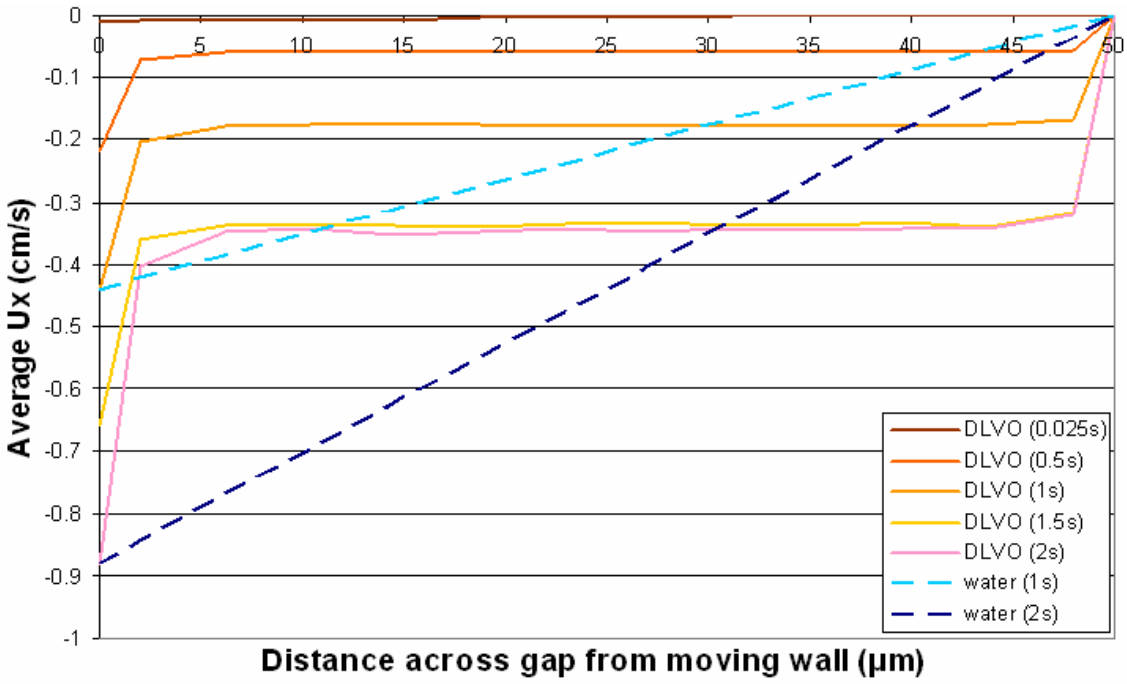

Figure 7.2: Fluid velocity profiles across the gap for the base model of 20% particle volume fraction (with DLVO forces)

The width of the plug appeared to reduce slightly over time as the sheared portion of the mixture extended farther into the bulk. This implies the bulk in the centre would eventually be brought up to speed with the rest of the fluid, and the plug would disappear, resulting in a more linear profile. As the sheared region grows in size, the shear gradient of the fluid next to the wall would decrease in intensity over time. This would produce the shear-thinning behaviour expected of particulate suspensions.

Explanations for the Flow Velocity Pattern

Both Barnes (1995) and Manneville et al (2004) explain that in non-homogenous mixtures (like suspensions) these types of "s-shaped" profiles can arise from wall slip between the particles in suspension and the solid walls. This idea is supported by Gibaud et al. (2009) and Kim (2009) who have also produced these s-shaped velocity profiles for cylindrical Couette flow (cf. Figure 7.3). Wall slip occurs due to the displacement of the dispersed phase away from the solid boundaries (Barnes, 1995). This creates a thin layer of the continuous phase against the wall. The typically lower viscosity of the continuous phase allows for easier flow over the boundary wall, thus resulting in higher shear gradients. Both Barnes (1995) and Buscall et al. (1993) expect there to be less slip at the outer, stationary wall. This behaviour can be found in Figure 7.2, where the velocity gradient at the stationary wall (right-hand side of the figure) is much smaller than at the moving wall (left-hand side). Mewis and Wagner (2011), note that slip is an adhesive failure that depends on both the suspension and the tool geometry, as well as the construction material. Alternatively, shear-banding is a cohesive failure of the material with itself, and is therefore a property of the material.

One way that slip can manifest itself is that the apparent viscosity measured in different size geometries can give different results when calculated in the conventional way. In particular, the viscosity decreases with decreasing geometry size (Barnes, 1995). This can explain the scaling effect of the gap width seen in Section 6.7.

The "s-shaped" profiles seen in Figure 7.2 have also been found by other researchers. For example, Naser (1997) and Bech et al. (1995) studied Couette and Poiseuille flow of non-Newtonian fluids using both experimental methods and CFD. They attributed these

velocity profiles to turbulence generated in the near-wall region. However, they assumed the fluid was a single-phase, homogenous fluid, which is not strictly true for suspensions.

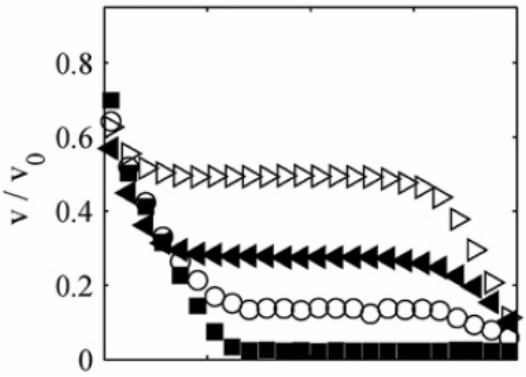

Figure 7.3: Gap velocity profiles of laponite suspension showing evolution of profile over time ($1< t <302$s, $\dot{\gamma} = 110s^{-1}$). Velocity values are scaled by the rotor velocity, v_0 (Gibaud et al., 2009)

Plug flow is often found with yield stress fluids in wall-bounded flows. An example of which is a Bingham plastic fluid in pipe flow, as shown in Figure 7.4. The profile of Figure 7.2 follows the same trend near the stationary wall, where the flow was faster than the wall speed. The profile becomes inverted at the moving wall, as the wall was moving faster than the fluid. However, the graphs shown in Chapter 6 do not show evidence of a yield stress. So this information only partially explains the behaviour seen here.

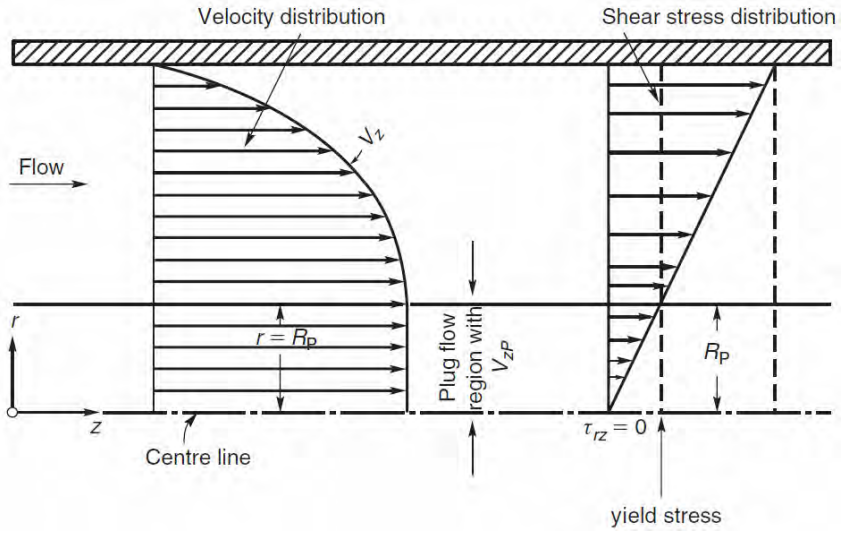

Figure 7.4: Velocity and shear stress profiles for laminar flow of a Bingham plastic fluid in a pipe (adapted from Chhabra and Richardson, 2008)

For shear-thinning liquids and mixtures with high solids concentration, slip can be a very real problem (Nguyen and Boger, 1983; Barnes, 1995). To eliminate slip, wall surfaces of concentric-cylinder rheometers are sometimes physically altered by roughening or profiling. An extreme case of this is the vane-in-cup type geometry, where a multi-bladed vane is used in place of the inner cylinder (Nguyen and Boger, 1983; Barnes and Nguyen, 2001). This type of geometry offers minimal surface area over which slip can occur. Thus vane geometries are often used for suspensions with high solids content.

7.1.2. Fluid Velocity Profiles for Longer Ramp Rate

Figure 7.5 shows velocity plots at different time intervals of the eight second ramp rate (for particles with DLVO forces). The final time corresponds to a shear rate of $176s^{-1}$. Similar trends to those of the base DLVO model were found (cf. Figure 7.2). The width of the plug flow region was seen to reduce slightly with time, as the region of sheared fluid expanded into the gap. Given a sufficient amount of time, the profile would tend towards a more linear shape. But, because the velocity profile shape did not change much over the eight seconds simulated here, it could be assumed the overall shape of the profile would not change drastically over the short time-frames considered in this work. This showed that the shorter, two-second ramp rate was acceptable because similar profiles were produced with longer ramp rates.

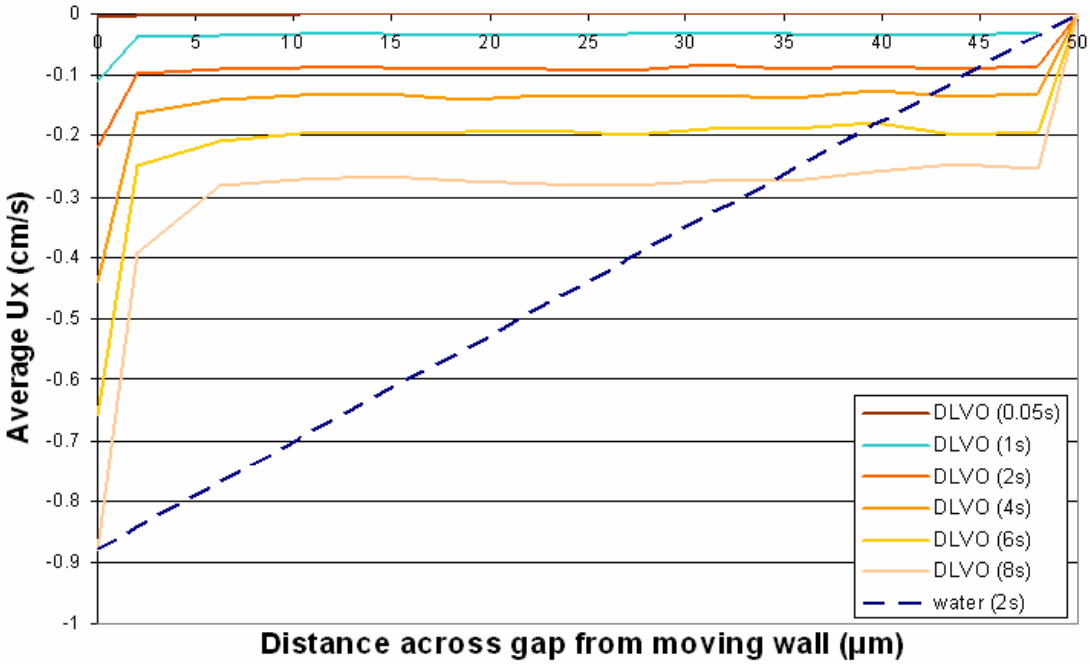

Figure 7.5: Gap velocity plots for eight second ramp rate (with DLVO forces)

7.1.3. Fluid Velocity Profiles for Larger Gap Widths

Larger gap widths produced similar velocity profiles to the 50µm case with DLVO forces. Figure 7.6 shows the fluid velocity in the gap for the 200µm gap width for a two second ramp rate (DLVO forces included). Velocities are compared against that for plain water (in the same geometry, at the final shear rate). Plug flow was again visible and found to stretch across almost the entire width of the gap, except for two to three cell layers in from the walls. Plain particles also showed evidence of plug flow in the majority of the domain, though there was a much more gradual change in fluid velocity near the moving wall when compared to the models that included DLVO forces.

Because plug flow was still prevalent in much of the domain, the shear gradient at the wall had a similar profile to the 50µm model (high gradient, over a narrow distance). Thus the measured force at the wall changed little, but the shear rate reduced drastically (as it was calculated based on the gap width). This caused the measured viscosity to become gap-dependent. As discussed in Section 7.1.1, this phenomenon was most likely the result of wall slip.

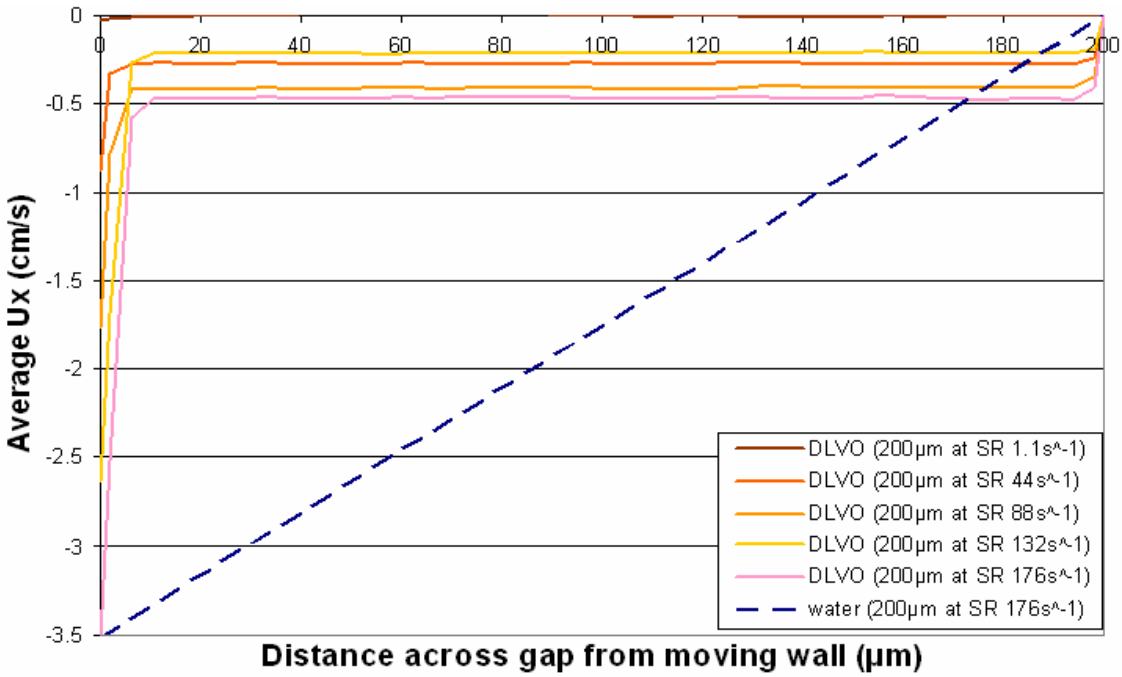

Figure 7.6: Fluid velocity in the gap at different shear rates for 200µm wide gap with DLVO particles and a two second ramp rate

7.2. PARTICLE VOLUME FRACTION

Rheology is greatly affected by the solids volume concentration. Therefore the model was tested for particle volume fractions up to 40%. This section demonstrates that the model predicts an increasing rheological complexity with increasing volume fraction, as found in numerous experimental studies (e.g. Barnes, 1999; Ndlovu, 2011).

7.2.1. Discussion of Rheograms

Trend lines have been plotted for the different data sets to better illustrate their general behaviour. Original data for the 20% volume fraction (black line) have also been included for comparison with their respective trend lines.

Plain particles

Figure 7.7 shows the resulting shear stress for plain particles at different volume fractions. There is a steady increase in shear stress with volume fraction. However, the size of the increase reduces as the volume fraction increases. The curve for 4.58% volume fraction showed little difference to that of water (with no particles), and so was not plotted. At low shear rates, the shear stress values were much higher for the larger volume fractions. All curves showed some amount of shear-thinning at higher shear rates. In all cases, there was no evidence of a yield stress. But this was unlikely to occur for plain particles, which had no attractive forces between them. Other reasons for the lack of yield stress are discussed in Section 6.1.

Particles with DLVO Forces

The DLVO force used here had a zeta potential of 0mV. This meant the force between the particles was very attractive, with no repulsion. Results for the different volume fractions are given in Figure 7.8. The addition of this DLVO force made the simulations unstable when compared to the plain particles, with less noticeable trends. However, increasing the particle volume fraction did generally increase the resulting shear stress. Also, as expected, the addition of DLVO forces increased the magnitude of the measured shear stress when compared to the plain particles in Figure 7.7. Using a less attractive DLVO potential improved the stability of the simulations (e.g. 32.5mV zeta potential). Again, no evidence of a yield stress was found.

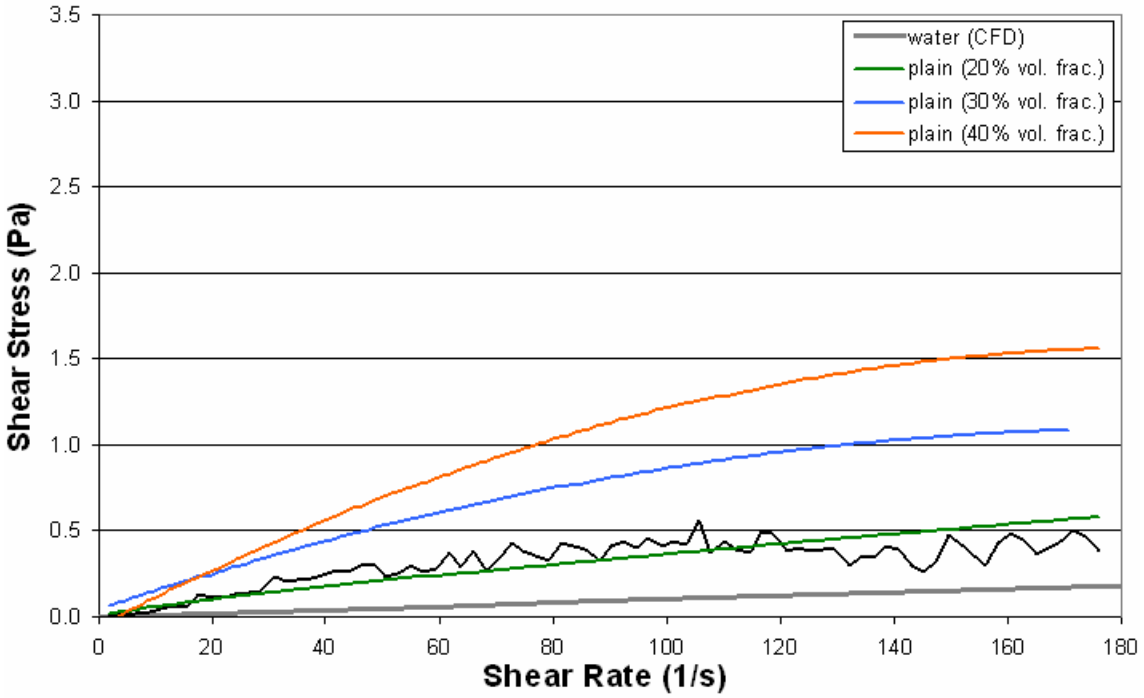

Figure 7.7: Shear stress vs. shear rate for different volume fractions (plain particles)

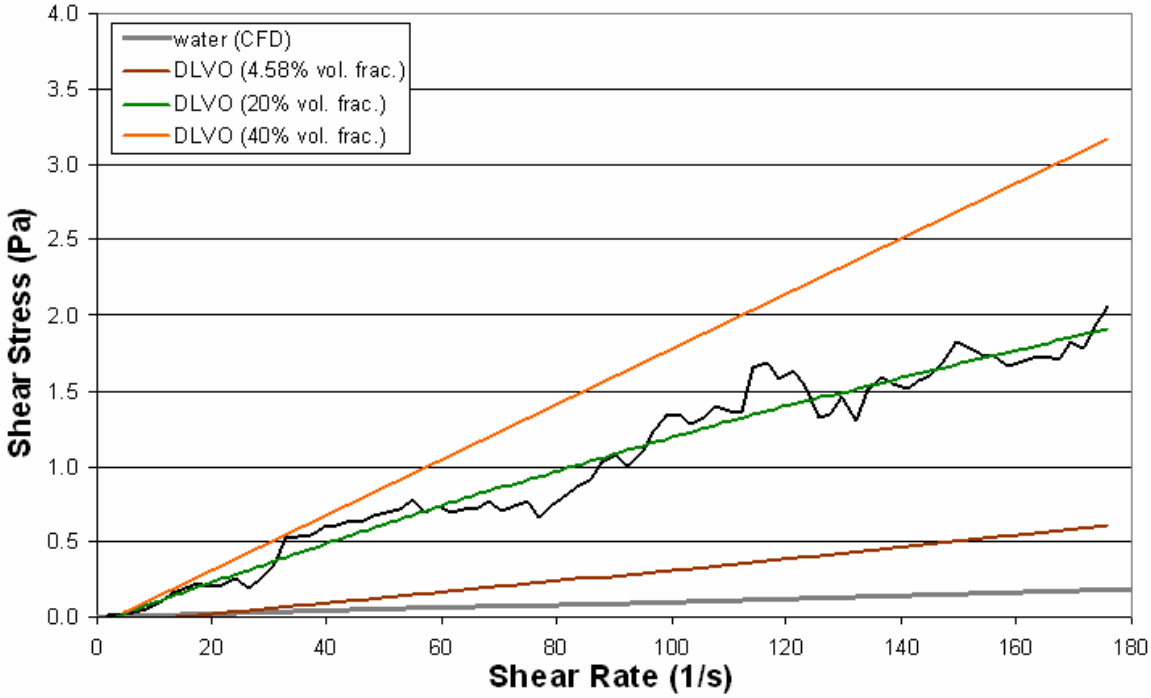

Figure 7.8: Shear stress vs. shear rate for different volume fractions (with DLVO forces)

7.2.2. Velocity Profiles across the Gap

Velocity plots are not shown here because the profile shapes were the same as for the 20% volume fraction models shown in Section 7.1.1. The magnitude of the bulk flow

velocity was also very similar for all these cases. For particles with DLVO forces, there was plug-like flow of the bulk mixture, with high shear in the cell layer against the wall. Plain particles produced similar profiles to those in Figure 7.1 for low volume fractions. However, as the volume fraction was increased above 20%, the profile tended more towards the profile exhibited by particles with DLVO forces (i.e. high shear in the first cell layer, with relatively constant fluid velocity in the bulk, cf. Figure 7.2).

7.3. PARTICLE SURFACE CHARGE

The attractive or repulsive nature of the DLVO forces between particles is affected by the particle surface charge. Thus the surface charge was altered to test the model's response to long-range inter-particle forces. This section shows that the model reacts appropriately to changes in surface charge (e.g. Johnson et al., 2000; Leong and Ong, 2003). A particle volume fraction of 20% was used here.

The base DLVO potential was generated from a zeta potential of 32.5mV (data for which was provided in Megías-Alguacil et al., 2000). Other potentials were chosen either side of the value to give a mix of responses. The extreme case of 0mV was also tested. For this potential, the (repulsive) electrostatic force component was no longer acting, which meant the DLVO potential was dominated by the (attractive) van der Waals interaction only. The different potentials, and their resulting forces, are plotted against particle separation distance in Figure 7.9 and Figure 7.10 respectively. Values in Figure 7.9 are non-dimensionalised by dividing the energy potential by k_B and T, where k_B is the Boltzmann constant, and T is the temperature.

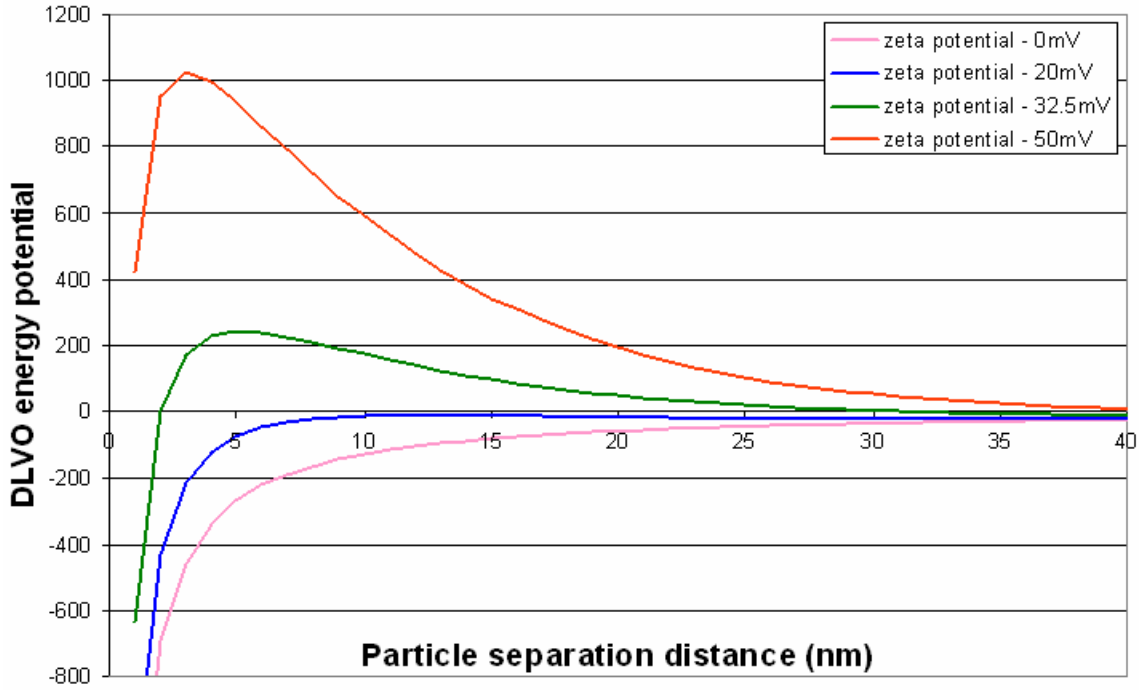

Figure 7.9: Graph showing the different DLVO potentials used (based on zeta potentials) as they change with separation distance (values non-dimensionalised by dividing through by $k_B.T$)

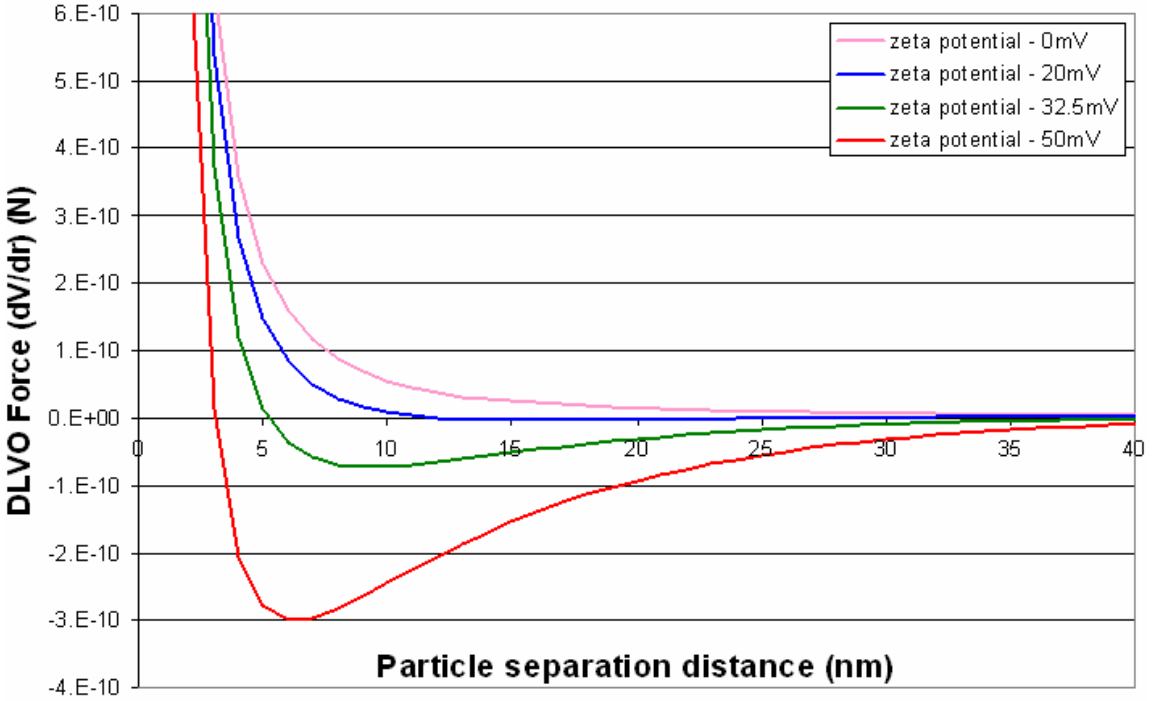

Figure 7.10: Graph of corresponding DLVO forces vs. separation distance for the potentials shown in Figure 7.9

7.3.1. Discussion of Rheograms

Figure 7.11 illustrates how the shear stress changes with the different DLVO potentials. Again, trend lines have been plotted for all the data sets, with original data only being shown for the 32.5mV potential. Lower zeta potentials for the zirconia particles imply a more positive DLVO energy potential, which means the attraction forces dominate. This is visualised in Figure 7.11 as the corresponding curves (0mV and 20mV) show much higher shear stress values. This was expected as the particles would tend to agglomerate and have a large effect on the fluid. These two curves also show a slight shear-thinning trend at higher shear rates. This is physically realistic as particle agglomerates would be broken up at higher shear rates, improving the flow and so reducing the measured viscosity (Barnes, 2000).

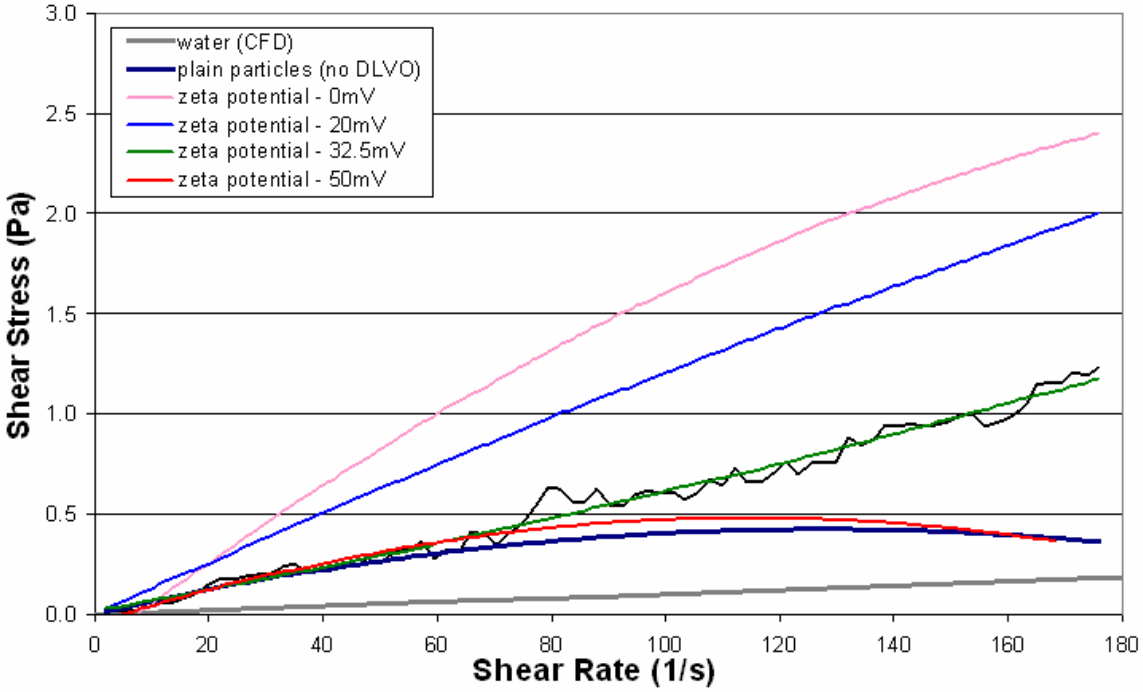

Figure 7.11: Shear stress vs. shear rate for different DLVO potentials

Alternatively, for the higher zeta potentials (32.5 and 50mV), one would expect to see a more repulsive interaction force. This was evident from the lower shear stress values. The fluid flows more freely because particles do not agglomerate as easily (discussed further in the following section). Another observation was that plain particles, with no DLVO forces, were equivalent to having a more repulsive interaction force (e.g. 50mV). This was because the particles had no driving mechanism that could make them agglomerate.

7.3.2. Velocity Profiles across the Gap

Figure 7.12 illustrates the differences in the fluid velocities across the gap for the different DLVO potentials. Only the profiles for the final solution time (2s) are shown. Both the 0mV and the 20mV cases indicated plug flow in the gap. This was expected as the two potentials were more attractive and so the particle body would move as one unit. The two repulsive potentials (32.5mV and 50mV) also showed some plug flow, but much less than for the other two potentials. This was because the sheared portion of the fluid extended farther into the fluid, which was possible because the particles were not held together as tightly by the less attractive DLVO force. The larger region of sheared fluid produced a much lower shear gradient at the moving wall, resulting in the lower measured shear stresses.

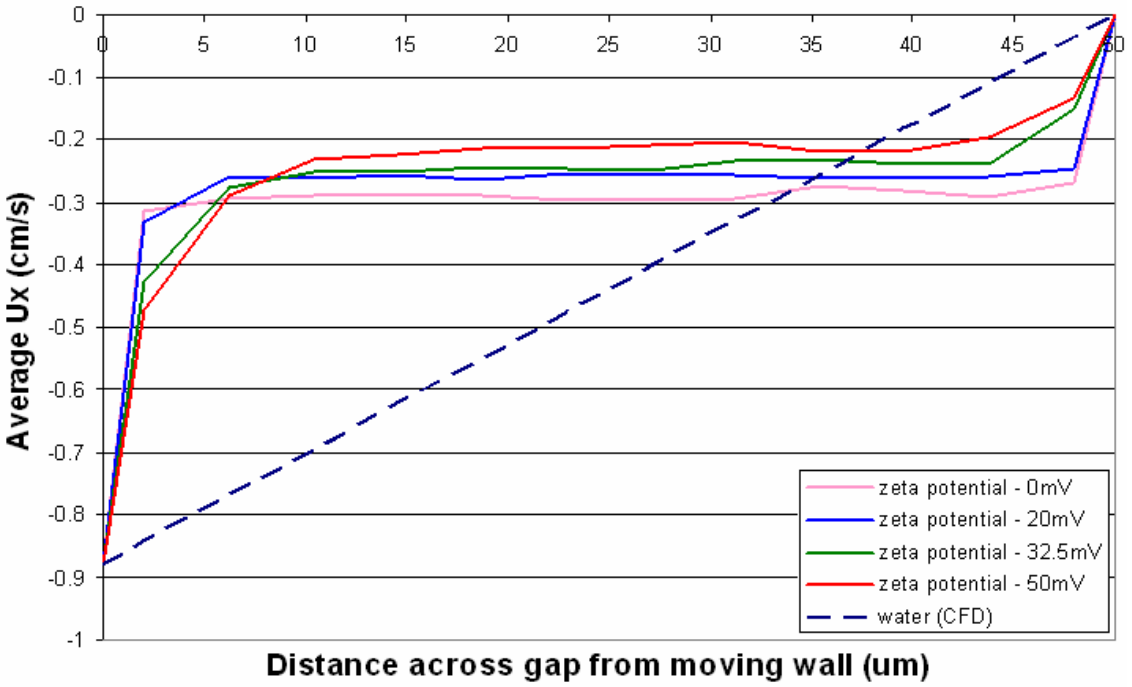

Figure 7.12: Fluid velocity profiles across the gap for each of the different DLVO potentials at the end of the simulation time (2s)

While not shown in the trend line in Figure 7.11, for the case of the 50mV DLVO potential there was a marked change in shear stress at $70s^{-1}$. This change was observed in the fluid velocity profile shown in Figure 7.13. Initially, the velocities indicated a relatively linear behaviour, like that of plain particles. This was expected as this potential was fairly repulsive. However, after a certain time, the velocity profile changed to a more

plug-flow type of profile, indicating that the particles had agglomerated. Closely-packed clusters of particles can be seen when viewing the 3D particle distribution, thereby confirming this idea (not easily shown here in 2D). This shows how the flow behaviour within the gap influences the measured shear stress, and the overall rheology of the suspension.

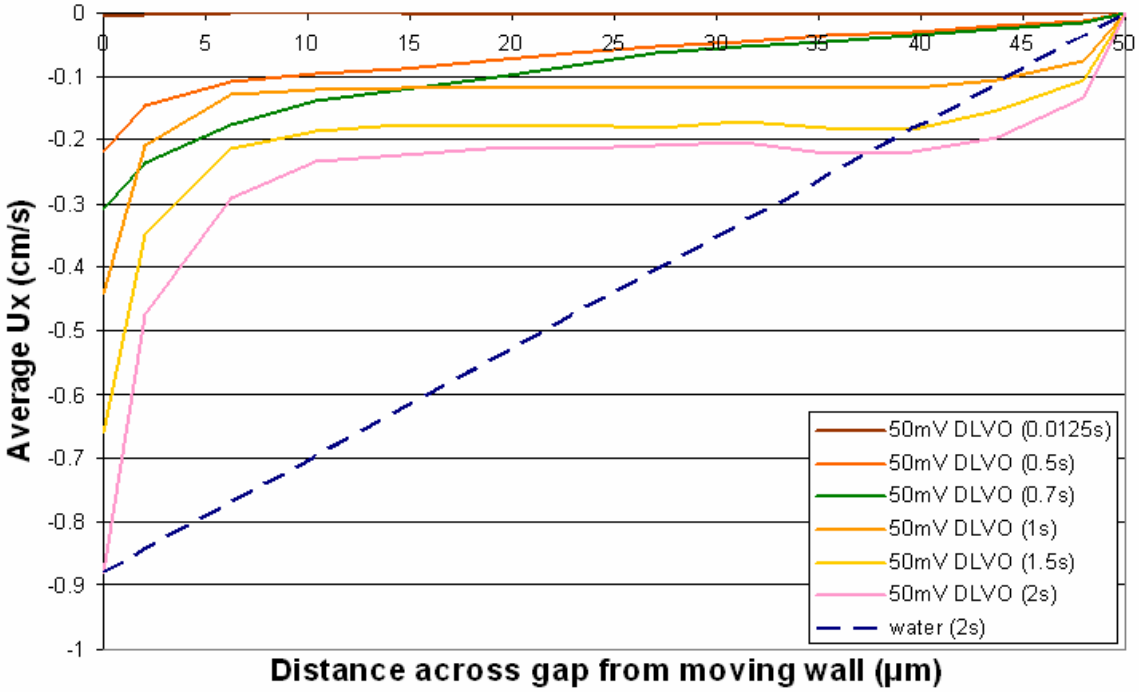

Figure 7.13: Fluid velocity profiles across the gap for the 50mV DLVO potential showing how velocity changes over time

7.4. COMPARISON WITH EXPERIMENTAL DATA

The primary aim of this work was to develop a methodology for the creation of a numerical model for the study of suspension rheology. To the author's knowledge, this was the first time a coupled CFD-DEM model was used to study rheology. In the process of developing this model, it was shown to produce correct trends for varying volume fraction and particle surface charge. This section compares the trends and magnitude of the coupled model results against the experimental data of Megías-Alguacil et al. (2000) for spherical zirconia particles. Full quantitative validation of this model would be encouraging, but was not expected for an initial investigation such as this.

Figure 7.14 shows experimental data for the 4.58 and 21.75% volume fractions. Results for the 20% volume fraction coupled model at two different gap widths are shown for comparison. As can be seen at higher shear rates, the curves show similar shear-thinning trends. However, the coupled model's results are much lower than the experimental data. It was expected that the model values be slightly lower than the experimental data due to slightly smaller particle sizes, and a slightly lower volume fraction (for the 20% case). However, the resulting discrepancy between the sets of 20% volume fraction data was still quite large for the 50µm base model. A better agreement was achieved with the 500µm model, which was the same gap width used by Megías-Alguacil et al. (2000). This clearly illustrated the gap-dependent nature of the coupled model results as observed in Section 6.7. Nonetheless, achieving results of the same order of magnitude as the experimental work from a preliminary model such as this is encouraging.

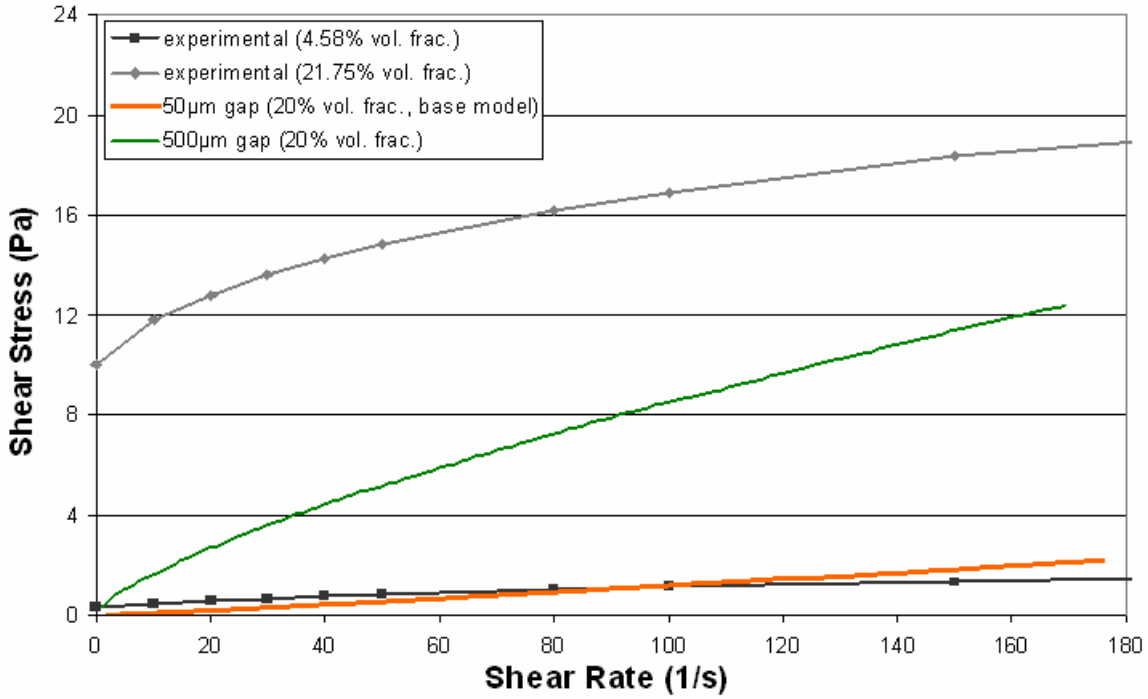

Figure 7.14: Comparison of coupled model with experimental data for zirconia particles

Gap-dependence of data is not ideal. But, a rheometer's gap width is seldom changed during experimental studies. Therefore results from the same rheometer, with the same gap width, would still be comparable. However, this gap-dependence does indicate that vane-type rheometers may be more appropriate for measuring complex rheology (e.g. particulate suspensions).

None of the rheograms for the coupled model showed evidence of a yield stress. In all cases, the curves tended towards zero shear stress at a shear rate of zero. As mentioned in Section 6.1, this could be due to the way the DEM particles were initialised, where little chance was given for particles to agglomerate (which could create a yield stress). A further influence was the presence of wall slip (Section 7.1.1), which was exacerbated by the quick ramp rates used. However, there may not be a true yield stress for this data, with the values only being extrapolated from higher shear rates. While Megías-Alguacil et al. (2000) did provide yield stress values, their graphed experimental data for zirconia (cf. Figure 5.6) did not indicate a clear yield stress. Instead their rheograms showed a steep drop in shear stress at low shear rates.

7.5. SUMMARY OF FINDINGS FOR RHEOLOGICAL TESTS

Rheological tests were performed with the model to determine it's response to these factors. Important findings are summarised here.

7.5.1. Fluid Velocity Profiles across the Gap

Plain particles showed velocity profiles similar to that of water, though with some lag. When DLVO forces were included, the profile changed dramatically. There were narrow regions of high velocity gradients at both walls, with plug flow in the centre of the gap. This behaviour was attributed to wall slip, where the particles migrated away from the near-wall region. Because of this, the expected linear profile for Couette flow was not reproduced. There was evidence of the plug-flow region narrowing over time (tending to a more linear profile), but this was not a significant effect during the time scales considered in this work.

7.5.2. Particle Volume Fraction

Increasing the volume fraction was shown to increase the magnitude of the measured shear stress in the model. This followed experimental trends. Particles with DLVO forces generated a higher shear stress than plain particles (for the same volume fraction). No yield stress was observed for these simulations.

7.5.3. Particle Surface Charge

Increasing the zeta potential resulted in a more repulsive DLVO force for the zirconia suspension considered here. A more repulsive DLVO force resulted in lower measured shear stresses, which was expected. This was because the particle-fluid mixture was able to flow more freely. For these cases, there were lower fluid velocity gradients at the wall, and the region of sheared fluid extended farther into the bulk, resulting in narrower plug flow regions. No yield stress was observed for these simulations.

7.5.4. Comparison with Experimental Data

The 20% volume fraction model was compared against experimental data of Megías-Alguacil et al. (2000). Correct shear-thinning trends were produced, but shear stress values for the 50μm box were much lower in magnitude than the experimental data. However, when the values for the 500μm gap width were compared, the values were similar in magnitude. This illustrated the gap-dependent nature of the results, which was influenced by wall slip. No yield stress was observed for these results.

7.5.5. Coupled CFD-DEM Model

The model indicated that wall slip occurs within the system. This resulted in gap-width dependent results, which are not ideal. Gap-width dependence may not be an issue, as most rheometers use similar gap widths, and thus results are still comparable. However, to mitigate this phenomenon, roughened wall surfaces or a vane-type rheometer may be more appropriate for particulate suspensions. Overall, the model produced reasonable responses to changing solids volume fraction and particle surface charge. Results are within an order of magnitude of experimental data, which is encouraging for a preliminary model such as this.

8. CONCLUSIONS

The aim of this thesis was to develop a methodology for the creation of a numerical model of a particulate suspension. A coupled CFD-DEM approach was chosen. As this method had not been used before to study suspension rheology, tests were conducted to determine the best operational parameters for this type of model (time step size, domain size, etc.). In order to do this, the complexity of the model was built up in stages.

First, single-phase fluids were modelled in a simplified rheometer geometry using CFD. Both Newtonian and non-Newtonian fluids were tested. The coupled model was formed by adding particles to a base fluid of water. Zirconia particles of 1.5μm in diameter were used. The domain shape and size was gradually changed from a full rheometer to that of a small orthogonal box in order to reduce computational expense. At each step in the process, the model was shown to be equivalent to that of the preceding step. DLVO inter-particle forces were included to simulate the forces due to particle surface charge. Once an appropriate range of model parameters had been determined, the model was tested with different particle volume fractions and different DLVO forces (due to different surface charges) to see if realistic rheological trends could be produced.

Conclusions are drawn on the performance of the model during the various stages of development. Section 8.1 summarises important findings from the CFD model tests that laid the ground work for the development of the coupled model. Appropriate model parameters for the coupled CFD-DEM model are discussed in Section 8.2. Outcomes of the rheological tests of particle volume fraction and surface charge are examined in Section 8.3. Finally, in Section 8.4, recommendations for future work are made.

8.1. CFD MODEL RESULTS

8.1.1. Rheometer Geometry

The single-gap rheometer model was preferred due to its simplicity and accuracy. The double-gap model required unnecessary additional computational expense. Moreover, the axi-symmetric DIN bob model was not as accurate as the other models. It also suffered

from secondary flow effect (Taylor vortices) at high shear rates. Thus a model shape based on the single-gap geometry would be the most suitable for further use.

8.1.2. Time Step Size

A time step size of 0.001s was found to be acceptable for all the single-phase CFD rheometer models tested here. Smaller time steps sizes were tested, but were found to be unnecessary as they did not improve the accuracy. Larger time steps were unstable at high shear rates.

8.1.3. Ramp Rate

A ramp rate reaching about $500s^{-1}$ in 30s was found to be acceptable. Faster ramp rates were not as accurate, while slower ramp rates were found to produce similar results. Thus this rate was used as the baseline ramp rate for the coupled model (the 2s ramp rate).

8.1.4. Gap Width

Reducing the gap width improved stability and accuracy. Moreover, narrow gap widths prevented secondary flow effects from forming at high shear rates. For the curved rheometer geometries, the smallest tested width of 500μm performed best. For the CFD model of the rectangular box, gap widths ranging from 50μm to 500μm were tested. Both the 50μm and 500μm geometries performed similarly to the 500μm wide single-gap rheometer model. Therefore the 50μm box was found to be equivalent to the larger rheometer models.

8.1.5. Pressure-Corrector Loops

Modelling of non-Newtonian fluids required four pressure-corrector loops in the PISO solver algorithm to produce stable results. Only two corrector loops were required for the Newtonian fluid. Therefore at least four loops should be used for the coupled model.

8.1.6. Model Geometry Size

Thin, axi-symmetric slices of full-sized geometries were found to be equivalent to the full-sized rheometer models. Further reducing the model size to a 50μm rectangular box was found to produce similar results as well. Therefore larger, full-sized rheometer models are not necessary.

8.2. CFD-DEM COUPLED MODEL RESULTS

8.2.1. Box Geometry

For computational efficiency reasons, the size and shape of the model was reduced to that of an orthogonal, rectangular box of length 50μm in each direction. CFD testing showed that this geometry was equivalent to larger, full-size rheometer geometries.

8.2.2. Coupled Model Formulation

As suggested by Zhou et al. (2010), the "Model A" formulation for CFD-DEM modelling was best suited for the type particle-fluid flows found in this work.

8.2.3. Explicit vs. Implicit Formulations

Using an implicit formulation for the DEM drag force was necessary for the stability of the simulation with the small particle size considered in this work. It was also more accurate than the explicit formulation as up-to-date particle velocities were used. The semi-implicit nature of the CFD momentum source term also contributed to solution stability. As a result, particle volume fractions larger than about 5% could be simulated.

8.2.4. CFD Mesh Size

CFD cell dimensions should be about 3-4 particles diameters in length. Larger cell sizes do not affect the results, nor do very small cells at the wall (≤ one particle diameter).

8.2.5. Time Step Size and Coupling Interval

The Rayleigh criteria (cf. Equation 3.4) for selecting the DEM time step was found to be best suited to this work, as it was more appropriate for large particle volume concentrations. The CFD time step (and thus the coupling interval) should be selected such that it is smaller than the particle response time (cf. Equation 3.31).

From the selection of the particle properties, the DEM time step size due to the Rayleigh criteria was calculated to be 2.5e-9s. For plain particles, it was found this time step could be raised to 1e-8s without significantly affecting the results. When DLVO forces were included the DEM time step could be raised to 2.5e-8s. However, higher time steps sizes

tended to produce largely constant viscosity values, with no shear-thinning trends. The coupling interval was kept at 100 for these tests.

Coupling intervals of 100 and 200 were found to be acceptable for all cases when using the base DEM time step of 2.5e-9s. For DEM time step sizes larger than 1e-8s, smaller coupling intervals of around 25 also provided good results. The bigger the increase in time step, the smaller the corresponding interval should be. Models that had different time step and coupling interval combinations, but the same resultant CFD time step size, produced similar behaviour.

Any combination of DEM time step and coupling interval that produced a CFD time step below 2.5e-7s resulted in the particles suddenly migrating away from the moving wall. Thus the model was not as sensitive to the DEM time step size as it was to the CFD time step size. Small DEM time steps increased the computational cost of the simulations.

8.2.6. Ramp Rate

Slower ramp rates (8 and 20s) produced higher shear stresses at low shear rates. However, they introduced some instability into the model as the fluid component became less dominated by convection. This led to particles suddenly migrating away from the boundary walls. To mitigate this behaviour, higher time steps had to be used in conjunction with slower ramp rates. For example, reducing the base ramp rate (2s) by a factor of 10 would require a corresponding increase in the DEM time step by a factor of 10 (for a constant coupling interval). For shear rates above $40s^{-1}$, there was not much improvement for slower ramp rates over the base (2s) ramp rate. The 2s ramp rate also showed good performance for the larger gap width simulations. Therefore the 2s ramp rate was thought to be acceptable for all cases.

8.2.7. Domain Size

Increasing the domain size in either the flow or vertical directions did not affect the results, while increasing the gap width (distance between solid walls) made a significant difference. Viscosity values scaled according to the gap width (relative to the 50μm box). This occurred because the change in gap width only scaled the shear rate values, but not the corresponding shear stress values (measured at the wall). This phenomenon was

thought to be due to wall slip occurring at the wall boundaries (cf. Section 7.1.1). Importantly, the gap width is not often changed in real concentric-cylinder rheometers, meaning the width normally stays constant throughout testing. Thus, results for the same rheometer geometry would still be comparable.

It was found that larger time step sizes and faster ramp rates could be used for the wider gaps. In fact, faster ramp rates (like the 2s ramp rate) were preferred for stability reasons. This also sped up the solution time. Rheograms appeared to be more stable (smoother) with increasing gap width. However, using too large a time step or coupling interval produced a more constant viscosity over the shear rate range, without any shear-thinning trends. This occurred when the resulting CFD time step was above 1.25e-6s for the 500μm gap, and 1e-6s for the 200μm gap.

8.3. RHEOLOGICAL TESTS

8.3.1. Fluid Velocity Profiles across the Gap

Plain particles showed a relatively linear velocity profile similar to that of water, though with some lag in the velocity magnitudes. Particles with DLVO forces produced an "s-shaped" velocity profile. These profiles comprised of narrow layers of highly sheared fluid against the walls, with a bulk region in the centre experiencing much less shear. Particles with less attractive DLVO forces produced a more gradual s-shaped profile, where the sheared region extended farther into the fluid bulk. These profiles had lower shear gradients at the wall, and therefore lower viscosities were measured. As the DLVO potential became more attractive, particles in the centre were more likely to agglomerate and so created a wider region of plug flow, which resulted in much narrower bands of high shear at the walls. The narrow regions of high shear at the wall indicated the presence of wall slip due to wall-depletion effects, where particles migrate away from the walls. This phenomenon has been documented by other researchers in the literature. Wall slip was the most likely reason for the gap-dependent results seen in Sections 6.7 and 7.4.

8.3.2. Particle Volume Fraction

Volume fractions ranging from 4.58 to 40% were tested. As expected, the model showed that increasing the volume fraction did generally increase the complexity of the mixture, thereby increasing measured shear stress across the whole shear rate range. This was true for both plain particles, and those with DLVO forces included. These trends follow those found in experimental work.

8.3.3. Particle Surface Charge

Zeta potentials ranging from 0 to 50mV were tested. The resulting DLVO potentials ranged from fully attractive 0mV (where van der Waals attraction dominated), to less attractive potentials (50mV). Plain particles represented the case where there was no attraction or repulsion forces between the particles. As expected, greater attraction forces between particles resulted in higher shear stresses. Less attractive DLVO potentials tended to produce values closer to that of plain particles at low shear rates. This showed that the model produced realistic rheological responses to changes in surface potential.

8.3.4. Comparison with Experimental Data

The 20% volume fraction model was compared against experimental data of Megías-Alguacil et al. (2000). Correct shear-thinning trends were produced. Shear stress values for the 50μm box were much lower in magnitude than the experimental data. However, the 500μm gap width achieved values of the same order of magnitude as the experimental data.

8.3.5. Coupled CFD-DEM Model

The model indicated that wall slip occurs within the system. This resulted in gap-width dependent results, which are not ideal. Gap-width dependence may not be an issue, as most rheometers use similar gap widths, and thus results are still comparable. However, to mitigate this phenomenon, roughened wall surfaces or a vane-type rheometer may be more appropriate for particulate suspensions. Overall, the model produced reasonable responses to changing solids volume fraction and particle surface charge. Results are within an order of magnitude of experimental data, which is encouraging for a preliminary model such as this.

8.4. RECOMMENDATIONS FOR FUTURE WORK

Following from the findings in this thesis, some recommendations can be made regarding enhancements to the model that could benefit from further investigation.

8.4.1. Gap Width

Due to the gap-dependent nature of the results, it is recommended that future studies with this model make use of gap widths that correspond to the apparatus used to generate the experimental data (e.g. 500μm in the case of this study).

8.4.2. Include the Effect of Curved Geometry

In Section 5.1 it was assumed that the flat edges of a box-shaped domain would be acceptable for this study. However, real concentric-cylinder rheometers have curved geometry. Therefore, to make the model more realistic, the model should be developed to include curved inner and outer walls. This would require the development of an axi-symmetric boundary condition for LIGGGHTS.

8.4.3. Investigate Methods to Reduce Wall Slip

Fluid velocity profiles across the gap in (cf. Section 7.1.1) indicated the existence of wall slip between the solid walls and the particle-fluid mixture. Work should be done to mitigate this phenomenon and so reduce its influence on the model results. A technique sometimes used in experiments to reduce wall slip is roughening of the wall surfaces. Another option would be to model a rheometer geometry that does not have smooth, flat, wall boundaries, such as a vane rotor. Both options would be suitable. However, both options would require a more complex geometry to be modelled.

8.4.4. Investigate Complex Particle Properties

With little modification, this model is capable of modelling particles of different size and shape. Different shapes can be created using the multi-sphere method, where complex particle shapes are built up using a collection of smaller spheres. This capability already exists in LIGGGHTS. By changing the shape and size of particles in the model, the rheology of more complex suspensions can be studied. For example, with different

particle shapes the effect of either an isotropic or anisotropic distribution of charge on a particle's surface can be investigated.

8.4.5. Experimental Validation against Different Suspensions

The model should be validated against a range of different particulate suspensions. Simple systems (similar to that used in this work), as well as more complex suspensions with different particle shapes and sizes should be assessed. In addition, the model's prediction of wall slip should be measured experimentally.

REFERENCES

T.B. Anderson and R. Jackson. A fluid mechanical description of fluidized beds. *Industrial & Engineering Chemistry Fundamentals*, 6(4):527-539, 1967.

K. Apostolou and A.N. Hrymack. Discrete element simulation of liquid-particle flows. *Computers and Chemical Engineering*, 32:841-856, 2008.

S.V. Apte, M. Martin and N.A. Patankar. A numerical method for fully resolved simulation (FRS) of rigid particle–flow interactions in complex flows. *Journal of Computational Physics*, 228:2712-2738, 2009.

H.A. Barnes, J.F. Hutton, and K. Walters. An introduction to rheology. Elsevier, 1989.

H.A. Barnes. A review of the slip (wall depletion) of polymer solutions, emulsions and particle suspensions in viscometers: its cause, character, and cure. *Journal of Non-Newtonian Fluid Mechanics*, 56:221-251, 1995.

H.A. Barnes. The yield stress - a review or 'παντα ρει' - everything flows? *Journal of Non-Newtonian Fluid Mechanics*, 81:133-178, 1999.

H.A. Barnes. A Handbook of Elementary Rheology. University of Wales, Institute of Non-Newtonian Fluid Mechanics, Wales, 2000.

H.A. Barnes and Q.D. Nguyen. Rotating vane geometry – a review. *Journal of Non-Newtonian Fluid Mechanics*, 98:1-14, 2001.

H.A. Barnes and K. Walters. in: B. Mena et al., Advances in Rheology (Eds.) Universidad Nacional Autonoma de Mexico, Mexico City, 1984, Proc. 9th International Congress on Rheology, Acapulco, vol. 4, p.45, 1984.

K.H. Bech, N. Tillmark, P.H. Alfredsson and H.I. Andersson. An investigation of turbulent plane Couette flow at low Reynold's numbers. *Journal of Fluid Mechanics*, 286:291-325, 1995.

R. Beetstra, M.A. Van der Hoef, and J.A.M. Kuipers. Drag force from lattice Boltzmann simulations of intermediate Reynolds number flow past mono- and bidisperse arrays of spheres. *AIChE Journal*, 2006.

R. Beetstra, M. A. van der Hoef and J. A. M. Kuipers. Drag Force of Intermediate Reynolds Number Flow Past Mono- and Bidisperse Arrays of Spheres. *AIChE Journal*, 53:489-501, 2007.

E.C. Bingham, and H. Green. Paint, a plastic material and not a viscous liquid; the measurement of its mobility and yield value. *Proceedings - American Society for Testing Materials*. 20:640-675, 1920.

R. Buscall, J.I. McGowan, and A.J. Morton-Jones. The rheology of concentrated dispersions of weakly attracting colloidal particles with and without wall slip. *Journal of Rheology*, 37(4):621-641, 1993.

CFDEM, produced by DCS Computing GmbH. website: www.cfdem.com.

R.P. Chhabbra and J.F. Richardson. Non-Newtonian flow and applied rheology, 2nd edition. Butterworth-Heinemann, Oxford, UK. 2008.

S.H. Cho, H.G Choi and J.Y. Yoo. Direct numerical simulation of fluid flow laden with many particles. *International Journal of Multiphase Flow*, 31:435-451, 2005.

K.W. Chu, B. Wang, A.B. Yu, A. Vince, G.D. Barnett and P.J. Barnett. CFD–DEM study of the effect of particle density distribution on the multiphase flow and performance of dense medium cyclone. *Minerals Engineering*, 22:893-909, 2009.

P.W. Cleary. The effect of particle shape on simple shear flows. *Powder Technology*, 179:144-163, 2007.

C.T. Crowe, M. Sommerfeld and T. Tsuji. Multiphase flows with droplets and particles. CRC Press LLC, USA, 1998.

P.A. Cundall, O.D.L Strack. A discrete numerical model for granular assemblies. *Geotechnique*, 29:47–65, 1979.

R.H. Davis, J.-M Serayssol and E.J. Hinch. The elastohydrodynamic collision of two spheres. *Journal of Fluid Mechanics*, 163:479-497, 1986.

N.G. Deen, M. Van Sint Annaland, M.A. Van der Hoef and J.A.M. Kuipers. Review of discrete particle modeling of fluidized beds. *Chemical Engineering Science*, 62:28-44, 2007.

B.V. Derjaguin and L. Landau. Theory of the stability of strongly charged lyophobic sols and of the adhesion of strongly charged particles in solutions of electrolytes. *Acta Physicochem*, 14:633–662, 1941.

R. Di Felice. The voidage function for fluid–particle interaction systems. *International Journal of Multiphase Flow*, 20:153–159, 1994.

A. Di Renzo and F.P. Di Maio. Comparison of contact-force models for the simulation of collisions in DEM-based granular flow codes. *Chemical Engineering Science*, 59:525-541, 2004.

S. Ergun. Fluid flow through packed columns. *Chemical Engineering Progress*, 48:89–94, 1952.

Y. Feng and A. Yu. Numerical simulation of the gas-solid flow in a fluidized bed by combining discrete particle method with computational fluid dynamics. *Third International Conference on CFD in the Minerals and Process Industries*, Melbourne, Australia, 2003. CSIRO.

J.H. Ferziger and M. Perić. Computational Methods for Fluid Dynamics. 3rd Edition. Springer, Berlin, Germany 2002.

Fluent® v.6.2 user guide, ANSYS, 2005.

J.A. Gant, I.T. Cameron, J.D. Litster and E.P. Gatzke. Determination of coalescence kernels for high-shear granulation using DEM simulations. *Powder Technology*, 170:53-63, 2006.

T. Gibaud, C. Barentin, N. Taberlet and S. Manneville. Shear-induced fragmentation of laponite suspensions. *Soft Matter*, 5:3026-3037, 2009.

D. Gidaspow. Multiphase flow and fluidization: continuum and kinetic theory descriptions with applications. Academic Press, San Diego, USA, 1994.

C. Goniva (Dr.). CFD-DEM coupling core developer at DCS Computing GmbH, Austria. web: www.cfdem.com.

C. Goniva, C. Kloss and S. Pirker. Towards fast parallel CFD-DEM: An open-source perspective. Open Source CFD International Conference, Barcelona, Spain, 12th-13th November 2009

C. Goniva, C. Kloss, A. Hager, and S. Pirker. An open source CFD-DEM perspective. *Proceedings of OpenFOAM Workshop*, Göteborg, June 22.-24, 2010.

C. Goniva, C. Kloss, N.D. Deen, J.A.M. Kuipers, and S. Pirker. Influence of rolling friction on single spout fluidised bed simulation. *Particuology*, 10:582-591, 2012.

D.Z. Gunes, R. Scirocco, J. Mewis and J. Vermant. Flow-induced orientation of non-spherical particles: effect of aspect ratio and medium rheology. *Journal of Non-Newtonian Fluid Mechanics*, 155:39-50, 2008.

J.P. Hartnett and R.Y.Z. Hu. *Journal of Rheology*. 33(4):671, 1989.

M. He, Y. Wang and E. Forssberg. Slurry rheology in wet ultrafine grinding of industrial minerals: a review. *Powder Technology*, 147:94-112, 2004.

M.R. Hestens and E.L. Steifel. Method of conjugate gradients for solving linear systems. *Journal of Research*, 29:409-436, 1952.

R.J. Hill, D.L. Koch and J.C. Ladd. Moderate-Reynolds-numbers flows in ordered and random arrays of spheres. *Journal of Fluid Mechanics*, 448:243–278, 2001.

J.E. Hilton, L.R. Mason and P.W. Cleary. Dynamics of gas–solid fluidised beds with non-spherical particle geometry. *Chemical Engineering Science*, 65:1584-1596, 2010.

A. Holzer and M. Sommerfeld. New simple correlation formula for the drag coefficient of non-spherical particles. *Powder Technology*, 184:361-365, 2008.

A. Holzer and M. Sommerfeld. Lattice Boltzmann simulations to determine drag, lift and torque acting on non-spherical particles. *Computers & Fluids*, 38:572-589, 2009.

B.P.B. Hoomans, J.A.M. Kuipers, W.J. Briels and W.P.M. van Swaaij. Discrete particle simulation of bubble and slug formation in a two-dimensional gas-fluidised bed: a hard-sphere approach. *Chemical Engineering Science*, 51:91-111, 1996.

J.P. Hughes, J.M. Davies, and T.E.R. Jones. Concentric cylinder end effects and fluid inertia effects in controlled stress rheometry: part I: numerical simulation. *Journal of Non-Newtonian Fluid Mechanics*, 77:79-101, 1998.

J.N. Israelachvili. Intermolecular and surface forces, 2nd edition. Academic Press, London. 1992.

R. I. Issa. Solution of the implicitly discretised fluid flow equations by operator-splitting. *Journal Computational Physics*, 62(1):40-65, 1986.

H. Jasak. Error Analysis and Estimation for the Finite Volume Method with Applications to Fluid Flows. Doctoral thesis. Imperial College of Science, London, UK, 1996.

R.W. Johnson (editor). The handbook of fluid mechanics. CRC Press/Springer. 1998.

S.B. Johnson, G.V. Franks, P.J. Scales, D.V. Boger, T.W. Healy. Surface chemistry–rheology relationships in concentrated mineral suspensions. *International Journal of Mineral Processing*, 58:267–304, 2000.

F.P. Kärrholm. Numerical modelling of diesel spray injection, turbulence interaction and combustion. Doctoral thesis. Chalmers University of Technology, Göteborg, Sweden, 2008.

S. Kim. Slip velocity and velocity inversion in a cylindrical Couette flow. *Physical Review E*, 79, 2009.

D.L. Koch and R.J. Hill. Inertial effects in suspension and porous-media flows. *Annual Review of Fluid Mechanics*, 33:619–647, 2001.

D.L. Koch and A.S. Sangani. Particle pressure and marginal stability limits for a homogeneous monodisperse gas fluidised bed: kinetic theory and numerical simulations. *Journal of Fluid Mechanics*, 400:229-263, 1999.

C. Kloss (Dr.). LIGGGHTS core developer at DCS Computing GmbH, Austria. web: www.cfdem.com.

C. Kloss, C. Goniva, A. Hager, S. Amberger and S. Pirker. Models, algorithms and validation for opensource DEM and CFD-DEM. *Progress in Computational Fluid Dynamics*, 12:140 – 152, 2012.

M. Kremmer and J.F. Favier. A method for representing boundaries in discrete element modelling – part II: kinematics. *International Journal for Numerical Methods in Engineering*. 51:1423-1436, 2001.

J.S. Laskowski and J.S. Pugh. Chapter 4 – Dispersion stability and dispersing agents in colloid chemistry in minerals processing, edited by J.S. Laskowski and J.S. Ralston, Elsevier, Amsterdam, Netherlands, pp. 151-161, 1992.

Y.K. Leong and B.C. Ong. Critical zeta potential and the Hamaker constant of oxides in water. *Powder Technology*, 134:249-254, 2003.

J. Li and J.A.M. Kuipers. Gas-particle interactions in dense gas-fluidized beds. *Chemical Engineering Science*, 58:711-718, 2003.

Y. Li, Y. Xu and C. Thornton. A comparison of discrete element simulations and experiments for "sandpiles" composed of spherical particles. *Powder Technology*, 160:219-228, 2005.

LIGGGHTS manual, Kloss et al, 2013.

E. Loth and A.J. Dorgan. An equation of motion for particles of finite Reynolds number and size. *Environmental Fluid Mechanics*, 9:187–206, 2009.

A.A. Mammoli. Towards a reliable method for predicting the rheological properties of multiphase fluids. *Engineering Analysis with Boundary Elements*, 26:861-869, 2002.

S. Manneville, L. Bécu and A. Colin. High-frequency ultrasonic speckle velocimetry in sheared complex fluids. *The European Physical Journal Applied Physics*, 28:361-373, 2004.

D. Markauskas. Discrete element modelling of complex axisymmetrical particle flow. *Mechanika*, Nr. 6(62), pp32-38, 2006.

I. Massalova (Prof.). Rheology Centre, Civil Engineering Department, Cape Peninsula University of Technology, Cape Town, South Africa.

J.B. McLaughlin. Inertial migration of a small sphere in linear shear flows. *Journal of Fluid Mechanics*, 224:261–274, 1991.

D. Megías-Alguacil, J.D.G. Durán and A.V. Delgado. Yield stress of concentrated zirconia suspensions: correlation with particle interactions. *Journal of Colloid and Interface Science*, 231:74-83, 2000.

R. Mei. An approximate expression for shear lift force on a spherical particle at a finite Reynolds. number. *International Journal Multiphase Flow*, 18:145–147, 1992.

J. Mewis and N.J. Wagner. Current trends in suspension rheology. *Journal of Non-Newtonian Fluid Mechanics*, 157:147-150, 2009.

J. Mewis and N.J. Wagner. Colloidal Suspension Rheology. Cambridge University Press, Cambridge, 2011.

T.G., Mezger. The Rheology Handbook. Vincentz Verlag, Hannover, 2002.

T. Mikami, H. Kamiya and M. Horio. Numerical simulation of cohesive powder behaviour in a fluidised bed. *Chemical Engineering Science*, 53:1927-1940, 1997.

T. Missana and A. Adell. On the applicability of DLVO theory to the prediction of clay colloids stability. *Journal of Colloid and Interface Science*, 230:150-156, 2000.

J.A. Naser. Prediction of Newtonian and non-Newtonian flow through concentric annulus with centerbody rotation. *International Conference on CFD in Mineral & Metal Processing and Power Generation*, CSIRO, 1997.

B. Ndlovu. The effect of phyllosilicate mineralogy and surface charge on the rheology of mineral slurries. Doctoral thesis. University of Cape Town, South Africa, 2011.

B. Ndlovu, M. Becker, E. Forbes, D. Deglon and J-P Franzidis. The influence of phyllosilicate mineralogy on the rheology of mineral slurries. *Minerals Engineering*, 24:1314-1322, 2011.

A. Nguyen and H.J. Schulze. Colloidal Science of Flotation. 1st Edition, Marcel Dekker, New York, 2004.

Q.D. Nguyen and D.V. Boger. Yield stress measurement for concentrated suspensions. *Journal of Rheology*, 27(4):321-349, 1983.

OpenCFD Ltd., OpenFOAM® User guide v.2.1.1, 2012.

OpenCFD Ltd., OpenFOAM® Programmer's guide v.2.1.1, 2012.

S.V. Patankar. Numerical Heat and Mass Transfer. Hemisphere Publishing Corporation, Washington, 1980.

N.A. Patankar and H.H. Hu. Finite Reynolds number effect on the rheology of a dilute suspension of neutrally buoyant circular particles in a Newtonian fluid. *International Journal of Multiphase Flow*, 28:409-425, 2002.

S.M. Peker and Ş.Ş. Helvacı. Solid-Liquid Two Phase Flow, 1st Edition. Elsevier, Amsterdam, Netherlands. 2008.

S. Plimpton, Fast parallel algorithms for short-range molecular dynamics, *Journal Computational Physics*, 117:1-19, 1995.

H. Rusche. Computational fluid dynamics of dispersed two-phase flows at high phase fractions. Doctoral thesis. Imperial College of Science, London, UK, 2002.

P.G. Saffman. The lift on a sphere in slow shear flow. *Journal of Fluid Mechanics*, 22:385–400, 1965.

J.-M. Serayssol and R.H. Davis. The influence of surface interactions on the elastohydrodynamic collision of two spheres. *Journal of Colloid and Interface Science*, 114(1):54-55, 1986.

N. Sharma and N.A. Patankar. A fast computation technique for the direct numerical simulation of rigid particulate flows. *Journal of Computational Physics,* 205:439-457, 2005.

M. Subbanna, Pradip and S.G. Malghan. Shear yield stress of flocculated alumina-zirconia mixed suspensions: effect of solid loading, composition and particle size distribution. *Chemical Engineering Science*, 53(17):3073-3079, 1998.

TA Instruments. Operator's manual – AR 1500EX rheometer. March 2010.

Y. Tsuji, T. Kawaguchi and T. Tanaka. Discrete particle simulation of two-dimensional fluidized bed. *Powder Technology*, 77:79-87, 1993.

M.A. van der Hoef, R. Beetstra and J.A.M. Kuipers. Lattice-Boltzmann simulation of low-Reynolds-number flow past mono- and bidisperse arrays of spheres: results for the permeability and drag force. *Journal of Fluid Mechanics*, 528:233-254, 2005.

H.K. Versteeg and W. Malalasekera. An Introduction to Computational Fluid Dynamics: The Finite Volume Method. 2nd Edition. Pearson Education, London, UK, 2007.

E.J.W. Verwey and J.T.G Overbeek. Theory of the stability of lyophobic colloids - The interaction of soil particle having an electrical double layer. Amsterdam, Elsevier, 1948.

A. Wachs. A DEM-DLM/FD method for direct numerical simulation of particulate flows: Sedimentation of polygonal isometric particles in a Newtonian fluid with collisions. *Computers and Fluids*, 38:1608-1628, 2009.

C. Wassgren and A. Sarkar. Video Lecture 06: Introduction to Soft-Particle DEM and Normal Contact Force Models - Part I, https://pharmahub.org/resources/128, 2008. Site last visited October 2014.

H.G. Weller, G. Tabor, H. Jasak and C. Fureby. A tensorial approach to computational continuum mechanics using object-oriented techniques. *Computers in Physics*, vol. 12, no. 6, pp620-631, 1998.

Y.C. Wen and Y.H. Yu. Mechanics of Fluidization. In *Chemical Engineering Progress Symposium Series*, 62:100–111, 1996.

F.M. White. Fluid Mechanics. 4th Edition. McGraw Hill. 1998.

R.W. Whorlow. Rheological techniques. 2nd Edition. Ellis Horwood. 1992.

B.H Xu and A.B. Yu. Numerical simulation of the gas-solid flow in a fluidized bed by combining discrete particle method with computational fluid dynamics. *Chemical Engineering Science*, 52:2785-2809, 1997.

B.H. Xu, A.B. Yu, S.J. Chew and P.Zulli. Numerical simulation of the gas-solid flow in a bed with lateral gas blasting. *Powder technology*, 109:13-26, 2000.

S. Yamamoto and T. Matsuoka. Dynamic simulation of rod-like and plate-like particle dispersed systems. *Computational Materials Science*, 14:169-176, 1999.

C. Yang, Y. Ding, D. York and W. Broeckx. Numerical simulation of sedimentation of microparticles using the discrete particle method. *Particuology*, 6:38-49, 2008.

C. Yin, L. Rosendahl, S.K. Kaer and H. Sorensen. Modelling the motion of cylindrical particles in a nonuniform flow. *Chemical Engineering Science*, 58:3489-3498, 2003.

W. Zhang, R. Noda and M. Horio. Evaluation of Lubrication force on colliding particles for DEM simulation of fluidised beds. *Powder Technology*, 158:92-101, 2005.

Z.W. Zhou, P.J. Scales, and D.V. Boger. Chemical and physical control of the rheology of concentrated metal oxide suspensions. *Chemical Engineering Science*, 56:2901–2920, 2001.

Z.Y. Zhou, S.B. Kuang, K.W. Chu and A.B. Yu. Discrete particle simulations of particle-fluid flow: model formulations and their applicability. *Journal of Fluid Mechanics*, 661:482-510, 2010.

H.P. Zhu, Z.Y. Zho, R.Y. Yang and A.B. Yu. Discrete particle simulation of particulate systems: theoretical developments. *Chemical Engineering Science*, 62:3378-3396, 2007.

BIBLIOGRAPHY

R.J. Hunter. Foundations of Colloid Science, Volume I. Oxford University Press, New York, USA, 1993.

APPENDIX A: NON-NEWTONIAN FLUID MODEL FOR OPENFOAM®

LIST OF FIGURES

LIST OF TABLES

A.1. HERSCHEL-BULKLEY CODE FOR V.1.6

This code is the description of the model for OpenFOAM® version 1.6. The code (shown below in the shaded box) also includes a bug-fix to change the sign in front of the "`pow(tone*tau0_/nu0_,n_)`" to a negative sign. With this sign correction, the last two terms in the brackets would cancel out when `tau0_/nu0_` equals the shear rate. This would return the expected value of $\eta = \tau_0/\dot{\gamma}$. This correction would however have little effect when `nu0_` is set to a very large value to approximate infinity (which more closely imitates yield stress at $\dot{\gamma} = 0$). In equation form, this Herschel-Bulkley model can be represented as:

$$\mu = \min\left[\mu_0 \quad \frac{1}{\dot{\gamma}}\left(\tau_y + k\left(\dot{\gamma}^n - \frac{\tau_y}{\mu_0}\right)^n\right)\right] \tag{A.1}$$

```
Foam::tmp<Foam::volScalarField>
Foam::viscosityModels::HerschelBulkley::calcNu() const
{
 dimensionedScalar tone("tone", dimTime, 1.0);
 dimensionedScalar rtone("rtone", dimless/dimTime, 1.0);

 tmp<volScalarField> sr(strainRate());

 return (min(nu0_,(tau0_ + k_* rtone *( pow(tone * sr(), n_)
       - pow(tone*tau0_/nu0_,n_))) / (max(sr(), dimensionedScalar
       ("VSMALL", dimless/dimTime, VSMALL)))));
}
```

A.2. HERSCHEL-BULKLEY MODEL FOR V.2.0.1

The code was changed slightly for OpenFOAM® versions 2.0.1 and 2.1.1. In particular, the "`-pow(tone*tau0_/nu0_,n_)`" term was removed. The reason for the change was not specified, though it had been suggested by other OpenFOAM® users that this term was not necessary. In equation form, this Herschel-Bulkley model can be represented as:

$$\mu = \min\left[\begin{matrix}\mu_0 \\ \frac{1}{\dot{\gamma}}\left(\tau_y + k\dot{\gamma}^n\right)\end{matrix}\right] \tag{A.2}$$

```
Foam::tmp<Foam::volScalarField>
Foam::viscosityModels::HerschelBulkley::calcNu() const
{
 dimensionedScalar tone("tone", dimTime, 1.0);
 dimensionedScalar rtone("rtone", dimless/dimTime, 1.0);

 tmp<volScalarField> sr(strainRate());

 return
 (
       min
       (
       nu0_,
       (tau0_ + k_*rtone*pow(tone*sr(), n_))
       /(max(sr(), dimensionedScalar ("VSMALL", dimless/dimTime, VSMALL)))
       )
 );
}
```

A.3. COMPARISON OF MODEL FORMULATIONS

Figure A. illustrates the shear stress curves for both version of the model. For each model version, two curves are shown: one for a "shallow" gradient Newtonian region and one for a "steep" gradient region. The steep gradient version corresponds to a large value of `nu0_` (η_0). As can be seen, the new model is equivalent to the old one for larger values of η_0. The difference for the lower η_0 value curve is assumed to be negligible for the purposes of this study. Model input parameters are given in the table below.

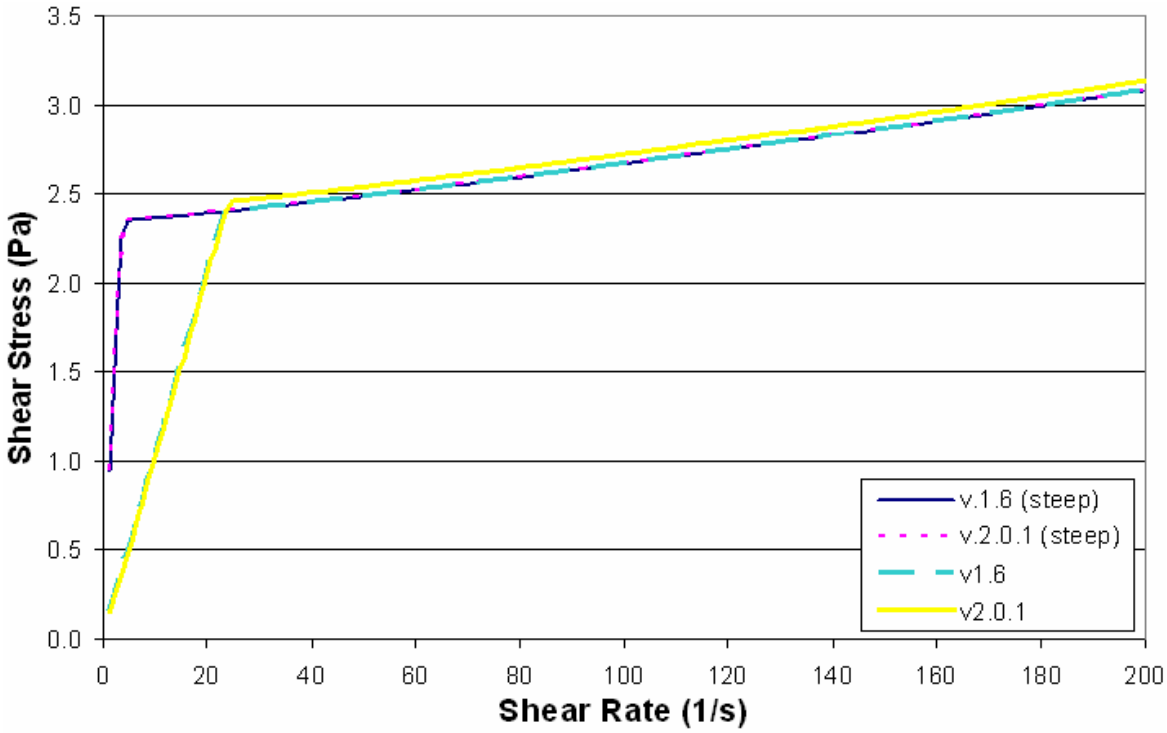

Figure A.1: Comparison of the two different HB model formulations, each for two different values of nu0_

Table A.1: Herschel-Bulkley model input parameters

Standard HB Model		**Modified for CFD (shallow)**		**Modified for CFD (steep)**	
τ_y	2.344 Pa	τ_y	2.4 Pa	τ_y	2.35 Pa
k	1.272e-3 Pa.s	k	1.272e-3 Pa.s	k	1.272e-3 Pa.s
n	1.2	n	1.2	n	1.2
		μ_0	0.1024 Pa.s	μ_0	0.6452 Pa.s

APPENDIX B: INPUT SCRIPTS FOR CFD RHEOMETER MODEL

B.1. controlDict

```
application           icoFoam;
startFrom             latestTime;
startTime             0;
stopAt                endTime;
endTime               35;
deltaT                0.001;
writeControl          timeStep;
writeInterval         1000;
purgeWrite            0;
writeFormat           ascii;      //binary
writePrecision        7;
writeCompression      uncompressed;
timeFormat            general;
timePrecision         6;
runTimeModifiable     yes;

// this is done to incorporate user-defined BC into this case
libs ("libtimeVaryingRotatingWallVelocity.so");

functions
(
    forces_1 //name of forces directory (instance of force calculation)
    {
    type                    forces;
    functionObjectLibs      ("libforces.so");
    outputControl           timeStep; //timeStep or outputTime
    outputInterval          1000;
    patches                 (innerRotWall);
    //writes to screen (and/or log file)
    log                     true;
    //reference density - water at 20 deg. C is used in this example
    rhoInf                  998.29;
    //Centre of rotation/Origin for moment calculations
    CofR                    (0 1 0);
    //values not used for this type of case
    //liftDir   (0 1 0);
    //dragDir   (0 0 1);
```

```
    //pitchAxis (0 1 0);
    //magUInf   1;          //free stream velocity magnitude
    //lRef      1.0;
    //Aref      1.0;
    }
);
```

B.2. fvSchemes

```
ddtSchemes
{
    Default           Euler;
}
gradSchemes
{
    Default           Gauss linear;
    grad(p)           Gauss linear;
    grad(U)           Gauss linear;
}
divSchemes
{
    Default           none;
    div(phi,U)        Gauss upwind;
    div((nuEff*dev(grad(U).T())))  Gauss linear;
}
laplacianSchemes
{
    Default                       none;
    laplacian(nuEff,U)            Gauss linear corrected;
    laplacian((1|A(U)),p)         Gauss linear corrected;
    laplacian(1,p)                Gauss linear corrected;
    laplacian(nu,U)               Gauss linear corrected;
}
interpolationSchemes
{
    Default           linear;
    interpolate(U)    linear;
```

```
}
snGradSchemes
{
    Default           corrected;
}
fluxRequired
{
    Default           no;
    p                 ;
}
```

B.3. fvSolution

```
solvers
{
     p PCG
     {
         preconditioner DIC;
         tolerance      1e-06;
         relTol         0.01;
     };
     U PBiCG
     {
         preconditioner DILU;
         tolerance      1e-05;
         relTol         0.1;
     };
}

PISO
{
    nCorrectors     2;
    nNonOrthogonalCorrectors 0;
    pRefCell        0;
    pRefValue       0;
}
```

B.4. transportProperties

```
transportModel  Newtonian;

//water density at 20 deg. C (air density = 1.2)
rho             rho [ 1 -3 0 0 0 0 0 ] 998.29;
//water kinematic viscosity at 20 deg. C (air kin. viscosity = 1e-05)
nu              nu [ 0 2 -1 0 0 0 0 ] 1.004e-06;
```

B.5. p

```
#include        "initialConditions" dimensions [ 0 2 -2 0 0 0 0 ];

internalField   uniform $pressure;

boundaryField
{
    cyclicEndFaces_half0
    {
        type           cyclic;
    }
    cyclicTopBottom_half0
    {
        type           cyclic;
    }
    innerRotWall
    {
        type           zeroGradient;
    }
    outerStatWall
    {
        type           zeroGradient;
    }
    cyclicEndFaces_half1
    {
        type           cyclic;
```

```
    }
    cyclicTopBottom_half1
    {
        type          cyclic;
    }
}
```

B.6. U

```
#include        "initialConditions" dimensions [ 0 1 -1 0 0 0 0 ];

internalField   uniform $flowVelocity;

boundaryField
{
    cyclicEndFaces_half0
    {
        type          cyclic;
    }
    cyclicTopBottom_half0
    {
        type          cyclic;
    }
    innerRotWall
    {
        type                timeVaryingRotatingWallVelocity;
        filename            "$FOAM_CASE/time_varying_omega";
        outOfBounds         clamp;
        origin              ( 0 0 0 );
        axis                ( 0 1 0 );
        value               uniform ( 0 0 0 );
    }
    outerStatWall
    {
        type          fixedValue;
        Value         uniform ( 0 0 0 );
    }
```

```
    cyclicEndFaces_half1
    {
        type           cyclic;
    }
    cyclicTopBottom_half1
    {
        type           cyclic;
    }
}
```

B.7. initialConditions

```
flowVelocity           (0 0 0);
pressure               0;
#inputMode             merge
```

APPENDIX C: INPUT SCRIPTS FOR COUPLED CFD-DEM BOX MODEL

C.1. controlDict

```
application           cfdemSolverPiso;
startFrom             startTime;        //*latestTime*
startTime             0;
stopAt                endTime;
endTime               2;
deltaT                0.00000025;
writeControl          adjustableRunTime;
writeInterval         0.0125;
purgeWrite            0;
writeFormat           ascii;
writePrecision        9;
writeCompression      uncompressed;
timeFormat            general;
timePrecision         9;
runTimeModifiable     no;
adjustTimeStep        no;
maxCo                 1;
maxDeltaT             1;

//done to incorporate user-defined BC into this case
libs ("libtimeVaryingRotatingWallVelocity.so");

functions
(
forces_innerWall //name of directory (instance of force calculation)
{
    type                    forces;
    functionObjectLibs      ("libforces.so");
    outputControl           timeStep;
    outputInterval          25000;      //0.025s equivalent
    patches                 (innerRotWall);
    pName                   p;
    UName                   U;
    rhoName                 rhoInf;     //Indicates incompressible
    log                     true;
    rhoInf                  0.997;      //reference density (water 20 deg.C)
    //Centre of rotation / Origin for moment calculations
```

```
    CofR              (0 0 1);

    //values not used for this type of case
    //liftDir         (0 1 0);
    //dragDir         (0 0 1);
    //pitchAxis       (0 1 0);
    //magUInf         20;
    //lRef            1.42;
    //Aref            0.75;
}
);
```

C.2. fvSchemes

```
ddtSchemes
{
    default         Euler;
}
gradSchemes
{
    default         none;
    grad(p)         Gauss linear;
    grad(U)         Gauss linear;
}
divSchemes
{
    default                             none;
    div(phi,U)                          Gauss limitedLinearV 1;
    div((nuEff*dev(grad(U).T())))       Gauss linear;
    div((nuEff*dev(T(grad(U)))))        Gauss linear;     //for v.2 coupling
    div((viscousTerm*dev(grad(U).T()))) Gauss linear;     //v.2.3 coupling
    div((nu*dev(grad(U).T())))          Gauss linear;     //mod A formulation
    div(((nu*rho)*dev(grad(U).T())))    Gauss linear;     //new for v.2.4.4
}
laplacianSchemes
{
    default                             none;
```

```
    laplacian(nuEff,U)                  Gauss linear uncorrected;
    laplacian((1|A(U)),p)               Gauss linear uncorrected;
    laplacian((voidfraction2|A(U)),p)   Gauss linear uncorrected;
    laplacian(DnuTildaEff,nuTilda)      Gauss linear uncorrected;
    laplacian(nu,U)                     Gauss linear uncorrected; //icoFoam
    laplacian(viscousTerm,U)            Gauss linear uncorrected; //v.2.3
    laplacian((nu*rho),U)               Gauss linear uncorrected; //v.2.4.4
}
interpolationSchemes
{
    default                                     none;
    interpolate(U)                              linear; //v.2.5.3
    interpolate((1|A(U)))                       linear; //v.2.5.3
    interpolate(U_0)                            linear; //v.2.5.3
    interpolate(((1|deltaT)*(voidfraction2|A(U))))   linear; //v.2.5.3
    interpolate((U*voidfraction))               linear; //v.2.5.3
    interpolate((Us*voidfraction))              linear; //v.2.5.3
    interpolate((Ksl|rho))                      linear; //v.2.5.3
}
snGradSchemes
{
    default                 none; //*uncorrected*
}
fluxRequired
{
    default         no;
    p               ;
}
```

C.3. fvSolution

```
solvers
{
    p
    {
        solver          PCG;
        preconditioner  DIC;
        tolerance       1e-07;
```

```
        relTol          0;
    }
    pFinal
    {
        solver          PCG;
        preconditioner  DIC;
        tolerance       1e-07;
        relTol          0;
    }
    U
    {
        solver          PBiCG;
        preconditioner  DILU;
        tolerance       5e-06;
        relTol          0;
    }
}
PISO
{
    nCorrectors     4;
    nNonOrthogonalCorrectors 0;
    pRefCell        0;
    pRefValue       0;
}
```

C.4. transportProperties

```
transportModel  Newtonian;

//cgs units for KINEMATIC viscosity
nu              nu [ 0 2 -1 0 0 0 0 ] 9.03e-03;
```

C.5. couplingProperties

```
//====================sub-models & settings==========================//
modelType             "A";
couplingInterval      100;
voidFractionModel     divided;    //or *centre* (divided is more accurate)
locateModel           engine;     //or *standard* (engine model is faster)
meshMotionModel       noMeshMotion;
regionModel           allRegion;
IOModel               basicIO;
dataExchangeModel     twoWayMPI;
averagingModel        dense;
clockModel            off;
forceModels
(
    KochHillDrag      //using new implicit drag correlation
    gradPForce        //used with model A
    viscForce         //used with model A
);
momCoupleModels
(
    implicitCouple
);
turbulenceModelType   "RASProperties";  //*LESProperties*
smoothingModel        off;              //for v.2.5.4

//====================sub-model properties===========================//
implicitCoupleProps
{
    velFieldName            "U";
    granVelFieldName        "Us";
    voidfractionFieldName   "voidfraction";
    KslLimit                5000000000;
}
KochHillDragProps
{
    velFieldName            "U";
    densityFieldName        "rho";
    voidfractionFieldName   "voidfraction";
```

```
    //interpolation;              //too unstable to use
    implDEM;                      //implicit drag correlation
}
gradPForceProps
{
    pFieldName              "p";
    densityFieldName        "rho";
    voidfractionFieldName   "voidfraction";   //for v.2.4.4
    velocityFieldName       "U";              //for v.2.4.4
    //interpolation;                          //too unstable to use
}
viscForceProps
{
    velocityFieldName       "U";
    densityFieldName        "rho";
    //interpolation;                          //too unstable to use
}
twoWayMPIProps
{
    maxNumberOfParticles    1000000;
    liggghtsPath            "../DEM/in.liggghts_init_first_coupling";
}
dividedProps
{
    alphaMin          0.1;
    scaleUpVol        1.0;
}
engineProps
{
    faceDecomp        false;      //better to have this off
    treeSearch        true;
}
```

C.6. liggghtsCommands

```
liggghtsCommandModels
(
    //runLiggghts
    //writeLiggghts
   execute      //old version - deprecated by "runLiggghts", but still valid
   execute      //old - deprecated by "writeLiggghts", but still valid
);

runLiggghtsProps
{
    preNo       false;            //recommended to leave it false
}
writeLiggghtsProps
{
    writeLast   on;               //off is not recommended
    writeName   "liggghts.restart";
    overwrite   on;
}

//for first execute (initialisation of LIGGGHTS)
executeProps0
{
    command
    (
        run
        $couplingInterval
    );
    runFirst                off;
    runLast                 off;
    //runOnce off;
    runEveryCouplingStep    on;
}

//for second execute (for starting coupled simulation after init)
//save every x timestep, where x is the same interval as OpenFOAM (set in
controlDict writeInterval)
executeProps1
```

```
{
    command
    (
        write_restart
        noBlanks
        dotdot
        slash
        DEM
        slash
        liggghts.restart_
        timeStamp
    );
    runFirst                off;
    runLast                 off;
    runEveryCouplingStep    off;
    runEveryWriteStep       on;
}
```

C.7. g

```
dimensions      [0 1 -2 0 0 0 0];
value           ( 0 0 -981);       //cgs units
```

C.8. p

```
dimensions      [0 2 -2 0 0 0 0];
internalField   uniform 0;

boundaryField
{
//------------------------------------------------------------------------
    cyclicTop
    {
        type            cyclic;
```

```
    }
    cyclicBottom
    {
        type            cyclic;
    }
    cyclicLeft
    {
        type            cyclic;
    }
    cyclicRight
    {
        type            cyclic;
    }
//------------------------------------------------------------------------
    innerRotWall            //rotating inner wall
    {
        type           zeroGradient;
    }
    outerStatWall           //stationary outer wall
    {
        type           zeroGradient;
    }
//------------------------------------------------------------------------
}
```

C.9. U

```
dimensions      [0 1 -1 0 0 0 0];
internalField   uniform (0 0 0);

boundaryField
{
//------------------------------------------------------------------------
    cyclicTop         //same BC for cyclicBottom/Left/Right
    {
        type            cyclic;
    }
```

```
//------------------------------------------------------------------------
    innerRotWall       //rotating inner wall
    {
        type            timeVaryingRotatingWallVelocity;
        fileName        "$FOAM_CASE/time_varying_omega";
        outOfBounds     clamp;           //*error|warn|clamp|repeat*
        origin          (0 0 0);
        axis            (0 0 1);
        value           uniform (0 0 0);
    }
    outerStatWall      //stationary outer wall
    {
        type         fixedValue;         //no slip;
        value        uniform (0 0 0);
    }
//------------------------------------------------------------------------
}
```

C.10. rho

This file goes in the `/0` directory with the other initial boundary conditions. It is necessary to set the correct fluid density. The default density value is 1. All `cyclic` boundaries are treated the same.

```
dimensions      [1 -3 0 0 0 0 0];
internalField   uniform 0.997;

boundaryField
{
    innerRotWall
    {
        type            calculated;
        value           $internalField;
    }
    outerStatWall
    {
        type            calculated;
```

```
        value           $internalField;
    }
    cyclicTop         //same BC for cyclicBottom/Left/Right
    {
        type            cyclic;
    }
}
```

C.11. Ksl, Us, voidFraction

The boundary conditions for `Ksl` (momentum transfer coefficient), `Us` (particle velocity) and `voidFraction` are the same, except for the units and initial values. These initial conditions are listed below, followed by a single example of the boundary conditions.

`Ksl` input parameters.

```
dimensions      [1 -3 -1 0 0 0 0];
internalField   uniform 0;
```

`Us` input parameters.

```
dimensions      [0 1 -1 0 0 0 0];
internalField   uniform (0 0 0);
```

`voidFraction` input parameters. A void fraction of 1 indicated the volume was completely filled with fluid.

```
dimensions      [0 0 0 0 0 0 0];
internalField   uniform 1;
```

Common boundary conditions for `Ksl`, `Us` and `voidFraction`. All `cyclic` boundaries are treated the same.

```
boundaryField
{
//------------------------------------------------------------------------
    cyclicTop         //same BC for cyclicBottom/Left/Right
    {
```

```
        type            cyclic;
    }
//--------------------------------------------------------------------------
    innerRotWall            //rotating outer wall
    {
        type            zeroGradient;
    }
    outerStatWall           //stationary inner wall
    {
        type          zeroGradient;
    }
//--------------------------------------------------------------------------
}
```

C.12. OpenFOAM in CGS Mode

Running in CGS (centimetre-gram-second) mode required adding a new `controlDict` file to the `$FOAM_INST_DIR/.OpenFOAM/$WM_PROJECT_VERSION/` directory on the local computer. Here `$FOAM_INST_DIR` is the relevant OpenFOAM® installation directory, and `$WM_PROJECT_VERSION` is the version of OpenFOAM®. In this file, `unitSet` is assigned to `CGS`. Standard coefficients in the CGS system also had to be included. The necessary excerpt for this file is given below.

```
DimensionedConstants
{
unitSet             CGS; // SI // USCS

CGSCoeffs
{
  universal
    {
      c         c [ 0 1 -1 0 0 0 0 ] 2.99792e+10; //speed of light in vacuum
      G         G [ -1 3 -2 0 0 0 0 ] 6.67429e-8; //gravitational constant
      h         h [ 1 2 -1 0 0 0 0 ] 6.62607e-27; //Planck's constant (erg.s)
    }
  electromagnetic
```

```
    {
      e         e [ 0 0 1 0 0 1 0 ] 4.803204e-10; //elementary charge (statC)
    }
  atomic
    {
      me        me [ 1 0 0 0 0 0 0 ] 9.10938e-28; //electron mass (g)
      mp        mp [ 1 0 0 0 0 0 0 ] 1.67262e-24; //proton mass (g)
    }
  physicoChemical
    {
      mu        mu [ 1 0 0 0 0 0 0 ] 1.66054e-24; //atomic mass unit (g)
      k         k [ 1 2 -2 -1 0 0 0 ] 1.38065e-16; //Boltzman constant
    }
  standard
    {
      //Standard pressure
      Pstd      Pstd [ 1 -1 -2 0 0 0 0 ] 1000000; //1 bar (barye)
      //Standard temperature [degK]
      Tstd      Tstd [ 0 0 0 1 0 0 0 ] 298.15; //same as SI unit system
    }
}
```

C.13. in.liggghts_init

Input script for LIGGGHTS. This particular script was used to initialise the particles in the volume before the coupled model could run. The reason this was done, was to allow the particle system to settle down and "equilibrate" to avoid unrealistic energy or velocity values at the start of the coupled run. Here the hash-tag symbol (#) denotes a comment line that only serves to add information, and is not a part of the executable code.

```
echo            both
atom_style      sphere
atom_modify     map array
processors      1 1 1       #single processor job
boundary        p f p       #p for periodicity in x and z directions
newton          off
```

```
communicate     single vel yes
units           cgs         #centimeter, gram, second

region          boundingBox block 0. 0.005 1.1 1.105 0. 0.005  units box
create_box      1 boundingBox

#too big a bin size creates "neighbour list overflow error"
neighbor        0.00005 bin
neigh_modify    delay 0
#----------------------------------------------------------------------
#Material properties required for granular pair styles
#Zirconia modulus = 88 GPa (88e10 in cgs units: 1 Pa = 10 dyne/cm^2)
fix        m1 all property/global youngsModulus peratomtype 88e7
fix        m2 all property/global poissonsRatio peratomtype 0.3
fix        m3 all property/global coefficientRestitution peratomtypepair 1 0.8
fix        m4 all property/global coefficientFriction peratomtypepair 1 0.05
#characteristicVelocity needed for gran/hooke/history
fix        m5 all property/global characteristicVelocity scalar 0.014
#----------------------------------------------------------------------
variable        diam equal 1.5e-4             #1.5 microns (cgs units)
variable        radNew equal (${diam}/2)
variable        density equal 6               #g/cm^3 with cgs units
variable        allCutoffs equal 1.54e-4      #40 nanometres + r1/2 + r2/2

#hybrid-overlay combines different pair_styles together (e.g. granular and
colloid)
pair_style      hybrid/overlay gran/hooke/history tangential_damping on
rolling_friction off cohesion off colloid/limit ${allCutoffs}
yukawa/colloid/limit 1.0408e6 ${allCutoffs}

pair_coeff      * * gran/hooke/history
#colloid potential with minimum distance limit
pair_coeff      * * colloid/limit 9.24e-13 2.78e-8 ${diam} ${diam} 1e-7
${allCutoffs}
#yukawa/colloid potential with minimum distance limit, and A = 3.6e-10 J/m
pair_coeff      * * yukawa/colloid/limit 3.6115e-5 ${allCutoffs} 1e-7
#----------------------------------------------------------------------
timestep        0.0000000001
#make sure number is correct so DEM and CFD output files at same time
variable   tsCoupling equal 1000000000
```

```
fix       gravi all gravity 0. vector 0.0 0.0 -1.0
#-----------------------------------------------------------------------
#wall boundaries
fix       innerBasicWall all wall/gran/hooke/history primitive type 1 yplane
1.1 varRotate x time_varying_omega clamp tangential_damping on
rolling_friction off cohesion off
fix       outerBasicWall all wall/gran/hooke/history primitive type 1 yplane
1.105 tangential_damping on rolling_friction off cohesion off
#-----------------------------------------------------------------------
#region and insertion
fix       pts1 all particletemplate/sphere 1 atom_type 1 density constant
${density} radius constant ${radNew}
fix       sphereOne all particledistribution/discrete 1 1 pts1 1.0

region    insertionBox block 0. 0.005 1.100085 1.104915 0. 0.005 units box
group     nve_group region insertionBox

#for particle fraction of 20%, need 14147 particles (50um cubic box)
fix       ins nve_group insert/pack seed 1 distributiontemplate sphereOne
insert_every once overlapcheck yes maxattempt 10 vel constant 0. 0. 0.
particles_in_region 14147 region insertionBox ntry_mc 10000
#-----------------------------------------------------------------------
#apply nve integration to all particles inserted as single particles
fix       particleIntegration nve_group nve/sphere
#checks if timestep exceeds a fraction of Rayleigh and Hertz timesteps
fix       ts all check/timestep/gran 10000 0.01 0.01
#-----------------------------------------------------------------------
#output settings, include total thermal energy
compute          ke_rot all erotate/sphere
thermo_style     custom step atoms ke c_ke_rot vol evdwl ecoul
thermo           10000
thermo_modify    lost ignore norm no
compute_modify   thermo_temp dynamic yes
#-----------------------------------------------------------------------
#insert the first particles so that dump is not empty
run       1
dump      dmp all custom 1000000 ../DEM/post/dump.liggghts_box_init id type
type x y z ix iy iz vx vy vz fx fy fz omegax omegay omegaz radius
unfix     ins   #stop inserting particles
```

```
run        1000000 upto      #run system for this number of timesteps

#force system values to zero before writing particle data
set        region boundingBox vx 0.0 vy 0.0 vz 0.0
set        region boundingBox omegax 0.0 omegay 0.0 omegaz 0.0

write_restart    liggghts.restart.box
```

C.14. in.liggghts_init_first_coupling

LIGGGHTS input script used for the DEM portion of the coupled run. It differs from the previous script in that much of the information on the initialised particles is read in from a "restart" file generated by the previous script. Here the hashtag symbol (#) denotes a comment line that only serves to add information. It is not a part of the executable code.

```
echo             both
atom_style       sphere
atom_modify      map array
processors       2 3 2       #12-core job
boundary         p f p       #p for periodicity in x and z directions
newton           off
communicate      single vel yes
units            cgs         #centimeter, gram, second

#read the restart file
read_restart     ../DEM/liggghts.restart.box
#set time step count back to 0 so force dumps match CFD
reset_timestep   0

#too big a bin size creates "neighbour list overflow error"
neighbor         0.00005 bin
neigh_modify     delay 0
#-----------------------------------------------------------------------
#Material properties required for granular pair styles
#Zirconia modulus = 88 GPa (88e10 in cgs units: 1 Pa = 10 dyne/cm^2)
fix        m1 all property/global youngsModulus peratomtype 88e7
```

```
fix       m2 all property/global poissonsRatio peratomtype 0.3
fix       m3 all property/global coefficientRestitution peratomtypepair 1 0.8
fix       m4 all property/global coefficientFriction peratomtypepair 1 0.05
#characteristicVelocity needed for gran/hooke/history
fix       m5 all property/global characteristicVelocity scalar 1.4
#------------------------------------------------------------------
variable        diam equal 1.5e-4             #1.5 microns (cgs units)
variable        radNew equal (${diam}/2)
variable        density equal 6               #g/cm^3 with cgs units
variable        allCutoffs equal 1.54e-4      #40 nanometres + r1/2 + r2/2

#pair_style not needed because specified in restart file
#but pair_coeff are not in restart file

pair_coeff      * * gran/hooke/history

#colloid potential with minimum distance limit
pair_coeff      * * colloid/limit 9.24e-13 2.78e-8 ${diam} ${diam} 1e-7
${allCutoffs}
#yukawa/colloid potential with minimum distance limit, and A = 3.6e-10 J/m
pair_coeff      * * yukawa/colloid/limit 3.6115e-5 ${allCutoffs} 1e-7
#------------------------------------------------------------------
timestep        0.0000000025
#make sure number is correct so DEM and CFD output files at same time
variable        tsCoupling equal 5000000
#make sure DEM and CFD output forces at same time (smaller interval)
variable        tsCouplingHalf equal ${tsCoupling}/2

fix       gravi all gravity 981 vector 0.0 0.0 -1.0
#------------------------------------------------------------------
#wall boundaries
fix       innerBasicWall all wall/gran/hooke/history primitive type 1 yplane
1.1 varRotate x time_varying_omega clamp store_force yes tangential_damping on
rolling_friction off cohesion off  #force not needed in initialisation phase
fix       outerBasicWall all wall/gran/hooke/history primitive type 1 yplane
1.105 tangential_damping on rolling_friction off cohesion off

#write wall forces - used with store force
compute   p all reduce sum f_force_innerBasicWall[1] f_force_innerBasicWall[2]
f_force_innerBasicWall[3]
```

```
fix       bb all ave/time 1 1 ${tsCouplingHalf} c_p[1] c_p[2] c_p[3] file
../DEM/stressFile3_basic.txt
#-----------------------------------------------------------------------
#cfd coupling
fix       cfd all couple/cfd couple_every 100 mpi   #new v.2.4.4
fix       cfd2 all couple/cfd/force/implicit
#-----------------------------------------------------------------------
#region and insertion
fix       pts1 all particletemplate/sphere 1 atom_type 1 density constant
${density} radius constant ${radNew}
fix       sphereOne all particledistribution/discrete 1 1 pts1 1.0

region    insertionBox block 0. 0.005 1.100085 1.104915 0. 0.005 units box
group     nve_group region insertionBox
#-----------------------------------------------------------------------
#apply nve integration to all particles inserted as single particles
fix       particleIntegration nve_group nve/sphere
#checks if timestep exceeds a fraction of Rayleigh and Hertz timestep
fix       ts all check/timestep/gran ${tsCoupling} 0.01 0.01
#-----------------------------------------------------------------------
#output settings, include total thermal energy
compute          ke_rot all erotate/sphere
thermo_style     custom step atoms ke c_ke_rot vol evdwl ecoul
thermo           ${tsCoupling}
thermo_modify    lost ignore norm no
compute_modify   thermo_temp dynamic yes
#-----------------------------------------------------------------------
#insert the first particles so that dump is not empty
dump      dmp all custom ${tsCoupling} ../DEM/post/dump.box_gran_cfd id type
type x y z ix iy iz vx vy vz fx fy fz omegax omegay omegaz radius
```

APPENDIX D: DESCRIPTION OF THE CFDEMSOVLERPISO SOLVER

D.1. EQUATIONS FOR "MODEL A" FORMULATION

Governing equations for the fluid phase of the Model A and B formulations are repeated here for the sake of convenience. The generic continuity equation is given by Equation D.1. Equations specific to Model A are given by Equation D.2 (Zhou et al., 2010). Equations with a, b, and c denote the momentum equation, the volumetric particle-fluid interaction force, and the DEM particle-fluid interaction force on particle *i* respectively.

$$\frac{\partial(\varepsilon_f)}{\partial t} + \nabla \cdot (\varepsilon_f \boldsymbol{u}) = 0 \tag{D.1}$$

For Model A:

$$\frac{\partial(\rho_f \varepsilon_f \boldsymbol{u})}{\partial t} + \nabla \cdot (\rho_f \varepsilon_f \boldsymbol{u}\boldsymbol{u}) = -\varepsilon_f \nabla p - \boldsymbol{F}_{pf}^{A} + \varepsilon_f \nabla \cdot \boldsymbol{\tau} + \rho_f \varepsilon_f \boldsymbol{g} \tag{D.2a}$$

where $$\boldsymbol{F}_{pf}^{A} = \frac{1}{V_{cell}} \sum_{i=1}^{n} \left(\boldsymbol{f}_{drag,i} + \boldsymbol{f}_i^{"} \right) \tag{D.2b}$$

$$\boldsymbol{f}_{pf,i} = \boldsymbol{f}_{drag,i} + \boldsymbol{f}_{\nabla p,i} + \boldsymbol{f}_{\nabla \cdot \tau,i} + \boldsymbol{f}^{"} \tag{D.2c}$$

and for Model B:

$$\frac{\partial(\rho_f \varepsilon_f \boldsymbol{u})}{\partial t} + \nabla \cdot (\rho_f \varepsilon_f \boldsymbol{u}\boldsymbol{u}) = -\nabla p - \boldsymbol{F}_{pf}^{B} + \nabla \cdot \boldsymbol{\tau} + \rho_f \varepsilon_f \boldsymbol{g} \tag{D.3a}$$

where $$\boldsymbol{F}_{pf}^{B} = \frac{1}{\varepsilon_f V_{cell}} \sum_{i=1}^{n} \left(\boldsymbol{f}_{drag,i} + \boldsymbol{f}_i^{"} \right) - \frac{1}{V_{cell}} \sum_{i=1}^{n} \left(\rho_f V_{p,i} \boldsymbol{g} \right) \tag{D.3b}$$

$$\boldsymbol{f}_{pf,i} = \frac{\left(\boldsymbol{f}_{drag,i} + \boldsymbol{f}_i^{"} \right)}{\varepsilon_f} - \rho_f V_{p,i} \boldsymbol{g} \tag{D.3c}$$

Here, for brevity, $\boldsymbol{\tau}$ represents viscous shear stress tensor, V_{cell} is the CFD cell volume, $f_{pf,i}$ the total fluid-particle interaction force on an individual particle *i*, and $\boldsymbol{f}_i^{"}$ is the sum of other, not-so-dominant, particle-fluid interaction forces such as: buoyancy, virtual mass, Saffman lift, Magnus force, etc. Generally, the drag, pressure gradient, and viscous forces are regarded as the dominant particle-fluid interaction forces (Zhou et al., 2010).

CFD coupling is achieved at the computational cell level with the volumetric particle-fluid interaction force ($\boldsymbol{F}_{pf}$), which is constructed from the particle-based forces. For the solid phase in DEM, this is achieved via the particle-fluid interaction forces, $\boldsymbol{f}_{pf,i}$.

In the CFDEM code, Equation D.2b is re-arranged to give (Goniva et al., 2010)

$$\boldsymbol{F}_{pf}^{A} = \rho_f K_{pf} \left(\boldsymbol{u}_f - \boldsymbol{u}_p \right) \tag{D.4}$$

where K_{pf} is the momentum exchange co-efficient. The particle-fluid interaction forces are lumped together into this term. For numerical reasons, this term is split into an implicit and an explicit term. In the code of the coupled solver (`cfdemSolverPiso`), K_{pf} is labelled `Ksl` (s for solid, l for liquid).

D.2. CODE FOR SOLVER VERSION 2.5.3

The entire code for version 2.5.3 of the `cfdemSolverPiso` solver is given below in the shaded boxes. Explanations of what the code segment mean are given for portions of the code. This version was intended to work with LIGGGHTS v.2.3.2 and OpenFOAM® v.2.01. Terms specific to the software code are highlighted in a different font style in the text.

`cfdemSolverPiso` is an evolution of OpenFOAM's `pisoFoam` solver. This means it is a transient solver for incompressible flow, using the PISO algorithm for pressure-velocity coupling. It can handle laminar flow, or either RAS or LES turbulence modelling. The necessary model is selected at run time. This solver version is designed specifically for implicit handling of the particle momentum exchange. Ferziger and Perić (2002) give a fairly standard overview of the PISO algorithm, but OpenFOAM® uses a notation and form closer to the theses of Jasak (1996) and Rusche (2002). For more information on how the OpenFOAM® solvers relate to the Rhie-Chow formulation, see Kärrholm (2008).

Note that the standard indentation of the lines of code has been altered slightly to improve readability. Some lines showing "additional information" that do not form part of the executable code (lines traditionally starting with `//`) have been omitted to reduce clutter. For the same reason, all references to the `clockModel` procedure that generates time usage statistics have been removed.

D.2.1. INITIALISATION

These header files contain source code for common tasks that are used in numerous applications. They are loaded now at the beginning of the run.

```
#include "fvCFD.H"
#include "singlePhaseTransportModel.H"
#include "turbulenceModel.H"

#include "cfdemCloud.H"
#include "implicitCouple.H"
#include "clockModel.H"

// * * * * * * * * * * * * * * * * * * * * * * * * * * * * * * * * * * * * //
```

Start of the main solver programme. More common header files are loaded. The mesh, variable value fields (e.g. velocity, pressure, density), and time are initialised now.

```
int main(int argc, char *argv[])
{
    #include "setRootCase.H"
    #include "createTime.H"
    #include "createMesh.H"
    #include "createFields.H"
    #include "initContinuityErrs.H"
```

Create the `particleCloud` instance of the `cfdemCloud` class.

```
    #include "readGravitationalAcceleration.H"
    cfdemCloud particleCloud(mesh);
    #include "checkModelType.H"
```

D.2.2. START TIME LOOP

Use the `runTime` object to control time stepping. The Courant (CFL) number is calculated now.

```
    while (runTime.loop())
    {
        Info<< "\nStarting time loop\n" << endl;
        Info<< "Time = " << runTime.timeName() << nl << endl;
        #include "readPISOControls.H"
        #include "CourantNo.H"
```

D.2.3. PARTICLE HANDLING

Particles values are updated when the `particleCloud` is evolved. The `Ksl volVectorField` (internal value field) is updated, as an implicit momentum source in this case. Boundary values of the `Ksl` field are then corrected. `Ksl`, defined in section 3.5.4 of this thesis, is the momentum exchange coefficient for the cell (labelled K_{pf}).

```
    particleCloud.evolve(voidfraction,Us,U);

    Info << "update Ksl.internalField()" << endl;
    Ksl.internalField() = particleCloud.momCoupleM(0).impMomSource();
    Ksl.correctBoundaryConditions();
```

Print out particle-related information for de-bugging purposes.

```
    #include "solverDebugInfo.H"
```

D.2.4. MOMENTUM PREDICTOR STEP

Set up the linear algebra for the momentum equation. This is an implicit velocity prediction. However, `phi`, the conservative flux of `U`, is handled explicitly using the last known value of `U`. Two tensor-derivative classes are employed; `fvc` (finiteVolumeCalculus) performs an explicit evaluation from pre-determined data and returns a geometric tensor field, whereas `fvm` (finiteVolumeMethod) returns a matrix representation of the operation. These classes are designed for specific operations. For example, divergence terms are represented by surface integrals over the control volumes. Thus the divergence function call is `div(phi,Q)`, where `phi` is the flux, a field whose

values are recorded on the cell faces, and `Q` is the quantity being transported by the flux, and is a field whose values are on the cell centres. For this reason, this operation cannot be represented as a function call of the form `div(phi*Q)`. An implicit source is constructed by the function `Sp(a,Q)`, thus specifying the dependent variable `Q` that must be solved for.

```
        {
            fvVectorMatrix UEqn
            (
                fvm::ddt(voidfraction,U)
              + fvm::div(phi, U)
              + particleCloud.divVoidfractionTau(U, voidfraction)
             ==
              - fvm::Sp(Ksl/rho,U)
            );
```

`UEqn` is corrected for by pressure and an explicit `Ksl` (momentum exchange) term. The pressure term is handled slightly differently depending on the selected coupling model (A or B). It is solved using the last known value of `p` on the RHS. This gives a velocity field that is not divergence free, but approximately satisfies momentum (see Equation. 7.31 of Ferziger and Perić, 2002). `UEqn` is then relaxed before it is solved. `grad(p)` uses cell face values of pressure. The operation `==` represents the mathematical equality between the two sides. The code automatically re-arranges the equation (all implicit terms go into the matrix, while all explicit terms end up in the source vector). For this to be possible, the chosen operator (`==` in this case) must have the lowest priority. This also emphasises that this symbol represents equality of the equation, and not an assignment.

```
            if (modelType=="B")
                UEqn == - fvc::grad(p) + Ksl/rho*Us;
            else
                UEqn == - voidfraction*fvc::grad(p) + Ksl/rho*Us;

            UEqn.relax();

            if (momentumPredictor)
                solve(UEqn);
```

D.2.5. PISO LOOP

Loop over explicit pressure-corrector loops. Normally the number of loops is set by `nCorr`, but now it can vary depending on the timestep fraction (which is usually 1).

```
            int nCorrSoph = nCorr + 5 * pow((1-
particleCloud.dataExchangeM().timeStepFraction()),1);
            for (int corr=0; corr<nCorrSoph; corr++)
```

From the previous solution of velocity, the diagonal term (`A()`) of the matrix is extracted and the reciprocal (`rUA`) is stored. Note that the matrix co-efficients are functions of `U` due to the non-linearity of convection. Interpolation transforms cell-centred values (`volField`) to face values (`surfaceField`).

```
            {
                volScalarField rUA = 1.0/UEqn.A();

                surfaceScalarField rUAf("(1|A(U))",
fvc::interpolate(rUA));
                volScalarField
rUAvoidfraction("(voidfraction2|A(U))",rUA*voidfraction);
```

Take a Jacobi pass and update `U` (see Jasak Equation 3.137 and Rusche Equation 2.43). `UEqn.H` is the right-hand side of the `UEqn` minus the product of "the off-diagonal terms and `U`". Note that since the pressure gradient is not included in the `UEqn` above, this gives us `U` without the pressure gradient. Also note that `UEqn.H()` is a function of `U`.

```
                U = rUA*UEqn.H();
```

Calculate the fluxes by dotting the interpolated (approximate) velocity field (at cell faces) with face normals. The `&` represents the dot product, and `mesh.Sf()` are the face-normal vectors. The `ddtPhiCorr` term accounts for the divergence of the face velocity field by taking out the difference between the interpolated velocity and the flux.

```
phi = (fvc::interpolate(U*voidfraction) & mesh.Sf() )
    + fvc::ddtPhiCorr(rUAvoidfraction, U, phi);

surfaceScalarField phiS(fvc::interpolate(Us*voidfraction) & mesh.Sf());
```

```
surfaceScalarField phiGes = phi + rUAf*(fvc::interpolate(Ksl/rho) *
phiS);

if (modelType=="A")
    rUAvoidfraction =
volScalarField("(voidfraction2|A(U))",rUA*voidfraction*voidfraction);
```

D.2.6. NON-ORTHOGONAL PRESSURE CORRECTOR LOOP

Next is an internal loop that iteratively corrects for non-orthogonality. The non-orthogonal part of the Laplacian is calculated from the most recent solution for pressure, using a deferred-correction approach. The pressure equation is then generated.

```
                for (int nonOrth=0; nonOrth<=nNonOrthCorr; nonOrth++)
                {
                    // Pressure corrector
                    fvScalarMatrix pEqn
                    (
                        fvm::laplacian(rUAvoidfraction, p) ==
fvc::div(phiGes) + particleCloud.ddtVoidfraction()
                    );
                    pEqn.setReference(pRefCell, pRefValue);
```

The pressure is solved based on the current point in the non-orthogonal correction cycle.

```
                    if
                    (
                        corr == nCorr-1
                     && nonOrth == nNonOrthCorr
                    )
                    {
                        pEqn.solve(mesh.solver("pFinal"));
                    }
                    else
                    {
                        pEqn.solve();
                    }
```

On the last non-orthogonality correction, the flux is corrected for the next pressure-corrector step using the most up-to-date pressure. The `.flux` method includes contributions from all implicit terms of the `pEqn` (the Laplacian). The flux, `phiGes`, is the "total" or "combined" flux for both phases.

```
                    if (nonOrth == nNonOrthCorr)
                    {
                        phiGes -= pEqn.flux();
                    }

                } //end non-orthogonal corrector loop
```

D.2.7. VELOCITY CORRECTIONS

Continuity errors are now solved. Both the sum of $\nabla \cdot (\texttt{phiGes}) + \frac{d}{dt}(\alpha_f)$ per timestep, and the cumulative value over successive timesteps are calculated.

```
                #include "continuityErrorPhiPU.H"
```

Add pressure gradient to interior velocity field values and boundaries to correct the approximate velocity field. Note that this pressure is not just a small correction to a previous pressure, but is the entire pressure field. Compare this to the use of p' in Ferziger and Perić, 2002 (Equation 7.37).

```
                if (modelType=="B")
                    U -= rUA*fvc::grad(p) - Ksl/rho*Us*rUA;
                else
                    U -= voidfraction*rUA*fvc::grad(p) - Ksl/rho*Us*rUA;

                U.correctBoundaryConditions();

            } //end piso loop
        } //end of fluid component loop
```

Solve the turbulence equations and correct the turbulence viscosity. For laminar flow, the turbulent viscosity is zero, therefore the effective viscosity is the laminar viscosity.

```
        turbulence->correct();
```

D.2.8. WRAPPING UP

Run-time information is written, and timing statistics are gathered. Then the time loop is started all over again. When the `runtime.loop()` reaches its end, the simulation finishes as expected when a value of 0 is returned.

```
        runTime.write();

        Info<< "ExecutionTime = " << runTime.elapsedCpuTime() << " s"
            << "  ClockTime = " << runTime.elapsedClockTime() << " s"
            << nl << endl;

    } //end of while(runTime…)

    Info<< "End\n" << endl;

    return 0;
} //end of simulation
```

D.3. CONTINUITY ERROR CALCULATIONS

Because the solver runs through an iterative process to achieve the final result, there needs to be some measure of how accurate the solution is becoming with successive iterations. Typically, the solution is checked to see how well mass is conserved. Ideally the change in mass should be zero (conservation of mass), unless mass is allowed to exit or leave the system through a boundary. For iterative solutions, the value should at least tend towards zero to indicate a converging solution.

To calculate this, the divergence of the cell-face mass flux is taken for every cell, and then added together. Because the flux out of one cell flows into the adjacent cell, all the internal field value cancel, and so only the flux at the boundaries is considered. This technique is quick and easy to calculate. This net flux is called the "global" continuity error in OpenFOAM®. The “cumulative” error is the sum of these global errors over all the past simulation time steps (or iterations for steady-state solvers) Sometimes the magnitude of the error is also of importance, as this should also tend to zero for a

converging solution. This is monitored via the "sum local" term, which adds together the magnitude of the cell-face fluxes of individual cells over the entire domain.

For a multiphase system, mass conservation also needs to be checked for the secondary phase (e.g. particle) as well. For CFDEM's `cfdemSolverPiso` solver, this was done by taking the divergence of the combined particle-fluid flux. The time derivative of ε_f was added to this value as well, as it is also a measure of how well the different phase's mass was conserved.